Université de Limoges

University of Limoges

ED 614 - Chimie , Environnement, Géosciences, Agrosciences (CEGA)

EA 7500 – Laboratoire PEIRENE

A thesis submitted to University of Limoges
in partial fulfillment of the requirements of the degree of

Doctor of Philosophy

Chimie Organique

Presented and defended by

Bhavya Khurana

On March 21, 2022

Antimicrobial formulation and functionalization of photosensitizers for antimicrobial photodynamic therapy (aPDT)

Thesis supervisor: Professor Vincent Sol and Professor Dr. Mathias O. Senge

JURY:

President of jury
Mme. Céline FROCHOT DR CNRS, LRGP, Université de Lorraine

Reporters
M. Santi NONELL MARRUGAT, Professor, Applied Photobiological Chemistry, QS School of Engineering, Universidad Ramon Llull

Mme. Francesca GUINTINI, Lecturer in Medicinal Chemistry, School of Pharmacy and Biomolecular Sciences, Liverpool John Moores University

Nothing in life is to be feared, it is only to be understood. Now is the time to understand more, so that we may fear less. **— Marie Skłodowska-Curie**

I seem to have been only like a boy playing on the seashore and diverting myself in now and then finding a smoother pebble or a prettier shell than ordinary, whilst the great ocean of truth lay all undiscovered before me. **— Isaac Newton**

It is strange that only extraordinary men make the discoveries, which later appear so easy and simple. **— Georg C. Lichtenberg**

DEDICATION

To the loving memory of my younger brother Vishav who passed away 9 years ago…years ago when I found your unfinished bucket list, that gave me a dream to live for and a goal to achieve. I hope you were here, and I miss you a lot….

To my parents, Seema and Yogesh who dreamt my dreams, always being a guiding force for my lows and a laughing soul for the best I got. If it weren't for you, I couldn't have made it so far. Thanks for all the unconditional support and believing in me and being patient with the times we have been apart.

To my loving elder brother Dr. Sumit, you have been my inspiration for perseverance and dedication to get what you aim for. Thanks for being an ear to my endless rants.

To my friends, the new and the old ones, who always cheered for me; thanks for being there through thick and thin: Dhruv, Anant, Neha, Manish, Aditi, Shweta, Karolis, Jessica, Susan, Elisabeth, Marc, Asterios, Nitika, Alina, Chris, Aurore, Piotr, Claire, Emma, João, Harry, Dáire, Manu, Zoi, Nidia, Jérémy, Veronica, Abdechakour. Thanks for sharing all those good moments with me and making life something special

ACKNOWLEDGEMENTS

Since my childhood the only thing that remained constant to my curiosity was the practical science which prompted me to pursue it as a career but there was always a barrier to my dreams, first lack of support to local PhD programs in science in my country and secondly as an international student to support myself and to manage things staying so far away from home. With Professor Senge's guidance I was able to apply for a great opportunity of a PhD position in project POLYTHEA whilst doing a M.Sc. research project with him. The road to PhD was still a few baby steps away when after being on the wait list, I finally got this prestigious PhD position in project POLYTHEA with Professor Vincent Sol in University of Limoges and Professor Dr. Mathias O. Senge in Trinity College Dublin.

Over the past three years of my PhD (2019-2022) several treasured memories will always stay with me, engraved in my heart. All the while handling the COVID repercussions and restrictions, the possibility of my manuscript work coming together is not only me but involves many different people, who have contributed in various but imperative ways. This journey would not have been possible without the support of all the lovely people including my mentors, my colleagues, and my family.

Firstly, I express a special gratitude to all the members of the jury and especially, Dr. Francesca Giuntini and Pr. Santi Nonell for accepting to be the referees and for investing time in the evaluation of my work.

I would also like to acknowledge the coordinator and manager of the project, Dr. Stéphanie Leroy-Lhez for giving me a chance to showcase my abilities and to learn and develop my scientific skills in Europe. A big thanks to Ms. Aurore Berthier for being a helping hand in literally everything, my experience in France has been amazing and easy because of you.

With a deep sense of gratitude, I would like to convey thanks to Pr. Vincent Sol, our UNILIM lab-head, for accepting me to join his group as a part of this project. The first thing he told me was I was the first ever Indian PhD student in chemistry with his lab group and with that I wanted him to feel proud to have me onboard. It has been my pleasure to be a member in your team. My French experience of PhD has been a smooth and enjoyable one with your support and guidance throughout. I will always fall short of words to express my gratitude towards Pr. Senge, who is my secondary supervisor, without him nothing was possible. A few years back

he met me in India as a part of visit to my university and a very brief interaction with him, ended up being the best thing ever happened to my life. He has been a guiding force for me to secure and complete my PhD, your care, and your vision for your students to succeed is why I have grown to my career and goals. Thanks for believing in me and trusting me to be part of

his amazing tetrapyrrole group also known famously as the "Senge group"

I would like to extend my gratitude towards the Senge team members Dr. Chris Kingsbury who helped with crystal structure evaluations and proofread my manuscript and Ms. Charlotte Vernisse who has helped me with the microbiological studies. All whilst doing the PhD, POLYTHEA gave me an opportunity to interact with people of different disciplines and academic backgrounds and my dear friends, the POLYTHEA fellows Emma, Zoi, Dáire, João, Nidia, Harry, Claire, Piotr, and Manuel. The discussions and brainstorming sessions on scientific problems as well the awesome outings to explore different cities and restaurants will be memories I would cherish for life. My special thanks to the Limoges students, Veronica, Abdechakour, and, especially, to Jérémy and the Trinity College Dublin students, Karolis, Jessica, Susan, Elisabeth, Marc, Asterios, Nitika, Alina, and Chris who made my journey throughout so easier and fun.

My very special thanks to Dhruv, my partner in crime from 2 years now, thanks for all the rides to and from college, lovely dinners you made for me and listening to my endless chitter chatters and being there for me always.

I fall short of words to express my gratitude for the support and strength that my family has given me all this while. Thank you, Papa, Mumma, and Sumit, the true and the great supporters of my life. I always knew that you believed in me and wanted the best for me. I would not have made it this far without you. Hope I made you all proud.

PUBLICATIONS

Publications covered in this manuscript.

- H. C. Sample, G. Emandi, B. Twamley, N.Grover, **B. Khurana**, V. Sol, M.O. Senge, Synthesis and Properties of BODIPY Appended Tetraphenylethylene Scaffolds as Photoactive Arrays, European Journal of Organic Chemistry, 2021, DOI: 10.1002/ejoc.202100629

- N. Grover, G. Emandi, B. Twamley, **B. Khurana**, V. Sol, M.O. Senge, Synthesis and structure of *meso*-substituted |20π] – Dibenzihomoporphyrins, European Journal of Organic Chemistry, 2020, DOI: https://doi.org/10.1002/ejoc.202001165

- **B. Khurana**, T-S Ouk, R. Lucas, M. O. Senge and V. Sol, Photosensitizer-hyaluronic acid complexes for antimicrobial photodynamic therapy, Journal of Porphyrins and Phthalocyanines, 2021, recently submitted.

- Picture award-Basic sciences

   o **B. Khurana**, V. Sol, M.O. Senge, Crystals of photoactive BODIPY dye in pattern spreading as tree branches in a flask**.** IPA 2021 Photogenic Science Contest Winners, Category: Basic science, 2021. https://www.internationalphotodynamic.com/new-blog/2021/11/21/ipa-2021-photogenic-science-contest-finalists-and-winners

Crystals of photoactive BODIPY dye in pattern spreading as tree branches in a flask

Other publications.

- **B. Khurana**, P. Gierlich, A. Meindl, L. C. Gomes-da-Silva and M. O. Senge, Hydrogels: soft matters in photomedicine, Photochemical & Photobiological Sciences, 2019, DOI: 10.1039/C9PP00221A

CONFERENCES ABSTRACTS

Posters:

- **Khurana B.**; Ouk, T.; Viana, M.; Sol, V.; Senge, M. O. (2020):. Synthesis of Photosensitizers and their (Bio)polymeric Hydrogel Platforms for Photo-Antimicrobial Applications, *27th Lecture Conference on Photochemistry*, 9/14-15, online, Abstract PM-04.

- **Khurana B.**; Ouk, T.; Viana, M.; Sol, V.; Senge, M. O. (2020):. Synthesis of Photosensitizers and their (Bio)polymeric Hydrogel Platforms for Photo-Antimicrobial Applications, *Photodynamic Therapy and Photodiagnosis Update 2020*, 11/5-6, online.

- **Khurana B.**; Ouk, T.; Sol, V.; Senge, M. O. (2021):, Antimicrobial photosensitizers and their formulations: A potential solution to current world scenario, *ACS spring*, 04/1-31,online.

- Grover N.; Emandi G.; Twamley B.; **Khurana B.**; Ouk, T.; Sol, V.; Senge, M. O. (2021):, Synthesis and structure of *meso*-substituted [20π]-dibenzihomoporphyrins, *ACS spring*, 04/1-31,online.

- **Khurana B.**; Ouk, T.; Sol, V.; Senge, M. O. (2021):, Antimicrobial photosensitizers and their formulations: A potential solution to current world scenario, *5th Photodynamic Day*, 05/18,online P3

- Grover N.; Emandi G.; Twamley B.; **Khurana B.**; Ouk, T.; Sol, V.; Senge, M. O. (2021):, Synthesis and structure of *meso*-substituted [20π]-dibenzihomoporphyrins, *5th Photodynamic Day*, 05/18,online P2

- **Khurana B.**; Ouk, T.; Sol, V.; Senge, M. O. (2021):, Antimicrobial photosensitizers and their formulations: A potential solution to current world scenario, *HighLIGHTing Science meeting-polythea*, 05/27-28,online P10.

- **Khurana, B.**; Ouk, T.; Vernisse, C.; Viana, M.; Lucas, R.; Senge, M.O.; Sol, V. (2021): Antimicrobial photosensitizers and their formulations: A potential solution to current

world scenario. *19ᵗʰ Congress of the European Society for Photobiology*, 08/30–09/03, online. Abstract P-1.3.22

Oral presentations:

- **Khurana, B.**; Sol, V.; Senge, M.O. (2019):"Synthesis of photosensible hydrogel for photo-antimicrobial applications" at the for Doctoral School 614 PhD day (01.04.19), Poitier, France.

- **Khurana B.**; Ouk, T.; Sol, V.; Senge, M. O. (2020):, Antimicrobial photosensitizers and their formulations: A potential solution to current world scenario, *Polythea Entrepreneurial School-polythea*, 08/-12,online

- **Khurana, B.**; Sol, V.; Senge, M.O. (2021): Crystals of photoactive BODIPY dye in pattern spreading as tree branches in a flask**.** IPA 2021 Photogenic Science Contest Winners, Category: Basic science. 09/13

Rights

This creation is available under a Creative Commons contract:

« Attribution-Non Commercial-No Derivatives 4.0 International »

online at https://creativecommons.org/licenses/by-nc-nd/4.0/

Table of Contents

Chapter 3. Relative singlet oxygen yield of photosensitizers

Chapter 4. Synthesis of BODIPY derivatives for aPDT

Chapter 5. Experimentation

Chapter 1. Introduction to antimicrobial photodynamic therapy (aPDT)

1. Introduction

1.1. The "ANTIBIOTIC" era

Sir Alexander Fleming was a pioneer in the field of antibiotics; with the discovery of penicillin in 1928, he set forward a new era in medicine, allowing effective treatments for a range of microbial infections. Since then, as shown in Figure 1.1, several families of antibiotics have been approved by the European Union (EU) and United States (US) regulatory bodies. These medicines act by targeting the cell wall and disrupting synthetic protein processes in the microbiome.[1]
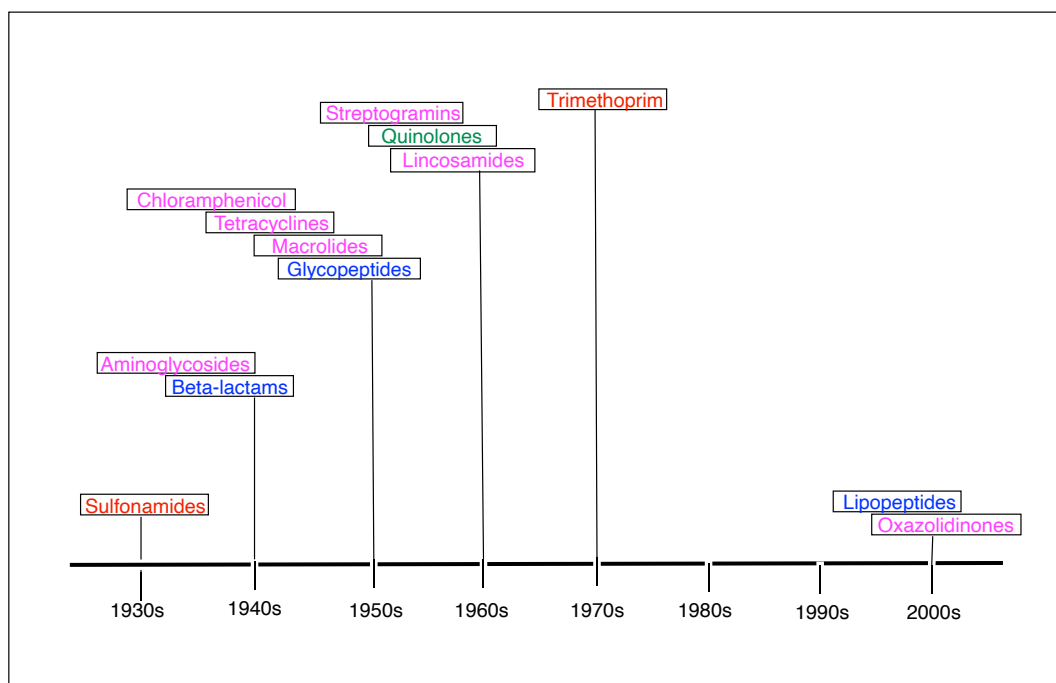
Figure 1.1. New classes of antibiotics. Colors refer to the principal target; red: inhibiting folic acid synthesis; blue: inhibiting the cell wall synthesis; pink: inhibiting the protein synthesis; green: inhibiting the DNA or RNA synthesis [1]

In the modern world, antibiotics are essential to handle infections by microbes and their related pathology.[2] However, antibiotics have become the "panacea" in medicine, used pre-emptively to treat infections of non-bacterial nature in humans, and to promote growth rates in animals.[3] Microbial infections that have been responsible for several deaths throughout centuries, threaten to return to a state of lacking effective treatment. As microorganisms replicate at rapid rates and mutate, an accelerated evolution

provides antimicrobial drug resistance; with selective pressure this becomes increasingly prevalent throughout the microbe population.[4] Resistance to drug treatment can co-occur via the formation of biofilms that penetrate the extracellular polymeric substances (EPS) auto-produced by the produced by the microorganisms, hindering penetration of the relevant antimicrobial drug.[5] As such, the adaptability of microorganisms to eradication strategies presents a danger to human health in addition to the environmental problems caused by stray biota. [6] Therefore, the American academy of periodontology (AAP) has recently embarked on a best evidence consensus (BEC) model of scientific inquiry that every new antimicrobial treatment is a valuable weapon to combat these infections caused by planktonic and biofilm-embedded microorganisms. [7]

The Gram stain allows a broad categorization of bacteria into two categories based on their surface composition. An example of such clinical drug-resistant isolates are the bacterial species of Gram-positive methicillin resistant-*Staphylococcus aureus* (MRSA), cephalosporin-resistant Gram-negative *Escherichia coli*, or carbapenem-resistant Gram-negative *Pseudomonas aeruginosa,* each a concerning source of global pandemics and environmental issues.[8,9] *Acinetobacter baumannii*, a Gram-negative bacterium often associated with hospital-acquired infections, acquires multi-drug resistance, which causes problems by triggering obstinate infections in wounds and burns, notably for people affected during military conflicts.[10] Other Gram-negative bacteria such as *Aggregatibacter sp*., *Porphyromonas sp.* and *Fusobacterium sp*. and Gram-positive ones, such as *Staphylococcus sp.* and Streptococcus *sp.,* lead to inflammation of tooth-supporting tissue, a disease known as periodontitis, and are often associated with antibiotic resistance.[11] Relative risks are localized; these have been mapped on a linear scale from lower values (green) to higher values (red), as shown in Figure 1.2.[12]
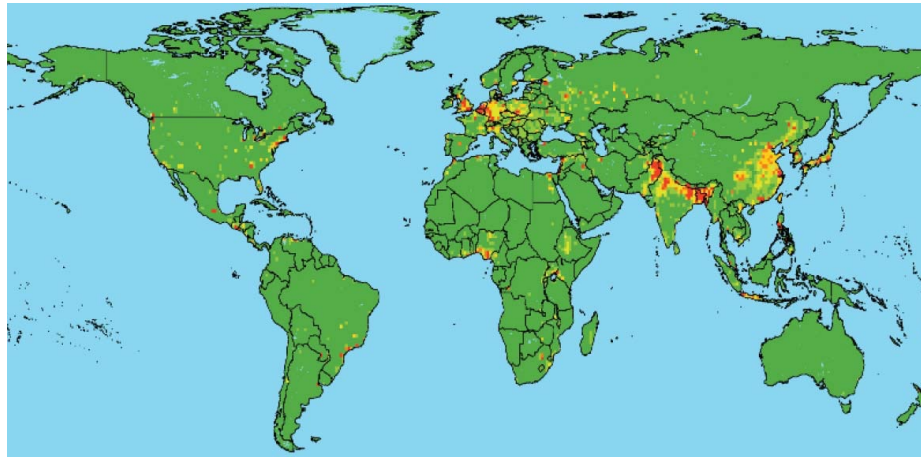
Figure 1.2. Global distribution of the relative risk of an emerging infectious disease event caused by drug-resistant pathogens. Categorized by standard deviations from the mean and mapped on a linear scale from green (lower values) to red (higher values).[12]*

*Reproduced with permission

Drug-resistant infections have a significant, continuing impact on health globally, uncountable mortality and morbidity and causing productivity loss of at least 1.5 billion euros in the EU and of about 5 billion dollars in the US per annum.[13]

The most prominent example is the current world situation involving a fight against COVID-19 and the SARS-CoV-2 virus, which has been evolving since its first report and has attained mutant forms.[14] The most recent as reported is the Omicron variant, which has caused a devastating loss of human lives and economic certainty.[15] Traditional treatments for viral infections involving chloroquine and its analogues (hydroxychloroquine) or remdesivir drug-based treatment have been used to treat COVID-19 patients.[16] In response to the deaths related to COVID-19 disease, effective new antiviral drugs or vaccinations have been expedited, but no strategy provides a 100% effective approach to maximize protection against these pathogens.[17]

An increased risk to human health is additionally caused by fungal strains (*e.g., Candida albicans*) that have developed drug resistance towards common antifungal agents such as amphotericin B, ketoconazole, itraconazol and fluconazole.[18] Even the protozoan parasitic infections undergo incomplete or ineffective treatment of leishmaniasis with drugs as prescribed, enhancing the drug resistance to as evaluated for *L. mexicana* and *L. braziliensis* isolates.[19]

Therefore, it is of utmost importance and priority to find alternatives to traditional antimicrobial therapies. In April 2014, the World Health Organization (WHO) had issued a warning on being on the cusp of a "post-antibiotic era" [20]. The growing resistance to

many antibiotics in recent years and the emergence of multidrug-resistant bacteria has diverted attention towards alternative antibacterial therapies. Among the novel, alternative therapies are bacteriophages, naturally occurring or synthetic antimicrobial peptides, and in recent years antimicrobial photodynamic therapy (aPDT) has been employed.[21,22]

1.1.1. A brief history of antimicrobial photodynamic therapy (aPDT)

In ancient times people have employed a traditional use of light combined with a photoactivated entity to treat skin diseases. It has been documented that in ~1200–2000 BC, Egyptian and Chinese physicians and Indian ayurvedic practitioners have used a combination of plant-based extracts and sunlight to treat skin infections, although many of these treatments are not scientifically validated.[23]

The modern approach to antimicrobial photodynamic therapy (aPDT) was first reported in 1900 by Oskar Raab in Munich when he observed that *Paramecium caudatum* was killed after staining with PS, acridine orange and subsequent exposure to light of suitable wavelengths.[24] Additional experimentation emphasized the importance of oxygen in the photodynamic action against the facultative anaerobic species *Proteus vulgaris*.[25] Figure 1.3 shows the results of the first antimicrobial photodynamic experiment using the eosin dye as a PS in combination with sunlight to kill *Streptococcus* bacteria.[26] In 1903, H. von Tappeiner and A. Jesionek treated skin tumors with topically applied eosin and white light. This phenomenon was coined "photodynamic action".[26, 27] At the onset of the 20th-century, Danish physician Niels Finsen proved the usage of photodynamic therapy by applying heat and light filtered through a carbon lamp to treat cutaneous *Lupus vulgaris*.[28]

Antimicrobial applications of the photodynamic process have been reignited in response to the first drug-resistant infections in the healthcare sector during the early 1990s.[29]

1.1.2. Antimicrobial photodynamic therapy (aPDT)

Photodynamic therapy (PDT) is clinically used as a minimally invasive therapeutic tool; cytotoxicity is induced by a light source that potentially exerts selective activity against malignant cells and infected tissue. This approach has found potential anti-microbial

uses in recent times against all types of microorganisms, such as Gram-positive and Gram-negative bacteria, fungi, parasites and even viruses.[30,31]

APDT alternatively known as photodynamic inactivation (PDI), or lethal photosensitization, or photodynamic antimicrobial chemotherapy (PACT), provides a possible way to eliminate microbe species efficiently, cost-effectively, and more importantly, without the associated mechanism of resistance.[32]

aPDT has several advantages over antibiotics. Firstly, aPDT offers precise targeting, and is considered triply site-specific due to: (1) preponderant association/uptake of PSs by the target cells compared to non-target cells, (2) the pharmacodynamic inertia of non-irradiated PSs, as well as (3) the site-confined irradiation of the infected area.[33] Consequently, systemic toxicity is largely absent outside the irradiated, PS-replete zone. Secondly, compared with antibiotics, no resistance is developed against aPDT PSs; even repeated treatment with aPDT did not lead to the selection of resistant strains.[34] This is due to the drug-light interval (the time between the PS and PDT) being too short for bacteria to develop resistance, and the near-absent dark toxicity, resulting in bacteria not having to engage adaptive survival mechanisms against the PSs. It is also difficult for bacteria to 'sense' that the oxidative stress emanates from the otherwise non-toxic PS, so any metabolic adaptations are directed elsewhere (e.g., antioxidant defense machinery).

Thirdly, targeted cells are eviscerated after PDT, rendering them too damaged to confer cross-generation adaptivity. Lastly, aPDT does not target a single site in bacteria, much different from conventional antibiotics. The reactive oxygen species (ROS) generated by aPDT targets various bacterial cell structures and other metabolic pathways.[35] In short, the treatment vector is perfect: precise, hyper-effective and unable to be guarded against, evaded, or learned from, while benign to surrounding tissue. These reasons underlie the potential utility of aPDT in combatting resistant strains in a non-minimally invasive and patient-friendly manner.

1.1.3.   aPDT against bacteria

The potential of aPDT against diseases of bacterial origin is vast, engaging many of the advantages as a treatment demonstrated above. This potential has not been exploited due to (a) the discovery and development of advanced antibiotics; (b) non-effectiveness against some well-known pathogens, especially Gram-negative bacteria, which have

poor results with known, traditional photosensitizing agents many of which are structurally like the crystal violet Gram stain.[36] The aPDT efficiency is therefore dependent on the structural entities of the cell wall of the target bacteria as described in detail in this section.

1.1.3.1. Gram-positive and Gram-negative bacteria

The bacterial domain has been classified into two subgroups based on their difference in the cell wall structure and the chemical composition, namely, Gram-positive, and Gram-negative bacteria, as differences in their Gram stain staining.[37]
As shown in Figure 1.3, the bacteria cell membrane is a complex multi-layered protective structure providing an innate immunity against the unpredictable and hostile environment. These structural differences between the cell walls of both kinds of bacteria reflect differences in their biochemical composition.[38]
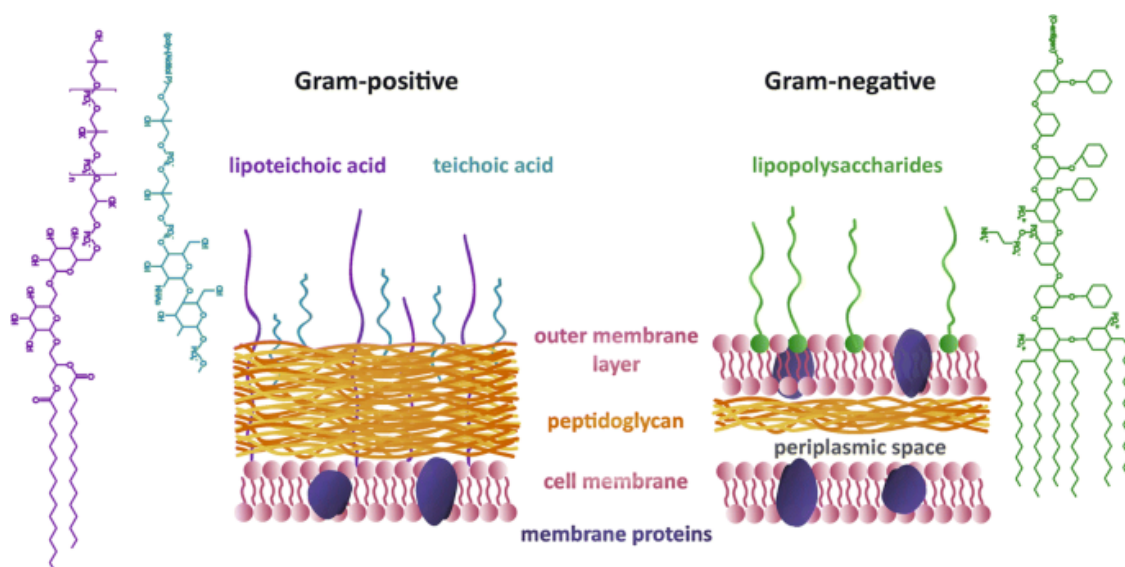
Figure 1.3. Schematic representation of the cell wall and cytoplasmic membrane structure in Gram-positive (left) and Gram-negative (right).[38]*
*Reproduced with permission

For Gram-positive bacteria, the principal constituent of the cell wall is multiple protective layers of peptidoglycan. *N*-Acetylglucosamine and *N*-acetylmuramic acid held together by peptide bridges constitutes the amino sugar backbone of such strains. This makes

up 40% to 80% of the cell wall weight, depending on the species, and has high tensile strength. Teichoic and teichuronic acids are also part of the cell wall of Gram-positive bacteria. Teichoic acids are polyol phosphate polymers, such as polyglycerol phosphate and polyribitol phosphate. Both acids are linked covalently to peptidoglycan.[38]

The peptidoglycan layer is also present in the cell wall of Gram-negative bacteria. Still, in contrast to Gram-positive bacteria encased with multiple layers of peptidoglycan, Gram-negative ones have only a single to a few macromolecular sheets. Indeed, the peptidoglycan makes up about 5% by weight of the Gram-negative cell wall, but it still plays a vital role as a solid protective barrier outside the cell membrane. The outer membrane component of Gram-negative bacteria has the predominant presence of lipids and proteins and some polysaccharides extending into the aqueous environment. This complex lipid-polysaccharide layer is known as lipopolysaccharide (LPS), a high molecular weight, powerfully negatively charged molecule. The outer membrane of Gram-negative bacteria has lipoprotein covalently linked to the diamino acid of the peptidoglycan, forming a complex called peptidoglycan-lipoprotein. Therefore, the lipoprotein is the bridge that joins the outer membrane to the cell wall peptidoglycan layer. Transport proteins (porins), another critical component of the cell wall of these bacteria, allow the passage of molecules through the outer membrane. This cell wall feature forms water-filled channels that work as a general or substrate-selective conduit for free diffusion of specific hydrophilic molecules, such as sugars and amino acids, and inorganic ions. The negative charge on LPS molecules provides a polyanionic external surface partly neutralized by divalent cations, such as Mg^{2+} and Ca^{2+} and is a connecting bridge adjacent to LPS molecules. The periplasmic space between the cell wall and the cell membrane is also important because it is a zone of tremendous enzymatic activity inside.[39]

1.1.4.   Mechanism of action in aPDT

The three essential elements of aPDT are: 1) a photosensitizer, 2) a source of light, and 3) molecular oxygen.[40]
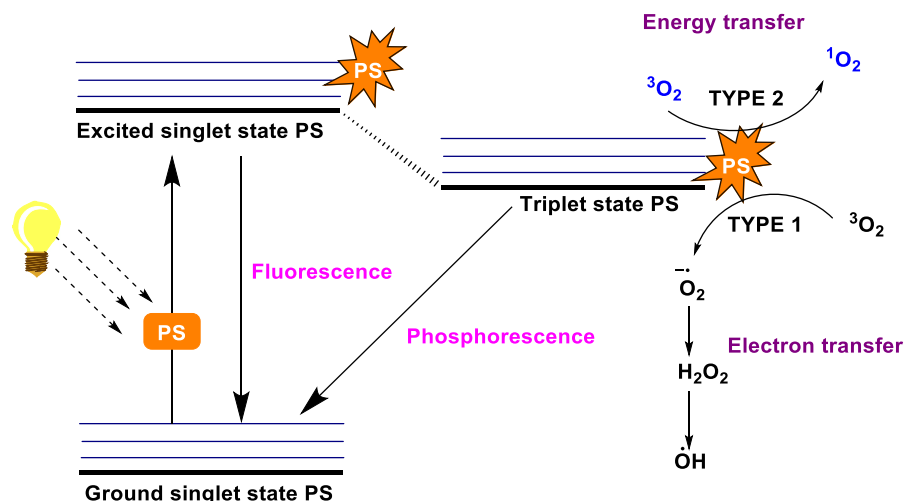
Figure 1.4. Schematic illustration of the main photophysical and photochemical processes involved in PDT.[117]

The photophysical processes taking place during aPDT are illustrated by the energy level diagram in Figure 1.4. The PS used in aPDT is a ground electronic singlet state (S_0) and, after irradiation with light of a suitable wavelength, is excited to a short-lived singlet state (S_m). The photosensitizer can return to the ground S_0-state, emitting the absorbed energy as fluorescence (used for diagnosis and imaging) or undergo intersystem crossing to the excited triplet state (T_1).[41] This transition is generally spin-forbidden, indicating that suitable PSs must have a high triplet-state quantum yield. The T_1-state is sufficiently long-lived to take part in different chemical reactions but will return to the S_0-state via phosphorescence or a non-radiative decay dependent on lifetime. Thus, our photosensitizer acts as a photocatalyst, promoted from its ground state to electronically excited state returns to that energy level via these three main pathways. Depending on the reactive species formed, aPDT is classified into two types. Type I relies on the interaction between the excited triplet state of photosensitizer ($^3PS^*$) and substrates from the target tissue. New radicals generated from photosensitizers and substrates interact with molecular oxygen and other molecules in the environment. In type II, the direct reaction of $^3PS^*$ and molecular oxygen gives rise to singlet oxygen [$^1O_2$], a highly reactive form of oxygen.[42,43]

1.1.5.   aPDT active photosensitizers

As established in the previous section a photosensitizer is a chromophore-based compound that can absorb photons from the incident light, thus producing ROS, a highly

active species. For clinical aPDT use, an ideal photosensitizer would possess the following properties:

- chemical purity and ease of synthesis for commercial use;
- photostability, high phototoxicity, low dark toxicity;
- chemical stability for transportation, storage and reconstitution;
- rapid exclusion from target tissues to minimize any side effect, minimal photosensitivity towards the subcutaneous tissues, good pharmacokinetic activity;
- the high quantum yield for ROS ($^1O_2$) generation;
- preferential association with bacteria versus mammalian host cells;
- suitable pharmacokinetics, and accumulation in bacteria or binding to the bacterial cell envelope.[44,45]

Typically, PSs are excited within the red part of the visible range <650 nm of light or closer to the near infra-red. First-generation PSs such as Photofrin are hampered by minimal light penetration of tissue. Second generation PSs, which absorb at longer wavelengths (>630 nm) like some synthetic or natural PSs where light penetrates tissue deeper without being impeded by other endogenous biomolecules, have a better activity for aPDT. Alternatively, third-generation photosensitizers, targeted PSs such as Visudyne (clinically used) are under development with enhanced sensitivity towards longer wavelengths of the illuminating light and better target specificity.[46]

PS binding to the bacterial cell and uptake is dependent on the type of bacterial species. Due to the unique structure of the cell envelope, Gram-positive pathogens are much more susceptible to anionic and neutral PS because of the thick but porous peptidoglycan layer on the outer surface. Gram-negative bacteria are less prone to take up exogenous compounds due to the extra outer cell membrane and the permeability barrier imparted by lipopolysaccharides.[47] Efficient antimicrobial candidate when tested in combination using the time-kill approach is achieved at a minimum of 2-log decrease or more in the number of colony-forming units.[48]

PSs used in aPDT are classified into four groups based on their structure and origin: synthetic dyes such as phenothiazinium dyes and borondipyrromethenes difluoroboradiazaindacene (BODIPY) dyes, tetra-pyrrole designs such as porphyrins, phthalocyanines and chlorins, natural PSs such as curcumin, hypericin, flavin,

chlorophyllin and phenalenone derivatives and nanostructures based on fullerenes and titanium oxides. Table 1.1 illustrates commonly studied antimicrobial PSs and sampled photodynamic properties.

Table 1.1. Commonly studied PSs and their photodynamic properties

Class	Example	Charge	Excitation maximum	Sample (bacteria)	Concentration of PS	Reduction of bacterial cultures	Ref.
Pheno-thiazinium	Methylene blue	Cationic	632nm	Dental plaques sample	25 µg/ml	8%	49
	Toluidine blue	Cationic	410nm	*S. mutans* *E. coli*	100 mg/l 35 µM	2-5 $\log_{10}$ 0.08 $\log_{10}$	50, 51
	Rose Bengal	Cationic	532nm	*E. faecalis* *P. aeruginosa*	10 µM	4 $\log_{10}$ 3 $\log_{10}$	52
	Dimethyl methylene blue	Cationic	635-652nm	*A. baumannii*	200 µM	2 $\log_{10}$	53
	New methylene blue	Cationic	635-652nm	*A. baumannii*	800 µM	3.2 $\log_{10}$	54
Natural PSs	Curcumin	Neutral	547nm	*S. mutans* *L. acidophilus*	0.75 to 5 g/l	$\geq$ 3 $\log_{10}$	55, 56
	Hypericin	Neutral	593nm	*S. aureus* *E. coli*	100 nM 1 µg/ml	4-5 $\log_{10}$ $\leq$ 0.2 $\log_{10}$	57, 58
	Flavin derivatives	Cationic	450nm	MRSA Enterohemorrhagic *E. coli*	50 µM 50 µM	5.1 $\log_{10}$ 6.5 $\log_{10}$	59
	Chlorophyllin	Neutral	400nm	*Bacillus cereus* *Listeria monocytogenes*	150 µM	2.4 $\log_{10}$	60
	Phenalenone	Neutral	363 nm	*S. Aureus* *E. faecalis*	5 µM 3 µM	9 $\log_{10}$ 3 $\log_{10}$	61
Tetra-pyrrole structures	Porphyrin derivatives	Cationic	446nm	*S. aureus* *P. aeruginosa* *E. faecalis*	10 µM 225 µM 100 µM	1-2 $\log_{10}$ 4 $\log_{10}$ No effect	62-64
	Phthalocyanine derivatives (Pc)	Neutral	670nm	*A. hidrophila*	2 mM	$\leq$ 0.5 $\log_{10}$	65
	Zn(Pc)	Cationic	690nm	*S. aureus* *P. aeruginosa*	64 ng/ml 26 µg/ml	5-6 $\log_{10}$ 5-6 $\log_{10}$	66-67
	Chlorin derivatives	Neutral	660nm	*S. aureus* *E. coli*	10 µg/ml 5 µg/ml	5 $\log_{10}$ 0.75 $\log_{10}$	68
	Chlorin derivatives	Cationic	532nm	*E. coli*	5 µg/ml	0.77 $\log_{10}$	69

1.1.6. Synthetic dyes

Phenothiazinium is a subgroup of synthetic dyes, and these PSs are planar, tricyclic, and aromatic molecules. which have been used in medicine for over 100 years.[70] The commonly used phenothiazinium dyes are methylene blue (MB) (**1.1**) and toluidine blue (TB) (**1.2**) as shown in Figure 1.6, have been used for their efficacy in aPDT due to the presence of the cationic charge, they have an affinity to bind to both Gram-negative and Gram-positive bacteria. MB and TB have been studied extensively for their effectiveness on planktonic bacteria and were tested against biofilm structures.[71]

Functionalization on phenothiazinium such as methylation induces a greater photo-inactivation and an increased production of ROS species. Recently, new derivatives such as dimethyl methylene blue (derived from MB) due to the presence of a high cationic charge have shown to be effective against bacterial cells.[72]

Other synthetic dyes are eosin Y (**1.3**), erythrosine (ERY) (**1.4**) and Rose Bengal (RB) (**1.5**) as shown in Figure 1.5; these have also been used as PSs for aPDT. These are anionic charged xanthene dyes derived from fluorescein.[73] These dyes show an absorption band in the green wavelength range of 480-550 nm and have shown significant activity against the production of biofilm growth as well and though they have demonstrated lower activity against Gram-negative bacteria, they are effective against the growth of Gram-positive bacteria.
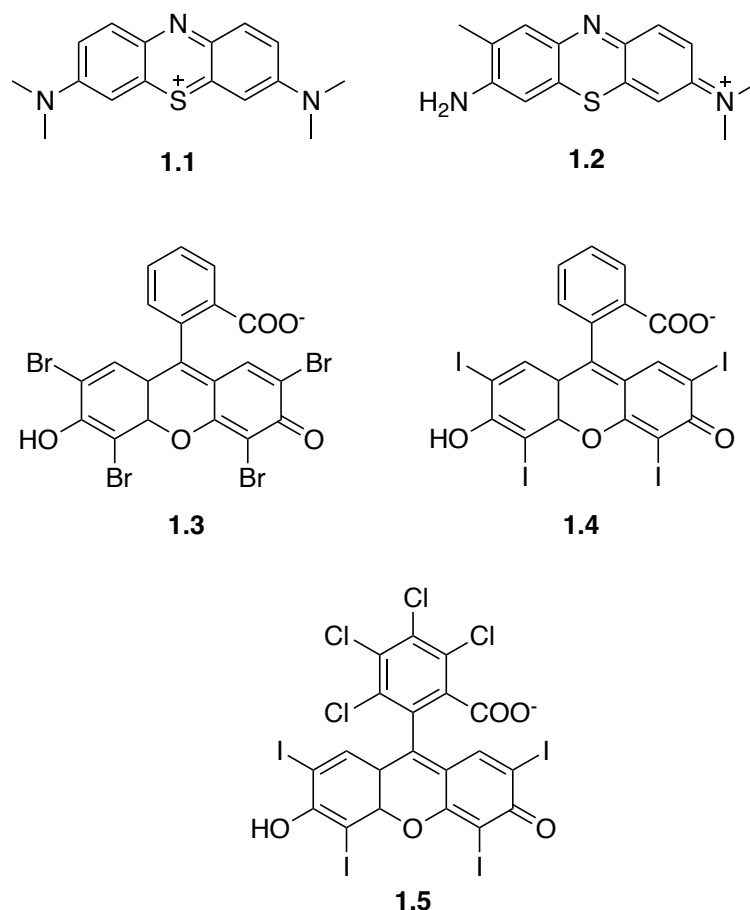
Figure 1.5. Chemical structure of Methylene Blue (**1.1**), Toluidine Blue (**1.2**), Eosin Y (**1.3**), Erythrosine (**1.4**) and Rose Bengal (**1.5**).

Compound **1.1** has been used in the sterilization of blood products since it has a high chemical affinity to nucleic acids and thus can be used against virus, including HIV, hepatitis.[74] Compound **1.2** has been predominantly used in the treatment of oral infections, for sterilizing dental cavities and root canals, and for treating periodontitis.[75]

Borondipyrromethenes difluoroboradiazaindacene (BODIPYs) (**1.6**) dyes as shown in Figure 1.6 have shown potential for antimicrobial inactivation and are used as components of antimicrobial coatings.[76] BODIPY dyes can be chemically modified to introduce negative or positive charges on the scaffold of this PS, and exhibit high singlet oxygen quantum yields, acting predominantly according to the Type II mechanism.[77] BODIPYs are well established as fluorescence imaging dyes in diagnostics as they possess intense color and fluorescence, high extinction coefficients, and do not undergo photobleaching.[78] Chemical modification of BODIPY dye leads to an increased excited triplet state and enhanced ROS formation. With appropriate modifications, BODIPY

dyes have been shown to have increased strength of interaction with bacterial target structures.[79]
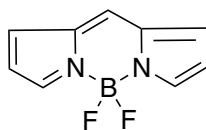
1.6

Figure 1.6. Chemical structure of BODIPY (**1.6**) dyes.

1.1.7.   Tetrapyrrole structures

Porphyrins (**1.7**) are a group of naturally occurring, intensely colored, tetrapyrrolic compounds as shown in Figure 1.7, which have found applications in several fields, ranging from fluorescence imaging to medicine.[80] Porphyrins have a strong absorption band around 400 nm (Soret band), and further absorption peaks between ~500-700 nm (Q-bands). Many porphyrin derivatives with different side groups have used as effective PSs for aPDT.
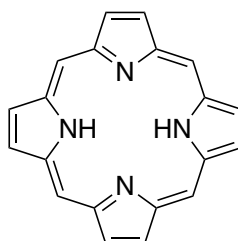
1.7

Figure 1.7. Chemical structure of porphyrin (**1.7**).

Introduction of cationic charge increases the predilection of the PS to the bacterial cell wall, hence mediating a better aPDT action against the bacterial strains. Porphyrins show several advantages over rival PSs; the absorption of light at 400 nm allows significant energy to be delivered, and the ease of modification around its molecular periphery allows the synthesis of charged derivatives with enhanced action against the microbes. An exemplar cationic PS based on porphyrin is TMPyP·4(I⁻) (5,10,15,20-tetrakis(1-methyl-4-pyridyl)porphyrin tetraiodide) (**1.8**) as shown in Figure 1.8, possessing a 4+ charge across the peripheral pyridinium rings.[81] It has been

demonstrated that this species has shown to be more active than the neutral/uncharged adduct of same porphyrin as against *B. cereus* endospores formation.[82]

1.8
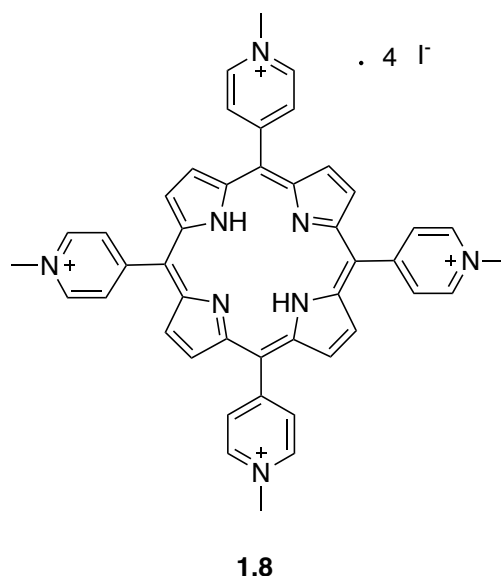
Figure 1.8. Chemical structure of TMPyP·4(I⁻) (**1.8**).

Chemical modifications on the parent TMPyP to introduce new functional groups, such as fluorine to alter electronic structure or carboxyl groups to increase water-solubility, give derivatives such as 5-(4-carboxy-10,15,20-tris(1-methylpyridinium-4-yl)porphyrin triiodide (Tri-Py⁺-Me-COOH, tricationic) (**1.9**), 5-(pentafluorophenyl)-10,15,20-tris(1-methylpyridinium-4-yl)-porphyrin triiodide (Tri-Py⁺-Me-PF, tricationic) (**1.10**) as shown in Figure 1.9.[82] This functionalization further enhances the action against bacterial endospore growth. This chemistry highlights opportunities to make more efficient PSs based on porphyrin macrocycles, using rational design, especially of ionic charge, to enhance antibacterial action with functionalities introduced in the macrocycle.
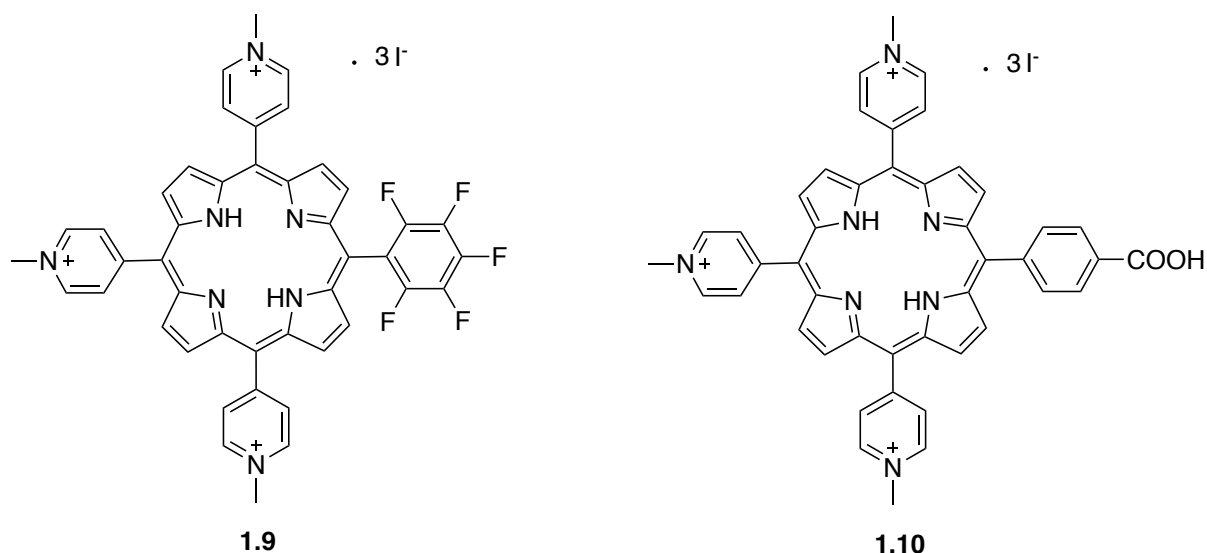
Figure 1.9. Tricationic derivatives a) Tri-Py⁺-Me-PF (**1.9**) (heavy atom) and b) Tri-Py⁺-Me-COOH (**1.10**).

Phthalocyanines (**1.11**) consist of four pyrrolic rings, connected via nitrogen atoms as shown in Figure 1.10. These PSs have higher absorption in the far-red region of the spectrum (650-700 nm) and hence has been used for applications where deep-tissue penetration by light is required.[83,84]
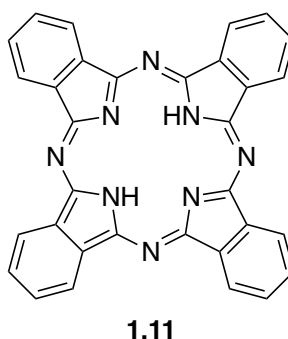
Figure 1.10. Chemical structure of phthalocyanine (**1.11**).

The addition of central metal ions, like Zn^{2+} (zinc phthalocyanine) (ZnPc) or Al^{3+} (aluminium phthalocyanine) (AlPc) have shown an enhancement in the production of singlet oxygen; ZnPc demonstrates a reported affinity for Gram-positive bacteria.[85,86] ZnPc, in conjunction with cationic groups or anti-membrane agents such as polymyxin or EDTA (ethylenediamine-tetraacetic acid), has been demonstrated as effective against Gram-negative bacteria.[87] Like the porphyrin macrocycle, phthalocyanine is amenable to chemical modification at the core and periphery, and enhancement of the aPDT activity of this macrocycle is actively researched. A few notable examples of

rationally designed molecules have been synthesized, which includes the water-soluble octa-cationic zinc Pc (**1.12**) shown in Figure 1.11, presumed to be effective against both Gram-negative and Gram-positive bacteria.[88] Also, it has been shown that cationic ZnPcs have a potency to eliminate *E. coli* from blood products, making it advantageous in sterilization.[89]

1.12
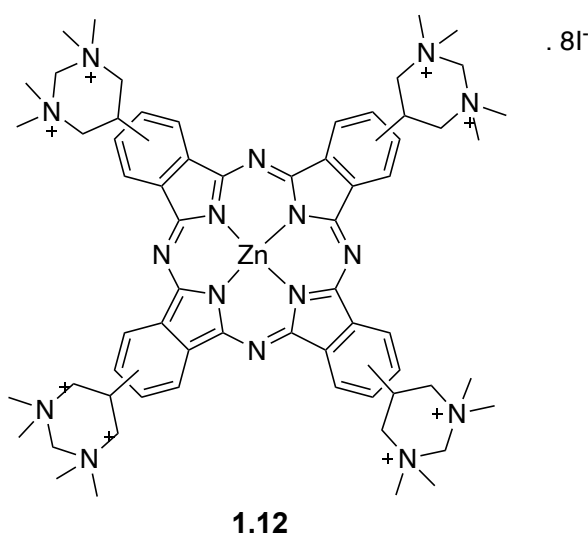
Figure 1.11. Chemical structure of octa-cationic phthalocyanine ligand (**1.12**).

Chlorins are second generation photosensitizers, having high photodynamic efficiency. E.g., chlorin *e6* (**1.13**) (C*e6*, Figure 1.12) – mediated aPDT has been shown to completely suppress the growth of *Porphyromonas gingivalis*, *Fusobacterium nucleatum*, and *Capnocytophaga gingivalis* and has also been shown to inhibit the human dental plaque species.[90] A significant reduction of clinical signs of redness and bleeding on probing (BOP) in periodontitis-induced beagle dogs has also been shown via the PS, C*e6*. Radachlorin® is an aqueous solution of three photosensitizers, including chlorin *e6* (90-95%) as the major ingredient, with sodium chlorin *p6* (5-7%); this has shown an effective PDT action against *Streptococcus mutans*.[91] Advantageous photophysical characteristics of this water-soluble chlorin mixture include the high quantum yield of singlet oxygen (75%), low toxicity in the dark, intense absorption band in the middle-red part of the spectrum, quicker kinetics in comparison with *Ce6* alone, and high phototoxicity make it uniquely powerful as a PDT therapeutic agent.[92]
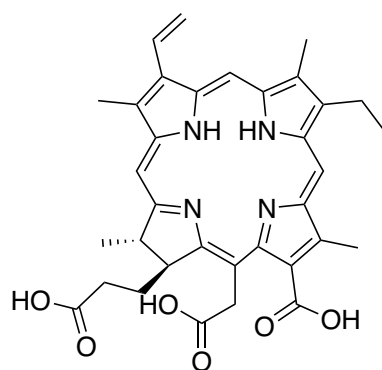
1.13

Figure 1.12. Chemical structure of chlorin *e6* (**1.13**).

1.1.8. Natural/semi-synthetic PSs

There are many naturally occurring compounds extracted from plants and other organisms which have potency as a photosensitizer upon absorption of white light or UV-A. Hypericin (**1.14**), curcumin (**1.15**) and chlorophyllin (semi-synthetic) (**1.16**) as shown in Figure 1.13 are three naturally derived compounds that have been extensively studied as photosensitizers over the years.[93,94]
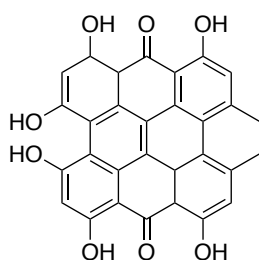
1.14
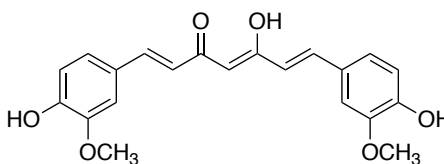
1.15
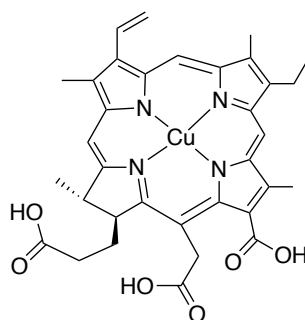
1.16

Figure 1.13. Chemical structure of hypericin (**1.14**), curcumin (**1.15**) and Cu-chlorophyllin (**1.16**).

Hypericum perforatum or St John's-wort is a plant that also demonstrates antiviral, antidepressant, antibacterial and antitumor characteristics.[95] It has been shown that

hypericin (**1.14**)-mediated aPDT renders Gram-positive bacteria inactive, including *Streptococci mutants*, *Lactobacilli mutants*, and *Propionibacterium acnes*.[96,89]. The photoactivity of hypericin against clinically isolated Gram-positive MRSA and *E. coli* produces extended-spectrum ß-lactamases.[89]

Curcumin (**1.15**) (Figure 1.13) is a natural PS isolated from the root of a plant called *Curcuma longa* having absorption in the range of 405-435 nm. It possesses a series of biological and pharmacological functions, being an antioxidant, having anti-inflammatory and anti-microbial properties and assisting in wound healing.[97] These innate properties of curcumin make it a favorable PS for the treatment of periodontal diseases. In terms of photo-biocidal effects, studies indicate that curcumin is 300 times more effective against the Gram-positive *S. aureus* than the Gram-negative *E. coli* and *Salmonella typhimurium*.[98]

Chlorophyllin (CHL) (**1.16**) refers to a family of derivatives of chlorophyll; cyclic tetrapyrroles with the heteroaromatic character of the underlying chlorin system. The reactivity of the peripheral substituents of this macrocycle allows facile modification of this molecule to introduce targeting functionalities.[99] CHL itself is not ideal as a PS, since the paramagnetic Cu^{2+} hinders the formation of long-lived excited states.[100] PSs derived from Cu-free CHL as shown in Figure 1.14, functionalized with three tertiary amines or three quaternary ammonium groups possessing the amphiphilic character with positive charge favors the compound to bind to the cell membranes and walls and aid in intracellular localization in mitochondria.[94]
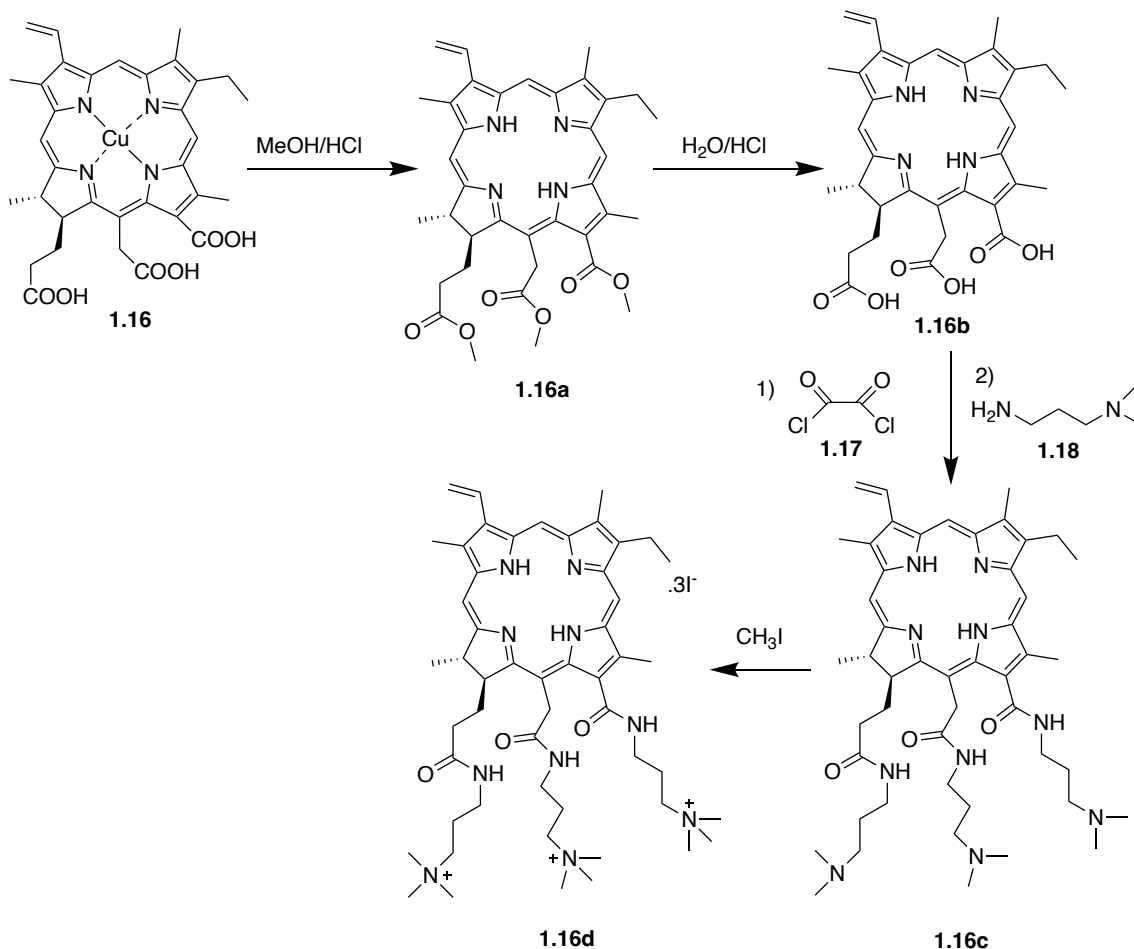
Figure 1.14. Synthetic route to chlorin with tertiary or quaternary ammonium groups. [94]

Popularity of this PS derives from the ease of semi-synthetic preparation; hydrophilic CHL can be isolated from water insoluble chlorophyll. Further synthetic steps allow these compounds to be tuned to optimum properties as a better PS.

1.2. Limitations of aPDT

It has been established that the advantages offered by aPDT could contribute to resolving the troubling issue of antimicrobial resistance and mutations by eliminating a spectrum of infectious microbes. However, the adoption of aPDT-active PSs still encounters significant challenges; these compounds are often poorly soluble in aqueous media, may lack photostability, and differ significantly in their pharmacological properties.[101] As planar, aromatic compounds the PSs are prone to π-π stacking and hydrophobic interactions, and majority of them aggregate in aqueous solution.[102]

The localization of PSs on the microorganism surface is dependent on several factors, with charge, molecular size, concentration of PSs, lipophilicity, and cell wall composition each playing a role.[103] Light-induced destruction of pathogens has proven more effective for Gram-positive bacteria due to their "single-layered" cell wall/membrane structure allowing deeper penetration of the PS.[104] The presence of a well-organized and thick outer membrane in Gram-negative bacteria renders these more resistant towards aPDT; the thickness of the outer membrane also limits the penetration of PS through the cell membrane and wall. This presents the necessity to design target-specific photosensitizers against such pathogens.

A multitude of pathogens can be targeted by aPDT; however, this technique is nonselective with respect to intracellular molecular targets — proteins, lipids, and nucleic acids are each affected by induced oxidative stress.[105] For cationic PSs, due to electrostatic mismatch between human cells and PSs, poor affinity of the sensitizer and limited efficacy of the treatment has been reported.[106] This can be seen as a positive; aPDT can target and eliminate pathogenic microbes while minimizing damage to human cells. Chlorophyll based PSs, even though having excellent aPDT potential, can often kill non-target organisms posing a risk to the ecosystem when used for environmental applications.[107] Photosensitivity, a common side effect of application of PSs to humans, confers side-effects such as redness and swelling. Rare allergic reactions have similarly been observed.[108]

Thus, a PS must be formulated in a way to minimize aggregation.[109] In addition, it should ideally be target-specific, biodegradable, cost-effective, non-toxic in the absence of light, and deliver PSs in their monomeric form to the target tissue.[110] Research has shown that selective targeting of the PSs to the target cell or tissue could be done by designing target specific delivery platforms based on peptides (polymyxin).[111],

nanocarriers (ZnO, AgO nanoparticles) [112], polysaccharides (maltodextrin, cyclodextrins) [113], polymers (polyvinyl alcohol (PVA)) [114] or biopolymers (hyaluronic acid) that have been formulated via physical, ionic, or covalent linkage.[115]

1.3. Drug Delivery Systems (DDS)

1.3.1.   Introduction

The advantage of incorporating a PS into the drug delivery system (DDS) is improved bioavailability, solubility, permeability, and selectivity. These DDS provide protection of PS against external factors including light and temperature.[116] The following properties allow the incorporation of a large amount of hydrophilic and hydrophobic PSs for better target selectivity. Further, these formulations could be functionalized structurally via the chemical attachment of ligands, enzymes, and antibodies to combat the very issue of microbial resistance.[117] The physicochemical characteristics of DDS affect the interaction with the biofilm matrix, as the smaller the size of the nanocarrier the better is the penetration into the biofilm. The surface charge of such a system is an important factor for the drug's efficacy, as the cationic charged DDS have greater penetration in the biofilm matrix as compared to anionic or unloaded platforms.[118] The size, loading capacity, functionalization of the DDS, as well as inherited properties of the PSs, modulates targeting in the cell membrane of the bacteria as well as the biofilms and can increase the antimicrobial activity under aPDT conditions.[119]

1.3.2.   Types of drug delivery system

Drug delivery systems are based on encapsulation of the drug in a biocompatible matrix, either a solvent, polymer, gel or lipid. Selected examples of drug delivery systems which have previously been used for aPDT are listed in Table 1.2 and expanded upon in this section. [120,137,146,150,153,160,174]

Table 1.2. Drug delivery systems based on biopolymers with characteristics used with a focus on aPDT improvement.

System		Approach	PS/$\lambda_{(nm)}$	Microorganism(s)
Drug Delivery Systems	**Bio-polymer hydrogel-cellulose**	Cellulose acetate dissolved in acetone	**TB** **RB** 610/545	MRSA, *Escherichia coli, Clostridium difficile, Bacteriophage,* and *C. albicans*
		Cellulosic fabric of β(1,4)-d-glucopyranose chains	**TMAP** [4+] **ZnTMAP** [4+]	*Staphylococcus aureus, E. coli,* and *Pseudomonas aeruginosa*
	Bio-polymer hydrogel-chitosan	Poly-β(1,4)-d-glucopyranosamine	**RB** **MB** 540	*Enterococcus faecalis P. aeruginosa*
	Cyclodextrins	Foam formulations constituted by the gel-forming polymer sodium alginate, the gelling agent calcium carbonate, the plasticizers sorbitol and glycerol, the foaming agent hydroxypropyl Methylcellulose, and as PS solubilizer agents β- and γ-cyclodextrins and polyethylene glycol 400	**Curcumin**	Infected wounds
	Synthetic polymeric hydrogel	Cross-linked poly (vinyl alcohol) (PVA)–borate complexes	**MB** **TMP** 635	MRSA
	Lipid-Delivery System	Liposomes	**TMPyP**	MRSA

1.3.2.1. Hydrogels

Hydrogels are a group of hydrophilic polymeric materials reticulated via chemical bonds and interactions, named for their ability to hold a large quantity of water within their three-dimensional (3D) network structures.[120] Today's understanding of polymeric hydrogel materials dates back to studies with poly(vinyl alcohol) (PVA) cross-linked with formaldehyde in the late 1940s, used for biocompatible implants for humans and marketed as "Ivalon".[121] In 1958, Danno synthesized a polyvinyl alcohol polymer using gamma-radiation, forming a cross-linked network of a hydrogel. [122] A key advance occurred in 1960, when Wichterle and Lim reported a polymeric cross-linked system of macromolecules based on poly(2-hydroxyethyl methacrylate) (pHEMA).[123,124] This material is currently used to manufacture soft contact lenses for eyes, the first successful mass-marketed cross-linked hydrogel material, now with decades of use demonstrating safety for humans. In the 1950s and 1960s Katchalsky worked extensively on polymeric networks and established the possibility to transfer chemical energy into mechanical strength.[125] This inspired in the early 1970s the development of stimuli specific second-generation hydrogel materials. These materials are characterized by stimuli-responsive activity with variation of temperature, pH, or the concentration of molecules in solution, affecting the cross-linking properties and the pore size of the hydrogels, allowing an additional targeting vector for drug-delivery. Examples of temperature-sensitive polymeric networks include poly(isopropylacrylamide) (PNIPAAm), poly(*N*-(2-hydroxypropyl)methacrylamide) (PHPMAm) and polyethene glycol (PEG)-polyester block copolymers; advances in the mid-1990s exploited physical interactions to cross-link the polymers to form hydrogel networks, enhancing the mechanical strength as well as degradation and thermal stability of the polymeric systems.[126] A third generation of hydrogels were established as an example of stereo-complexed materials by block-copolymers via forming an inclusion complex possessing metal-ligand coordination in addition to peptide cross-link interactions. Hydrogels with incorporated metals are widely used for sensing applications utilizing photoluminescent hydrogels for pH sensing.[127,128]

Continuing research into the dynamics of these types of DDS has led to a proliferation of these stimuli responsive "smart polymers"; polymeric cross-linked hydrophilic networks possessing tunable properties which can be triggered externally, or by physiological responses.[129,130] Common techniques include *in situ* cross-linking of the

hydrogels, radical polymerization, formation of double-network polymers, by a combination of natural and synthetic polymeric materials which allow one component to be selectively modified, or by forming composite polymeric formulations with small inorganic molecules.[131] These materials possess ideal platform properties for biological applications, chiefly controlled drug delivery (PS) to the target site.

The polymer source may be natural or synthetic, but they function in the same way, are used to carry PSs loaded from the dispersion medium (i.e. water) to the target.[132] Macro-scale gels (>1 mm) persist at the site of infection for a longer interval of time due to their inherent low fluidity whereas microgels and nanogels, due to their small size, enable the PSs to effectively reach the target sites while retaining the advantages of a gel hence are emerging as an effective carrier material in aPDT.[133,134] Gels can be further modified with different functionalities or with other targeting agents altering the biological or physical properties, allowing improved biodistribution, pharmacokinetics, cell uptake, and target selectivity.[134] Antimicrobial hydrogels have been used widely in clinical settings; well-known examples include bactericidal silver-hydrogel coatings for medical device sterilization and their application in wound dressings to support wound healing.[135]

Both hydrophobic and hydrophilic PSs can be included in a microgel/nanogel system via physical (encapsulation) or chemical (conjugation) methods as shown in Figure 1.15. Due to their fluidity, hydrogels can deliver more active material to the site of infection than a decorated surface. The size of the nanogel mesh, the flexibility of the polymeric chains, the reticulation density, and their ability to incorporate and bind with water molecules modulates the structural and mechanical properties of hydrogels and can be expected to similarly affect medicinal properties.[136]
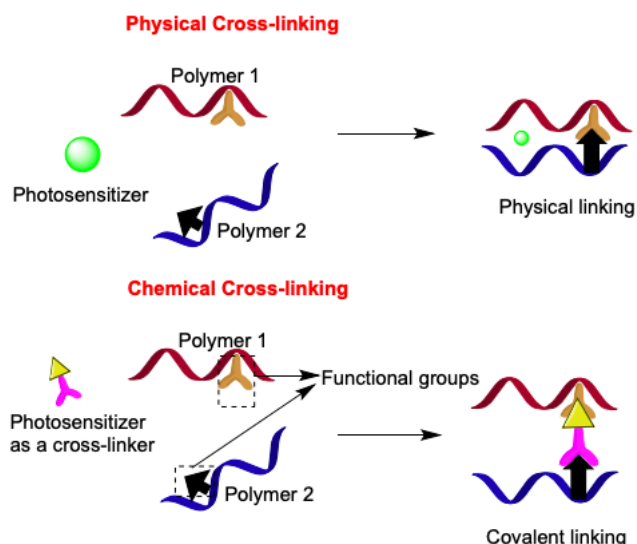
Figure 1.15. Different strategies for incorporating photosensitizers in hydrogels. [120]

1.3.2.2. Synthetic-polymer derived hydrogels with PSs

In aPDT, polymeric hydrogels have been used to encapsulate PSs via loading or are built from polymers known to have inherent photoactivity against microbes. Several PSs (RB, porphyrins and derivatives, curcumin, among others) have been encapsulated in biocompatible polystyrene (**1.19**), polyethylene glycol (PEG) (**1.20**), polyester (**1.21**), or polyacrylamide (PAA) (**1.22**) based polymers (Figure. 1.16) and used in aPDT.
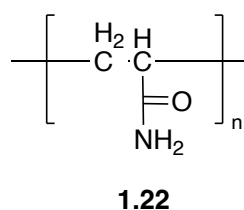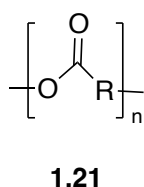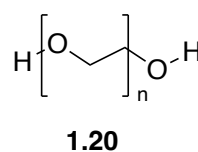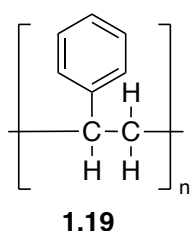
Figure 1.16. Examples of synthetic polymers (polystyrene (**1.19**), PEG (**1.20**), polyester (**1.21**) and PAA (**1.22**)) used for hydrogel formation with PSs.

Incorporation into these polymeric hydrogel networks have helped to overcome the issue of solubility of common photosensitizers in the aqueous medium, reducing aggregation of the PSs and reducing the dark toxicity as induced by some PSs.[120] Cross-linked polyvinyl alcohol (PVA)-borate hydrogels have been used as an effective aPDT DDS. When conjugated with two cationic charged PSs – MB and TMPyP they allowed effective treatments for wounds infected with both planktonic cells and biofilm-grown MRSA.[137] The antibacterial activity of MB incorporated into polyacrylamide (PAA) based hydrogel matrices showed an effective activity against bacterial suspensions and biofilms.[138] Photodithazine (PDZ) was formulated in a natrosol-based hydrogel to improve its topical application against the fungal species of *Candida albicans*, *Candida glabrata*, and *Candida tropicalis* biofilms.[139] PDZ incorporated in the hydrogel has shown to be more effective over the *C. albicans* species, giving a possibility to treat oral candidiasis. Subsequently, the antimicrobial photodynamic activity of the cationic (5-[4-2-(2-(2- acrylamidoethoxy)ethoxy)ethyl]-carboxyphenyl-10,15,20-tris(4-*N*-methylpyridyl)porphyrin trichloride and metal derivatives (Pd(II) and Cu(II) complexes) cross-linked with polyacrylamide exhibit cytotoxic effect on *E. coli* suspensions providing a potential application for water sterilization as shown in Figure 1.17.[140] Also, hydrogels based on poly(2-hydroxyethyl methacrylate) (pHEMA) incorporated with NO donors [Mn[PaPy$_3$)(NO)].ClO$_4$] showed improved and effective antimicrobial activity against Gram-negative bacterium *P. aeruginosa*.[141]

Surface localization of TMPyP electrostatically bound in acrylate hydrogels has been shown to decrease bacterial colonization and could possibly be used as intraocular lens biomaterials to prevent endophthalmitis (ocular infections).[142] Linear polymeric amidoamines have been used to prepare conjugates with other aPDT active PSs such as the BODIPY-NMe dye and have been shown to be active against the Gram-negative *E. coli* Gram-positive *S aureus*, respectively.[143] Iontophoretic release of PSs from a polyelectrolyte hydrogel for potential wound healing loaded on poly(methyl vinyl ether-co-maleic acid) gel with either MB or TMP was achieved and it showed an effective aPDT potency against MRSA and *Burkholderia cepacian*.[144]
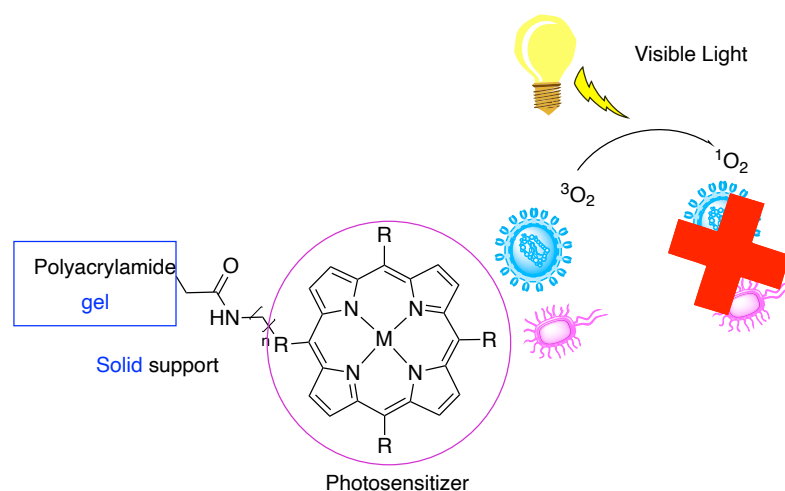
Figure 1.17. Schematic drawing of the photodynamic inactivation of microorganisms by singlet oxygen generated by the photosensitizer immobilized on a polyacrylamide support.[140]

1.3.2.3. Bio-polymer derived hydrogels with PSs

Compared with synthetic polymers, biopolymers have received greater attention, due to their biocompatibility, bioactivity, and biodegradability.[145] The chemical structure of some biopolymers used to synthesize hydrogels – those incorporating PSs active for aPDT – are illustrated in Figure 1.18. Well-known examples in this class include cellulose (**1.23**), chitosan (**1.24**), hyaluronic acid (**1.27**), gelatin and polysaccharides such as cyclodextrin (CD) (**1.25**-**1.26**).
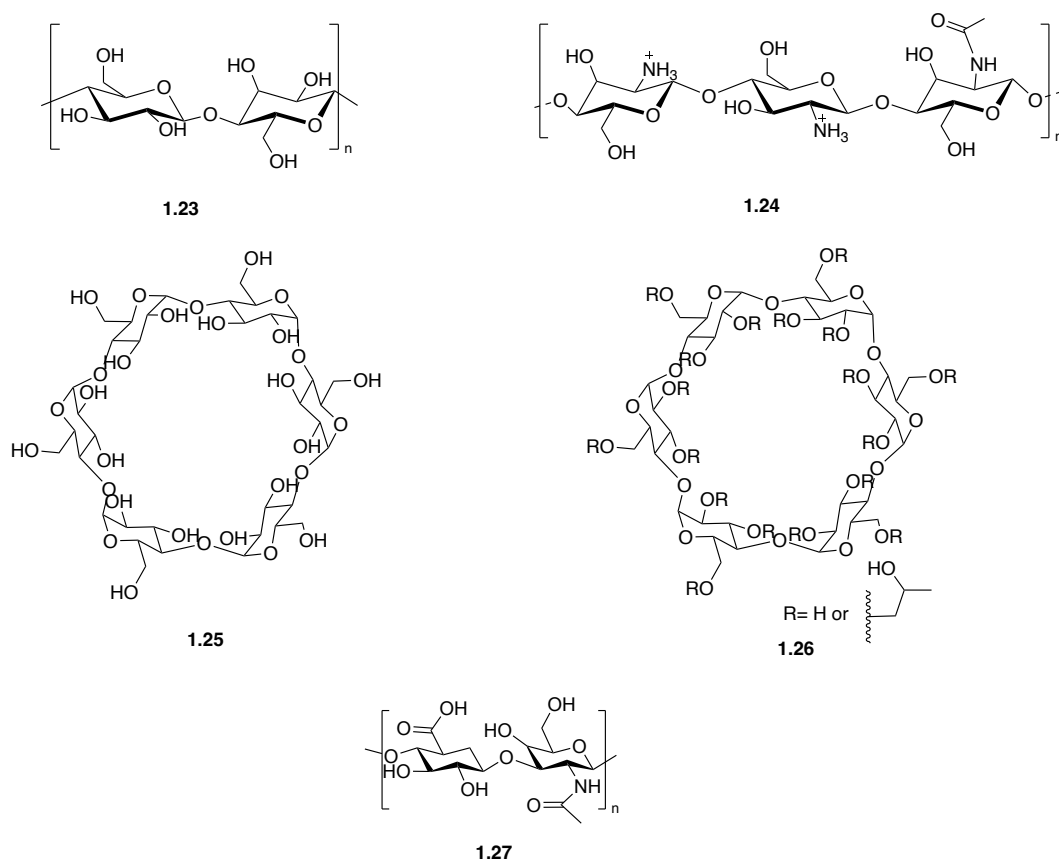
Figure 1.18. Structures of drug delivery systems including cellulose, chitosan, cyclodextrin and hyaluronic acid.

1.3.2.3.1. Cellulose

Cellulose (**1.23**) is the most abundant biopolymer in nature, occurring principally in the cell walls of plants. It is a high molecular weight polymer with the empirical formula $[C_6H_{10}O_5]_n$ which is renewable, non-toxic, colorless, and odorless.[146] Structurally, cellulose is composed of D-glucopyranose units linked via β(1–4) linkages. This polymer is hydrophilic, biocompatible, biodegradable and is mechanically robust, all advantageous for DDS use. These properties also account for its use in a vast array of fields and, being a carbohydrate, it possesses high compatibility with biological systems.[147]

A chemically modified derivative of cellulose acetate has been used to encapsulate PSs such as RB and TB as a biopolymeric coating to investigate the ability against microbes in hospital conditions.[148] A white fluorescent lamp (with two prominent bands of λ = 545 and 610 nm) was used to eradicate disease-causing bacteria *E. coli*, bacteriophage *Clostridium difficile*, the yeast *Candida albicans*, and MRSA. These photoactive

coatings were prepared by dissolving cellulose acetate polymer in acetone, and both PSs (RB and TB) were added in appropriate concentrations. The tests against the microbial populations showed PSs can retain their antimicrobial properties when embedded in the biopolymer since the levels of cell death achieved (up to five-million-to-one (6.7 log) reduction) should be more than sufficient for surface disinfection in a hospital setting.

Cellulose impregnated with the porphyrinic PS, 5,10,15,20-tetrakis(4-*N,N,N*-trimethylammoniumphenyl)porphyrin (TMAP^{4+}) or its zinc(II) complex (ZnTMAP^{4+})has similarly shown photo-bactericidal effects. [149] This was shown by incubating the bacteria suspension of Gram-positive, *S. aureus* and Gram-negative, *E. coli* and *Pseudomonas aeruginosa* with both photoactive cellulosic fabrics in the dark and in light with different light intensities and time-intervals. Although the Gram-negative bacteria were less susceptible to this aPDT regimen than the Gram-positive bacterium, the cellulose based ZnTMAP^{4+} photoactive material showed remarkable efficacy against *P. aeruginosa*, highlighting the role of core modification in biocidal effects.

The Sol laboratory in Limoges, where work presented in this manuscript was performed, also obtained a novel antimicrobial platform by grafting PS, 5-(4-propargyloxyphenyl)-10,15,20-tritolylporphyrin(Zn^{2+}) (**1.28**) on cotton fabric derived cellulose via azidation (**1.23a**) followed by "Click-Chemistry" with acetylenic group of the porphyrin in Figure 1.19. This material displayed an antimicrobial action against *E. coli* and *S. aureus*, making this platform a potential photo-bactericidal formulation (**1.29**) applicable for industrial as well as for household utilizations.[150]
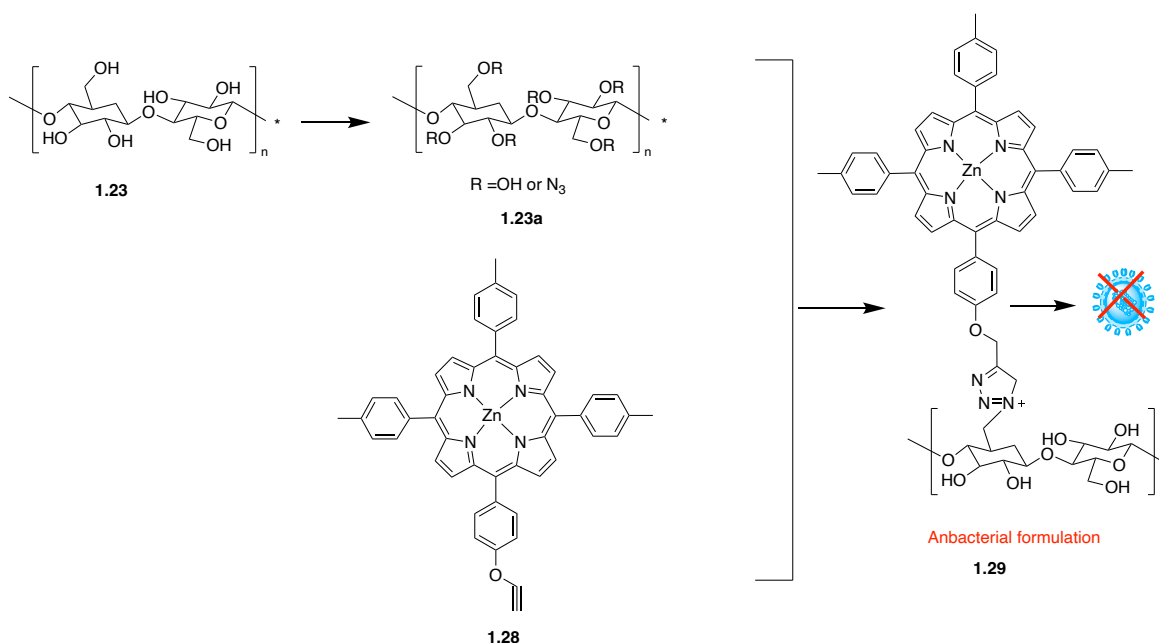
Figure 1.19. Cellulose derivatization to form antibacterial surfaces with PSs.[150]

Sodium alginate (SA), pectin (PC), and carboxymethyl cellulose (CMC) have also been used for preparing films containing chlorin *p6* or MB. The photodynamic efficacy of Cp6-SA-PC-CMC films is higher for MRSA as compared with MB-SA-PC-CMC films due to insignificant binding to the film components.[151]

1.3.2.3.2. Chitosan

Chitosan (CS) (**1.24**) is a naturally occurring polycationic polymeric natural structural element of fungal cells walls and crustacean exoskeletons, usually obtained by chitin acid hydrolysis. It is composed of *N*-acetyl-*D*-glucosamine and *β*-1,4-linked *D*-glucosamine. Interaction of the polycationic charges of this platform with the microbial surface potentiates the aPDT of PSs. This polymer is biocompatible, biodegradable, and displays an attractive broad-range antimicrobial activity and is easily modifiable due to a large number of hydroxyl and free amino groups.[152] It has been shown that ERY-grafted CS is efficient against the bacteria and fungi such as *P. aeruginosa* (Gram-negative), *S. mutans* (Gram-positive), and *Candida albicans* (fungi).[153] Furthermore, the chitosan-coated indocyanine green (ICG)-loaded poly(lactic-co-glycolic acid) (PLGA) showed adherence to the bacterial cell wall of Gram-negative *P. gingivalis*, as well as other periodontal pathogens, *Fusobacterium nucleatum* and *Aggregatibacter actinomycetemcomitans*.[154] It is thus proving to be an efficient tool against the

periodontal pathogens, including *P. gingivalis*. The nano formulation was obtained by coupling of RB with CS with the coupling agent 1-ethyl-3-(3-dimethyl aminopropyl)-carbodiimide (EDC). Biological assays were performed on the biofilms of *E. faecalis* and *P. aeruginosa*.[155,156] It was shown that this formulation adheres to bacteria cells and to biofilm extracellular polymeric substances (EPSs) which results in a higher uptake into the biofilms, enhancing the aPDT potency.

Chitosan formulation in combination with MB is efficient against planktonic bacterial growth and biofilm formation of Gram-negative bacteria *P. acnes*.[157] The antimicrobial action of this formulation was achieved at a concentration of 12.5 µg/mL of MB and it was observed that reduction of 1.9 log10 biofilm was obtained at a concentration of 75 µg/mL MB. It was seen that the formulation exhibits adhesion to the skin patches thus making this formulation a very effective platform for localized infections.

Decoration of chitosan with zinc phthalocyanine-colistin (**1.30**) results in an antibacterial formulation for both treatment and sterilization, particularly against multidrug-resistant Gram-negative strains such as *P. aeruginosa*.[158] This kind of formulation, as shown in Figure 1.20, enhances the solubility of PSs, making them a promising treatment option.
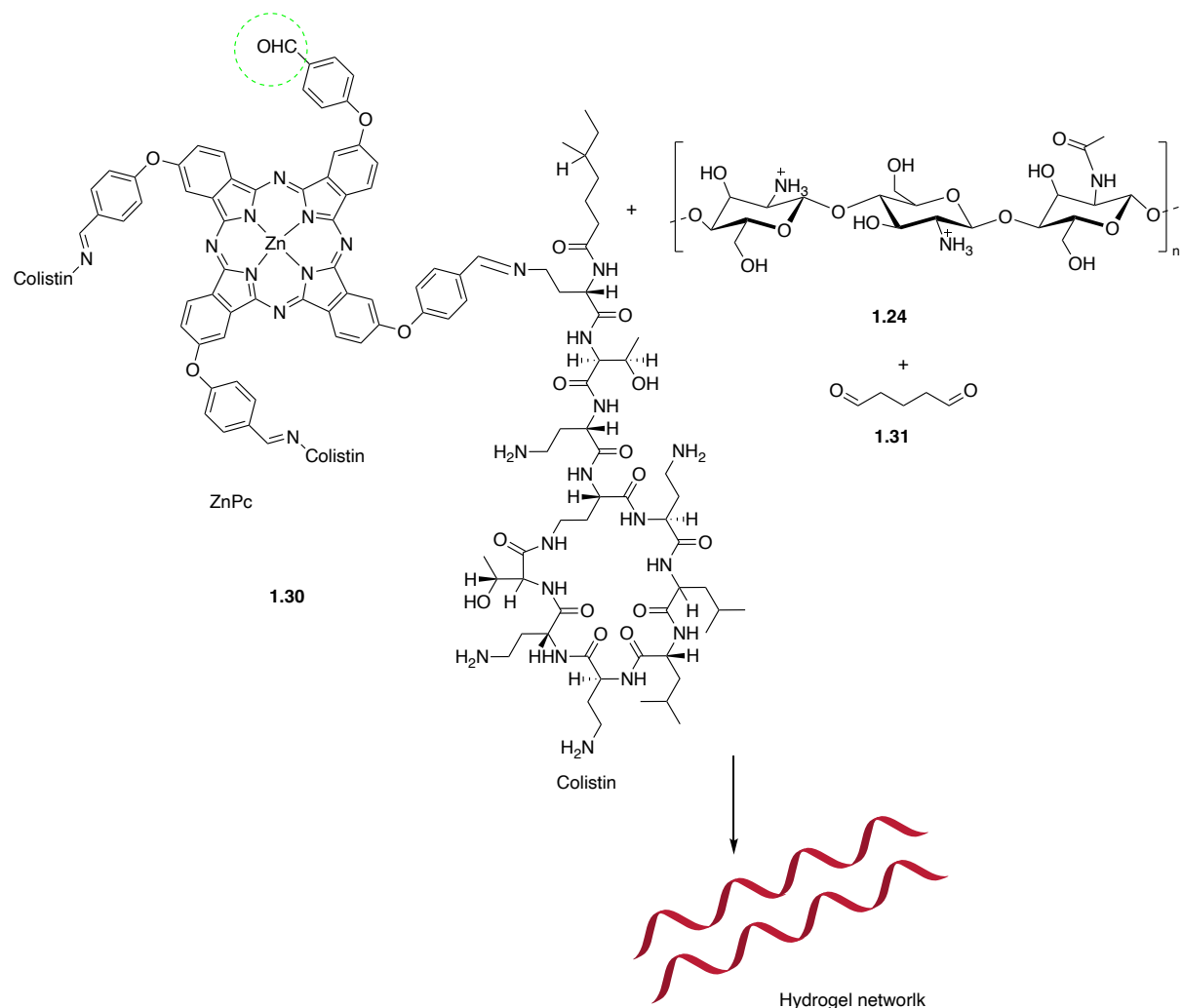
Figure 1.20. Synthesis of ZnPc-colistin-chitosan hydrogel.[158]

1.3.2.3.3. Hyaluronic Acid

Hyaluronic acid (HA) (**1.27**), as shown in Figure 1.19, is a naturally occurring, biocompatible anionic biopolymer having unique physicochemical and distinctive biological activities.[159] It is a linear polysaccharide skeleton of β-1,4-linked D-glucuronic acid (β-1,3) *N*-acetyl-D-glucosamine disaccharide and is found as a non-sulfonated glycosaminoglycan (GAG) in the extracellular matrix (ECM) of higher animals.[160] Unmodified HA has found an essential utility in applications involving drug delivery, tissue engineering, viscous-supplementation and it has natural wound healing properties.[161] Chemical modification of HA can help tailor the physicochemical properties and *in vivo* residence time of HA while retaining its natural biocompatibility and biodegradability.[162,163] Functional modifications of carboxylic groups on HA was used to formulate polymer-drug conjugates via a covalent conjugation with the

synthesized PS with HA and itis a powerful platform to improve aPDT.[164] Such platforms can be used as an alternative to traditional antimicrobial medicines to treat localized infections.

Formulation obtained by crosslinking collagen-hyaluronic acid with 1-ethyl-(3-3-dimethylaminopropyl) carbodiimide hydrochloride (EDC.HCl), fabricated with the antibiotics tobramycin or ciprofloxacin assist wound healing and sterilization.[165] A formulation fabricated with 0.4 mg/ml of ciprofloxacin has exhibited cytotoxic effects on fetal human dermal fibroblasts, making these polymeric platforms ideal candidates to be explored for aPDT.

Curcumin, as explained earlier, is a naturally occurring antibiotic molecule which has been explored for its aPDT potential; solid dispersions of curcumin with methyl-β-CD, HA and hydroxypropyl methylcellulose (HPMC) or an intercalated system with both HA and HPMC have been formulated.[166] The intercalated formulation has been tested for *in vitro* photoinactivation of *E. faecalis* and *E. coli*, displaying a log 6 reduction of colony for both strains at a concentration of about 0.5–10mM, under illumination with blue light. This formulation is therefore promising for wound treatment and sterilization.

Silver nanoparticles (AgNPs) are known to exhibit an antibacterial effect, but the major disadvantage of such NPs is the underlying toxicity to human cells.[167] Antibacterial applications of such NPs could be enhanced by binding these molecules onto HA, making a strong synergistic framework of photosensitive metal-organic hybrids.[168] This platform has shown an enhanced biocompatibility due to presence of negatively charged HA preventing the bleaching of the Ag ions. The target bacteria secrete an enzyme (hyaluronidase) degrading the HA, triggering the release of the positively charged nanoparticles of silver and enhancing the antimicrobial activity of this platform preserving the ability to generate reactive oxygen species (ROS). This platform has shown an enhanced effect against multidrug-resistant bacteria infected wounds.

HA based composite hydrogel conjugated with an antimicrobial-peptide [AMP, KK(SLKL)3KK] with HA via a Schiff's base reaction was synthesized to attain a long-lasting antimicrobial activity.[169] The primary amines are derived from peptides (lysine residues) and aldehyde groups from HA. This hydrogel formulation has shown an effective injectability, high biostability, and an impressive mechanical strength. These composite systems have a shown an excellent broad-spectrum antibacterial activity *in vitro* and *in vivo*.

1.3.3. Lipid Delivery Systems

It is important to have high production of ROS species to achieve an improved and effective aPDT. The hydrophobic nature of the PSs as synthesized often causes aggregation in aqueous media. This aggregation reduces the aPDT efficacy by depleting the formation of singlet-oxygen species due to a self-quenching effect in the excited state.[170] Lipid delivery systems (LIP), encapsulating and protecting non-target cells from the PS cytotoxicity, can preserve the monomeric forms of the PSs and result in improved aPDT.[171] These kinds of DDSs have a number of advantages; an enhanced loading capacity of PSs compared to other systems, allowance for the incorporation of both hydrophilic and hydrophobic PS species, better biodegradability, biocompatibility and the synergistic activities of positively charged and highly fluid components of LDS, all of which enhance uptake and phototoxicity.[172,173]

1.3.3.1. Liposomes

Liposomes (specifically phospholipids) as shown in Figure 1.21, are derivatives of LIPs, spherical vesicles capable of forming a closed bilayer structure. These can be varied on the order of micrometers and have been widely investigated due to their lipidic structure's similarity with human cell membranes.[174,175] Liposomes are used as a pharmaceutical tool to improve the efficacy of aPDT efficacy and drug targeting due to their non-toxic nature, biocompatibility with human cells and ability to incorporate near-quantitative amounts of PSs, and promoting controlled release.[176]
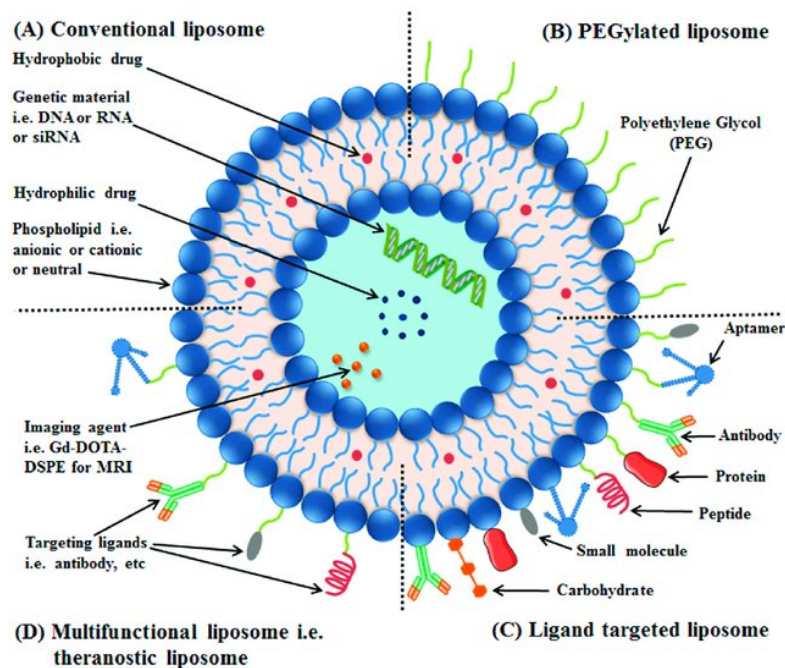
Figure 1.21. Conventional liposomes are made of phospholipids (A); PEGylated/stealth liposomes contain a layer of polyethylene glycol (PEG) at the surface of liposomes (B); targeted liposomes contain a specific targeting ligand to target an infection site (C); and multifunctional such as theragnostic liposome (D) for diagnosis and treatment.[176]*

*Reproduced with permission

The flexibility inherent in the structural chemistry of such vehicles allows the incorporation of several hydrophilic and hydrophobic PSs, making them ideal DDS in a clinical setting. Physical properties such as the composition of lipids, bilayer fluidity, and a surface charge may influence the drug behavior and modulate their pharmacokinetic profile and biodistribution into the body.[177]

It has been shown that liposomes behave differently in biological systems depending on their surface charge (positive, neutral, or negative) and their ability to bind to the surface.[178] Cationic liposomes have been used to incorporate aluminium chloride phthalocyanine, this aPDT formulation used against cariogenic bacteria in dental cavity disinfection.[179] Against *Porphyromonas gingivalis*, using a fluorescent lipid incorporated in the liposome membrane, antibacterial effect of aPDT mediated by free or liposome-encapsulated zinc phthalocyanine was also evaluated.[180] The PS used showed a decreased dark toxicity as individual PS, enhanced photochemical stability, and a strong absorption in the red region in this matrix, which may facilitate light penetration into tissues. Almost 99% of liposomes bonded to *P. gingivalis*, while the neutral liposomal vehicles showed poor binding. Thus, in accordance with the results,

cationic liposomes are expected to retain the photosensitizer when attached to the biofilm, prolonging the period of attachment and acting as a local reservoir of the PS. Cationic porphyrin 5-(1-dodecanoylpyridinium-4-yl)-10,15,20-triphenylporphyrin (TDPyP), incorporated on a poly-cationic LIP named as *N*-[1-(2,3-dioleoyloxy)propyl]-*N,N,N*-trimethylammonium chloride (DOTAP) similarly showed inactivation of MRSA.[181]

1.4. Objective and outline of the manuscript

Even though aPDT is emerging as a potential tool against the worlds tormenting issue of increasing number of drug-resistant pathogens, most PSs used for conventional therapies lack selectivity, target specificity and can undergo self-quenching in biological media due to aggregation. Several strategies to enhance the activity of such PSs have been discussed above which allows for a better solubility and selectivity of the PSs towards the target microbe. This can include combining the PS with a drug delivery system or chemically altering the molecular skeleton of the PS with functionalities which induces better potency towards the site of infection.

Overall, our aim in this manuscript is to explore the multiverse of aPDT potential and enhancement of PSs via different functionalization strategies which includes conjugating with carrier molecules or post functionalization of these molecular probes itself. Finally getting a standout strategy for a better aPDT. To achieve this, In Chapter 2 we synthesized two potential PSs which have been reported in literature for their antimicrobial activity but lack target selectivity and are relatively less soluble or aggregate in aqueous media. With an aim to work on these drawbacks these PSs were conjugated with a drug delivery platform. Hyaluronic acid biopolymer offers an excellent advantage of being biocompatible and has been used in skin industry for formulations of products. This polymer has anionic molecular skeleton with functionalities that could be modified to introduce our PSs covalently onto them. These PSs have a primary amine functionality and are covalently conjugated onto the COOH functionality of hyaluronic acid biopolymer as shown in Figure 1.22.
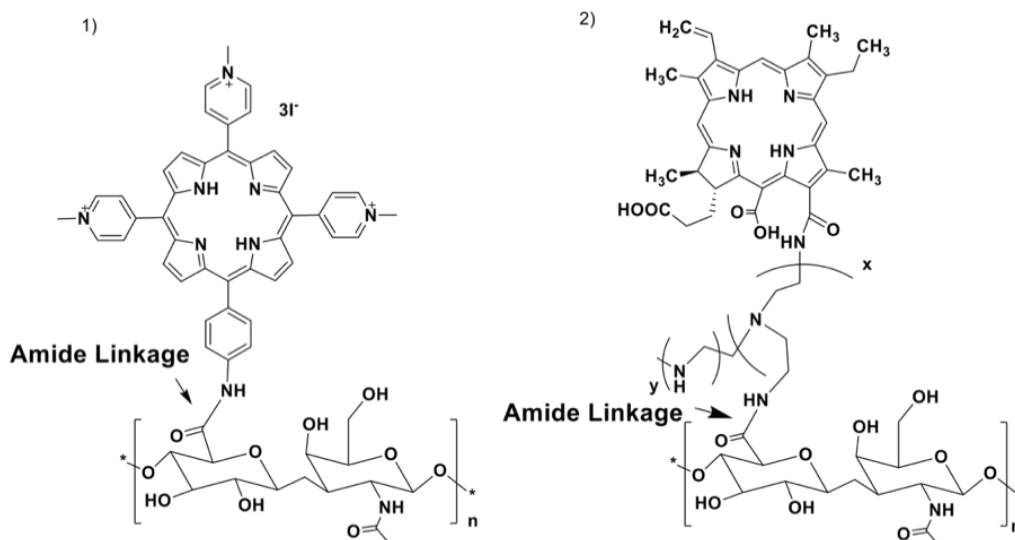
Figure 1.22. Covalent formulations with aPDT active for PSs.

These conjugates have been evaluated for their inhibition abilities as against the cultures of both Gram-negative and Gram-positive bacteria to test efficiency of such platforms. This strategy marks the first example of use of hyaluronic acid conjugates with PSs although such not the best one as we expected. Nevertheless, it opens a new window of exploration of such conjugates in future with other PSs or linkers to establish better linkage of PSs onto such platforms.

In Chapter 3, relative singlet oxygen yields of synthesized porphyrins and BODIPY derivatives by Senge-lab members were evaluated using the standard diphenyl benzofuran (DPBF) singlet oxygen degradation assay. DPBF molecule degrades in presence of singlet oxygen produced by PSs gives an insight to the photobiological activity of such synthesized chromophores and establishes the grounds of their efficiency to be evaluated against the microbes.

These degradation assays have been used for BODIPY dyes synthesized in the next chapter, this can derive the best post-functionalization influence of the BODIPY scaffolds on the photophysical/photochemical properties of PSs to be used in aPDT.

Lastly in Chapter 4 with an aim to build up a library of fluorescent aPDT active PSs and addressing the innate solubility issues, low selectivity with the bacterial culture, different functionalization strategies were applied to obtain derivatives of PSs. Our major focus for this part of the manuscript is to recognize the efficiency of such scaffolds for aPDT and to give a standout synthetic strategy for future exploration of similar probes in aPDT. Thus, we report a synthesis of library of BODIPY dyes which have been modified on

their molecular skeleton to address the PS related issues for an efficient activity in biological evaluations including inhibiting the growth of the infective bacteria and their biofilms. The protocol involved synthesizing different *meso*-N-heterocyclic BODIPY dye scaffolds and further introducing cationic charge or synthesizing zwitter ionic species onto the *N*-heteroatom using different functionalities which make them ideal candidates to interact with a wider stratum of microbes as shown in Figure 1.23.

N-heterocycle as *meso* substituent on BODIPY dye

Ar =

X ⟶ Introduction of charge to enhance the aPDT potential

Ar =

X = Functionality to introduce charge on *N*-heterocycle
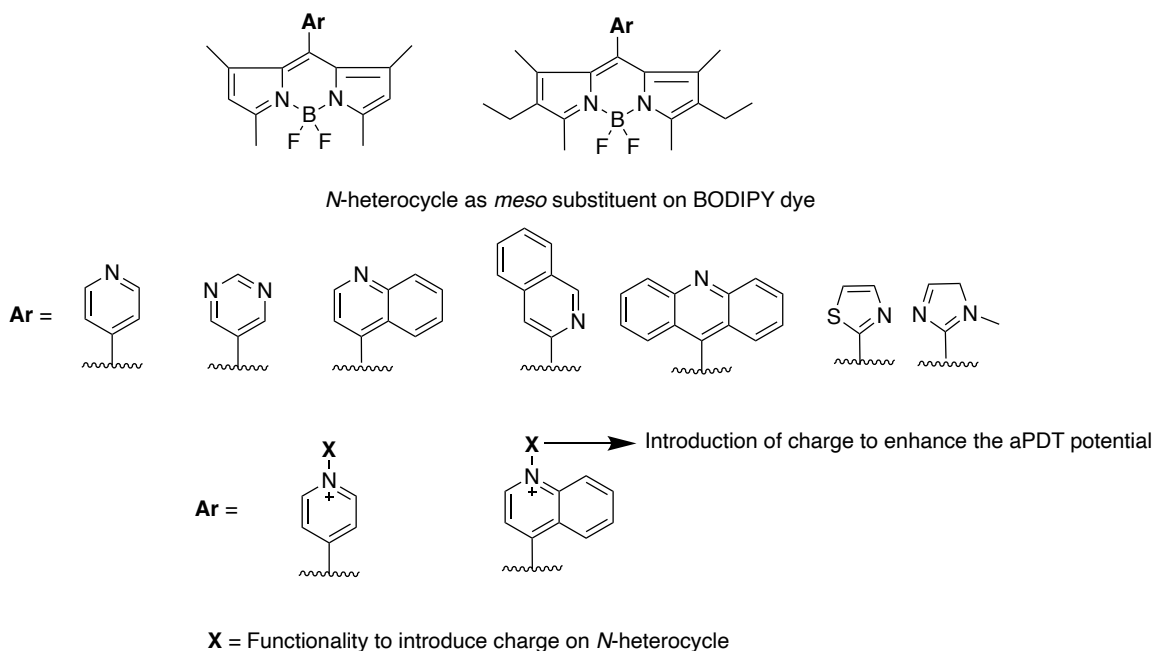
Figure 1.23. The *meso*-N-heterocycle BODIPY dyes investigated in Chapter 3.

The protocol involves successive introduction of cationic charges and water solubilization groups (methyl, carboxylate and etherate) onto the BODIPY. This strategy allows converting the hydrophobic BODIPYs to the corresponding water-soluble dyes without hurting their optical properties. These derivatives were tested for production of singlet oxygen species using the DPBF degradation assay to access the photobiological activity of such compounds. Finally, these derivatives were subjected to MIC/MBC analytical assays to evaluate the aPDT potential of these derivatives with Gram-strains of bacteria along with the inhibition and eradication of biofilms protecting the infection causing bacteria. Another strategy with aim to make water soluble derivatives with multiple carboxylate functionalities on the BODIPY scaffold B-C derivatives at the boron atom were synthesized under Grignard reaction condition to yield derivatives as shown in Figure 1.24. These derivatives were further subjected to synthesis protocol of *N*-

functionalized carboxylate derivatives to have a hyper-soluble derivative with tri-cationic species of the molecular scaffold of the BODIPY.
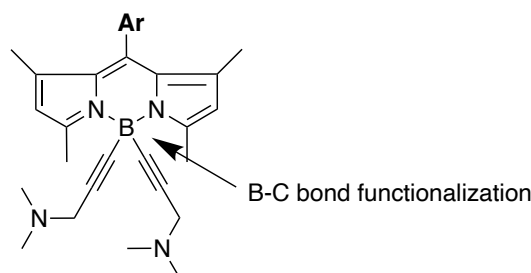
Figure 1.24. B-C derivatives of BODIPY dyes investigated in Chapter 3.

Another strategy used by introduction of heavy-atom (Iodine) and conjugates (intermediate trimethyl silyl derivatives and dimer) as shown in Figure 1.25 with other chromophores onto the core of *meso*-N-heterocycle BODIPYs were synthesized with aim to enhance the optical window of such derivatives which in turn enhances the aPDT potential of such derivatives as tested for production of singlet oxygen and inhibition bacterial cell cultures via MIC/MBC assays. This strategy involved double Sonogoshira cross-coupling conditions to form dyad BODIPY chromophore.
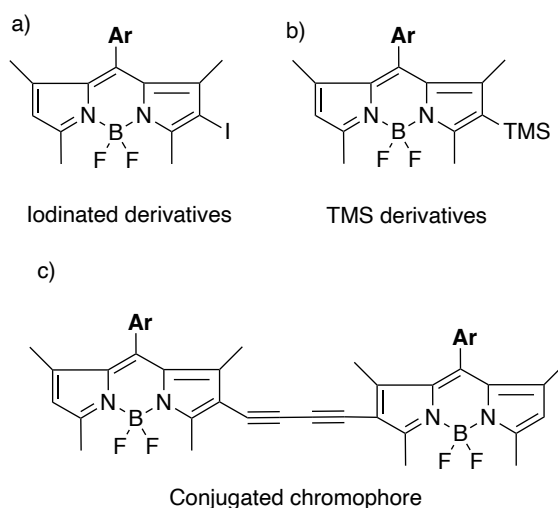
Figure 1.24. a) Heavy-atom (iodinated-) derivative b) TMS derivative and c) dimer of BODIPY dyes investigated in Chapter 3.

All the studies and synthesis done accomplishes the goal of our manuscript to develop new strategies to make PSs more efficient enhance their activity for aPDT.

1.5. Terms and abbreviations

3D: Three-dimensional

aPDT: Antimicrobial photodynamic therapy

AlPc: (phthalocyaninato)aluminium(II)

BODIPY: Borondipyrromethene difluoroboradiazaindacene

BOP: Bleeding on probing

CMC: Carboxymethyl cellulose

CS: Chitosan

CPAT: Chemiluminescent photodynamic antimicrobial therapy

ClAlPc: Chloro-aluminium phthalocyanine.

CQDs: Carbon quantum dots

Ce6: Chlorin e6

CMC: carboxymethyl cellulose

CDs: Cyclodextrins

DDS: Drug-delivery systems

DOTAP: *N*-[1-(2,3-dioleoyloxy)propyl].-*N,N,N*-trimethylammonium chloride

DPBF: 1,3-Diphenylisobenzofuran

EDTA: Ethylenediamine-tetraacetic acid

ESBL: Extended-spectrum ß-lactamases

EPS: Extracellular polymeric substance

ECM: Extracellular matrix

EPS: Extracellular polymeric substances

EDC.HCl: 1-ethyl-(3-3-dimethylaminopropyl) carbodiimide hydrochloride

EU: European Union

ERY: Erythrosine

GAG: Glycosaminoglycan

HA: Hyaluronic acid

Hp: Hematoporphyrin dihydrochloride

HPMC: hydroxypropyl methylcellulose

ICG: Indocyanine green

LIP: Lipid delivery systems

LPS: Lipopolysaccharide

*M*THPC: 5,10,15,20-Tetrakis(*m*-hydroxyphenyl)chlorin

MRSA: Methicillin resistant-*Staphylococcus aureus*

MB: Methylene blue

NP: Nanoparticle

PVA: Poly(vinyl alcohol)

PHPMAm: Poly(*N*-(2-hydroxypropyl)methacrylamide)

PEG: Polyethene glycol

PHEMA: Poly(2-hydroxyethyl methacrylate)

PNIPAAm: Poly(isopropylacrylamide)

PDI: Photodynamic inactivation

PACT: Photodynamic antimicrobial chemotherapy

PBS: Phosphate-buffered saline

PC: Pectin

PLGA: Poly(lactic-co-glycolic acid)

PC: Pectin

PDT: Photodynamic therapy

PPa: Pheophorbide a

PAA: Polyacrylamide

PDZ: Photodithazine

PVA: Polyvinyl alcohol

PS: Photosensitizer

RB: Rose Bengal

ROS: Reactive oxygen species

SA: Sodium alginate

SS: Sonosensitizer

SA: Sodium alginate

TMAP^{4+}: 5,10,15,20-Tetrakis(4-*N,N,N*-trimethylammoniumphenyl)porphyrin

TDPyP: 5-(1-Dodecanoylpyridinium-4yl)-10,15,20-triphenylporphyrin

TMPyP: 5,10,15,20-Tetrakis(1-methyl-4-pyridyl)-porphyrin, tetra-p-tosylate salt

TMP: 5,10,15,20-(*N*-methyl-4-pyridyl) porphyrin tetra iodide

TB: Toluidine blue

US: United States

WHO: World health organization

ZnPc: (phthalocyaninato)zinc(II)

1.6. References

1. Högberg LD, Heddini A and Cars O. *Trends Pharmacol. Sci.* 2010; **31**: 509-515.

2. 2.Beceiro A, Tomás M and Bou G. *Clin. Microbiol. Rev.* 2013; **26**: 185-230.

3. 3. Jassim SAA and Limoges RG. *World J. Microbiol. Biotechnol.* 2014; **30**: 2153-2170.

4. Andersson DI and Hughes D. *FEMS Microbiol. Rev.* 2011; **35**: 901-911.

5. Donlan RM and Costerton JW. *Clin. Microbiol. Rev.* 2002; **15**: 167-193.

6. Bengtsson-Palme J, Kristiansson E and Larsson DGJ. *FEMS Microbiol. Rev.* 2018; **42**: 68-80.

7. Garoy EY, Gebreab YB, Achila OO, Tekeste DG, Kesete R, Ghirmay R, Kiflay R and Tesfu T. *Can. J. Infect. Dis. Med. Microbiol.* 2019; **2019**.

8. Mills MP, Rosen PS, Chambrone L, Greenwell H, Kao RT, Klokkevold PR, McAllister BS, Reynolds MA, Romanos GE and Wang HL. *J. Periodontol.* 2018; **89**: 737-742.

9. Torgersen H, Lassen J, Jelsoe E, Rusanen T and Nielsen TH. *J. Biolaw Bus.* 2003; **3**: 53-59.

10. Alsan M and Klompas M. *J. Clin. Outcomes Manag.* 2010; **17**: 27-35.

11. How KY, Song KP and Chan KG. *Front. Microbiol.* 2016; **7**: 1-14.

12. Jones KE, Patel NG, Levy MA, Storeygard A, Balk D, Gittleman JL and Daszak P. *Nature* 2008; **451**: 990-993.

13. Dadgostar P. *Infect. Drug Resist.* 2019; **12**: 3903-3910.

14. Harvey WT, Carabelli AM, Jackson B, Gupta RK, Thomson EC, Harrison EM, Ludden C, Reeve R, Rambaut A, Peacock SJ and Robertson DL. *Nat. Rev. Microbiol.* 2021; **19**: 409-424.

15. Petersen E, Ntoumi F, Hui DS, Abubakar A, Kramer LD, Obiero C, Tambyah PA, Blumberg L, Yapi R, Al-Abri S, Pinto T de CA, Yeboah-Manu D, Haider N, Asogun D, Velavan TP, Kapata N, Bates M, Ansumana R, Montaldo C, Mucheleng'anga L, Tembo J, Mwaba P, Himwaze CM, Hamid MMA, Mfinanga S, Mboera L, Raj T, Aklillu E, Veas F, Edwards S, Kaleebu P, McHugh TD, Chakaya J, Nyirenda T, Bockarie M, Nyasulu PS, Wejse C, Muyembe-Tamfum J-J, Azhar EI, Maeurer M, Nachega JB, Kock R, Ippolito G and Zumla A. *Int. J. Infect. Dis.* 2022; **114**: 268-272.

16. Singh A, Shaikh A, Singh R and Singh AK. *Diabetes Metab. Syndr. Clin. Res. Rev.* 2020; **14**: 277-281.

17. Bi Y, Xia G, Shi C, Wan J, Liu L, Chen Y, Wu Y, Zhang W, Zhou M, He H and Liu R. *Fundam. Res.* 2021; **1**: 193-212.

18. Zaidi KU, Mani A, Parmar R and Thawani V. *Open Biol. Sci. J.* 2018; **4**: 1-6.

19. Nagle AS, Khare S, Kumar AB, Supek F, Buchynskyy A, Mathison CJN, Chennamaneni NK, Pendem N, Buckner FS, Gelb MH and Molteni V. *Chem. Rev.* 2014; **114**: 11305-11347.

20. Dhingra S, Rahman NAA, Peile E, Rahman M, Sartelli M, Hassali MA, Islam T, Islam S and Haque M. *Front. Public Health* 2020; **8**: 1-22.

21. Khan AA, Manzoor KN, Sultan A, Saeed M, Rafique M, Noushad S, Talib A, Rentschler S and Deigner HP. *Int. J. Mol. Sci.* 2021; **22**: 1-40.

22. Prestinaci F, Pezzotti P and Pantosti A. *Pathog. Glob. Health* 2015; **109**: 309-318.

23. Nille GC and Chaudhary AK. *J. Ayurveda Integr. Med.* 2021; **12**: 172-177.

24. Dai T, Fuchs BB, Coleman JJ, Prates RA, Astrakas C, St. Denis TG, Ribeiro MS, Mylonakis E, Hamblin MR and Tegos GP. *Front. Microbiol.* 2012; **3**: 1-16.

25. Maisch T, Bosl C, Szeimies RM, Lehn N and Abels C. *Antimicrob. Agents Chemother.* 2005; **49**: 1542-1552.

26. Jodlbauer A, von Tappeiner H. *Munch. Med. Wochenschr.* 1904; **5**1:1096-1097.

27. Hamblin MR. *Photochem. Photobiol.* 2020; **96**: 506-516.

28. Møller KI, Kongshoj B, Philipsen PA, Thomsen VO and Wulf HC. *Photodermatol. Photoimmunol. Photomed.* 2005; **21**: 118-124.

29. Hamblin MR and Hasan T. *Photochem. Photobiol.* 2004; **3**: 436-450.

30. Agostinis P, Berg K, Cengel KA, Foster TH, Girotti AW, Gollnick SO, Hahn SM, Hamblin MR and Juzeniene *A. CA Cancer J. Clin.* 2011; **61**: 250-281.

31. Yano S, Hirohara S, Obata M, Hagiya Y, Ogura S ichiro, Ikeda A, Kataoka H, Tanaka M and Joh T. *J. Photochem. Photobiol. C Photochem. Rev.* 2011; **12**: 46-67.

32. Wozniak A and Grinholc M. *Front. Microbiol.* 2018; **9**:1-19.

33. Liu Y, Qin R, Zaat SAJ, Breukink E and Heger M. *J. Clin. Transl. Res.* 2015; **1**: 140-167.

34. Kashef N, Huang YY and Hamblin MR. *Nanophotonics* 2017; **6**: 853-879.

35. Li H, Zhou X, Huang Y, Liao B, Cheng L and Ren B. *Front. Microbiol.* 2021; **11**: 1-9.

36. Sperandio FF, Huang YH and Hamblin MR. *Recent Pat. Antiinfect. Drug Discov.* 2013; **8**: 108-120.

37. Nakonechny F, Firer MA, Nitzan Y and Nisnevitch M. *Photochem. Photobiol.* 2010; **86**: 1350-1355.

38. Pajerski W, Ochonska D, Brzychczy-Wloch M, Indyka P, Jarosz M, Golda-Cepa M, Sojka Z and Kotarba A. *J. Nanoparticle Res.* 2019; **21**:186-198.

39. Redeker C and Briscoe WH. *Langmuir* 2019; **35**: 15739-15750.

40. Klausen M, Ucuncu M and Bradley M. *Molecules* 2020; **25**: 5239-5269.

41. Nguyen MT, Matsuo M, Niemann S, Herrmann M and Götz F. *Front. Microbiol.* 2020; **11**: 1-15.

42. Miller KP, Wang L, Benicewicz BC and Decho AW. *Chem. Soc. Rev.* 2015; **44**: 7787-7807.

43. Ion RM. *Coatings* 2021; **11**: 1-21.

44. Wilkinson F, Helman WP and Ross AB. *J. Phys. Chem. Ref. Data* 1993; **22**: 113-262.

45. Castano AP, Demidova TN and Hamblin MR. *Photodiagn. Photodyn. Ther.* 2004; **1**: 279-293.

46. Josefsen LB and Boyle RW. *Br. J. Pharmacol.* 2008; **154**: 1-3.

47. Abrahamse H and Hamblin MR. *Biochem. J.* 2017; **473**: 347-364.

48. Jenkins SG and Schuetz AN. *Mayo Clin. Proc.* 2012; **87**: 290-308.

49. Fontana CR, Abernethy AD, Som S, Ruggiero K, Doucette S, Marcantonio RC, Boussios CI, Kent R, Goodson JM, Tanner ACR and Soukos NS. *J. Periodontal Res.* 2009; **44**: 751-759.

50. Zanin ICJ, Lobo MM, Rodrigues LKA, Pimenta LAF, Höfling JF and Gonçalves RB. *Eur. J. Oral Sci.* 2006; **114**: 64-69.

51. Fekrazad R, Zare H and Vand SMS. *Photodiagn. Photodyn. Ther.* 2016; **15**: 213-217.

52. Shrestha A and Kishen A. *Photochem. Photobiol.* 2012; **88**: 577-583.

53. Ragàs X, Dai T, Tegos GP, Agut M, Nonell S and Hamblin MR. *Lasers Surg. Med.* 2010; **42**: 384-390.

54. Phoenix DA and Harris F. *Trends Mol. Med.* 2003; **9**: 283-285.

55. Najafi S, Khayamzadeh M, Paknejad M, Poursepanj G, Fard MJK and Bahador A. *J. Lasers Med. Sci.* 2016; **7**: 21-25.

56. Dahl TA, Mcgowan WM, Shand MA and Srinivasan VS. *Arch. Microbiol.* 1989; **151**: 183-185.

57. García I, Ballesta S, Gilaberte Y, Rezusta A and Pascual Á. *Future Microbiol.* 2015; **10**: 347-356.

58. Yow CMN, Tang HM, Chu ESM and Huang Z. *Photochem. Photobiol.* 2012; **88**: 626-632.

59. Maisch T, Eichner A, Späth A, Gollmer A, König B, Regensburger J and Bäumler W. *PLoS One* 2014; **9**: 1-18.

60. Paskeviciute E, Zudyte B and Luksiene Z. *J. Photochem. Photobiol. B Biol.* 2018; **182**: 130-136.

61. Bresolí-Obach R, Gispert I, Peña DG, Boga S, Gulias Ó, Agut M, Vázquez ME and Nonell S. *J. Biophotonics.* 2018; **11**: 54-71.

62. Collins TL, Markus EA, Hassett DJ and Robinson JB. *Curr. Microbiol.* 2010; **61**: 411-416.

63. Di Poto A, Sbarra MS, Provenza G, Visai L and Speziale P. *Biomaterials* 2009; **30**: 3158-3166.

64. Cieplik F, Späth A, Regensburger J, Gollmer A, Tabenski L, Hiller KA, Bäumler W, Maisch T and Schmalz G. *Free Radic. Biol. Med.* 2013; **65**: 477-487.

65. Bertolini G, Rossi F, Valduga G, Jori G and van Lier J. *FEMS Microbiol. Lett.* 1990; **71**: 149-155.

66. Strakhovskaya MG, Antonenko YN, Pashkovskaya AA, Kotova EA, Kireev V, Zhukhovitsky VG, Kuznetsova NA, Yuzhakova OA, Negrimovsky VM and Rubin AB. *Biochem.* 2009; **74**: 1305-1314.

67. Segalla A, Borsarelli CD, Braslavsky SE, Spikes JD, Roncucci G, Dei D, Chiti G, Jori G and Reddi E. *Photochem. Photobiol. Sci.* 2002; **1**: 641-648.

68. Karygianni L, Ruf S, Follo M, Hellwig E, Bucher M, Anderson AC, Vach K and Al-Ahmad A. *Appl. Environ. Microbiol.* 2014; **80**: 7324-7336.

69. Mesquita MQ, Dias CJ, Neves MGPMS, Almeida A and Faustino MAF. *Molecules* 2018; **23**: 2424-2471.

70. de Menezes HD, Tonani L, Bachmann L, Wainwright M, Braga GÚL and von Zeska Kress MR. *J. Photochem. Photobiol. B Biol.* 2016; **164**: 1-12.

71. Tegos GP and Hamblin MR. *Antimicrob. Agents Chemother.* 2006; **50**: 196-203.

72. Thesnaar L, Bezuidenhout JJ, Petzer A, Petzer JP and Cloete TT. *Eur. J. Pharm. Sci.* 2021; **157**: 105603.

73. Youf R, Müller M, Balasini A, Th F, Müller M, Hascoët A, Jonas U, Schönherr H, Lemercier G, Montier T and Gall T Le. *Pharmaceutics* 2021: **13**; 1995-2051.

74. Mundt JM, Rouse L, Van Den Bossche J and Goodrich RP. *Photochem. Photobiol.* 2014; **90**: 957-964.

75. Liu PF, Zhu WH and Huang CM. *Curr Drug Metab*. 2009: **10**; 90-94.

76. Cullen AA, Rajagopal A, Heintz K, Heise A, Murphy R, Sazanovich I V., Greetham GM, Towrie M, Long C, Fitzgerald-Hughes D and Pryce MT. *J. Phys. Chem. B* 2021; **125**: 1550-1557.

77. Prieto-Montero R, Prieto-Castañeda A, Sola-Llano R, Agarrabeitia AR, García-Fresnadillo D, López-Arbeloa I, Villanueva A, Ortiz MJ, de la Moya S and Martínez-Martínez V. *Photochem. Photobiol.* 2020; **96**: 458-477.

78. Zheng Q, Xu G and Prasad PN. *Chem. Eur. J.* 2008; **14**: 5812-5819.

79. Kocaoglu O, Carlson EE. *Nat Chem Biol.* 2016; **12**: 472-478

80. Josefsen LB and Boyle RW. *Theranostics* 2012; **2**: 916-966.

81. Snyder JW, Lambert JDC and Ogilby PR. *Photochem. Photobiol.* 2006; **82**: 177-184.

82. Oliveira A, Almeida A, Carvalho CMB, Tomé JPC, Faustino MAF, Neves MGPMS, Tomé AC, Cavaleiro JAS and Cunha A. *J. Appl. Microbiol.* 2009; **106**: 1986-1995.

83. Abid S, Hassine SB, Richy N, Camerel F, Jamoussi B, Blanchard-Desce M, Mongin O, Paul F and Paul-Roth CO. *Molecules* 2020; **25**; 239-269.

84. Zhou Y, Wang D, Zhang Y, Chitgupi U, Geng J, Wang Y, Zhang Y, Cook TR, Xia J and Lovell JF. *Theranostics* 2016; **6**: 688-697.

85. Mehraban N, Musich PR and Freeman HS. *Appl. Sci.* 2019; **9**: 1-14.

86. Akpe V, Vernet E, Madu C, Obirai JC and Brismar H. *ChemPlusChem* 2014; **79**: 671-679.

87. Ghorbani J, Rahban D, Aghamiri S, Teymouri A and Bahador A. *Laser Ther.* 2018; **27**: 293-302.

88. De Filippis MP, Dei D, Fantetti L and Roncucci G. *Tetrahedron Lett.* 2000; **41**: 9143-9147.

89. Galstyan A. *Chem. Eur. J.* 2021; **27**: 1903-1920.

90. Karygianni L, Ruf S, Follo M, Hellwig E, Bucher M, Anderson AC, Vach K and Al-Ahmad A. *Appl. Environ. Microbiol.* 2014; **80**: 7324-7336.

91. Fekrazad R, Bargrizan M, Sajadi S and Sajadi S. *Photodiagn. Photodyn. Ther.* 2011; **8**: 249-253.

92. Sorkhdini P, Moslemi N, Jamshidi S, Jamali R, Amirzargar AA and Fekrazad R. *J. Periodontol.* 2013; **84**: 793-800.

93. Siewert B and Stuppner H. *Phytomedicine* 2019; **60**: 152985.

94. Uchoa AF, Konopko AM and Baptista MS. *J. Braz. Chem. Soc.* 2015; **26**: 2615-2622.

95. Joanne B, Anderson LA and Phillipson. *J. Pharm. Pharmacol.* 2001; **53**: 583-600

96. Soria-Lozano P, Gilaberte Y, Paz-Cristobal M, Pérez-Artiaga L, Lampaya-Pérez V, Aporta J, Pérez-Laguna V, García-Luque I, Revillo M and Rezusta A. *BMC Microbiol.* 2015; **15**: 1-8.

97. Prasad S, Tyagi AK and Aggarwal BB. *Cancer Res. Treat.* 2014; 46: 2-18.

98. Dias LD, Blanco KC, Mfouo-Tynga IS, Inada NM and Bagnato VS. *J. Photochem. Photobiol. C Photochem. Rev.* 2020; **45**: 100384-100419.

99. Becker RS and Allison JB. *J. Phys. Chem.* 1963; **67**: 2662-2669.

100. Senge MO, Ryan AA, Letchford KA, MacGowan SA and Mielke T. *Symmetry* 2014; **6**: 781-843.

101. Sułek A, Pucelik B, Kobielusz M, Barzowska A and Dąbrowski JM. *Int. J. Mol. Sci.* 2020; **21**: 1-34.

102. Gjuroski I, Furrer J and Vermathen M. *Molecules* 2021; **26**: 1942-1985.

103. Zhang QY, Yan Z Bin, Meng YM, Hong XY, Shao G, Ma JJ, Cheng XR, Liu J, Kang J and Fu CY. *Mil. Med. Res.* 2021; **8**: 1-25.

104. Klausen M, Ucuncu M and Bradley M. *Molecules* 2020; **25**: 5239-5269.

105. Hu X, Huang YY, Wang Y, Wang X and Hamblin MR. *Front. Microbiol.* 2018; **9**: 1-24.

106. Malatesti N, Munitic I and Jurak I. *Biophys. Rev.* 2017; **9**: 149-168.

107. Azizullah A and Murad W. *Environ. Impact Assess. Rev.* 2015; **50**: 156-157.

108. Galli SJ, Tsai M and Piliponsky AM. *Nature* 2008; **454**: 445-454.

109. Luksiene Z and Brovko L. *Food Eng. Rev.* 2013; **5**: 185-199.

110. Lucky SS, Soo KC and Zhang Y. *Chem. Rev.* 2015; **115**: 1990-2042.

111. Zhou F, Lin S, Zhang J, Kong Z, Tan BK, Hamzah SS and Hu J. *Photodiagn. Photodyn. Ther.* 2021; **37**: 102677-102685.

112. Sethi D and Sakthivel R. *J. Photochem. Photobiol. B Biol.* 2017; **168**: 117-123.

113. Benavent C, Torrado-Salmerón C and Torrado-Santiago S. *Pharmaceuticals* 2021; **14**: 397-411.

114. Galstyan A, Majiya H and Dobrindt U. *Nanoscale Adv.* 2022; **4**: 200-210.

115. Deda DK, Iglesias BA, Alves E, Araki K and Garcia CRS. *Molecules* 2020; **25**: 1-31.

116. Patra JK, Das G, Fraceto LF, Campos EVR, Rodriguez-Torres MDP, Acosta-Torres LS, Diaz-Torres LA, Grillo R, Swamy MK, Sharma S, Habtemariam S and Shin HS. *J. Nanobiotechnology* 2018; **16**: 1-33.

117. Gupta A, Mumtaz S, Li C, Hussain I, Vincent M and States U. *Chem. Soc. Rev.* 2019; **48**: 415-427.

118. Dos Santos Ramos MA, Da Silva PB, Spósito L, De Toledo LG, Bonifácio B vidal, Rodero CF, Dos Santos KC, Chorilli M and Bauab TM. *Int. J. Nanomedicine* 2018; **13**: 1179-1213.

119. Wang Y, Jin Y, Chen W, Wang J, Chen H, Sun L, Li X, Ji J, Yu Q, Shen L and Wang B. *Chem. Eng. J.* 2019; **358**: 74-90.

120. Khurana B, Gierlich P, Meindl A, Gomes-Da-Silva LC and Senge MO. *Photochem. Photobiol. Sci.* 2019; **18**: 2613-2656.

121. Tadavarthy SM, Moller JH and Amplatz K. *Am. J. Roentgen.*, 1975; **125**: 609–616.

122. Danno A. *J. Phys. Soc. Japan* 1958; **13**: 722-727.

123. Islands F and Survey D. *Nature* 1960; **185**: 63-64.

124. Kang-Mieler JJ, Rudeen KM, Liu W and Mieler WF. *Eye* 2020; **34**: 1371-1379.

125. Katchalsky A and Michaeli I. *J. Polym. Sci.* 1955; **15**: 69-86.

126. Kopček J and Kopečková P. *Adv. Drug Deliv. Rev.* 2010; **62**: 122-149.

127. Fujiwara T, Mukose T, Yamaoka T, Yamane H, Sakurai S and Kimura Y. *Macromol. Chem. Phys.* 2001; **202**: 204-208.

128. Kirakci K, Šícha V, Holub J, Kubát P and Lang K. *Inorg. Chem.* 2014; **53**: 13012-13018.

129. Jochum FD and Theato P. *Chem. Soc. Rev.* 2013; **42**: 7468-7483.

130. Chen S and Singh J. *Int. J. Pharm.* 2005; **295**: 183-190.

131. Graham NB and McNeill ME. *Biomaterials* 1984; **5**: 27-36.

132. Szafraniec-Szczęsny J, Janik-Hazuka M, Odrobińska J and Zapotoczny S. *Polymers* 2020; **12**: 1-25.

133. Zhang X, Xia LY, Chen X, Chen Z and Wu FG. *Sci. China Mater.* 2017; **60**: 487-503.

134. Karg M, Pich A, Hellweg T, Hoare T, Lyon LA, Crassous JJ, Suzuki D, Gumerov RA, Schneider S, Potemkin II and Richtering W. *Langmuir* 2019; **35**: 6231-6255.

135. Polívková M, Hubáček T, Staszek M, Švorčík V and Siegel J. *Int. J. Mol. Sci.* 2017; **18**: 419-443.

136. Vasile C, Pamfil D, Stoleru E and Baican M. *Molecules* 2020; **25**: 1539-1607.

137. Donnelly RF, Cassidy CM, Loughlin RG, Brown A, Tunney MM, Jenkins MG and McCarron PA. *J. Photochem. Photobiol. B Biol.* 2009; **96**: 223-231.

138. Wu J, Xu H, Tang W, Kopelman R, Philbert MA and Xi C. *Antimicrob. Agents Chemother.* 2009; **53**: 3042-3048.

139. Carmello JC, Alves F, Mima EG de O, Jorge JH, Bagnato VS and Pavarina AC. *Photodiagn. Photodyn. Ther.* 2017; **17**: 194-199.

140. Spagnul C, Turner LC, Giuntini F, Greenman J and Boyle RW. *J. Mater. Chem. B* 2017; **5**: 1834-1845.

141. Halpenny GM, Steinhardt RC, Okialda KA and Mascharak PK. *J. Mater. Sci. Mater. Med.* 2009; **20**: 2353-2360.

142. McCoy CP, Craig RA, McGlinchey SM, Carson L, Jones DS and Gorman SP. *Biomaterials* 2012; **33**: 7952-7958.

143. Castano AP, Mroz P and Hamblin MR. *Nat. Rev. Cancer* 2006; **6**: 535-545.

144. Fallows SJ, Garland MJ, Cassidy CM, Tunney MM, Singh TRR and Donnelly RF. *J. Photochem. Photobiol. B Biol.* 2012; **114**: 61-72.

145. Reddy MSB, Ponnamma D, Choudhary R and Sadasivuni KK. *Polymers* 2021; **13**: 1105-1156.

146. Trovatti E, Fernandes SCM, Rubatat L, Perez D da S, Freire CSR, Silvestre AJD and Neto CP. *Compos. Sci. Technol.* 2012; **72**: 1556-1561.

147. Mishra RK, Sabu A and Tiwari SK. *J. Saudi Chem. Soc.* 2018; **22**: 949-978.

148. Decraene V, Pratten J and Wilson M. *Appl. Environ. Microbiol.* 2006; **72**: 4436-4439.

149. Rahimi R, Fayyaz F and Rassa M. *Mater. Sci. Eng. C* 2016; **59**: 661-668.

150. Ringot C, Sol V, Granet R and Krausz P. *Mater. Lett.* 2009; **63**: 1889-1891.

151. Sharma M, Dube A and Majumder SK. *Lasers Med. Sci.* 2021; **36**: 763-772.

152. Joseph SM, Krishnamoorthy S, Paranthaman R, Moses JA and Anandharamakrishnan C. *Carbohydr. Polym. Technol. Appl.* 2021; **2**: 100036.

153. Atay HY. *Funct. Chitosan*. 2020; **6**: 457-489.

154. Chi M, Qi M, Lan A, Wang P, Weir MD, Melo MA, Sun X, Dong B, Li C, Wu J, Wang L and Xu HHK. *Int. J. Mol. Sci.* 2019; **20**: 278-307.

155. Qin Y and Li P. *Int. J. Mol. Sci.* 2020; **21**: 499-518.

156. Spagnul C, Turner LC and Boyle RW. *J. Photochem. Photobiol. B Biol.* 2015; **150**: 11-30.

157. Frade ML, de Annunzio SR, Calixto GMF, Victorelli FD, Chorilli M and Fontana CR. *Molecules* 2018; **23**: 473-489.

158. Bayat F and Karimi AR. *Int. J. Biol. Macromol.* 2019; **129**: 927-935.

159. Kogan G, Šoltés L, Stern R and Gemeiner P. *Biotechnol. Lett.* 2007; **29**: 17-25.

160. Gupta RC, Lall R, Srivastava A and Sinha A. *Front. Vet. Sci.* 2019; **2019**: 6-192.

161. Khunmanee S, Jeong Y and Park H. *J. Tissue Eng.* 2017; **8**: 1-16.

162. Vogus DR, Evans MA, Pusuluri A, Barajas A, Zhang M, Krishnan V, Nowak M, Menegatti S, Helgeson ME, Squires TM and Mitragotri S. *J. Control. Release* 2017; **267**: 191-202.

163. Schanté CE, Zuber G, Herlin C and Vandamme TF. *Carbohydr. Polym.* 2011; **85**: 469-489.

164. Huang G and Huang H. *Drug Deliv.* 2018; **25**: 766-772.

165. Wikene KO, Hegge AB, Bruzell E and Tonnesen HH. *Drug Dev. Ind. Pharm.* 2015; **41**: 969-977.

166. Park SN, Kim JK and Suh H. *Biomaterials* 2004; **25**: 3689-3698.

167. Ferdous Z and Nemmar A. *Int. J. Mol. Sci.* 2020; **21**: 2375-2406.

168. Zhang Y, Sun P, Zhang L, Wang Z, Wang F, Dong K, Liu Z, Ren J and Qu X. *Adv. Funct. Mater.* 2019; **29**: 1-9.

169. Suo H, Hussain M, Wang H, Zhou N, Tao J, Jiang H and Zhu J. *Biomacromolecules* 2021; **22**: 3049-3059.

170. Yoon HK, Lou X, Chen YC, Koo Lee YE, Yoon E and Kopelman R. *Chem. Mater.* 2014; **26**: 1592-1600.

171. Chen CT, Chen CP, Yang JC and Tsai T. *Antiinfect. Drug Discov.* 2013; **8**: 100-107.

172. Lakshmi PK, Kalpana B and Prasanthi D. *Syst. Rev. Pharm.* 2013; **4**: 26-30.

173. Miao L, Lin J, Huang Y, Li L, Delcassian D, Ge Y, Shi Y and Anderson DG. *Nat. Commun.* 2020; **11**: 2424-2437.

174. Riaz MK, Riaz MA, Zhang X, Lin C, Wong KH, Chen X, Zhang G, Lu A and Yang Z. *Int. J. Mol. Sci.* 2018; **19**: 195-222.

175. Beltrán-Gracia E, López-Camacho A, Higuera-Ciapara I, Velázquez-Fernández JB and Vallejo-Cardona AA. *Cancer Nano.* 2019; **10**; 1-40.

176. Riaz MK, Riaz MA, Zhang X, Lin C, Wong KH, Chen X, Zhang G, Lu A and Yang Z. *Int. J. Mol. Sci.* 2018; **19**.

177. Bozzuto G and Molinari A. *Int. J. Nanomedicine* 2015; **10**: 975-999.

178. Sercombe L, Veerati T, Moheimani F, Wu SY, Sood AK and Hua S. *Front. Pharmacol.* 2015; **6**: 1-13.

179. Longo JPF, Leal SC, Simioni AR, De Fátima Menezes Almeida-Santos M, Tedesco AC and Azevedo RB. *Lasers Med. Sci.* 2012; **27**: 575-584.

180. Fischer CL, Walters KS, Drake DR, Dawson D V., Blanchette DR, Brogden KA and Wertz PW. *Int. J. Oral Sci.* 2013; **5**: 130-140.

181. Ferro S, Ricchelli F, Monti D, Mancini G and Jori G. *Int. J. Biochem. Cell Biol.* 2007; **39**: 1026-1034.

Chapter 2. Formulating photosensitizer-conjugates and their antimicrobial evaluation

## 2. Cationic porphyrins and chlorins and their application in aPDT

2.1. PSs in aPDT.

As has been established, porphyrin and chlorin based photosensitizers (PSs) undergo photoactivation with a suitable wavelength of light, inducing an oxidative damage to the bacterial cell wall via production of reactive oxygen species (singlet oxygen and free radicals).[1,2]

2.1.1. Cationic porphyrins

An efficient PDT against microbes (aPDT) requires that the PS is co-located with the target cells prior to irradiation with light. Cationic PSs have been the most popular candidates used for aPDT, due to an enhanced and effective interaction to the charged surface of the bacterial cell wall, especially gram-negative species which have proved difficult to eliminate.[3]

In the literature, there are several examples of efficient aPDT when bacteria are treated with cationic porphyrins. TMPyP, a typical cationic porphyrin, has been studied intensively for its antimicrobial activity; research has indicated that it can also induce photodynamic inactivation (PDI) of *E. coli* via production of singlet oxygen under illumination with light.[4] TMPyP has also shown very promising activity against radiation resistant *Dinococcus radiodurans* bacteria under illumination with blue light.[5] A newly synthesized porphyrin-based photosensitizer, Exeporfinium chloride (XF-73) (**2.1**) as shown in Figure 2.1, has demonstrated an efficiency as a PS against the MRSA species and exploring the potential of such PSs for sterilization per se.[6]
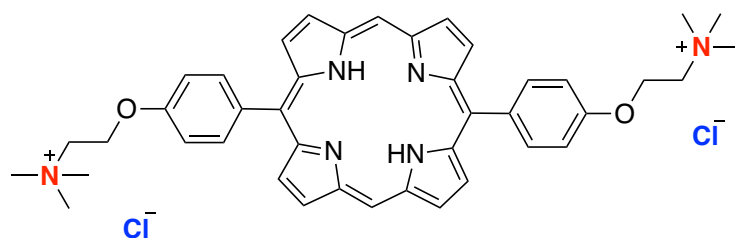
2.1

Figure 2.1. Structure of XF-73 (**2.1**).

Tricationic porphyrinoids such as 2,7,12-tris(trimethyl-*p*-tolyl)-17-(*p*-(methoxymethyl)phenyl)porphycene (NMe₃MeO-TBPo) (**2.2**) and its predecessor 2,7,12-tris(α-pyridinio-*p*-tolyl)-17-(*p*-(methoxymethyl)phenyl)porphycene (Py₃MeO-TBPo) (**2.3**), have been shown to inactivate Gram-positive *S. aureus* and Gram-negative *P. aeruginosa* and *E. coli*.[7] These compounds are shown in Figure 2.2.
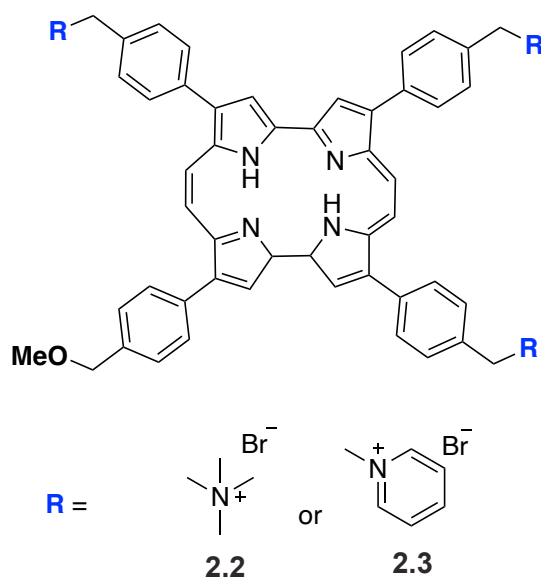

Figure 2.2. Tricationic 2,7,12-tris(trimethyl-*p*-tolyl)-17-(*p*-(methoxymethyl)phenyl)porphycene (NMe₃MeO-TBPo) (**2.2**) and 2,7,12-tris(α-pyridinio-*p*-tolyl)-17-(*p*-(methoxymethyl)phenyl).porphycene (Py₃MeO-TBPo) (**2.3**).

Typhoid is a common and recurring infection in humans, caused by contact with untreated water bearing the parasite. It has been established that photoinactivation of *Salmonella typhimurium* can be achieved by the cationic ruthenium derivative of 5,10,15,20-tetra(4-pyridyl)porphyrin (RuTPyP) (**2.4**) or its Zn(II) complex (ZnRuTPyP) (**2.5**) complexes, as shown in Figure 2.3.[8] These derivatives display effective formation of reactive oxygen species (ROS) under irradiation of light with substantial singlet oxygen quantum yields of 0.02 and 0.36 for RuTPyP and ZnRuTPyP, respectively in DMSO measured under irradiation with 200 mW cm^{-2} halogen lamp .
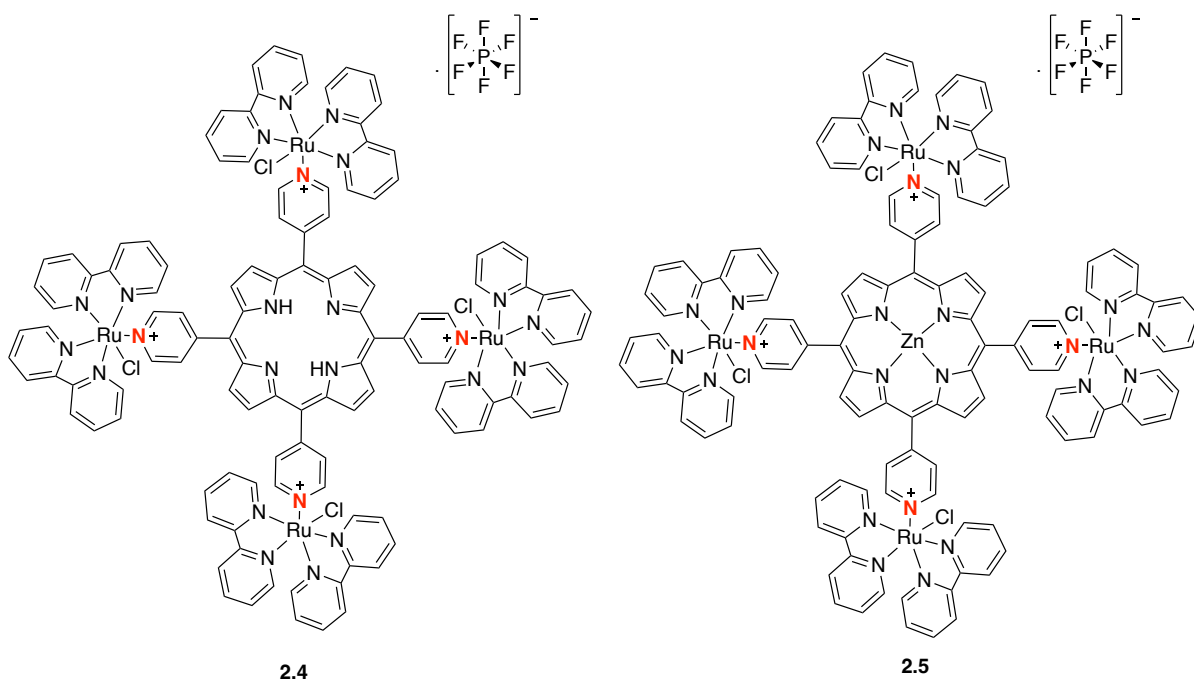
Figure 2.3. Structures of cationic porphyrins *meso*-tetra-(pyridyl)porphyrin (RuTPyP) (**2.4**) and Zn(II) complex containing peripheral Ru(II)-bipyridyl (ZnRuTPyP) (**2.5**).

These examples establish that cationic porphyrins are promising candidates to be tested and explored for their aPDT potential. Introduction of further modifications to the porphyrin periphery allows to explore the structure/activity relationships beyond the introduction of charge.

2.1.2.   Chlorins

Energy is the critical impetus for life; most of the energy available to lifeforms flows from the sun to the earth as visible light. As such, the pigments which perform this function are both readily available and evolutionarily optimized; none is better known than the central photoactive molecule of the plant photosystem, chlorophyll-a.[9] This molecule is so central to life, that its color is synonymous with life itself ("greenery"), its expression acting as the epicenter of supporting and balancing all ecosystems on land.

Chlorophyll-derived chlorins are heterocyclic aromatic moieties related to porphyrin, having three pyrrole rings and one reduced 3,4-dihydropyrrole (pyrroline) ring coupled via methine linkages. This molecule, especially the 'special pair' thereof in photosystem-II,

has become important to photochemistry, as its absorption maxima lies at the red end of the visible region (660-800 nm) where human tissue is generally translucent, which indeed makes these moieties an ideal PS to establish a higher depth of treatment in PDT.[10]

Several chlorin PS candidates have been derived from this natural-source, or synthesized from simple chemical units, and have been evaluated for their therapeutic action as PDT agents. Semisynthetic chlorins can be classified on the basis of their chemical constitution into two different classes: hydrophobic PSs, based on pheophorbide (Pba) (**2.6a**) and its derivatives and amphiphilic PSs, chlorin-*e6* and chlorin *p6* (C*p6*) (**2.6b**) and hydrophilic purpurin-18 (Pp-18) (**2.6c**) derivatives.[11] The chlorin Pp-18 has been used for PDT; with an advantageous absorption peak at 695 nm; this PS allows deeper penetration at the site of infection.[12] This molecule, however, possesses a chemical instability due to the presence of an anhydride ring which readily reacts with nucleophiles. Upon reaction with water, this yields another photosensitizer, chlorin *p6*, as shown in Scheme 2.1.
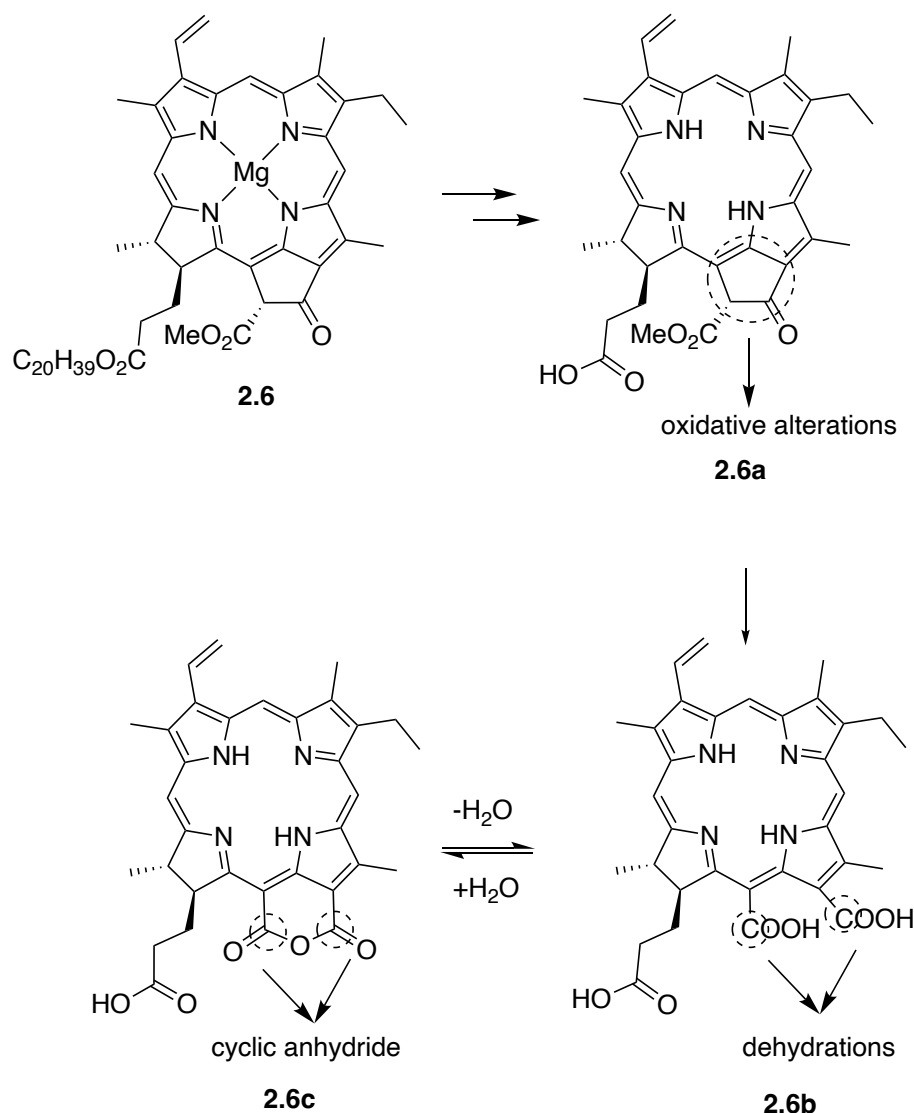
Scheme 2.1. The biological degradation process of chlorophyll *a* (**2.6**) to synthesis of derivatives pheophorbide a (**2.6a**), chlorin *p-6* (**2.6b**) and purpurin-18 (**2.6c**)

Though possessing all the important characteristics of an ideal PS and having a viable production of singlet oxygen (quantum yield 0.7 in DCM), the reactivity of anhydride ring as explained above makes this molecule unsuitable for use in PDT. Modifications of this molecule to yield relatively stable adducts have been proposed; the general strategies engaged are shown in Figure 2.4. An example of one strategy which has been thoroughly investigated is Pp-18 covalently functionalized with a peptide, by reaction of the carboxyl group with the amidogen radical of the peptide.[13] Peptide conjugates have enhanced hydrophilicity and well-ordered assembly as an advantage over the parent PS. Alternatively, functionalization of Pp-18 methyl ester by electrophilic addition of C(3)-vinyl group and subsequent substitution at 20-*meso*-position with an electrophile

gave chloro-substituted or bromo-substituted derivatives with regioselectivity, optimizing the photophysical activity (i.e. PLQY) of this PS through the heavy atom effect.[14]
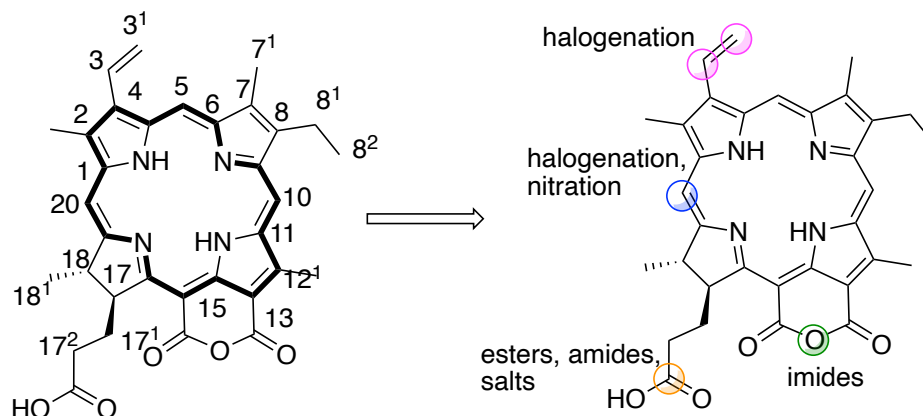

Figure 2.4. Numbered molecular structure of purpurin 18 (**Pp-18**) and positions of frequent modifications. The **Pp-18** molecule is usually modified to improve its photochemical properties, for example, by halogenation (pink and blue dots) or nitration (a blue dot), or derivatized by conjugation reactions with peptides or other tumor cell-targeting molecules (an orange dot) and cyclic anhydride to form imides (a green dot).[13,14]

Several functionalization of Pp-18 makes this PS more usable for PDT, with targeting groups and stability adjustments; the most stable derivative C*p6* has been used for PDT intensively. C*p6* was first introduced as a potential anionic PS in the 1980s and its chemical skeleton has three acidic carboxyl groups in the lower periphery of the molecule and has a absorption maxima at around 400 nm and is known to be efficient for production of singlet oxygen species (quantum yield ~0.60 in ethanol).[11,15] This class of Pp-18 derivative PS molecules has great potential applications in aPDT that have been explored only to a limited degree in literature studies.

It has been demonstrated that the related chlorin derivative C*e6* showed complete suppression of infections caused by microbes *Porphyromonas gingivalis*, *Fusobacterium nucleatum*, and *Capnocytophaga gingivalis*.[16] This derivative has also shown a 90% efficacy to eliminate the human dental plaque species.[17] The commercially available and clinically proven radachlorin is composed of C*e6*, C*p6*, and purpurin-5; each has a high quantum yield of singlet oxygen, low dark toxicity, absorption maxima in visible spectrum and high phototoxicity, making this combination a unique pharmacological agent. As a photosensitizer for aPDT this preparation has been shown to be active against *Streptococcus mutans* and for treatment of

periodontitis.[18]

## 2.2. Formulations PSs for aPDT

The PSs described above have innate properties of being PDT-active against the infectious and world-troubling microbes, with charges on the molecular skeleton enhancing the interaction with bio-membranes and aiding solubility in biological media. A conjugated formulation with a nano-scale drug-carrier can potentially enhance the selectivity of the PS in both action and solubility, augmenting these high-potency molecules interactions with the infected microbial surfaces and ensuring rapid elimination from the site of infection.[19,20]

2.2.1.   Cationic PSs-formulations for aPDT

With enhanced solubility, no dark toxicity, and sufficient adherence time for the interaction of the photosensitizer at the site of infection, aPDT with this binary PS/DDS approach is gaining clinical interest.[21] In recent years, the research and development of antimicrobial drug-delivery systems has been extensive, and the inclusion of PSs into these platforms is a promising approach for aPDT. [22,23] This combination is ideal for wound dressings, where a higher level of local drug concentration on surface, and minimal diffusion, is ideal.[24]

An example of a cationic porphyrin conjugate prepared by the Sol group at the University of Limoges, with 5-(4-aminophenyl)-10,15,20-tris(4-*N*-methylpyridinium)porphyrin triiodide with polypeptide polymyxin is shown in Scheme 2.2. This binary system possesses positively charged residues on a PDT agent, in addition to a known Gram-negative targeting antibiotic motif, allowing simple formulation with two methods of causing cell death.[25]
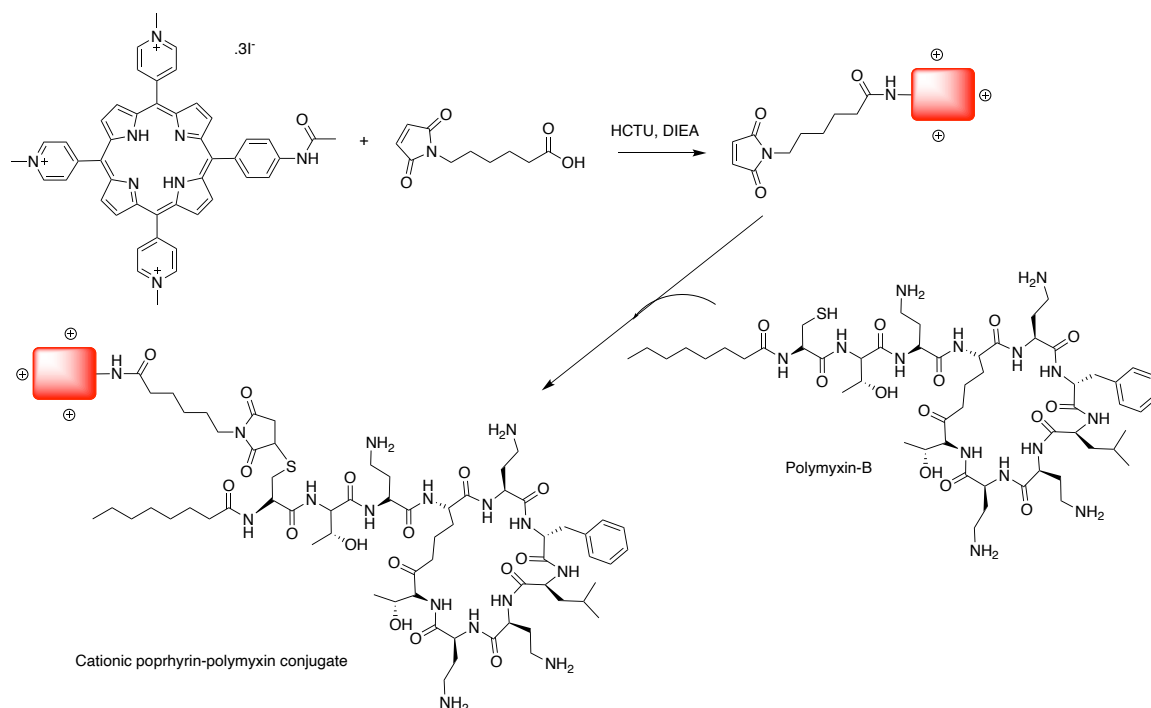
Scheme 2.2. Synthetic route of cationic porphyrin-Polymyxin B conjugate.

The conjugate showed an effective inhibition of Gram-positive strain of *Staphylococcus aureus* and most important against an enhanced inhibition against the Gram-negative *P. aeruginosa* and *E. coli*. It was demonstrated that the porphyrin-peptide conjugate adhered to the cell walls of the Gram-negative strains selectively, and caused damage, induced by production of singlet oxygen.

Another carrier platform for tricationic porphyrins was prepared on cellulose paper using a 1,3,5-triazine derivative as a linker and it was evaluated for its antimicrobial potential as shown in Scheme 2.3.[26] Antimicrobial activity of this conjugate was evaluated against Gram-positive *S. aureus* and Gram-negative *E. coli*. This formulation successfully inhibited the microbes under light illumination, making this carrier a novel platform with cationic PSs for aPDT.
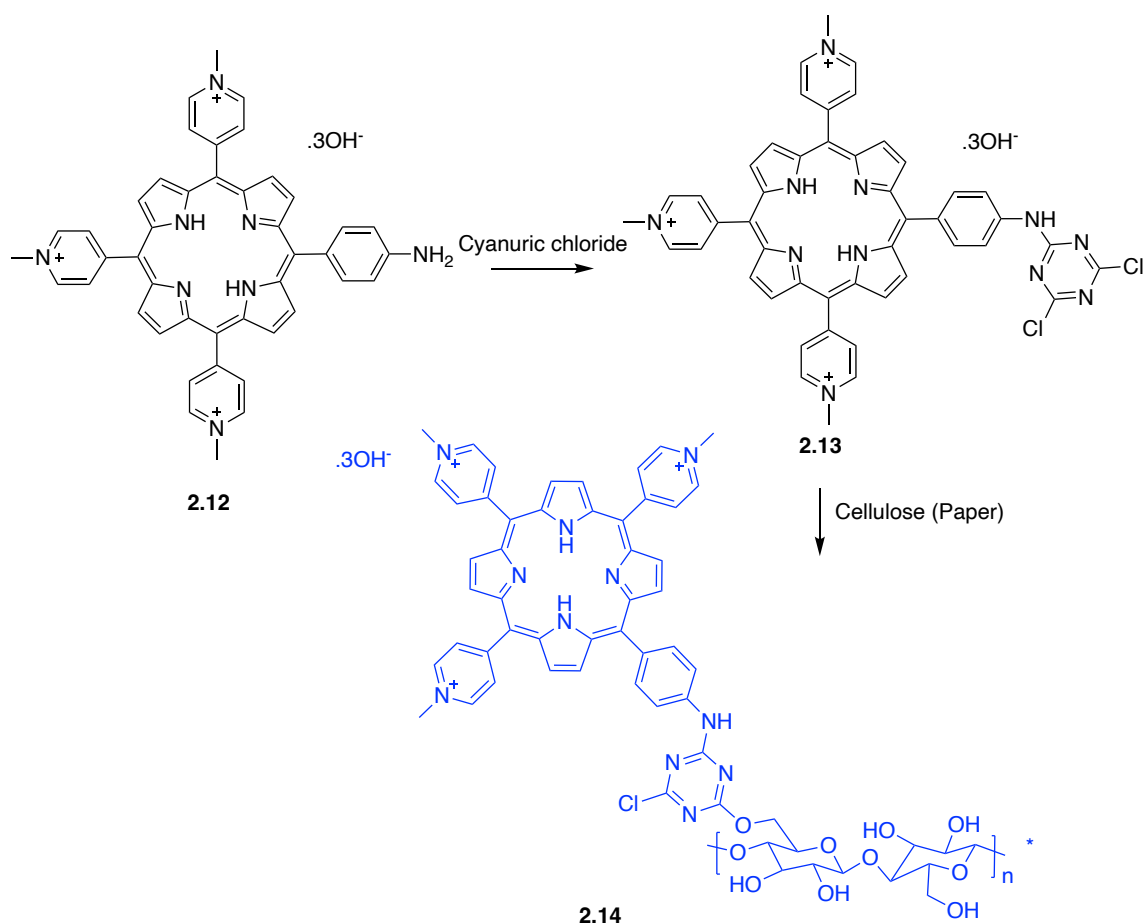
Scheme 2.3. Synthetic route to photo-antimicrobial filter paper. [26]

2.2.2.   Chlorin-formulations for PDT

As explained earlier Pp-18 can readily undergo ring opening of the anhydride ring to form a chlorin p6 form of the PS, and this property has been explored for reaction with a nucleophilic agent forming a conjugate with poly-L-lysine (pl-c*p6*). It allowed inactivation of the methicillin-resistant *Staphylococcus aureus* (MRSA) and *P. aeruginosa*. Similar derivatives have been shown to inhibit the hyperinflammatory response of infections; hence, mediating wound healing process, reducing risk of infection complications.[27]

The polycationic conjugates of C*e6* with polyethylene (PEI) (PEI-c*e6*) showed an inhibition of pathogenic *S. aureus*, *E. faecalis* (Gram-positive) and *E. coli* (Gram-negative) bacteria and the yeast *Candida albicans* after irradiation with appropriate spectrum of light.[28,29] These conjugates have also shown an inhibition of multi-drug resistant localised *Acinetobacter baumannii* bacterium.

Purpurin 18 (Pp-18) when reacted with polyethyleneimine (PEI) has shown to yield a water-soluble conjugate of chlorin shown in Scheme 2.4.[30]
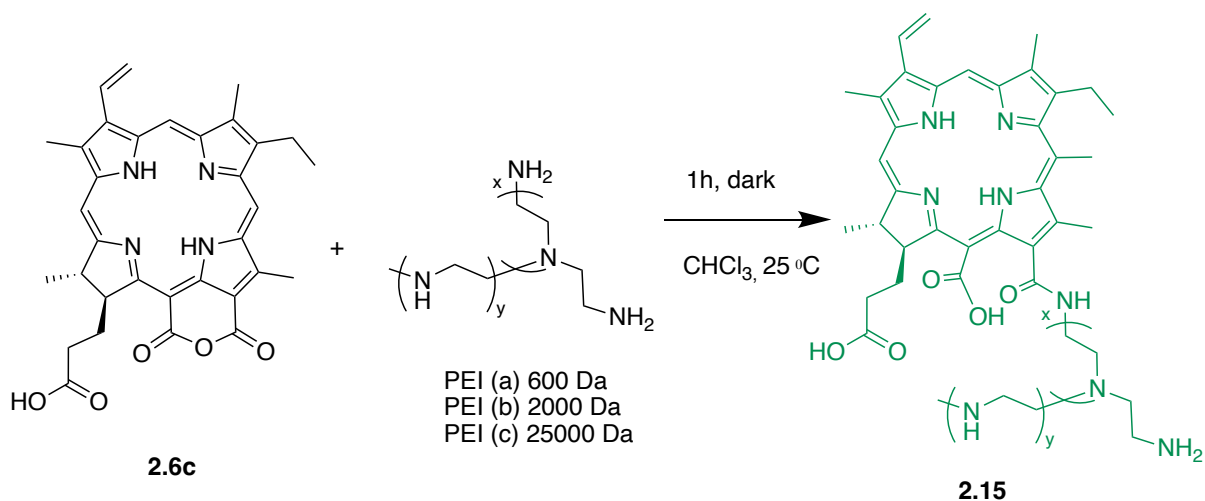
Scheme 2.4. Synthesis of photosensitizers bearing PEI 600 Da (a), 2000 Da (b), 25,000 Da (c).[30]

This formulation of the PS with PEI has been covalently grafted on cellulose nanocrystals (CNCs) obtained by hydrolyzation with sulfuric acid solution (64% w/w) as shown in Scheme 2.5.
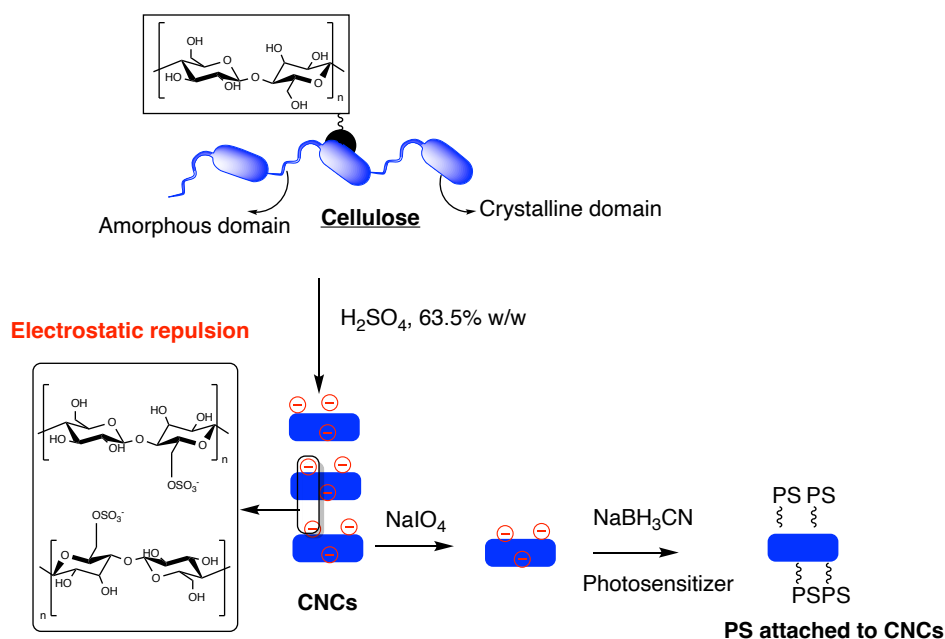
Scheme 2.5. Synthesis of photosensitizer-CNCs derivatives. [30]

*

These CNCs grafted with Pp18-PEI have been evaluated with the keratinocyte cell line (HaCat) using MTT assay and the complex showed an optimal PDT activity.

2.2.3. Hyaluronic acid polymer conjugate with PSs

HA (**2.16**) biopolymer is a non-sulfated glycosaminoglycan composed of repeating units of the disaccharide *β*-1,4-*D*-glucuronic acid–*β*-1,3 *N*-acetyl-*D*-glucosamine.[31] It possesses an inherent biocompatibility and bio-functionality and has beneficial physicochemical properties, such as high-water retention and viscoelastic properties, making this biopolymer a right choice for bio-applications in several fields of medicine specifically in cosmetology.[32] The HA chains can be cross-linked, either chemically or physically, to form DDS. The physicochemical properties, stability, and half-life of the native HA can be improved by modifying its structure and forming a conjugate.[33] After the reaction, the HA conjugates can maintain the biocompatibility and biodegradability that characterize the unmodified material.[34] The disaccharide units of HA possess three sites that may undergo chemical modification: the carboxyl group, hydroxyl group, and *N*-acetyl group as shown Figure 2.5.[35]
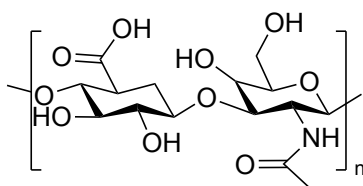
2.16

Figure 2.5. Structure of hyaluronic acid (**2.16**).

HA conjugated with chlorin derivative chlorin *e6* (C*e6*) has been evaluated for its efficiency in PDT.[36] The formulation with HA was prepared with reducible disulfide bonds (HSC) of the HA biopolymer encapsulating perfluoro hexane (PFH) within the PFH@HSC nanoparticles as illustrated in figure 2.6. These conjugates act via passive and active tumor-targeting. Nanoparticle photoactivation from "OFF" to "ON" is mediated by redox responsiveness of the conjugate. With an advantage of acting as a diagnostic

dye, the chlorin is incorporated into PFH@HSC; this conjugate acts as a dual imaging-guided PDT in treatment of hypoxic tumors.
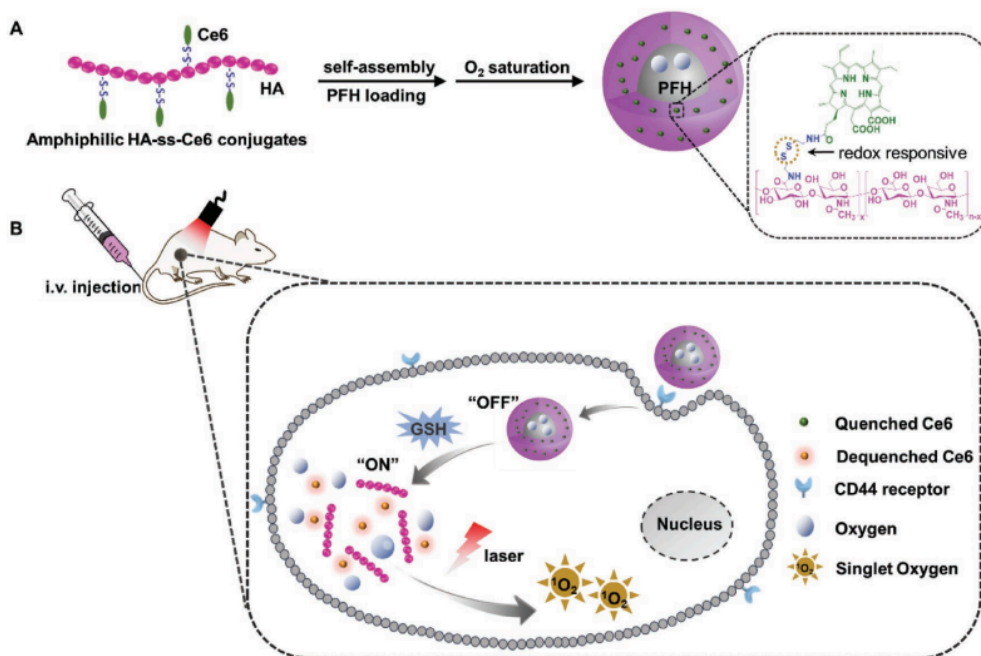

Figure 2.6. Schematic illustration of redox-activatable and oxygen self-enriched nano photosensitizers for enhancement tumor photodynamic therapy (PDT). A) The preparation process of PFH@HSC nanoparticles. B) The mechanism of PFH@HSC nanoparticles for selective and efficient PDT against hypoxic tumor cells.[36]*

*Reproduced with permission

Several additional HA conjugates with PSs efficient for aPDT are described in chapter 1. Formulations with this biopolymer make the conjugate more biocompatible and with rapid clearance from the site of infection imploring the further study of conjugates with PSs as described above to evaluate their efficiency in aPDT. Functional modification of carboxylic groups on HA has been used to formulate polymer-drug conjugates via a covalent conjugation with the synthesized PS with HA and it is a powerful platform to improve aPDT.[33] Such platforms can be used as an alternative to traditional antimicrobial medicines to treat localized infections.

2.3. Synthesis of PSs and PS-HA conjugates for aPDT

Chlorin *p6* (purpurin-18 derived) and porphyrin-based (cationic 5-(4-aminophenyl)-10,15,20-tris(4-*N*-methyl pyridinium)porphyrin triiodide) PSs have been synthesized in this chapter. These PSs have been established for having efficient therapeutics for aPDT against the two strains of bacteria. These PSs have been selected for synthesis and to form a covalent conjugate as they possess a primary amine function which has been used to covalently graft these PSs on the COOH functionality of hyaluronic acid (HA) platform via an amide link.

2.3.1. Extraction and synthesis of purpurin-18 (2.17) chlorin *p6*-PEI (2.18) conjugate

To synthesize the chlorin *p6*-PEI (**2.18**) conjugate we extracted and chemically modified the chlorin to obtain purpurin-18 (Pp-18) (**2.17**) using a previously described procedure from the blue-green algae *Spirulina maxima* as shown in scheme 2.6.[30,37] The resulting compound was characterized via spectroscopy which giving the characteristic ^{1}H spectrum of a chlorin macrocycle and the presence of an absorption band at 413 nm confirming the formation of the adduct.
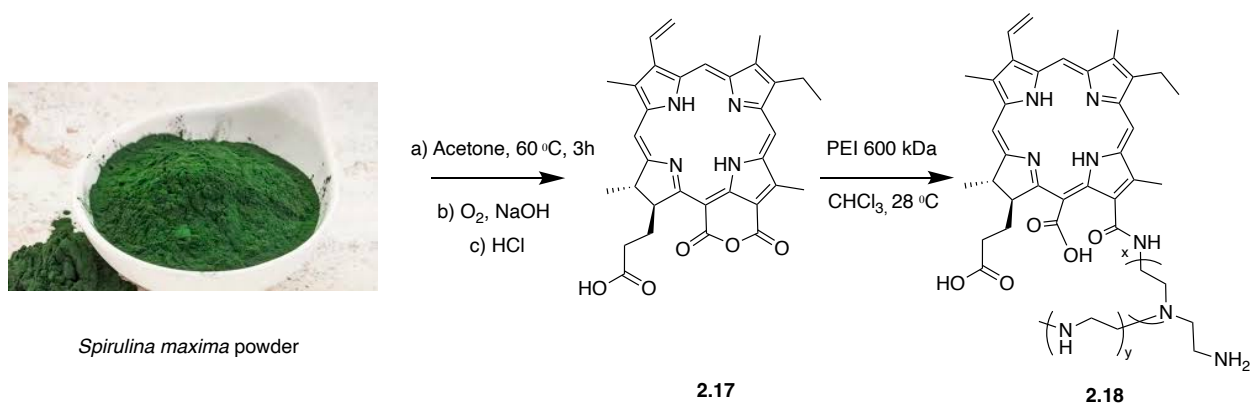
Scheme 2.6. Extraction of purpurin-18 (**2.17**) from *Spirulina maxima* and chemical modification to chlorin-*p6* (**2.18**).[30]

The macrocycle of **2.17** possesses an anhydride exocyclic ring which can react very quickly with nucleophilic groups such as a primary amine (PEI). Thus, **2.17** was reacted

with polyethyleneimine (PEI) (600 Da) in CHCl$_3$ for 1 hour and a color change from purple to green. UV-vis spectroscopy confirmed the formation of derivative **2.18** with characteristic of chlorin *p6* absorbance at 665 nm (hypsochromic effect of Q (IV) band) as shown in Figure 2.7.
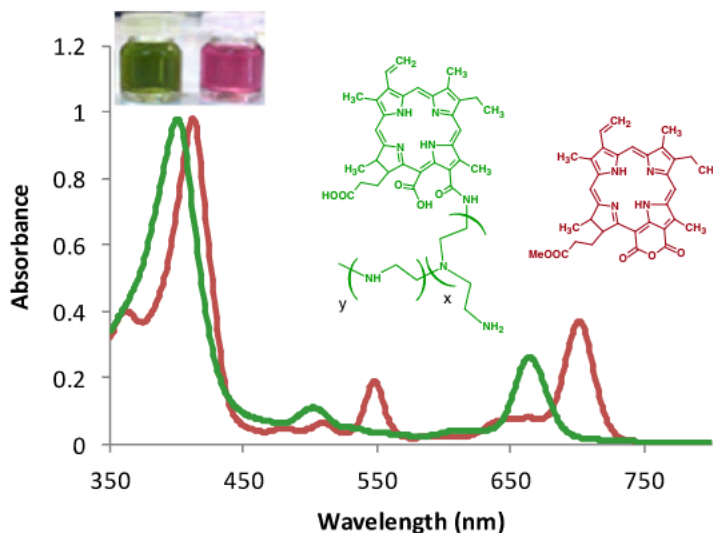
Figure 2.7. UV-vis spectra of Pp-18 (red) (**2.17**) and Pp-18-PEI (green) (**2.18**) in CHCl$_3$.

Thus, this change reflected the modification of the macrocycle conjugation by opening of the anhydride system to form the chlorin *p6*-PEI (**2.18**) as shown in Scheme 2.6.

2.3.2. Synthesis of cationic-5-(4-aminophenyl)-10,15,20-tris(4-*N*-methyl pyridinium)porphyrin triiodide (2.24)

In order to obtain the cationic porphyrin macrocycle with amine functionality, 5-(4-acetamidophenyl)-10,15,20-tris(4-pyridyl)porphyrin **2.22** was prepared according to classical Little condensation reaction following which condensation of 4-acetamidobenzaldehyde (**2.19**), 4- pyridyl carboxaldehyde (**2.20**) and pyrrole (**2.21**) was done in propionic acid as shown in Scheme 2.7.[25]

After purification by silica column chromatography, a purple powder in a literature verified yield of 4% was obtained. The formation of the PS was verified by NMR and UV-vis spectroscopy with an absorbance maximum (λmax$_{H2O}$) at 415 nm.
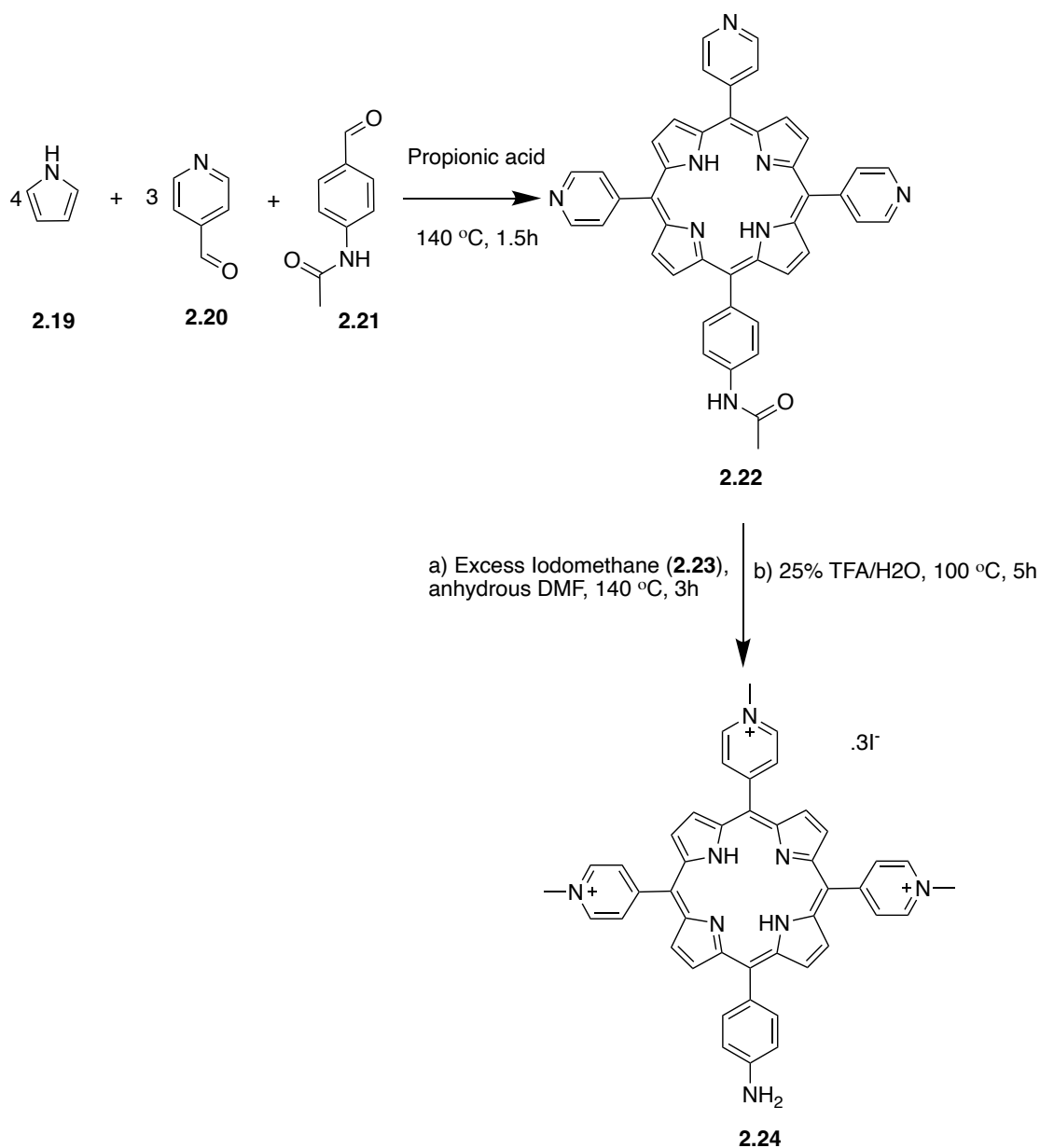
Scheme 2.7. Chemical synthesis of 5-(4-acetamidophenyl)-10,15,20-tris(4-pyridyl)porphyrin (**2.22**) and further introducing cationic charge via methylation to synthesize 5-(4-aminophenyl)-10,15,20-tris(4-*N*-methyl pyridinium)porphyrin triiodide (**2.24**).

Compound **2.22** was further modified to prepare the cationic derivative via methylation with excess iodomethane (**2.23**), followed by reduction with H_2O/TFA. This yielded the final cationic, 5-(4-aminophenyl)-10,15,20-tris(4-*N*-methyl pyridinium)porphyrin triiodide **2.24**. Methylation and acidic hydrolysis of the acetamide group resulted in a good yield of 82%, which is in accordance with the literature.[25]

These macrocyclic PSs were obtained with primary amine function, which is further conjugated with biopolymeric platform of hyaluronic acid.

2.3.3. Hyaluronic acid (HA)-PS conjugates (chlorin *p6*-PEI-HA (2.25) and CP-HA (2.26))

These two PSs, **2.18** and **2.24**, were further covalently grafted on hyaluronic acid (HA) as shown in Scheme 3 *via* an amide link yielding conjugate chlorin *p6*-PEI-HA (**2.25**) and CP-HA (**2.26**). The conjugates with HA were synthesized in aqueous media thus carboxylic acid activation of HA (**2.16**) was achieved by EDC/NHS as shown in Scheme 2.8.
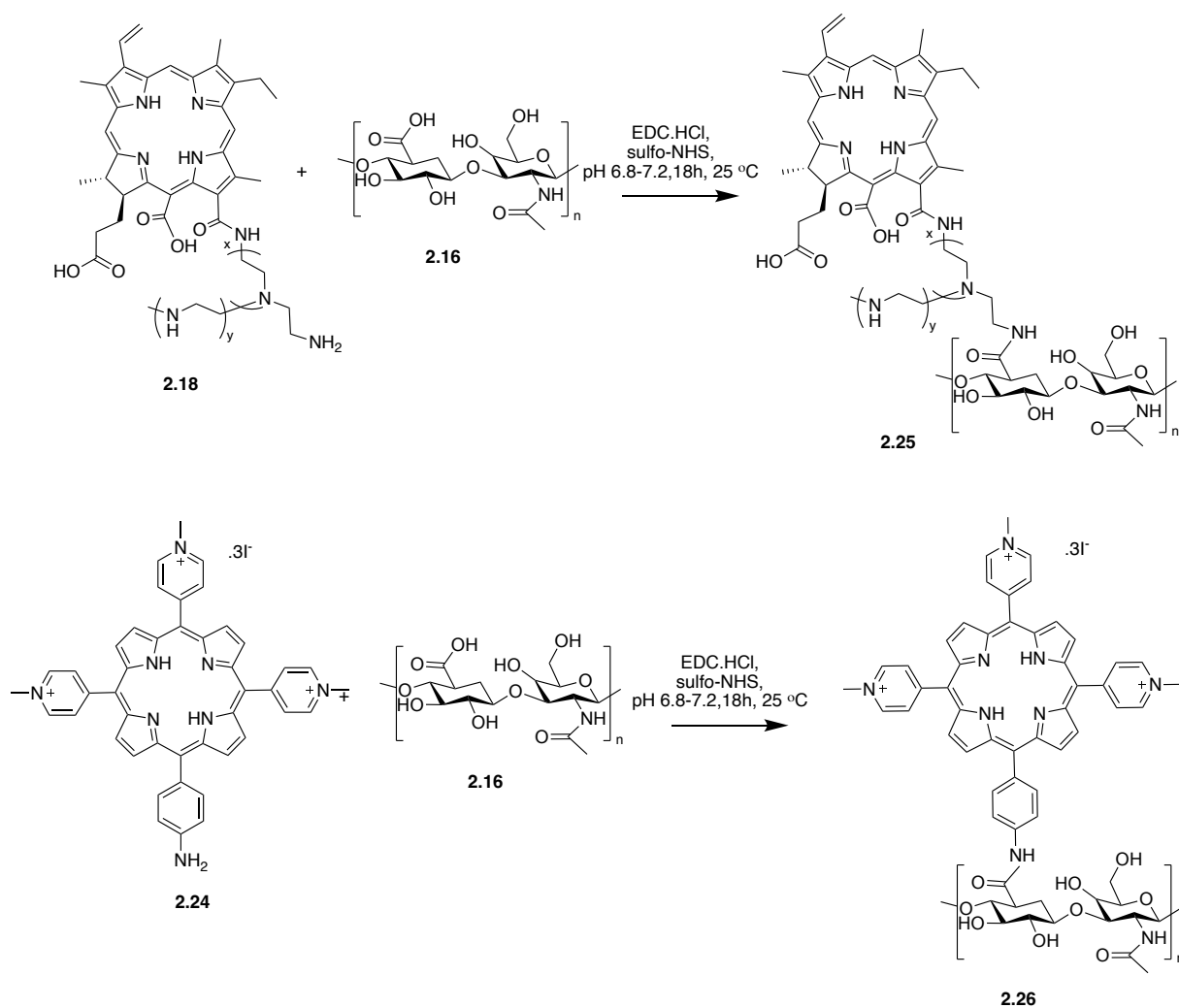
Scheme 2.8. PSs **2.18** and **2.24** covalently grafted on hyaluronic acid (HA) (**2.16***) via* an amide link yielding HA-PS conjugates **2.25** and **2.26**.

This resulted in the formation of covalent conjugates of HA-PS (**2.25** and **2.26**) which were further characterized as detailed in the following.

2.3.3.1. Differential scanning calorimetry (DSC)

The thermal analysis profiles of the dried samples (with or without PSs) were obtained as the temperature was increased from room temperature to 250 °C at a rate of 10 °C/min under N_2 atmosphere. Calorimetric analysis of these conjugates yields classic thermograms (Figure 2.8.) in which we observe an endothermic peak resulting from loss in water from the conjugate and an exotherm was observed at 80 °C and at 240 °C, a characteristic feature of HA biopolymer.[38]

a)
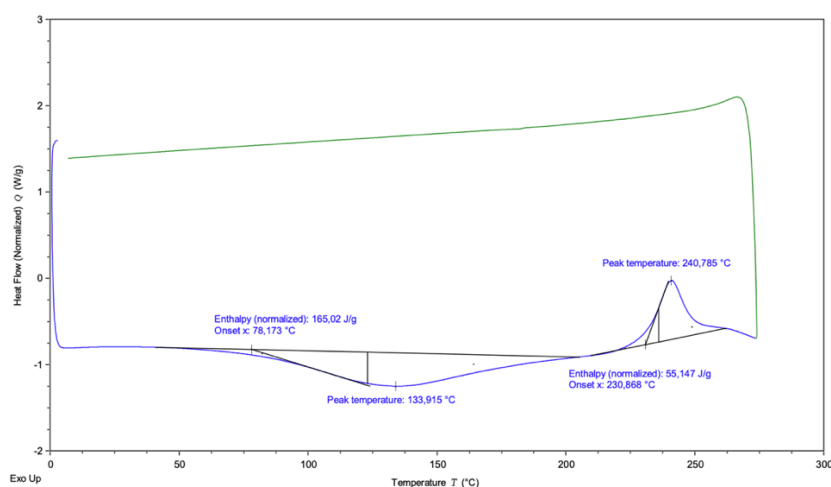
b)
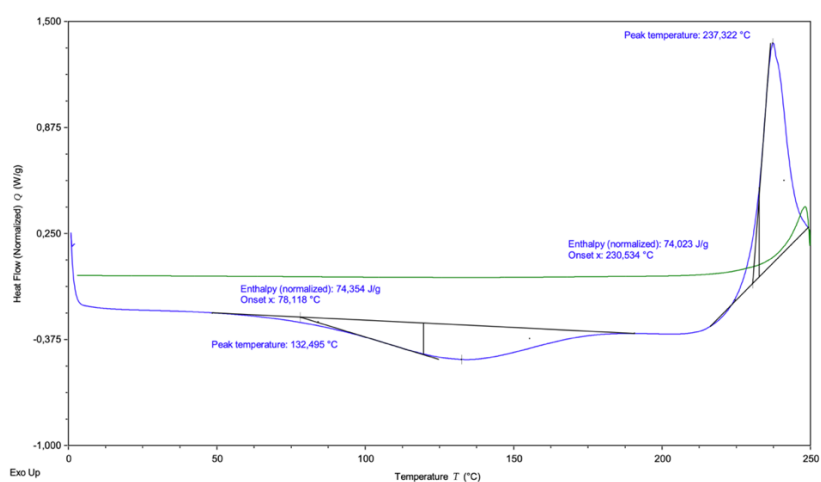
Figure 2.8. DSC analysis of conjugate formulations a) chlorin *p6*-PEI-HA (**2.25**) b) CP-HA (**2.26**).

2.3.3.2. Scanning electron microscopy (SEM) characterization

Representative SEM images in Figure 2.9 of the dried samples (with PSs) show homogenous dispersion of the samples and cross-linking pattern with an average size of 105 ± 103 nm for **2.25** and 215 ± 105 nm for **2.26**. These compounds present macro-porous structures with irregular pores are an indication of the conjugated PSs with HA which is important for biomedical applications.[39]

a)
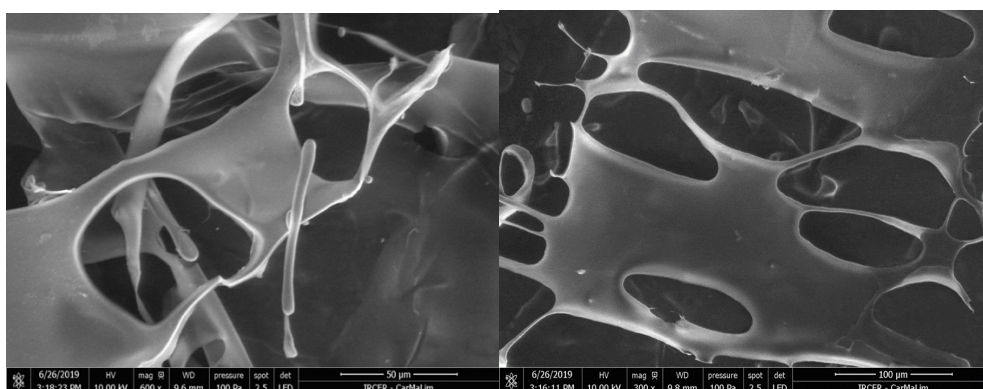
b)
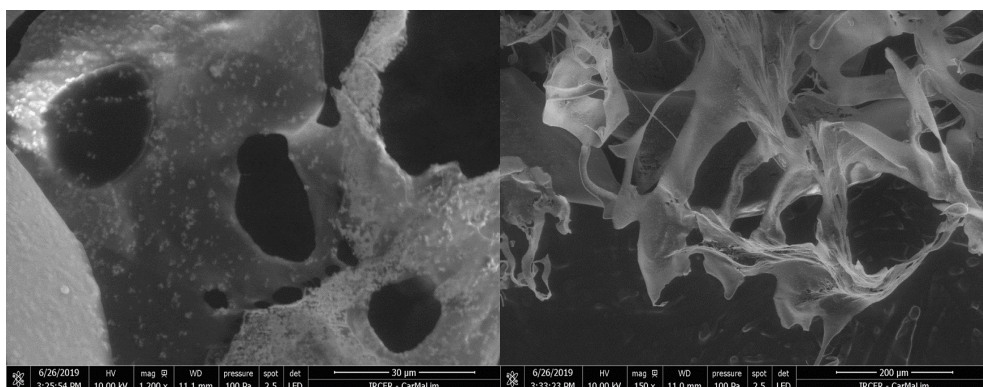
Figure 2.9. SEM analysis of conjugate formulation a) chlorin *p6*-PEI-HA (**2.25**) b) CP-HA (**2.26**).

2.3.3.3. Infra-red (IR) spectral evaluation

The covalent grafting of HA and photosensitizers that bear a primary amine function (**2.18** and **2.24**) was confirmed by FTIR measurements. The corresponding FTIR spectra of HA-photosensitizer-conjugates are displayed in Figure 2.10. Compared to the spectrum of HA alone (black line) which possessed characteristic absorption band around 3360 cm^{-1} assigned to stretching vibration of hydroxyl groups of hyaluronic acid and peaks at 2930 and 1340 cm^{-1} (stretching and deformation vibrations of C-H bond), the conjugate **2.26** showed new signals that correspond to photosensitizers (1570, 1250, 810 cm^{-1}). The absorption band for this conjugate at 3325 cm^{-1} and 1642 cm^{-1} can be attributed to the amide functional group that forms between the amine and carboxylic groups. The IR spectrum of the dried conjugate samples for **2.25** (Figure 2.10, red line) showed the presence of PEI characteristic peaks at 2947 and 2930 cm^{-1} and chlorin characteristic bands at 1574 cm^{-1}, 1596 cm^{-1} and 1644 cm^{-1}, respectively.[40,41]
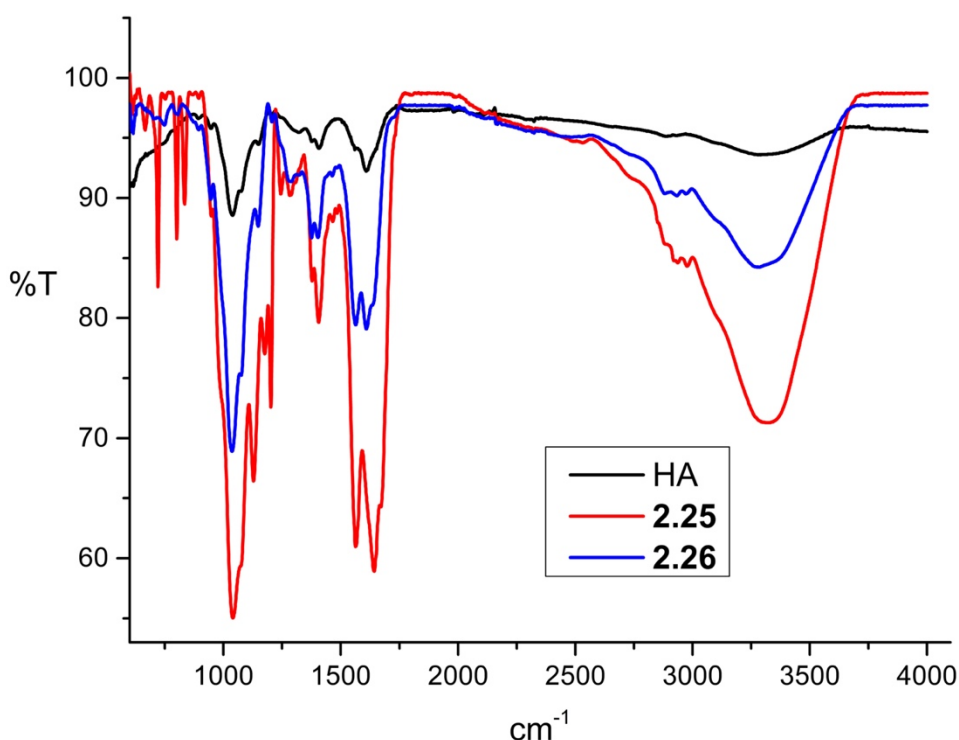
Figure 2.10. IR spectrum of HA-PS conjugates **2.25** and **2.26** in comparison to HA alone.

2.3.3.4. Dynamic light scattering (DLS) analyses of conjugates

The DLS showed a 245 nm hydrodynamic diameter. After formulation of the hyaluronic acid with PSs, the hydrodynamic diameter of conjugate **2.25** increased to 342 ± 52.8 nm and for **2.26** increased to 435.1 ± 35.1 nm. The zeta potential for **2.25** was found to be -34 and for **2.26** was determined as -29.3 due to acid moieties of the hyaluronic acid.[42]

2.3.3.5. UV-vis analysis to identify the percentage conjugation of PS on HA

The UV/visible absorption properties of photosensitizers **2.18** and **2.24** remained intact after binding to HA as shown in Figure 2.11. The number of photosensitizers bound to HA was estimated by UV-visible absorption at the maximum of Soret bands (between 40 and 440 nm) using a calibration curve of free PSs **2.18** and **2.24.** The relative molar percentage of photosensitizers in the conjugate was determined based on monomer concentration to be 18% for conjugate **2.26** and 3% for **2.25**. The difference in yield could be explained by the low grafting reactivity of the PS, **2.18** with the condition used. Indeed, at the end of the reaction, we observed many PS in the reaction medium. The low grafting molar % of **2.18** grafted on HA is the reason for no singlet oxygen production as evaluated by ergosterol degradation assay and, hence, it was not used further for biological assays against bacteria.
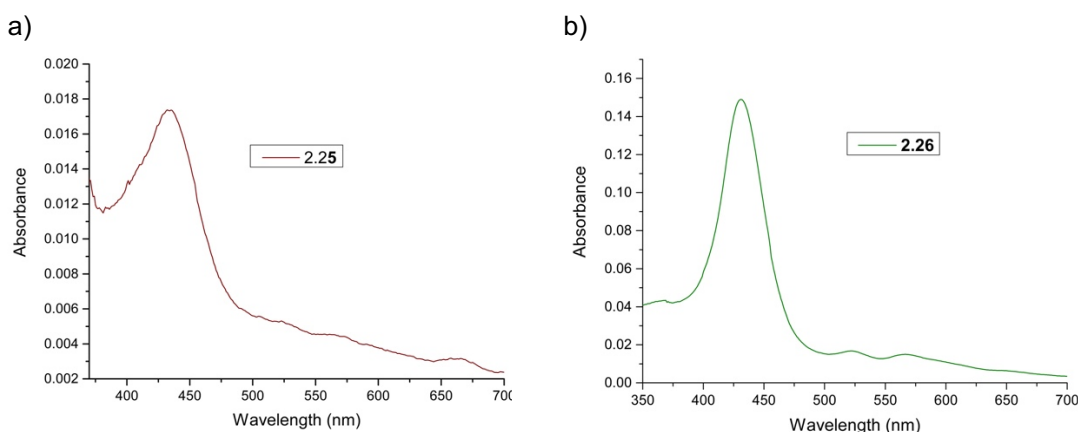
Figure 2.11. The UV/visible absorption spectra (in water) of PS **2.18** a) Chlorin *p6*-HA (**2.25**) and PS **2.24** b) CP-HA after binding to HA (**2.26**).

2.3.3.6. Rheological behavior of the PS-HA conjugate.

As shown in Figure 2.12, non-conjugated HA, and modified HA (*i.e.,* chlorin *p6*-PEI-HA (**2.25**) and CP-HA (**2.26**)) displayed similar rheological behavior. Indeed, the viscosities of the three samples decreased with increasing shear rate. These results illustrated the shear-thinning behavior of hyaluronic acid and of the two other derivatives. Moreover, above 10 s^{-1}, all the samples displayed a Newtonian behavior. Looking closer at the impact of the functionalization of HA on the viscosity in this domain, the less viscous sample is chlorin *p6*-PEI-HA (**2.25**). The modification of HA with chlorin *p6* seems to allow for macromolecular motions, when compared to HA. In addition, CP-HA (**2.26**) indicated intermediate values of viscosities in the Newtonian area. Thus, inter-macromolecular interactions appear to be promoted by cationic porphyrin groups, as compared to chlorin *p6*.
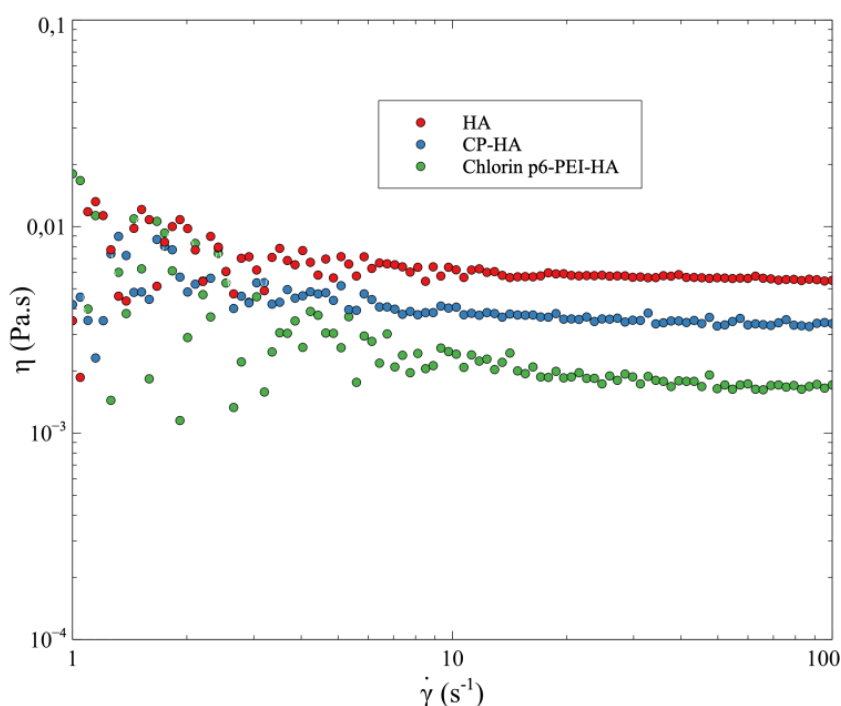
Figure 2.12. Viscosity (h) as a function of shear rate for HA, chlorin *p6*-PEI-HA (**2.25**), and CP-HA (**2.26**).

To complete these analyses, oscillatory shear flow experiments were carried out in the linear viscoelastic range for CP-HA (**2.26**) as shown in Figure 2.13. The storage modulus (G') and the loss modulus (G″) values globally increased over the entire range of the angular frequency investigated. The complex viscosity remained constant up to 30 rad.s⁻

[1]. No elasticity dominated properties were highlighted according to this oscillatory experiment as an ideal cross-linked conjugate formulation.
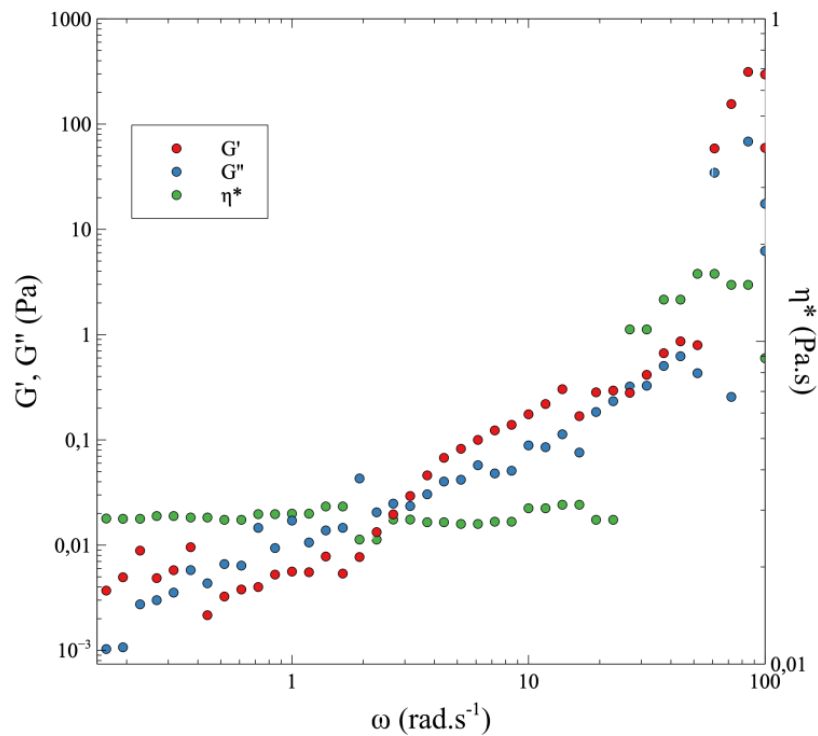
Figure 2.13. Storage modulus (G′) and loss modulus (G″) as functions of angular frequency for CP-HA (**2.26**).

As these conjugates are water soluble, these conjugates can set a landmark to explore more modifications in the PS or HA chemical skeleton to improvise the aPDT potential of such formulations.

These formulations have been evaluated for their efficacy against the microbes using the tradition growth assays and determination of inhibition concentration to identify the efficacy of such conjugate formation strategy.

2.4. Antimicrobial evaluation of HA-PS conjugates

A small bacterium can change the dynamics of the world for years, as the situation has been recently. It is important to have some potential solutions to the very basis of the infections caused by microbes. As explained earlier in this chapter a positive charge on the PS molecule enhances the binding and penetration of the PS efficiently into the cell. With conjugated platforms as synthesized above the target specificity and biocompatibility of the formulation and overall efficiency for aPDT is expected to be enhanced.

We evaluated our conjugates for inhibition of the Gram-positive *S. aureus* and Gram-negative *E. coli* species via diffusion agar assays and MIC evaluations, to determine the efficiency of our platforms.

2.4.1.   Diffusion test on agar

Growth inhibition studies of the formulation of chlorin *p6*-HA (**2.24**) showed a negligible activity and for CP-HA (**2.26**) showed comparatively less inhibition as compared to their unbound PSs against the of *S. aureus* in light and almost negligible activity for *E. coli* in neither light nor dark conditions as shown in Figures 2.14 and 2.15. Furthermore, to achieve more precise data about the antimicrobial properties of the formulations in comparison with PSs photoinactivation assays were performed. As the formulation of chlorin *p6*-HA (**5**) only a negligible inhibition of the bacterial growth no further evaluations were performed.

Figure 2.14. Anti-microbial evaluation of the 5-(4-aminophenyl)-10,15,20-tris(4-*N*-methylpyridinium)porphyrin triiodide (**2.24**) and chlorin *p6*-PEI (**2.18**) as compared with hyaluronic acid conjugate derivatives of CP-HA (**2.26**) and chlorin *p6*-PEI-HA (**2.25**) with *S. aureus* in dark and in light.

Escherichia coli
Gram-negative bacteria

a) Dark conditions
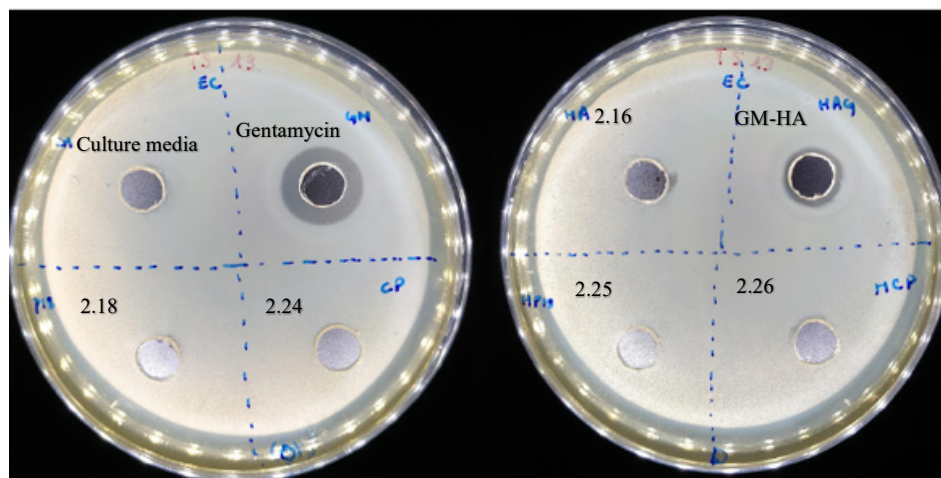
b) Light conditions
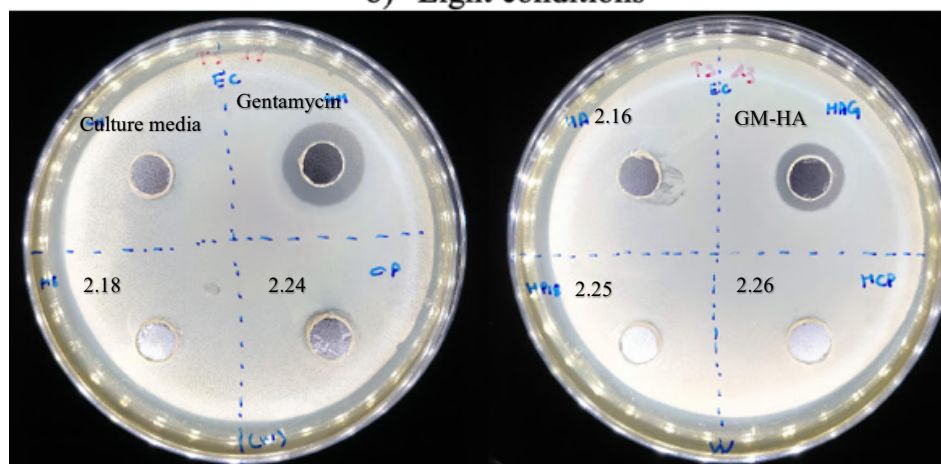
Figure 2.15. Anti-microbial evaluation of the 5-(4-aminophenyl)-10,15,20-tris(4-*N*-methylpyridinium)porphyrin triiodide (**2.24**) and chlorin *p6*-PEI (**2.18**) as compared with hyaluronic acid conjugate derivatives of CP-HA (**2.26**) and chlorin *p6*-PEI-HA (**2.25**) with *E. coli* in dark and in light conditions.

2.4.2. Photoinactivation of bacterial cells

The photodynamic activity of the photosensitizer (**2.24**) conjugated with HA (**2.26**) was tested *in vitro* against *S. aureus*, as a model of Gram-positive bacteria. The experimental results are reported in Table 2.1. The microplate was incubated at 37°C for 5h with white LED light (total fluence: 25J/cm²) or in the dark. Then, 500 µL of 2-fold concentrated TS broth and glucose (25mM) were added in each well and the microplate was incubated at 37°C for 24h.

Table 2.1. MIC (µM) evaluation of **CP-HA** (**2.26**) as compared with the individual PS (**2.24**)

Bacterial strains	PS/PS-HA conjugates	MIC	MIC
		Dark	Light
S. aureus	**2.24**	200 µM	100 µM
	2.26	> 700 µM	700 µM
E. coli	**2.24**	> 200 µM	200 µM
	2.26	> 700 µM	700 µM

The inhibition activity as against the bacteria for the conjugates is not what was expected this could be due to presence of negative charges on the biopolymer of hyaluronic acid which could neutralizes the charge on the cationic porphyrin (**2.24**). This could cause a reduction in the interaction of the conjugate with the bacterial cell wall.

2.5. Conclusion and future perspective

The conjugate platform cross-linked with photosensitizers has ideal properties of increased solubility in aqueous media and an ability to produce singlet oxygen (in case of CP-HA (**2.26**)). The conjugates obtained from synthesis and covalent linkages on HA when tested for photo bactericidal applications shows some antimicrobial activity in the presence of light. However, the presence of strong negative charges due to the carboxylic acid functions of the biopolymer decreases the interaction between the conjugate and the bacterial walls. Thus, after illumination, the singlet oxygen produced is not close enough to the bacterial walls to have a significant PDT effect. Nevertheless, these conjugates facilitate the formulation and medical application of PSs, and it could be envisaged to increase the number of incorporated PSs and/or to associate other polymers to obtain composites capable of interacting more easily with the bacterial walls. Another strategy to possibly enhance the antimicrobial action would be to use a reticulation agent like DTPA anhydride as recently published by Sol group in Limoges.[43] This strategy introduces the spacer molecule between the biopolymeric chains and use the free carboxylic groups of the HA to covalently graft the cationic PSs or chlorins as described previously or introduce the PSs via ionic interactions between the PS and carboxylate functionalities of HA and reticulating agents.

2.6. References

1. Wiehe A, O'Brien JM and Senge MO. *Photochem. Photobiol. Sci.* 2019; **18**: 2565-2612.

2. Cieplik F, Deng D, Crielaard W, Buchalla W, Hellwig E, Al-Ahmad A and Maisch T. *Crit. Rev. Microbiol.* 2018; **44**: 571-589.

3. Le Guern F, Sol V, Ouk C, Arnoux P, Frochot C and Ouk TS. *Bioconjug. Chem.* 2017; **28**: 2493-2506.

4. Müller A, Preuß A and Röder B. *J. Photochem. Photobiol. B Biol.* 2018; **178**: 219-227.

5. Nitzan Y and Ashkenazi H. *Photochem. Photobiol.* 1999; **69**: 505-510.

6. Maisch T, Bosl C, Szeimies RM, Lehn N and Abels C. *Antimicrob. Agents Chemother.* 2005; **49**: 1542-1552.

7. Ruiz-González R, Agut M, Reddi E and Nonell S. *Int. J. Mol. Sci.* 2015; **16**: 27072-27086.

8. Gonçalves PJ, Bezzerra FC, Teles A V., Menezes LB, Alves KM, Alonso L, Alonso A, Andrade MA, Borissevitch IE, Souza GRL and Iglesias BA. *J. Photochem. Photobiol. A Chem.* 2020; **391**: 112375.

9. Pettai H, Oja V, Freiberg A and Laisk A. *FEBS Lett.* 2005; **579**: 4017-4019.

10. Pavlíčková V, Škubník J, Jurášek M and Rimpelová S. *Appl. Sci.* 2021; **11**: 1-25.

11. Yoon I, Li JZ and Shim YK. *Clin. Endosc.* 2013; **46**: 7-23.

12. Zenkevich E, Sagun E, Knyukshto V, Shulga A, Mironov A, Efremova O, Bonnett R, Songca SP and Kassem M. *J. Photochem. Photobiol. B Biol.* 1996; **33**: 171-180.

13. Zhou J, Gao ZJ, Cai JQ, Li LL and Wang H. *Langmuir* 2020; **36**:1559-1568.

14. Liu R, Yin J, Li J, Wu J, Chen G, Jin Y and Wang J. *Chin. J. Org. Chem.* 2012; **32**: 544-551.

15. Wawrzyńska M, Kałas W, Biały D, Zioło E, Arkowski J, Mazurek W and Strządała L. *Arch. Immunol. Ther. Exp. (Warsz).* 2010; **58**: 67-75.

16. Pfitzner A, Sigusch BW, Albrecht V and Glockmann E. *J. Periodontol.* 2004; **75**: 1343-1349.

17. Soukos NS, Mulholland SE, Socransky SS and Doukas AG. *Lasers Surg. Med.* 2003; **33**: 161-168.

18. Sorkhdini P, Moslemi N, Jamshidi S, Jamali R, Amirzargar AA and Fekrazad R. *J. Periodontol.* 2013; **84**: 793-800.

19. Amir, Weber, Beard, Bomyea T. *J. Biomed. Nanotechnol.* 2008; **23**: 1-7.

20. Singh S, Hussain A, Shakeel F, Ahsan MJ, Alshehri S, Webster TJ and Lal UR. *Int. J. Nanomedicine* 2019; **14**: 2301-2325.

21. Khurana B, Gierlich P, Meindl A, Gomes-Da-Silva LC and Senge MO. *Photochem. Photobiol. Sci.* 2019; **18**: 2613-2656.

22. Pierau L and Versace DL. *Materials* 2021; **14**: 1-33.

23. Belali S, Savoie H, O'Brien JM, Cafolla AA, O'Connell B, Karimi AR, Boyle RW and Senge MO. *Biomacromolecules* 2018; **19**: 1592-1601.

24. Bernhard S and Tibbitt MW. *Adv. Drug Deliv. Rev.* 2021; **171**: 240-256.

25. Le Guern F, Sol V, Ouk C, Arnoux P, Frochot C and Ouk TS. *Bioconjug. Chem.* 2017; **28**: 2493-2506.

26. Mbakidi JP, Herke K, Alvès S, Chaleix V, Granet R, Krausz P, Leroy-Lhez S, Ouk TS and Sol V. *Carbohydr. Polym.* 2013; **91**: 333-338.

27. Sahu K, Sharma M, Sharma P, Verma Y, Rao KD, Bansal H, Dube A and Gupta PK. *Photomed. Laser Surg.* 2014; **32**: 23-29

28. Huang L, Zhiyentayev T, Xuan Y, Azhibek D, Kharkwal GB and Hamblin MR. *Lasers Surg Med.* 2011; **43**: 313-323.

29. Tegos GP, Anbe M, Yang C, Demidova TN, Satti M, Mroz P, Janjua S, Gad F and Hamblin MR. *Antimicrob. Agents Chemother.* 2006; **50**: 1402-1410.

30. Drogat N, Granet R, Le Morvan C, Bégaud-Grimaud G, Krausz P and Sol V. *Bioorg. Med. Chem. Lett.* 2012; **22**: 3648-3652.

31. Gupta RC, Lall R, Srivastava A and Sinha A. *Front. Vet. Sci.* 2019; **2019**: 6-192.

32. Khunmanee S, Jeong Y and Park H. *J. Tissue Eng.* 2017; **8**: 1-16.

33. Huang G and Huang H. *Drug Deliv.* 2018; **25**: 766-772.

34. Vogus DR, Evans MA, Pusuluri A, Barajas A, Zhang M, Krishnan V, Nowak M, Menegatti S, Helgeson ME, Squires TM and Mitragotri S. *J. Control. Release* 2017; **267**: 191-202.

35. Schanté CE, Zuber G, Herlin C and Vandamme TF. *Carbohydr. Polym.* 2011; **85**: 469-489.

36. Hu DR, Zhong L, Wang MY, Li HH, Qu Y, Liu QY, Han R, Yuan LP, Shi K, Peng JR and Qian ZY. *Adv. Funct. Mater.* 2019; **29**: 1-14.

37. Little RG, Anton JA, Loach PA and Ibers JA *J. Heterocycl. Chem.* 1975;**12**: 343-349.

38. Collins MN and Birkinshaw C. *J. Mater. Sci. Mater. Med.* 2008; **19**: 3335-3343.

39. Storozhylova N, Crecente-Campo J, Cabaleiro D, Lugo L, Dussouy C, Simões S, Monteiro M, Grandjean C and Alonso MJ. *Regen. Eng. Transl. Med.* 2020; **6**: 201-216.

40. Chen BK, Su CT, Tseng MC and Tsay SY. *Polym. Bull.* 2006; **57**: 671-681.

41. Jain B, Uppal A, Gupta PK and Das K. *Photochem. Photobiol.* 2009; **85**: 927-933.

42. Chiesa E, Dorati R, Conti B, Modena T, Cova E, Meloni F and Genta I. *Int. J. Mol. Sci.* 2018; **19**: 2310-2336.

43. Elkihel A, Christie C, Vernisse C, Ouk TS, Lucas R, Chaleix V and Sol V. *ACS Appl. Biol. Mater.* 2021: 2-10.

Chapter 3. Relative singlet oxygen yield of photosensitizers

3. Relative singlet oxygen yields via DPBF degradation assay

3.1. Background and molecular design

The basic principle of aPDT – the selective uptake of the active PS and subsequent irradiation and eradication, requires a light source of an appropriate wavelength matching the spectral wavelength of photosensitizing dye.[1] A photon of light is absorbed by a photosensitizer molecule, exciting this molecule from a singlet ground singlet state (S_0) to an excited short-lived singlet state (S_1). This state will undergo non-radiative transitions including an intersystem crossing (ISC), changing the multiplicity of the photosensitizer electronic state from a singlet to a longer-lived triplet state.[2]

Under aPDT conditions, this PS can decay back to the ground state via two different processes as illustrated in Figure 3.1 – either by spontaneous phosphorescence or through energy transfer with proximal oxygen species. This process can produce reactive oxygen species, either oxygen-centered radicals and radical ions (type I), or its formation of an excited singlet oxygen diatom (type II). Both of these processes will occur in any given setup, and the ratio between the type I and type II processes depends on the kind of photosensitizer irradiated.[3,4] Therefore, it becomes important to quantify the generation of singlet oxygen of the photosensitizer to understand the basic parameters of aPDT efficacy of a PS.

Several singlet oxygen detection probes have been investigated and have been described in the literature.

3.1.1. Singlet oxygen ($^1O_2$) detection probes

The detection of singlet oxygen, as distinct from the ground state diatom, requires measurement of the rate of some chemical reaction which is specific to this species. The probe consists of a chromophore and $^1O_2$ receptor, in which formation of endoperoxides (EP) or 1,2-dioxetanes species disrupts the absorbing system. The most common probes used, as shown in Figure 3.2, incorporate both motifs and interact directly with $^1O_2$ oxygen.[5] The change in the electronic structure of the sensor molecule can be monitored using different spectroscopic techniques such as NMR, EPR, UV-vis absorption, or fluorescence (Table 3.1).[6]
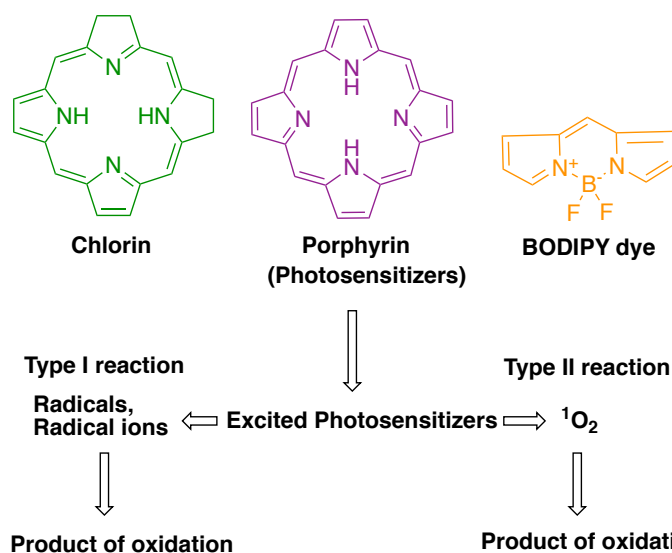
Figure 3.1. Reaction types after excitation of the photosensitizer to produce ROS species.[2]

Table 3.1. Spectroscopic detection methods for singlet oxygen with different sensor molecules.

Property	Sensor molecule	Changes caused by singlet oxygen
Light absorption	9,10-Diphenylanthracene (DPA)	Absorption decreases at 355 nm
Light absorption	9,10-Anthracenediyl-bis(methylene) dimalonic acid (ABDA)	Absorption decreases at 382 nm
Light absorption	9,10-Anthracenedipropionic acid (ADPA)	Absorption decreases at 400 nm
Light absorption	Anthracene-9,10-bisethanesulfonic acid (AES)	Absorption decreases at 360, 378 and 400 nm
Light absorption	1,3-Diphenylisobenzofuran (DPBF)	Absorption decreases at 415 nm
Fluorescence	9-[2-(3-Carboxy-9,10-diphenyl)anthryl] -6-hydroxy-3H-xanthen-3-one (DPAX)	Fluorescence induced endoperoxide formation
Fluorescence	9-[2-(3-Carboxy-9,10-dimethyl)anthryl] -6-hydroxy-3H-xanthen-3-one (DMAX)	Fluorescence induced endoperoxide formation
Chemiluminescence	2-Methyl-6-phenyl-3,7 -dihydroimidazo[1,2-a]pyrazin-3-one (CLA)	Strong chemiluminescence
Fluorescence	Singlet oxygen sensor green (SOSG)	Strong green fluorescence
EPR	2,2,6,6, -Tetramethylpiperidine (TEMP)	Change in EPR spectrum
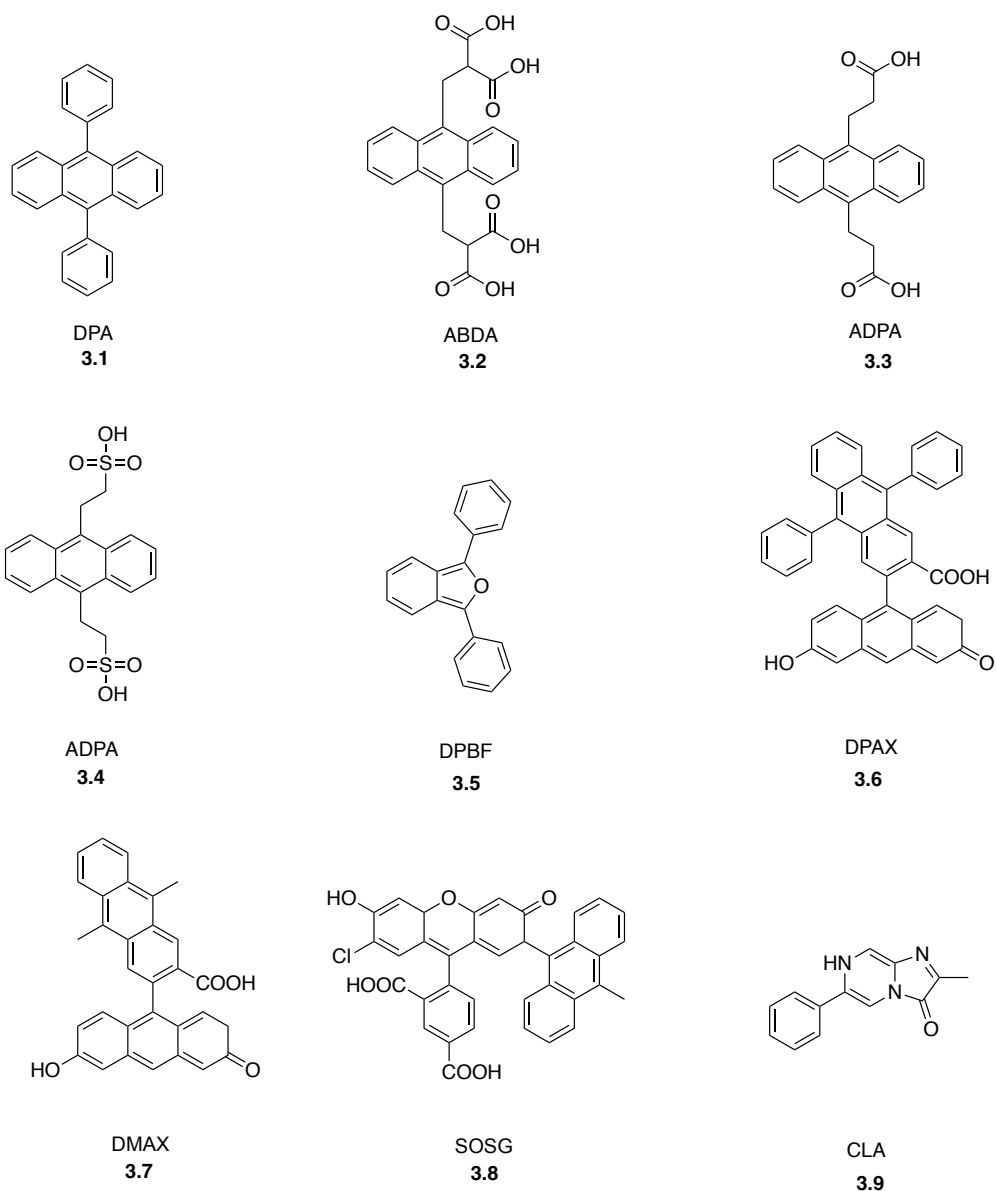
Figure 3.2. Singlet oxygen ($^1O_2$) sensitive molecular reporters.

1,3-Diphenylisobenzofuran (DPBF), parent of the 1,3-diarylisobenzofuran class, has a highly-reactive diene core that can scavenge unstable and short-lived dienophiles in a Diels-Alder reaction.[7,8] DPBF is one of the most widely used compounds for spectrophotometric detection of singlet oxygen due to its rapid and irreversible reaction with $^1O_2$ providing a clear absorption and fluorescence signal. DPBF, when incorporated in model biological membranes and excited at 410 nm, shows a fluorescence emission spectrum with a maximum at 455 nm.[9]

DPBF effectively suppresses the triplet state and therefore has effectively no self-photosensitization (i.e., does not act as PS to generate $^1O_2$). In the presence of singlet

oxygen, DPBF (**3.5**) decomposes to 1,2-dibenzoylbenzene (**3.11**) via the formation of an unstable endoperoxide (**3.10**) via cycloaddition as shown in scheme 3.1.[10]

Endoperoxide derivative

1, 2-dibenzoylbenzene

3.5   **3.10**   **3.11**
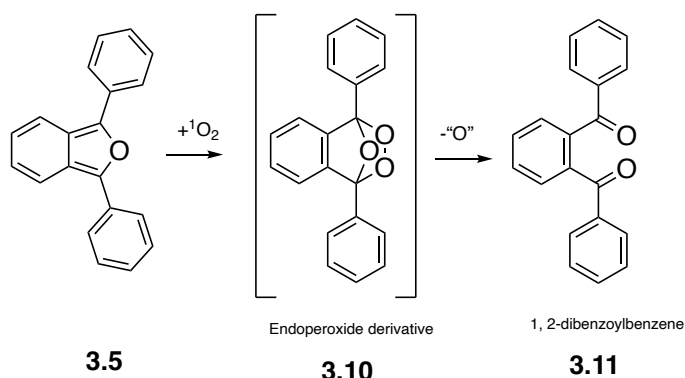
Scheme 3.1. The singlet oxygen reaction of DPBF (**3.5**) to produce **3.11** degraded product.

A decrease in absorption at this wavelength is linear in proportion to the amount of singlet oxygen adduct formed.[11]

The primary advantage of using the DPBF degradation assay is that it reacts with $^1O_2$ in an essentially diffusion-limited reaction and thus has a very high sensitivity, trapping up to 50% of all $^1O_2$ in alcohol/water or micellar solution. This setup is ideal for environments where only small amounts of $^1O_2$ are produced.[12]

3.1.2.   DPBF degradation probes for PSs (relative singlet oxygen quantum yield)

Our group (the Senge group) at Trinity College Dublin have published various articles in which the DPBF singlet oxygen probe method was used for determining the $^1O_2$ production of PSs.[13] For example, the library of BODIPY-anthracene and -pyrene dyads in Figure 3.3 showed promise for applications in photodynamic therapy; these were evaluated with the DPBF degradation probes to quantify the PSs efficiency for formation of singlet oxygen species.
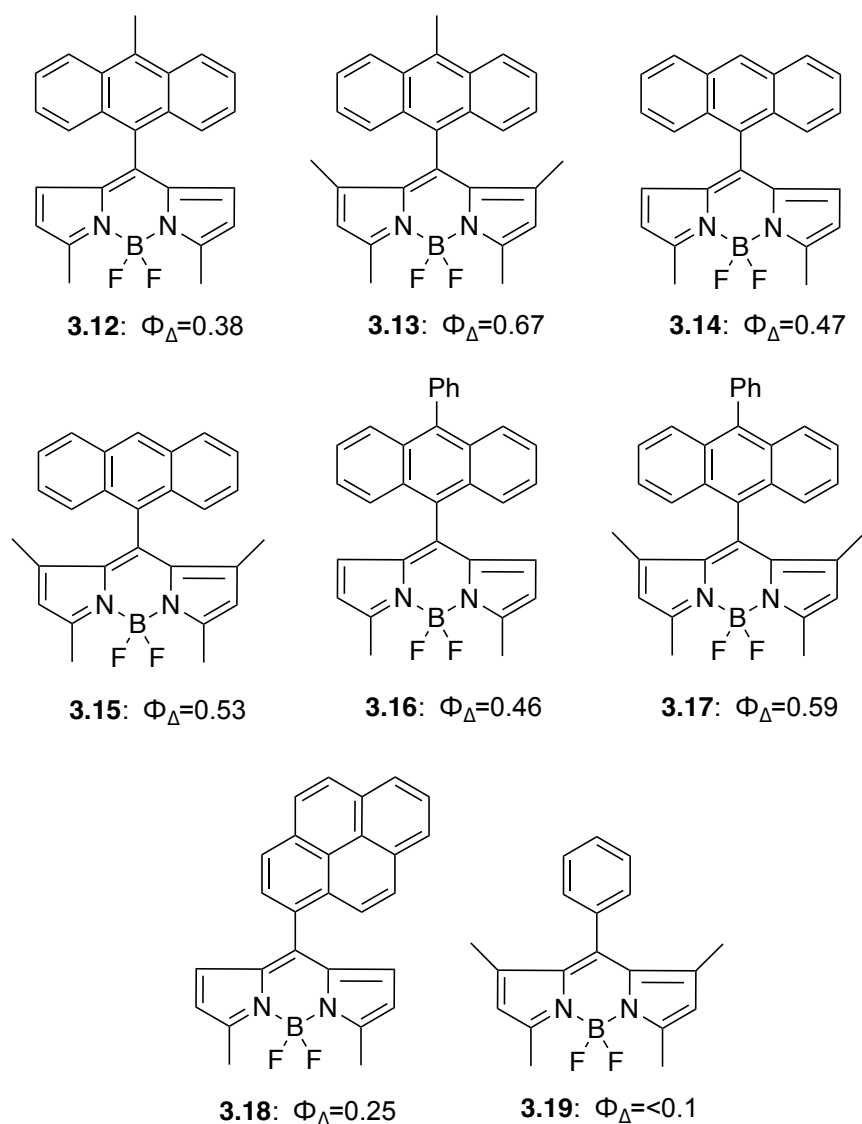
Figure 3.3. Library of BODIPY-anthracene (**3.12**-**3.17**) and -pyrene (**3.18**) dyads and phenyl (**3.19**) and their relative singlet oxygen quantum yields (Φ_Δ) in EtOH.

These dyes were functionalized to produce water-soluble derivatives to enhance the application of such dyes in PDT and interaction with biological media as shown in Figure 3.4.[14] With introduction of water-soluble groups on such dyes the production of singlet oxygen as evaluated with DPBF degradation assays remains almost unaffected; hence, removing the drawback of aggregation and quenching these derivatives become a better candidate for PDT. The singlet oxygen production is determined by measuring the relative singlet oxygen quantum yield (Φ_Δ) with known PSs, in this case RB.
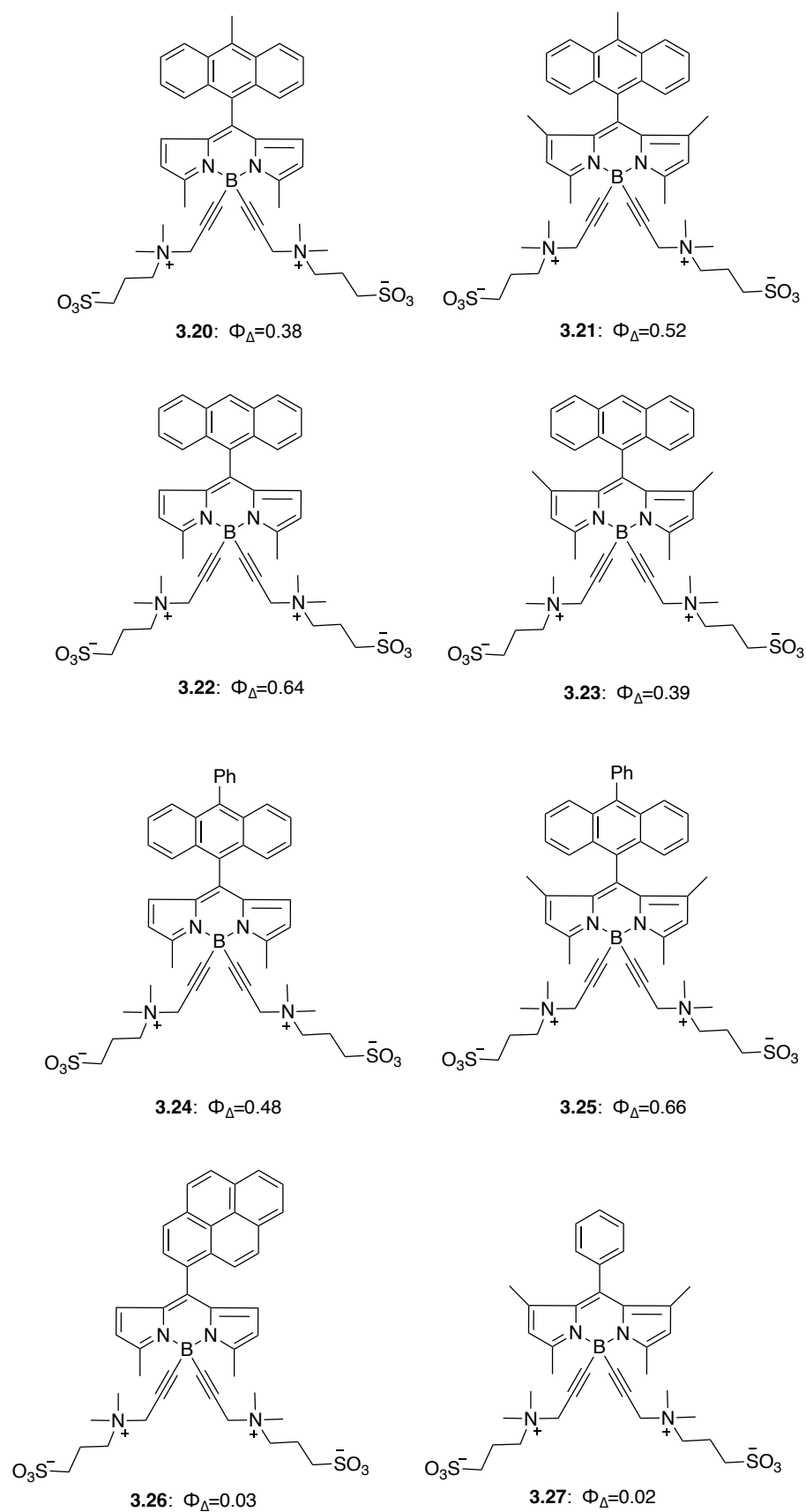
Figure 3.4. Library of water-soluble anthracene- (**3.20**-**3.25**), pyrene- (**3.26**) or phenyl- (**3.27**) BODIPY dyads and their relative singlet oxygen quantum yields (Φ_Δ) in EtOH.

Hydrogel drug delivery systems conjugated with hydrophobic PSs were synthesized in Senge group and evaluated with DPBF degradation assays and determined for their efficiency to produce singlet oxygen. Protoporphyrin-IX (Pp1X) conjugated with poly(N-isopropylacrylamide) (PNIPAM) polymer to synthesize hydrogel **3.28**, PpIX-dimethylester (PpIX-DME)-PNIPAM hydrogel (**3.29**) and pheophorbide (Pba)-PNIPAM hydrogel **3.30** were synthesized as shown in Figure 3.5 The DPBF degradation assay showed a decrease in absorption over time, indicating higher efficacy as compared to 5,10,15,20-tetraphenyl porphyrin (H$_2$TPP).[15]

3.28: Φ_Δ=1.24

3.29: Φ_Δ=0.84

3.30: Φ_Δ=1.0
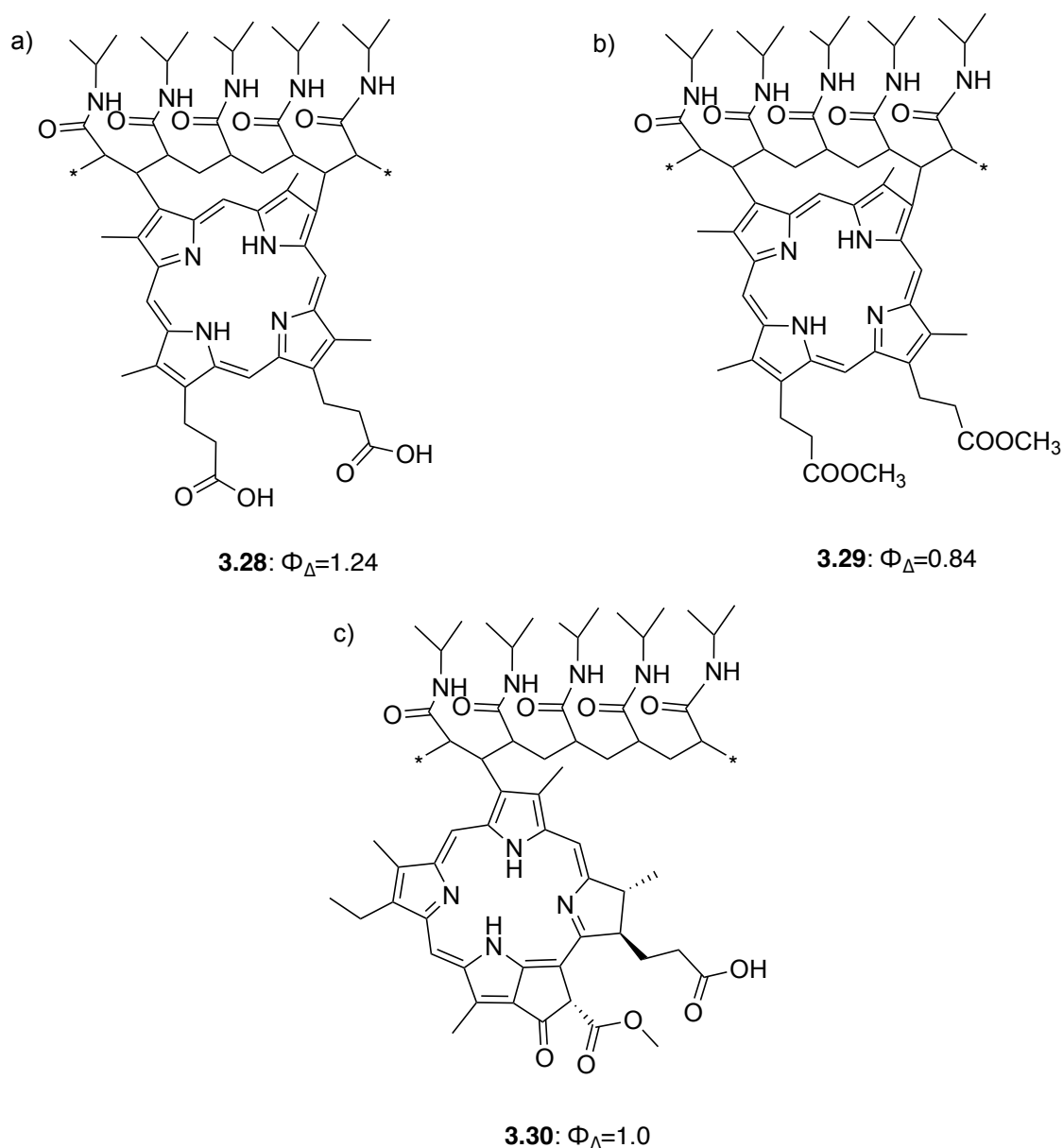
Figure 3.5. PS-conjugated hydrogels of a) PpIX-PNIPAM (**3.28**), b) PpIX-DME-PNIPAM (**3.29**) c) Pba-PNIPAM (**3.30**) and their relative singlet oxygen quantum yields (Φ_Δ) in DCM.

These experiments showed that all the PS- conjugated PNIPAM hydrogels produce singlet oxygen efficiently, and that the detection system functions under these conditions. The hydrogel formulation presumably reduces the aggregation of porphyrins increasing the efficiency of singlet oxygen production in PNIPAM-based hydrogels as compared to the PSs alone.

3.2. Relative singlet oxygen quantum yield measurements of photosensitizers

As mentioned in the previous section, generation of singlet oxygen can be measured effectively via DPBF degradation assay. This was performed as described in the following section.

3.2.1. Singlet oxygen measurements of *meso*-substituted dibenzihomoporphyrins

Bench-stable di(*p/m*-benzi)homoporphyrins were synthesized by Dr. Ganapathi Emandi through acid-catalyzed condensation of dipyrrole derivatives with aryl aldehydes. Core-modified expanded porphyrins have been actively investigated for application as photosensitizers.[16] These compounds are shown in Figure 3.6.
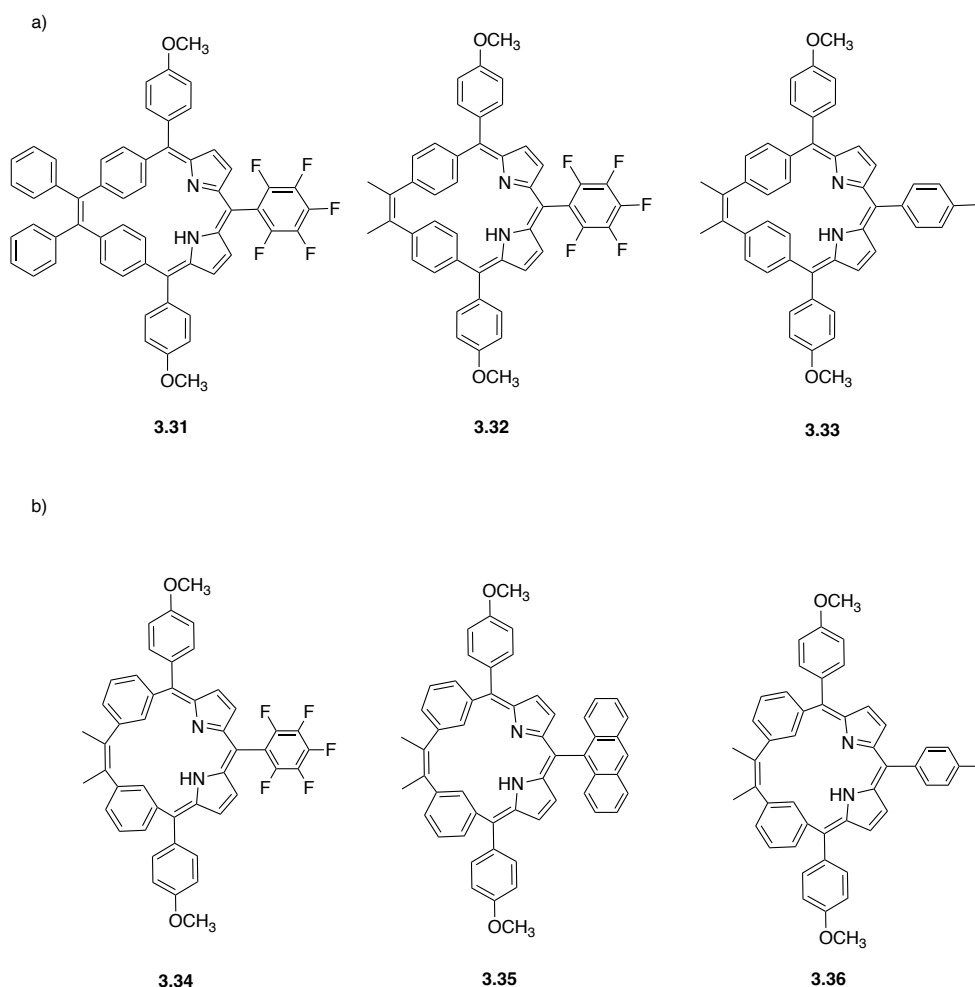
Figure 3.6. Structures of a) di(*p*-benzi)homoporphyrin derivatives (**3.31**-**3.33**) and b) di(*m*-benzi)homoporphyrin (**3.34**-**3.36**) derivatives.

These PSs exhibited a strong absorption band between 600-700 nm and act as efficient photosensitizers for the formation of singlet oxygen. UV absorbance degradation assay of DPBF in the presence of di(*p/m*-benzi)homoporphyrin derivatives (**3.31**-**3.36**) and compared to reference PS, H_2TPP (degradation plots in Figure 3.7).[17] UV-degradation plots and time-dependent degradation curves measured in DCM:MeOH (1:1) are illustrated in Figure 3.8 (di(*p*-benzi)homoporphyrin (**3.31**-**3.33**)) and Figure 3.9 (di(*m*-benzi)homoporphyrin (**3.34**-**3.36**)) respectively. The derived values for relative quantum yields are collated in Table 3.2.

a)

b)
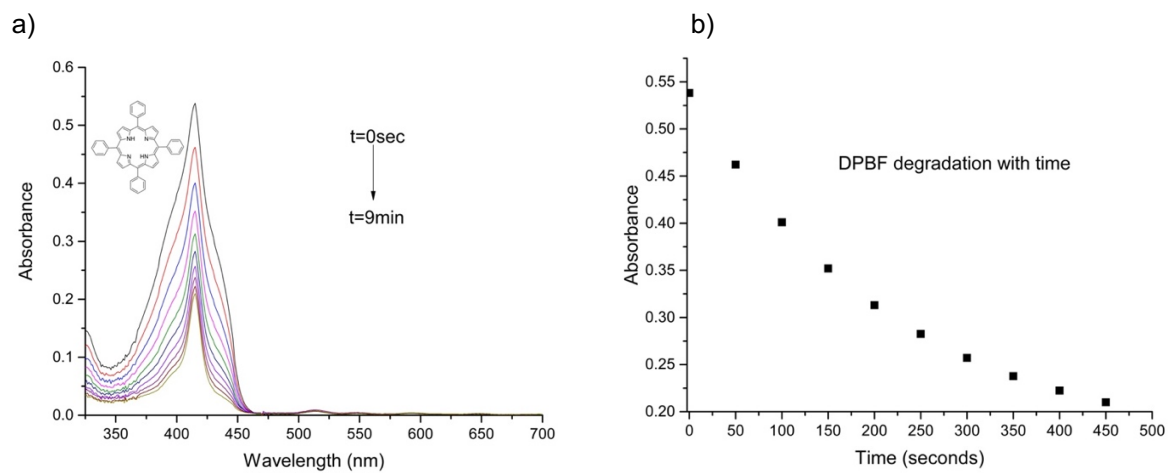
Figure 3.7. a) UV-Vis spectra and b) time dependent DPBF degradation plots for reference PS, H$_2$TPP measured at 415 nm solution.
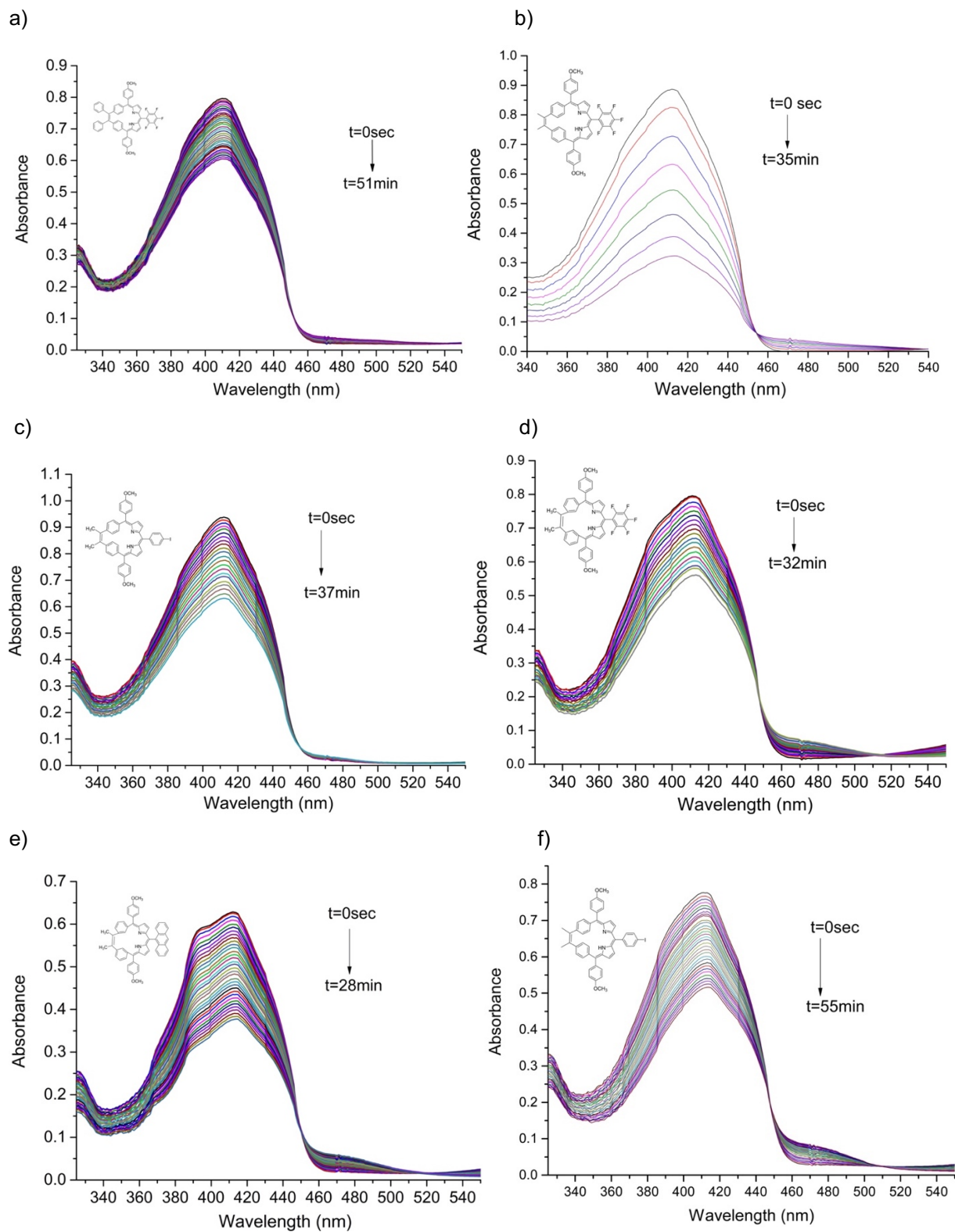
Figure 3.8. UV-vis degradation of DPBF by di(p/*m*-benzi)homoporphyrin derivatives (**3.31**-**3.36**) (a-f) at 415 nm.
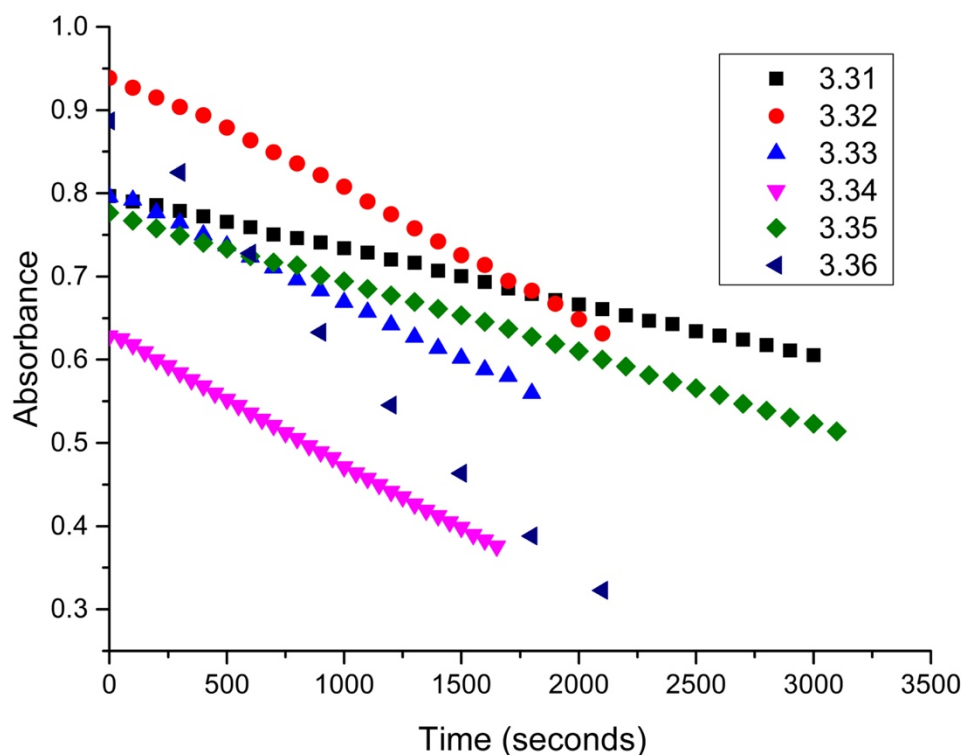
Figure 3.9. Time dependent DPBF degradation via di(*p/m*-benzi)homoporphyrin derivatives (**3.31**-**3.36**) at 415 nm.

Table 3.2 shows the values of relative singlet oxygen quantum yield obtained for these molecules. Compound **3.33** exhibited the lowest singlet oxygen quantum yield, and **3.32** the highest value, but each well below the reference compound.

Table 3.2. Relative singlet oxygen production of for di(*p/m*-benzi)homoporphyrins (**3.31**-**3.36**) in DCM/MeOH (1:1) using H_2TPP, Φ_Δ = 0.62 as a reference.

Di(*p/m*-benzi)homoporphyrin derivatives	Singlet oxygen quantum yield (Φ_Δ)
3.31	0.11
3.32	0.23
3.33	0.05
3.34	0.11
3.35	0.14
3.36	0.07

The potency of derivatives **3.31** and **3.32** is likely due to the electronic contributions of the fluorine atom. For derivative **3.35** with anthracene, singlet oxygen production is potentially enhanced by this moiety which has been reported to form endoperoxides under irradiation with light with an enhanced singlet oxygen quantum yield.[18] The related macrocycles of such derivatives have not been reported to be active for DPBF degradation assay. Thus, this study is the first one to establishes the basis of these macrocycles for exploration of potential in PDT.

3.2.2. Singlet oxygen measurements with BODIPY-appended tetraphenylethene (TPE)

Novel tetra-BODIPY-appended TPE derivatives (BODIPY-TPE) illustrated in Figure 3.10 were synthesized, each with differences in spacing between the TPE and BODIPY cores to study their aggregation-induced emission (AIE) properties. The conjugates were studied for their efficiency to produce singlet oxygen species ($^1O_2$) when measured via DPBF degradation assay as described. Hence, these molecules have a potential activity as PSs for PDT.[19]

The decrease in DPBF UV-absorption and time dependent degradations for BODIPY-TPE (**3.37** and **3.38**) derivatives is shown in Figures 3.11 and 3.12. Similar to the previous experiment the DPBF degradation assay was measured in DCM:MeOH (1:1) in a concentration of 0.15 mol.L^{-1}. The relative quantum yields were calculated with reference to H$_2$TPP as shown previously in Figure 3.7.[17]

3.37　　　　　**3.38**
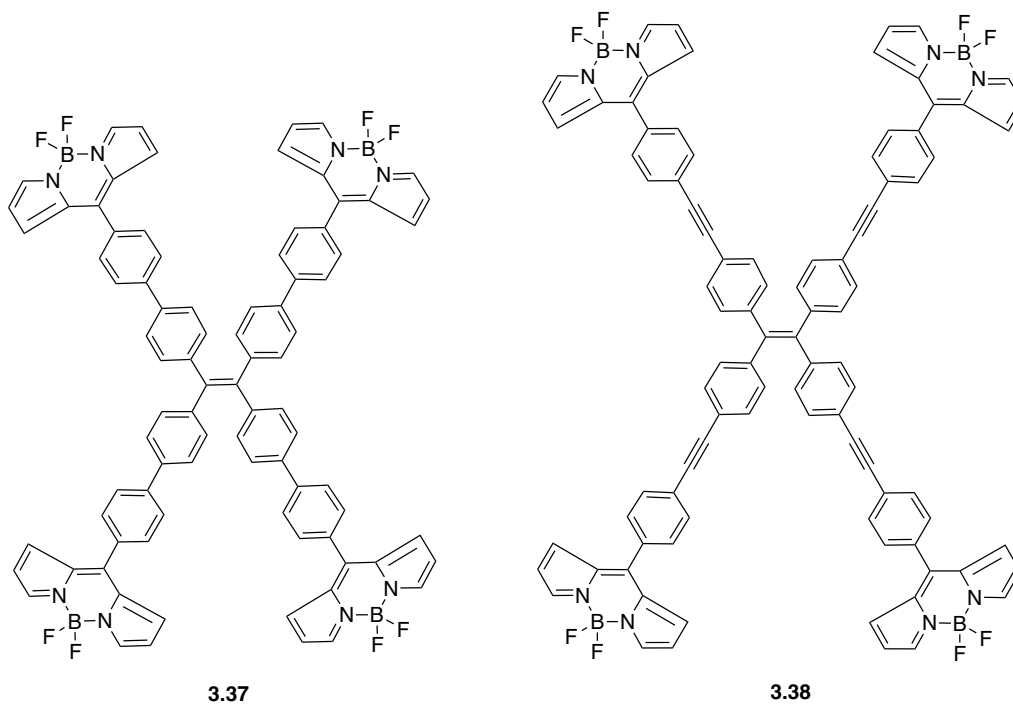
Figure 3.10. Tetra-BODIPY-appended TPE derivatives (BODIPY-TPE (**3.37** and **3.38**)) used for DPBF degradation assay for singlet oxygen production.

a)

b)
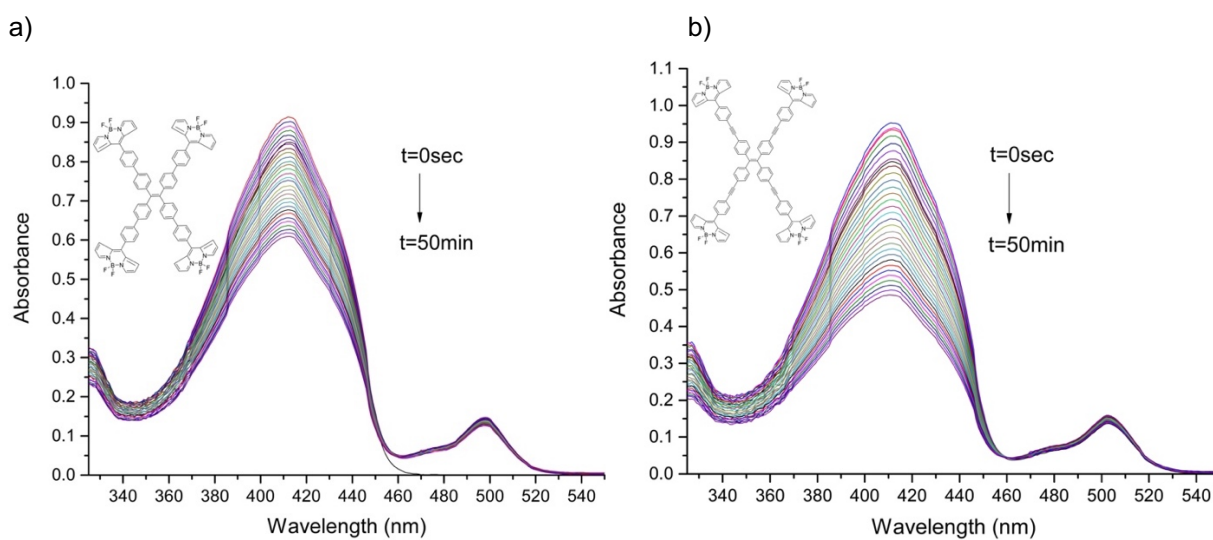
Figure 3.11. UV-vis degradation plots of DPBF in presence of BODIPY-TPE (a) **3.37** and b) **3.38** derivatives at 415 nm.
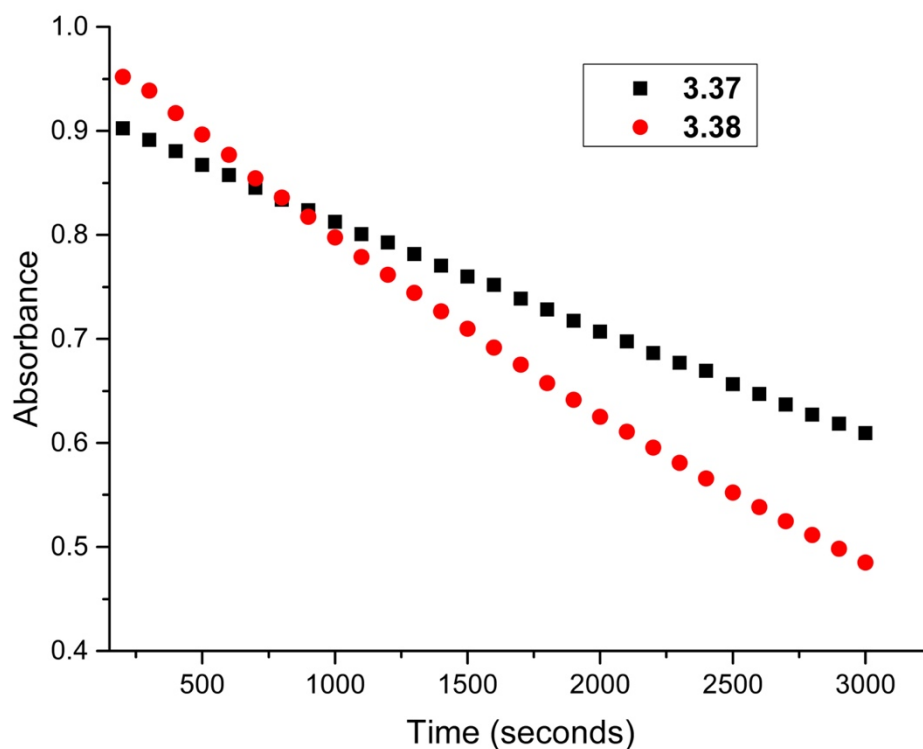
Figure 3.12. Time dependent DPBF degradation at 415 nm over time for BODIPY-TPE (**3.37** and **3.38**) derivatives in DCM/MeOH (1:1).

Table 3.3 shows the singlet oxygen quantum yield for BODIPY-TPE derivatives; these are adequate as photosensitizers utilized for PDT.

Table 3.3. Relative singlet oxygen production of for BODIPY-TPE (**3.37** and **3.38**) in DCM/MeOH (1:1) using H_2TPP, $\Phi_\Delta = 0.62$ as a reference.

BODIPY-TPE derivatives	Singlet oxygen quantum yield (Φ_Δ)
3.37	0.09
3.38	0.15

.

Compound **3.37** had a relative singlet oxygen yield smaller than compound **3.38** The introduction of an additional acetylene spacer and the corresponding increase in conjugation presumably leads to this enhanced yield.[20]

3.2.3. Singlet oxygen measurements of brominated porphyrins

Previous studies have reported that the addition of a bromine substituent can have profound effects on the photodynamic reactivity of porphyrins as compared to the non-brominated parent molecule.[21] PS associated singlet-oxygen generation benefits from exploitation of the heavy-atom effect, in which the presence of a higher molecular weight atom enhances spin-forbidden processes. Photosensitizers based on similar porphyrins with different bromine atom substituent placement are therefore expected to show varying singlet-oxygen generation profiles.[22]

A series of brominated porphyrin derivatives (**3.39**-**3.41**) as shown in Figure 3.13 were synthesized as potential PSs.

3.39   **3.40**

3.41
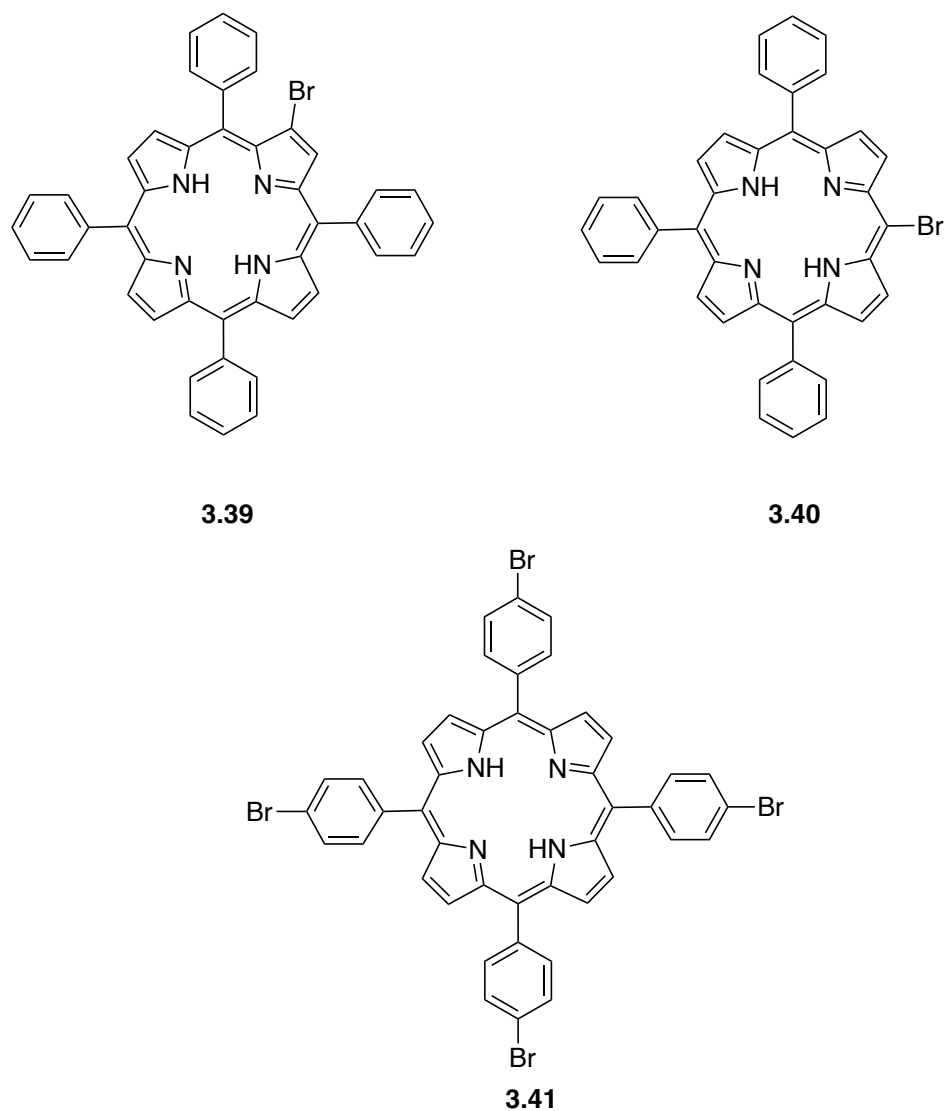
Figure 3.13. A series of brominated porphyrins (**3.39**-**3.41**).

UV absorbance degradation assay of DPBF in the presence of brominated porphyrin derivatives (**3.39**-**3.41**) and compared to reference PS, Methylene Blue (MB) (degradation plots in Figure 3.14).[23] Time-dependent degradation and UV-degradation plots and curves measured in DCM:MeOH (1:1) are illustrated in Figures 3.15 and 3.16 respectively for these PSs. The consequential values for relative quantum yields are assembled in Table 3.4.
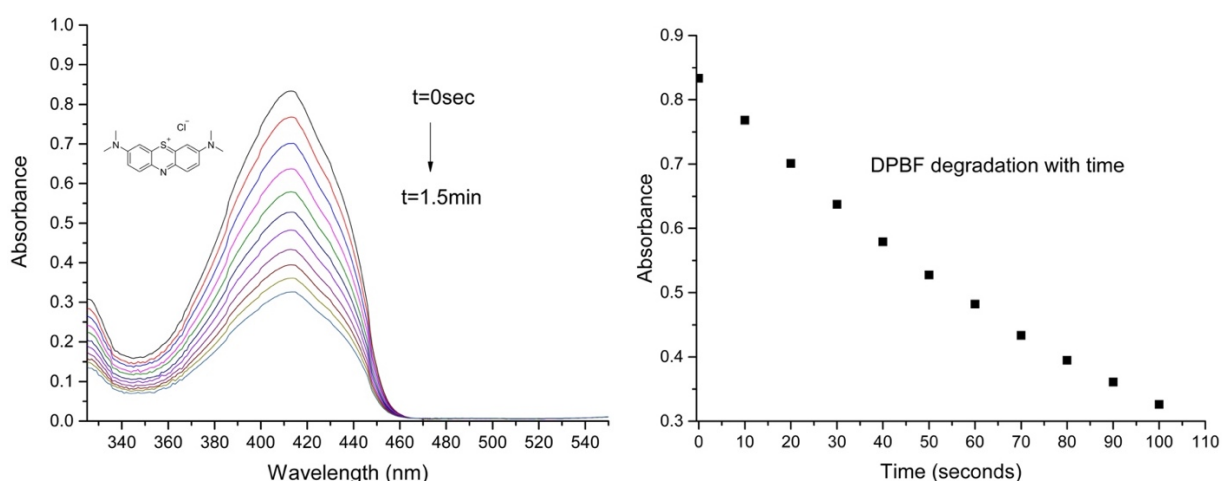
Figure 3.14. a) UV-Vis spectra of DPBF degradation and (b) DPBF consumption via MB at 415 nm.
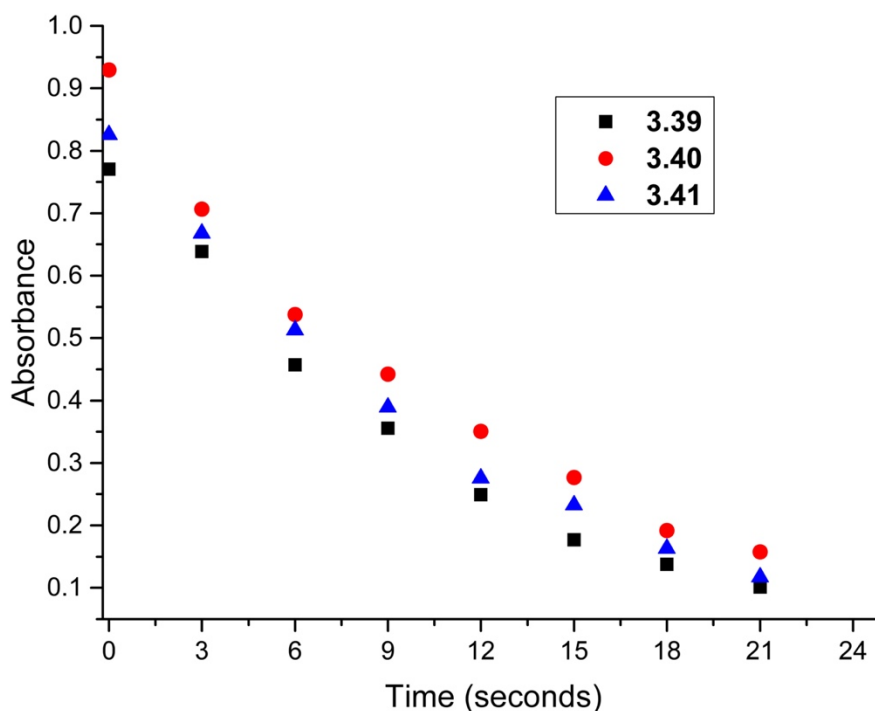
Figure 3.15. DPBF consumption measured at 415 nm over time for brominated porphyrin derivatives (**3.39**-**3.41**) derivatives.
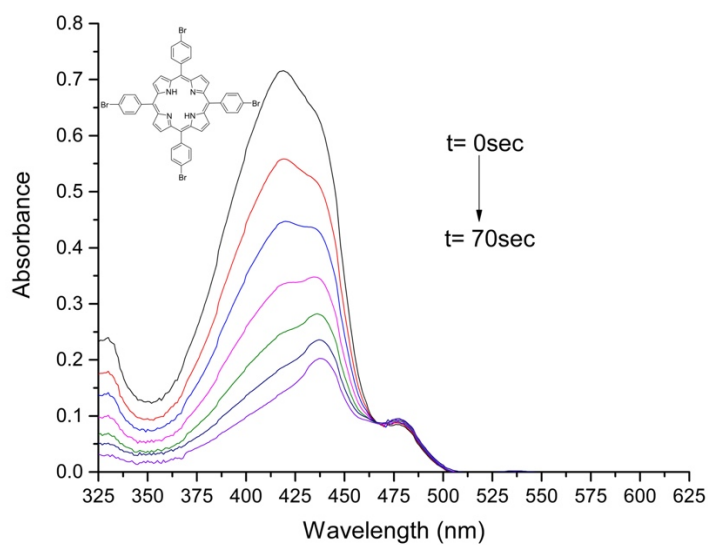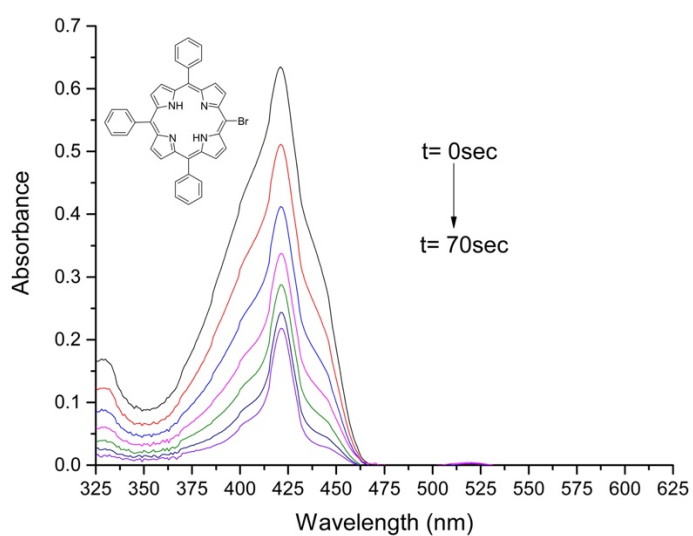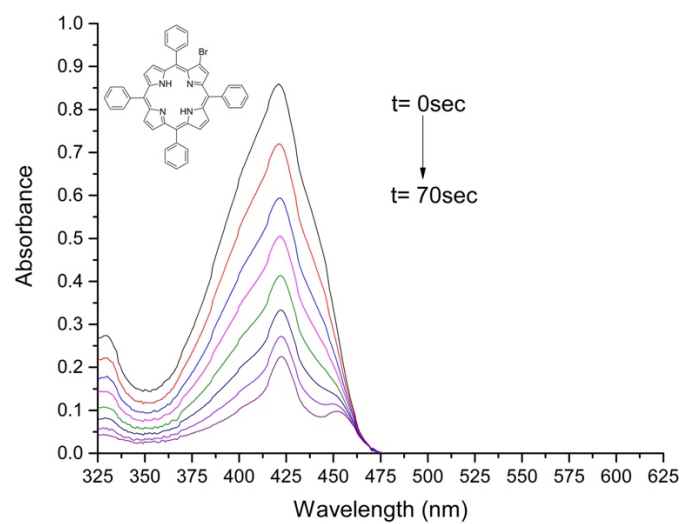
Figure 3.16. UV-vis DPBF consumption measured at 415 nm over time for brominated derivatives of porphyrins (**3.39**-**3.41**).

From the data in Table 6, we can see that the brominated porphyrins are each effective PS species, comparable to (for **3.40**) or exceeding (**3.39** and **3.41**) the H_2TPP reference.

Table 6. Relative singlet oxygen production of for brominated derivatives DCM/MeOH (1:1) using MB, Φ_Δ =0.50 as a reference.

Brominated porphyrins	Singlet oxygen quantum yield (Φ_Δ)
3.39	0.76
3.40	0.57
3.41	0.80

Given the relative stability of the Br atom, and the ease with which this can be introduced to the porphyrin skeleton, Br substitution is a highly effective strategy for PS enhancement.

3.3. Conclusion

In conclusion, the efficacy of photosensitizers to be utilized in PDT or aPDT application can be evaluated via chemical assays such as the DPBF degradation assay giving a preliminary insight into the production of ROS species, an important element for an effective applied PDT. These assays provide reference for relative quantification of amount of $^1O_2$ generated in an experiment. Several photosensitizers synthesized in the lab were evaluated in this chapter and in the next chapter (functionalized BODIPY dyes) to get an insight to the efficacy of such macrocycles. Under irradiation with light the PS in study produces ROS species which disrupts the chemical structure of the DPBF molecule, due to production of endoperoxide derived side products which causes a decrease in intensity of absorption maxima of the molecule which confirms the photoactivity of such molecules.

Constant efforts are put in by scientists to synthesize PSs active for PDT by functionalizing the macrocycles of known PSs to develop the best candidate for therapeutics. This functionalization enhances the photoactivity of the molecules and thus they can be pre-evaluated with DPBF degradation assays and further subjected to photophysical evaluations or for biological assays. Thus, such probes have been a vital tool for assessment of the applicability of the PSs based on tetrapyrroles or dipyrromethene dyes as synthesized in the lab in pre-clinical studies.

3.4. References

1. Kharkwal GB, Sharma SK, Huang YY, Dai T and Hamblin MR. *Lasers Surg. Med.* 2011; **43**: 755-767.

2. Bacellar IOL, Tsubone TM, Pavani C and Baptista MS. *Int. J. Mol. Sci.* 2015; **16**: 20523-20559.

3. Tripathy BC and Oelmüller R. *Plant Signal. Behav.* 2012; **7**: 1621-1633.

4. Dysart JS and Patterson MS. *Phys. Med. Biol.* 2005; **50**: 2597-2616.

5. Gunduz H, Kolemen S and Akkaya EU. *Coord. Chem. Rev.* 2021; **429**.

6. Krajczewski J, Rucińska K, Townley HE and Kudelski A. *Photodiagn. Photodyn. Ther.* 2019; **26**: 162-178.

7. Song D, Cho S, Han Y, You Y and Nam W. *Org. Lett.* 2013; **15**: 3582-3585.

8. Żamojć K, Zdrowowicz M, Rudnicki-Velasquez PB, Krzymiński K, Zaborowski B, Niedziałkowski P, Jacewicz D and Chmurzyński L. *Free Radic. Res.* 2017; **51**: 38-46.

9. Zhang XF and Li X. *J. Lumin.* 2011; **131**: 2263-2266.

10. Fudickar W and Linker T. *ChemPhotoChem* 2018; **2**: 548-558.

11. Entradas T, Waldron S and Volk M. *J. Photochem. Photobiol. B Biol.* 2020; **204**: 111787.

12. Luengas SLP, Marin GH, Aviles K, Acuña RC, Roque G, Nieto FR, Sanchez F, Tarditi A, Rivera L and Mansilla E. *Cancer Biother. Radiopharm.* 2014; **29**: 435-443.

13. Filatov MA, Karuthedath S, Polestshuk PM, Callaghan S, Flanagan KJ, Wiesner T, Laquai F and Senge MO. *ChemPhotoChem* 2018; **2**: 606-615.

14. Callaghan S, Filatov MA, Savoie H, Boyle RW and Senge MO. *Photochem. Photobiol. Sci.* 2019; **18**: 495-504.

15. Belali S, Savoie H, O'Brien JM, Cafolla AA, O'Connell B, Karimi AR, Boyle RW and Senge MO. *Biomacromolecules* 2018; **19**: 1592-1601.

16. Grover N, Emandi G, Twamley B, Khurana B, Sol V and Senge MO. *Eur. J. Org. Chem.* 2020: 6489-6496.

17. Wu WT, Zhan LY, Fan WY, Wu XY, Pan QW, Huang L, Li ZT, Zheng JT, Wang YF and Wu MB. *Macromol. Chem. Phys.* 2014; **215**: 280-285.

18. Callaghan S, Flanagan KJ, O'Brien JE and Senge MO. *Eur. J. Org. Chem.* 2020; 2735-2744.

19. Sample HC, Emandi G, Twamley B, Grover N, Khurana B, Sol V and Senge MO. *Eur. J. Org. Chem.* 2021; 4136-4143.

20. Ke H, Li W, Zhang T, Zhu X, Tam HL, Hou A, Kwong DWJ and Wong WK. *Dalton Trans.* 2012; **41**: 4536-4543.

21. Picard N, Ali H, Van Lier JE, Klarskov K and Paquette B. *Photochem. Photobiol. Sci.* 2009; **8**: 224-232.

22. Ravikumar M, Kathiravan A, Neels A and Mothi EM. *Eur. J. Inorg. Chem.* 2018; **2018**: 3868-3877.

23. Li W, Li L, Xiao H, Qi R, Huang Y, Xie Z, Jing X and Zhang H. *RSC Adv.* 2013; **3**: 13417-13421.

Chapter 4. Synthesis of BODIPY derivatives for aPDT

4. Synthesis of BODIPY derivatives for aPDT

4.1. Background and molecular design

The synthesis of difluoroborondipyrromethene (4,4-difluoro-4-bora-3a,4a-diaza-*s*-indacene, BODIPY) dyes was first reported by Treibs and Keuzer in 1968.[1] In the 1990s the potency and stability of these dyes as fluorescence markers and in tunable LASERs was reported; this attracted much scientific attention to this class of organic compounds.[2] With strong absorption and tunable fluorescence, coupled with the ease of synthesis of a library of these molecules, these compounds have found diverse biomedical applications.[3]

BODIPY dyes are part of the class of dipyrrin fluorophores, a class of generally visible-active organic dyes with a modifiable periphery and heterocyclic skeleton providing a simple η^2 chelate of nitrogen atoms with a single anionic charge.[4] The characteristic features of these dyes includes chemical robustness, high thermal and photochemical stability, absorption and fluorescence bands in the visible region around 500 nm, high molar extinction coefficients and high fluorescence quantum yields (φF).[5,6]

The structure of BODIPY (**4.1**) dyes features a skeleton of a dipyrromethene ligand, with two pyrrole units linked via a methine bridge, chelating a BF_2 moiety. BODIPY dyes do not obey Hückel's aromaticity rule ($4n+2$ π electrons). The IUPAC numbering system of BODIPY core shows eight functional positions as shown in Figure 4.1.
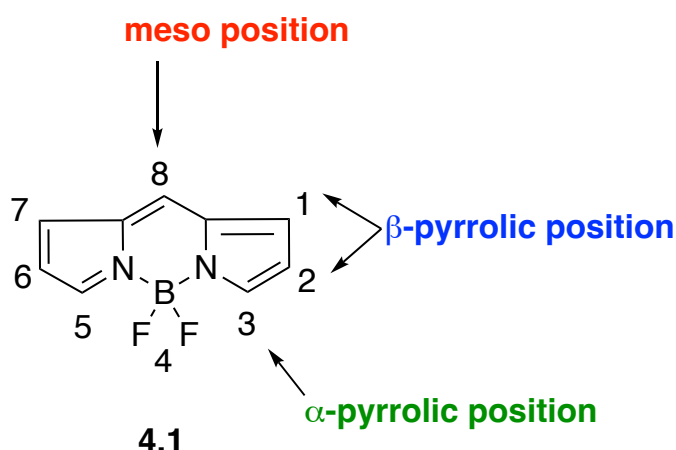
Figure 4.1. BODIPY dye core and its IUPAC numbering system.

4.2. Synthetic methodologies

The chemistry of BODIPY dyes can be potentially tuned to obtain the desired antimicrobial activity; the simplest approach being the attachment of a pyridinium derivative.[7] The formation of a library of compounds related to this motif, including many N-heterocycles, allows understanding the relevant parameters of this chemical landscape (i.e., the development of a quantitative structure-activity relationship).[8] Dipyrromethene ligands can be prepared by using pyrroles and a condensation partner, generally an aldehyde, then subsequently complexing with BF_2 in the presence of a base. This procedure affords a BODIPY in reasonable yields after workup.[9]

4.2.1. Strategies to synthesize BODIPY dyes

BODIPY compounds can be formed by combining pyrrole (**4.2**) and acyl chloride (**4.3**) as shown in Scheme 4.1.[10] The coupling of these two reactants produces an intermediate acylpyrrole which cannot be isolated and is further reacted with another pyrrole to afford dipyrromethene (**4.4**). Addition of boron trifluoride ($BF_3 \cdot Et_2O$) under basic conditions yields the final BODIPY adduct (**4.5**). This approach has been used conventionally to synthesize *meso*-alkyl-substituted BODIPYs where an alkyl aldehyde may be unreactive.
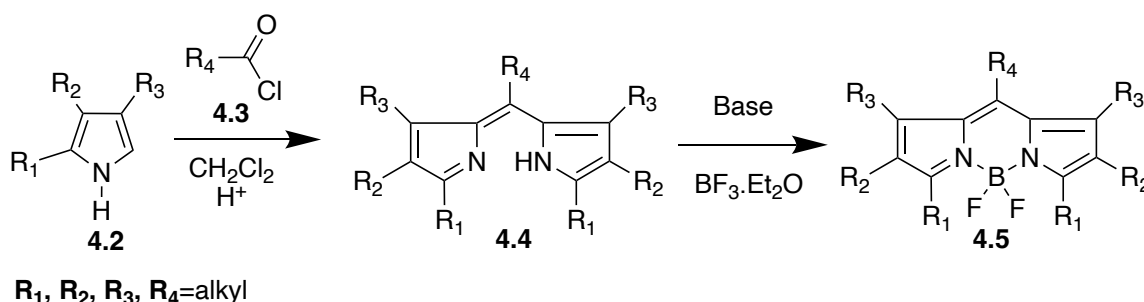
Scheme 4.1. Synthetic route to *meso*-alkyl-substituted BODIPY (**4.5**) dyes using acyl chloride (**4.3**)

The more versatile and commonly used procedure to synthesize BODIPYs is a one-pot synthetic route as illustrated in Scheme 4.2. This occurs via an acid-catalyzed (typically trifluoroacetic acid) condensation reaction of an aromatic aldehyde (**4.6**) with two equivalents of the pyrrole (**4.7**), resulting in the formation of dipyrromethane molecule (**4.8**).[11] This moiety is relatively unstable towards light, air, or acid; it reacts readily with

an oxidizing agent 2,3-dichloro-5,6-dicyano-1,4-benzoquinone (DDQ) yielding dipyrromethene or dipyrrin which is stable. Without further purification, under basic conditions, boron trifluoride (as $BF_3 \cdot Et_2O$) is added to the crude dipyrrin (**4.9**), which results in the formation of highly fluorescent, red-to-orange colored BODIPY (**4.10**) dye in 10-30% from starting materials. This reaction can be performed in an organic solvent (e.g., dry CH_2Cl_2); for an unsubstituted pyrrole precursor (R_1-R_3 = H), the pyrrole itself is used as reaction solvent, to prevent porphyrin or oligomer formation by significant excess of this reagent. Products which can be formed without the use of chlorinated solvents are far more environmentally friendly.

This second reaction strategy is used in this chapter as it provides an easy pathway to synthesize BODIPY derivatives with uncharged N-heterocycle units as *meso* substituents that can be further functionalized. These dyes are expected to be robust and allow many post-synthetic modifications, principally substitution at the N-position of the appended heterocycle and halogenation/coupling reactions at the pyrrole. The functionalization diversity obtained following this synthetic route and subsequent functionalization is the reason we used this method of synthesis to obtain a library of substituted BODIPY scaffolds with different functional groups.
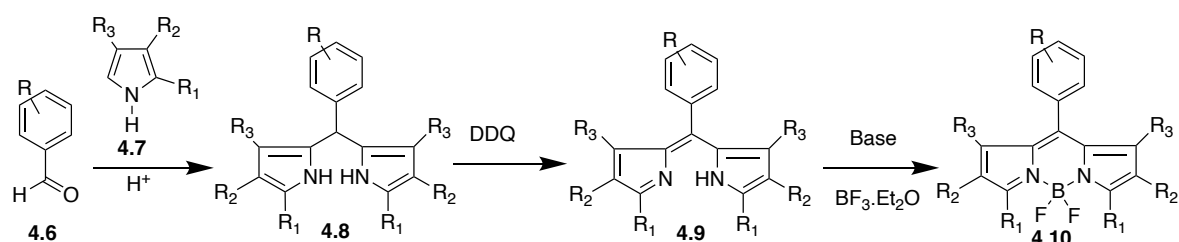
Scheme 4.2. Synthetic route to *meso*-substituted BODIPY (**4.10**) dyes using aromatic aldehyde (**4.6**) and pyrrole (**4.7**).

4.2.2. Derivatization of the BODIPY framework

The relative ease of synthesis and functionalization of BODIPY dyes is due to electron deficiency, which allows chemical modifications to often proceed under less forcing conditions than other aromatics. A rich chemistry of functionalized BODIPY compounds with different linkers, receptors, and several important organic molecules or bioconjugates is known, via different types of reactions.[12]

Possible modifications for the BODIPY core are as follows:

i) Electrophilic substitutions at the 2, 6-positions.[12-14]

The 2,6-positions of the BODIPY skeleton, when unsubstituted, can undergo electrophilic aromatic substitution reactions akin to those encountered for aryl units. Water-soluble sulfonate groups can be appended to the hydrophobic core of BODIPY dye. This modification does not influence the optical properties of the BODIPY core, making these modifications useful for biological applications. Furthermore, the introduction of heavy atoms such as halogens (usually Br or I) causes a bathochromic shift in absorption and emission bands which quenches the fluorescence intensity relative to the parent dye.

ii) Nucleophilic substitution at the 3, 5-positions.[12,15-17]

Halogens such as chlorine or iodine are good leaving groups; due to the electron-deficient BODIPY core, a 3,5-dimethyl BODIPY readily undergo nucleophilic substitution reactions. Several nucleophiles can be used, forming carbon to carbon, nitrogen, oxygen, or sulfur bonds, adding the advantage of possible extended conjugation, enabling a bathochromic shift in the spectrum. The 3,5-positions are reactive for palladium mediated cross-coupling reactions such as Sonogoshira coupling, Suzuki coupling and Heck coupling. This allows the incorporation of functional groups such as ethynyl, and aryl-substituents to form long-wavelength BODIPY-based fluorescent biosensing materials and bio-labels.[12]

iii) Functionalization at the C-8 position.[18-20]

The C-8 position of the BODIPY core has been used for the incorporation of molecules such as ion capture ligands, water solubilizing groups, donor-acceptor groups, and biomolecules. This modification site is the most versatile, and has been used widely to produce molecules, such as the BODIPY-anthracene dyads (BADs). In the context of this manuscript, this strategy was utilized to make several molecules active for antimicrobial photodynamic therapy.

iv) Replacement of the *meso*-carbon with nitrogen to form aza-BODIPY dyes.[18, 21,22]

A class of dyes related to the BODIPY by replacement of the C8 atom with nitrogen, named aza-BODIPYs, can be formed via Michael addition reactions or via the reaction

of phthalonitrile and arlymagnesium bromides. The introduction of an electronegative nitrogen atom affects the HOMO-LUMO energy gap through stabilization of the LUMO causing a bathochromic spectral shift. This moiety has been used as a promising fluorophore for in vivo molecular imaging and theragnostic applications.

v)   Fusion of aromatic rings to the pyrrole units.[23-25]

Fusing aromatic rings to pyrrole precursors (e.g., indole or isoindole) causes red-shifted absorption and emission bands of the synthesized BODIPY dyes. Strategies such as the use of aryl-fused pyrroles or retro Diels-Alder syntheses of norbornane-derived pyrroles can be used to derive these extensively π-conjugated systems. These BODIPY dyes have found extensive use in molecular imaging.[23]

vi)   Nucleophilic substitution of the fluorine at the boron center.[14]

The replacement of the fluorine atoms by, e.g., ethynyl or oxyanion nucleophiles has been performed to derivatize BODIPY dyes with enhanced photostability, forming highly luminescent redox-active complexes. Substitution of the fluorine atoms generally employs the use of organometallic reagents, typically an organolithium or Grignard complex.

The BODIPY dyes synthesized via each of these post-synthetic functionalization methods shift the emission maximum to the 510-800 nm range; those with crowded substitution patterns have additional advantages of having higher extinction coefficients ($\varepsilon > 50,000$), enhanced photo- and chemical stability and insensitivity towards the solvent polarity.[26,27] It has also been shown that electrochemical properties of the BODIPYs can be tuned followed by modification on the pyrrolic core; these tuning strategies of the BODIPY core have enhanced the utility of this molecule in fields of cell imaging, biolabeling or as chemical sensors as multiple chemically similar but photochemically distinct labels can be employed simultaneously.[28,29]

With the versatility of this molecule well established, it is important to note the most common drawback encountered, the aggregation and induced quenching of florescence in aqueous media.[29] Strategies to avert aggregation include introduction of static charge to introduce repulsion and use of drug-delivery systems; these strategies are both employed in this investigation to enhance utilization in biological strata most importantly in aPDT.

4.3. Applications of BODIPY dyes

As previously stated, BODIPY dyes have been studied and explored for their applications since the early 1990s, as a readily accessible, versatile, biocompatible, and stable fluorophore.[30] Researchers have explored the use of such dyes in molecular biolabeling, cell imaging, chemical sensing, solar cells, and two-photon absorption.[31] among other emerging uses. In the last decade, the BODIPY dyes have been reported to be potential PS in aPDT, though few of examples of such dyes designed for this purpose exist in literature. The current state of research is summarized below.

4.3.1. BODIPY dyes in antimicrobial photodynamic therapy (aPDT)

Obviously, for a PS active for aPDT it is necessary that the PS be soluble in water. Often by using specific solubilizing functionalities a charged group introduced to the molecular backbone can be provided to ensure a good degree of interaction between the bacterial cell wall and the PS itself.[32]. Several dyes based on porphyrin and similar macrocycles possessing these characteristics are typically rigid and planar structures at their core, and have large, conjugated surface.[33] However, a disadvantage to using such dyes is the weak absorption in the visible region, a lack of target specificity, and a tendency to aggregate at high concentrations.[34][35]

Some research indicates that an extension of the π-conjugation through substitution with styryl, aryl and ethynyl aryl substituents at the 1, 3, 5, and/or 7-positions or aromatic ring fusion, or formation of aza-BODIPY formation, etc. can significantly enhance and red-shift the absorption band, allowing overlap with the optical window for tissue penetration in the 650-1000 nm region.[36]. The incorporation of heavy atoms such as halogens to the BODIPY dye enhances the rate of intersystem crossing to the triplet state, which is generally low in BODIPY dyes, thus enabling the production of singlet oxygen by decreasing the fluorescence quantum yield.[37] In addition, a few water-soluble BODIPY derivatives have been synthesized by functionalization with sulfonic groups, phosphonates, sulfonated peptide chains or oligo-ethylene glycol chains.[38]

4.3.1.1.   Examples of BODIPY dyes used in aPDT

To generate efficient BODIPY PS for effective aPDT it is important to employ all the above modifications simultaneously, to synthesize red-wavelength BODIPY photosensitizers (i.e., those that absorb > 600 nm) with improved singlet oxygen production, enhanced water solubility and effective cell interaction and penetration. A difficult task, steps toward this ideal PS have been taken by the addition of cationic charges to the BODIPY dye or the exploitation of the heavy atom effect.[39]

The first report of aPDT efficiency of BODIPY dye was published in 2012 by Orlandi and coworkers wherein they synthesized BODIPY dyes with a *meso*-pyridinium group and 2,6-disubstituted with iodine atoms as shown in Figure 2.[40] These dyes (**4.11** and **4.12**) showed efficacy against a broad spectrum of microbial species (*S. xylosus* and *E. coli*) as shown in Table 4.1. BODIPY dyes **4.12** also an efficient inhibition of growth bacterial biofilm of Gram-negative *P. aeruginosa*. This evidences the need for the introduction of cationic charges for increased interaction with the cell membrane of the target microbe.
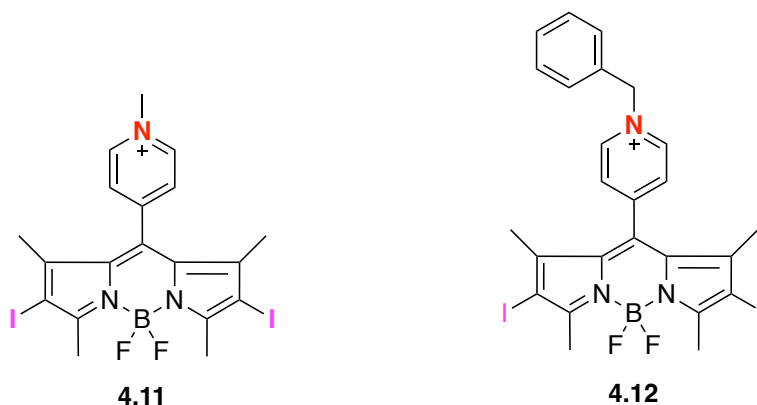
Figure 4.2. Cationic BODIPY dyes derivatives (**4.11** and **4.12**) active for aPDT.

Table 4.1. Photodynamic minimal inhibitory concentrations (MIC) of BODIPYs 4.22 and 4.12 for *S. xylosus* and *E. coli* irradiated at 20.7 W/cm^2

BODIPY	Gram-bacteria	MIC (µM)
	E. coli	
4.11		1.25 ± 0.57
4.12		6.60 ± 2.88
	S. xylosus	
4.11		0.31 ± 0.13
4.12		0.83 ± 0.36

The heavy atom effect via halogen addition is very important, as this can enhance the spin-forbidden process which enhances the aPDT efficiency of the BODIPY dyes [44]. Some examples of this are illustrated in Figure 4.3 (BODIPY dye derivatives **4.13**-**4.22**) where a series of mono- and di-halogenated BODIPYs bearing electron-donating substituents have been described.[41] They showed effective aPDT against the Gram-positive species of *B. subtilis* and Gram-negative species of *E. coli*. Another report of such heavy atom effects showed for BODIPYS with *meso*-acetoxymethyl moieties and substituted at the 2,6-positions with bromine or iodine as shown in Figure 3b. Both dyes could inactivate the Gram-negative species of *E. coli* and the BODIPY dye with bromine (**4.23**) was more efficient than the one substituted with iodine (**4.24**).[42]

4.13: **R**=H, X=H
4.14: **R**=H, X=**Br**
4.15: **R**=CH$_3$, X=H
4.16: **R**=CH$_3$, X=**Br**
4.17: **R**=*tBu*, X=H
4.18: **R**=*tBu*, X=**Br**
4.19: **R**=N(CH$_3$)$_2$, X=H
4.20: **R**=N(CH$_3$)$_2$, X=**Br**
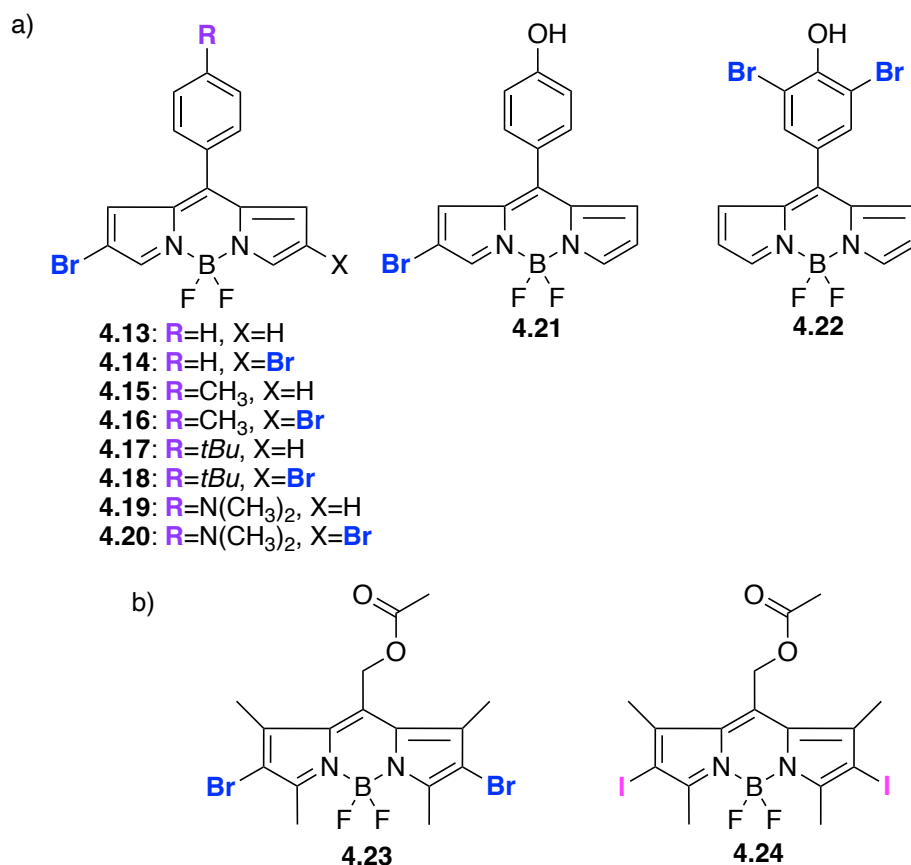
Figure 4.3. BODIPY dye derivatives with a) mono- and brominated BODIPYs bearing electron-donating substituents and BODIPYS and *meso*-acetoxymethyl moiety (**4.13**-**4.22**) and b) substitution at 2,6-position with halogens such as bromine (**4.23**) and iodine (**4.24**) atoms.

A hexa-brominated BODIPY derivative with a *meso*-aniline substituent conjugated to Au nanorods, as shown in Figure 4.4, showed an enhancement in the singlet oxygen

quantum yield (Φ_Δ) enhanced from 0.64 of the parent BODIPY (**4.25**) to 0.76 upon conjugation with 4-AuNR (**4.26**), both very high values due to the heavy atom effect.[43]
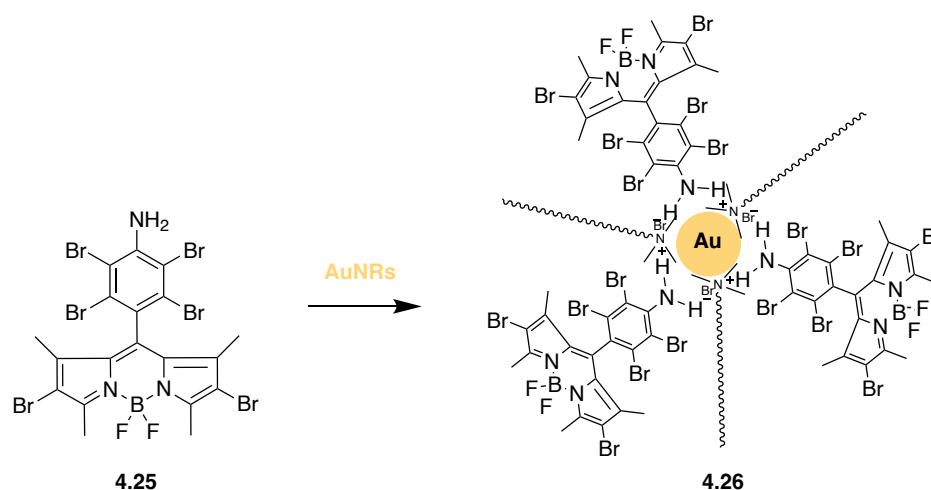
Figure 4.4. Conjugation of BODIPY (**4.25**) dyes with AuNRs (**4.26**).

BODIPY dyes can be conjugated with carbohydrates to obtain conjugates active for aPDT; one such example is a recent work published by the Senge group in Dublin where BODIPY were conjugated via nucleophilic aromatic substitution with amines (**4.27-4.33**) and thio-carbohydrates (**4.34-4.41**) on the *para*-fluorine atoms. These conjugates as shown in Figure 4.5 displayed a significant phototoxic assay as against the Gram-positive *S. aureus* and Gram-negative *P. aeruginosa*.[44] A very effective inactivation of both these strains was observed by dibrominated thiol derivatives (**4.34-4.35** and **4.40-4.41**) in 3 log stages suggesting that such glycosylated, dibrominated BODIPYs could be promising candidates for aPDT.
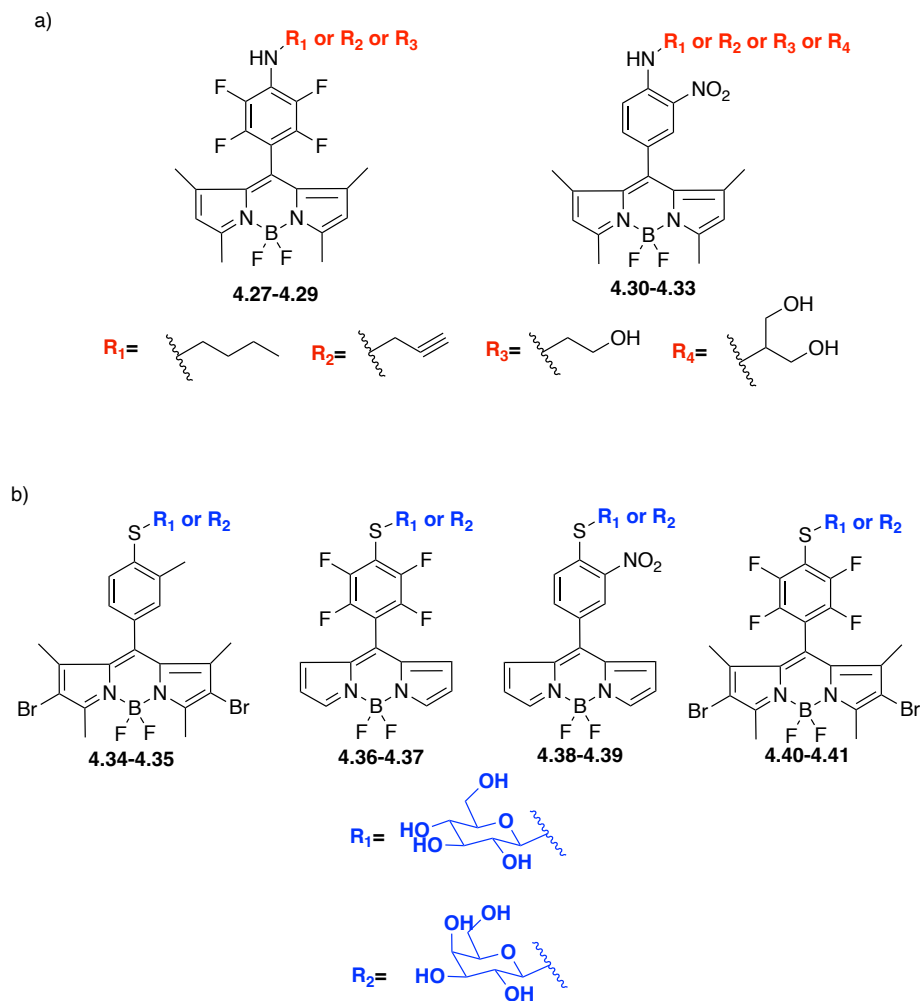
Figure 4.5. Conjugation of BODIPY dyes: a) amine (**4.27**-**4.33**) b) thio (**4.34**-**4.41**) carbohydrates.

4.4. BODIPY scaffolds synthesized

Throughout the manuscript it was emphasized how important it is that a molecule to be used in biological research has a strong interaction with the microbial cells, along with an enhanced solubility in biological medium. The BODIPY dyes have long been established to have remarkably high quantum yield for singlet oxygen production along with good photostability.[14] However, as is often the case with large π-system containing molecules, poor interactions with cell structures and limited solubility hampers their use as biological probes. Also, BODIPYs are known to have high fluorescence quantum yields and thus deactivates the singlet excited state through ISC. This reduces the formation of production of $^1O_2$ (Φ_Δ) species. Therefore, it becomes of utmost importance to develop molecules which can overcome these limitations for aPDT.

Synthesis of the described BODIPY compounds have the apart from being time-efficient, has an added advantage of being a convergent approach– that one heterocycle-bearing precursor can be the starting material to innumerate final compounds. Hence a library of BODIPY dyes was synthesized with *meso*-aryl-substitutions which can be post-functionalized with moieties improving their potential for aPDT. The first functionalization strategy was to introduce ionizable substituents on a N-heteroatom of the *meso*-heterocycle or by replacement of fluorides on boron in the 4-position via N-alkyne-Grignard reagents making these dyes charged water-soluble derivatives for enhanced aqueous solubilization.[45] The second strategy used in this chapter was to introduce heavy atoms by halogenation at the 2,6-positions to enhance the photophysical and cytotoxic activity against bacteria. Finally, extended π-conjugates of these molecules were synthesized via double Sonogoshira cross-coupling reaction via 2-position post-functionalization enhances the optical window of the compounds towards the bathochromic shifts and hence increases the usability of these scaffolds for deep tissue treatments.[40]

4.5. Results and discussion

4.5.1.　　Synthesis of aPDT active BODIPY dyes

4.5.1.1.　*meso*-N-heterocyclic BODIPY

The ease of synthesizing this scaffold from aryl aldehydes via condensation with two pyrroles affords the simplest and a direct route to add functionality and derive diverse derivatives of the BODIPY fluorophore. Following the classic three-step, one-pot strategy was employed in the BODIPY synthesis as shown in Scheme 4.3. A library of 15 *meso*-aryl BODIPYs (**4.46**-**4.60**) from commercially obtained 2,4-dimethylpyrrole (**4.46**-**4.53**) and 3-ethyl-2,4-dimethyl pyrrole (**4.54**-**4.60**) and different aldehydes (Table 4.2) was obtained.
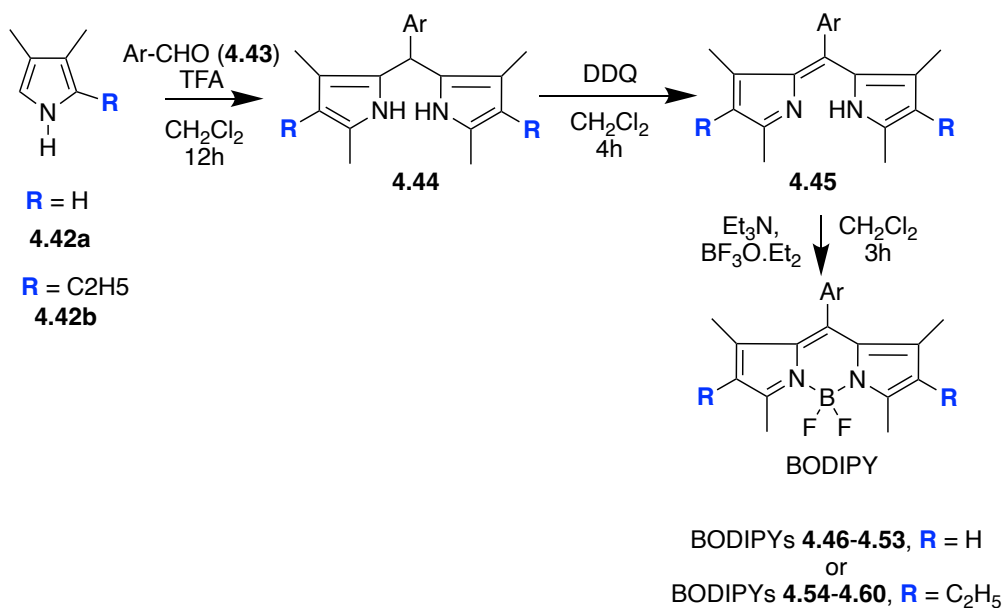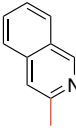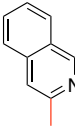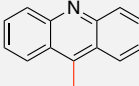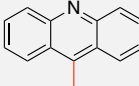
Scheme 4.3. Synthesis of library of *meso*-aryl-BODIPYs.

meso-Aryl BODIPYs (**4.46**-**4.60**) were synthesized by condensing two pyrroles (2,4-dimethylpyrrole (**4.42a**) or 3-ethyl-2,4-dimethylpyrrole (**4.42b**)) units with a desired arylaldehyde in anhydrous dichloromethane. Acid catalyst, TFA is added which promotes the condensation via protonation or chelation to the carbonyl oxygen of the aldehyde, thus introducing partial positive charge on the carbonyl carbon and hence promoting nucleophilic attack by pyrrole. TFA facilitates this process to form dipyrromethane (**4.44**) derivative, which is relatively unstable. After 12 h of stirring at

room temperature under inert atmosphere of argon, oxidizing agent DDQ was added which facilitates the formation stable dipyrromethene (**4.45**) species. These species are deprotonated by a base Et$_3$N and then exposed to an excess of boron complexing agent, BF$_3$·OEt$_2$ to obtain the desired library of BODIPYs (**4.46**-**4.60**). Target compounds are obtained as green, orange, or deep red crystals in 5 to 20% yields as shown in Table 4.2.

Table 4.2. Percentage yields of new *meso*-aryl-BODIPY derivatives (**4.46**-**4.60**).

BODIPY (2,4-dimethylpyrrole derivatives)	Ar	% Yield	BODIPY (3-ethyl-2,4-dimethylpyrrole derivatives)	Ar	% Yield
4.46		16	4.54		15
4.47		8	4.55		10
4.48		20	4.56		14
4.49		14	4.57		13
4.50		14	4.58		13
4.51		15	4.59		13
4.52		8	4.60		5
4.53		21			

A side product, a tripyrrin **4.59a** is observed as shown in Figure 4.6. whilst synthesis of BODIPY **4.59**, resulted from a rearrangement mechanism is such reaction conditions.
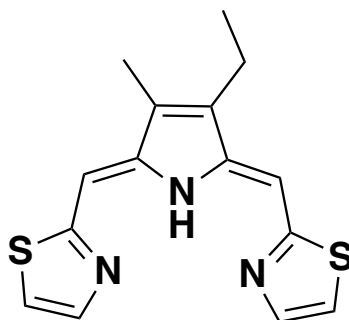
Figure 4.6. Side product, tripyrrin **4.59a** obtained whilst synthesis of BODIPY **4.59.**

4.5.1.2. Water-soluble BODIPYs

The *meso*-N-aryl BODIPY derivatives (**4.46**, **4.54**, **4.48** and **4.56**) described in the previous sections offer reactive points for post-functionalization with ionizable groups to enhance the utilization window of such derivatives in aPDT due to improved membrane interactions and solubility.[55,56] The first examples to be prepared with this strategy were obtained via a facile one-step synthesis of methyl iodide (**4.62**) functionalized derivatives **4.46a**, **4.54a**, **4.48a** and **4.56a**, respectively, as illustrated in Scheme 4.4.

BODIPYs **4.46**, **4.48**, **R** = H
or
BODIPYs **4.54**, **4.56**, **R** = C$_2$H$_5$

CH$_3$I (**4.61**)

AcCN, 82 °C
1.5h

BODIPYs **4.46a**, **4.48a**, **R** = H
or
BODIPYs **4.54a**, **4.56a**, **R** = C$_2$H$_5$
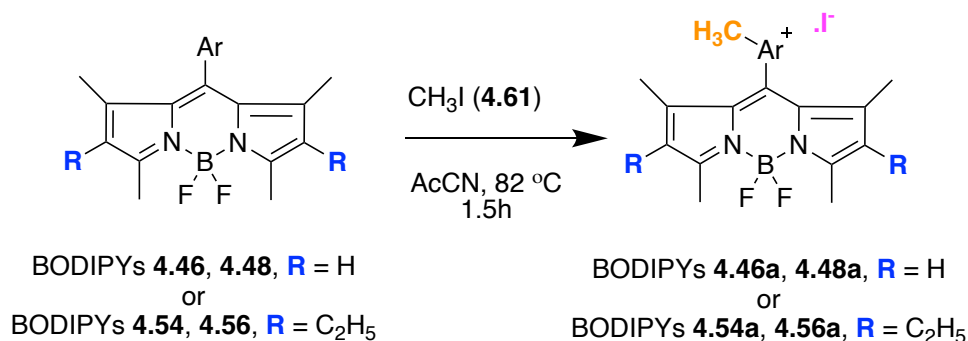
Scheme 4.4. Synthesis of charged water-soluble *meso*-methyl-BODIPYs **4.46a**, **4.54a**, **4.48a** and **4.56a**.

The reaction mixture was refluxed for 1.5 h with *meso*-N-aryl-BODIPYs and methyl iodine in presence of AcCN. The products of the reactions revealed a substitution at the N-heteroatom of the *meso*-aryl ring of the substituted BODIPY compounds confirmed by NMR spectra and UV shifts.

Following similar synthetic lines, a second series of water-soluble zwitter ionic with carboxylate functionality (**4.46b**, **4.54b**, **4.48b** and **4.56b**) and etherate functionality (**4.46c**, **4.54c**) was synthesized as shown in Scheme 4.5 and Scheme 4.6, respectively.
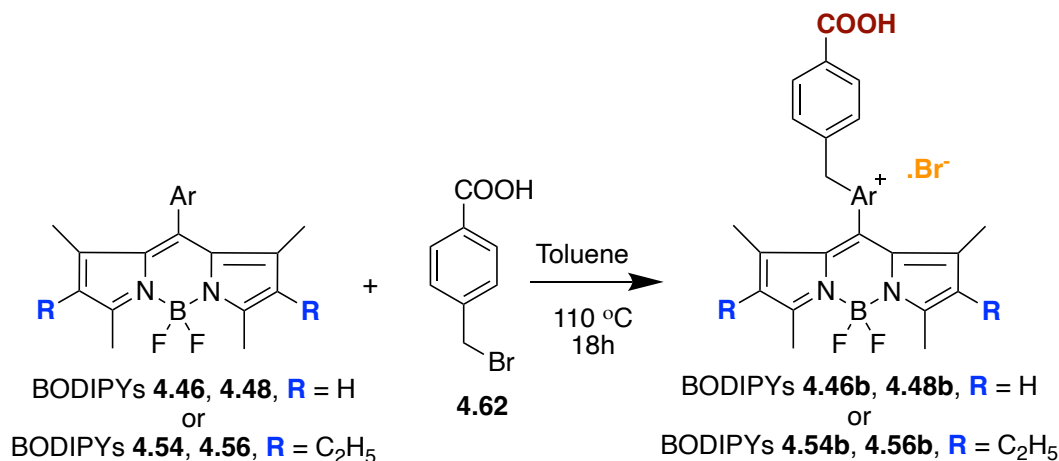
Scheme 4.5. Synthesis of charged water-soluble *meso*-methyl benzoate-BODIPYs **4.46b**, **4.54b**, **4.48b** and **4.56b**.

The reaction mixture was refluxed for 18h with the previously synthesized *meso*-N-aryl-BODIPYs and functionalized with 4-bromomethyl benzoic acid (**4.62**) or 4-bromobutyl phenyl ether (**4.63**) on the N-heteroatom of the BODIPY scaffold in presence of toluene, resulting in formation of zwitter ionic species of corresponding BODIPY scaffolds.
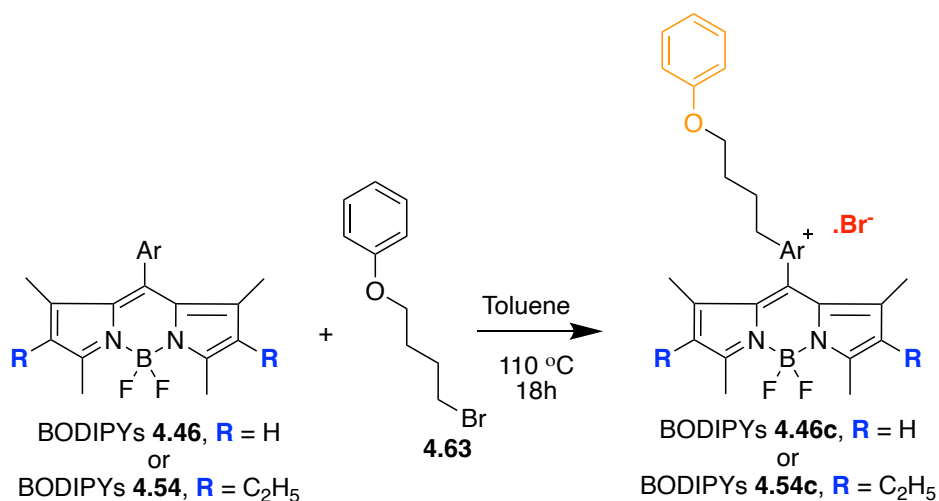
Scheme 4.6. Synthesis of charged water-soluble *meso*-butylphenyl etherate-BODIPYs **4.46b**, **4.54b**

Another strategy to prepare water-soluble derivatives of the corresponding BODIPYs is to synthesize boron-ethynyl-substituted carboxylate derivative.[45] A two-step synthesis

was employed with the aim to graft the carboxylate residues onto boron atom using the ethynyl Grignard reagent as shown in Scheme 4.7.
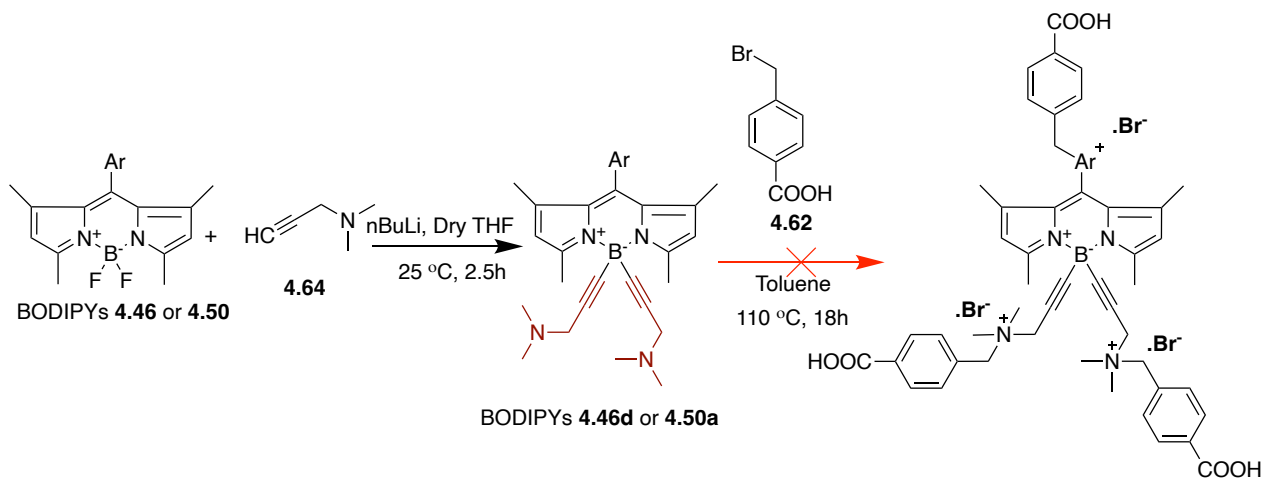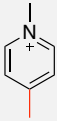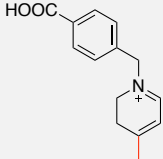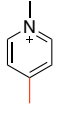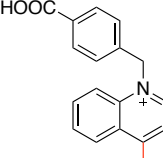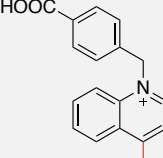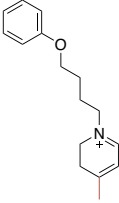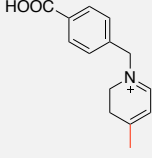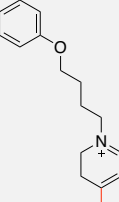
Scheme 4.7. Synthesis of boron-ethynyl-substituted carboxylate derivatives (**4.46d** and **4.50a**).

To synthesize the BODIPY derivatives **4.46d** and **4.50a**, the dimethylamino moieties were introduced onto the boron atom via replacement of the fluoride atoms with the Grignard reagent 1-(N,N-dimethylamino)-prop-2-yne (**4.64**) to synthesize derivatives 26 and 27 in yields of 30-45%. Then an attempt to quaternate these scaffolds with 4-bromomethyl benzoic acid was done.[45] The reaction did not yield the expected product but a mixture of compounds which were difficult to separate and isolate due to lack of solubility in organic solvents.

Target charged water-soluble derivatives are obtained as orange, or deep red crystals in 60 to 85% yields as illustrated in Table 4.3.

Table 4.3. Percentage yields of water-soluble BODIPY derivatives.

BODIPY	Ar	% Yield	BODIPY	Ar	% Yield
4.46a		81	**4.54b**		75
4.54a		73	**4.48b**		63
4.48a		85	**4.56b**		68
4.56a		75	**4.46c**		70
4.46b		82	**4.54c**		72

4.5.1.3. Heavy-atom derivatives of BODIPYs

The 2,6-positions of the BODIPY core have known to readily undergo a nucleophilic attack by halide ions such as iodide.[40] This knowledge in hand, BODIPYs (**4.46**, **4.49**, **4.51** and **4.53**) underwent iodination in the presence of NIS (**4.65**) in DCM at room temperature for 2 hours to yield red crystalline monoiodo-BODIPYs (**4.46e**, **4.49a**, **4.51a** and **4.53a**) in 42-77% yields (Table 4.4) as shown in Scheme 4.8. Alkyl-halides are the most used precursors in organic synthesis for production of ionizable species of PSs. Halogens (iodine or bromide) acts as a very good leaving group and undergoes S_NAr reactions.

BODIPYs **4.46**, **4.49**, **4.51** or **4.53**   **4.65**   BODIPYs **4.46e**, **4.49a**, **4.51a** or **4.53a**
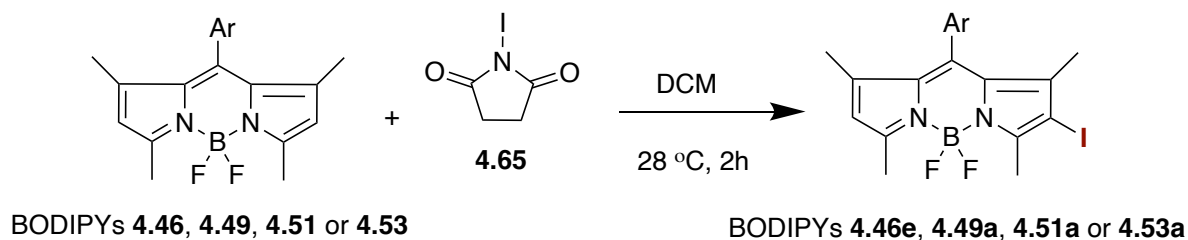
Scheme 4.8. Synthesis of 2-functionalized iodinated derivatives (**4.46e, 4.49a, 4.51a and 4.53a**)

4.5.1.4.   BODIPYs with extended π-conjugated systems

Iodination allows for further functionalization and introduction of another chromophore (dimerization) onto the BODIPY core at 2-position has been achieved by two successive Sonogashira cross-coupling reactions under standard conditions as shown in Scheme 4.9. A conjugated derivative **4.66** was obtained after coupling of BODIPY **4.46e** and BODIPY **4.46g** as shown in Scheme 8.
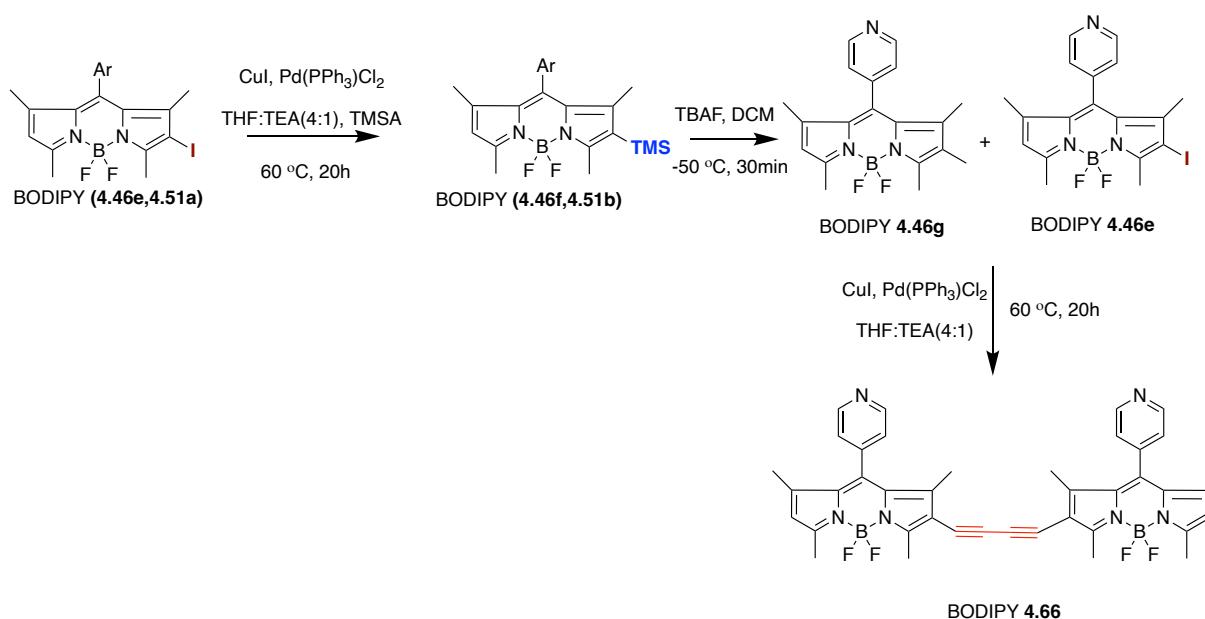
Scheme 4.8. Synthesis of extended π-conjugated BODIPY (**4.66**).

This was achieved by performing first Sonogashira cross-coupling of derivative **4.46e** with trimethylsilyl acetylene (TMSA) and derivative **4.46f** was obtained and purified with a 78% yield. This derivative was then deprotected (BODIPY **4.46g**) -50 ºC in the presence of TBAF and a pink solid was obtained and purified in 85% yield. The molecule was then subjected to a second Sonogoshira cross-coupling; however, the cross-coupling reaction did not proceed as expected and only a homo-coupled product

(**4.66**) was isolated 42% yield**.** Some difficulties in the purification of **4.66** were met, due to the poor solubility of this derivative in common solvents. ^{1}H NMR revealed the structural details of the complex but was unspecific as to the nature of the bridge, which was confirmed with elucidation of the X-ray crystal structure. TMS derivative **4.51a** was also obtained in 65% yield following a similar procedure as described above from compound **4.51b**; dimerization of this compound into a coupled derivative using the same procedure as above was unsuccessful.

The synthesized library of differentially functionalized BODIPYs allowed for the investigation for effect of such functionalization on the photophysical and cytotoxic properties. All BODIPYs were characterized by ^{1}H- and ^{13}C-NMR, HRMS and by X-ray crystallography. Analysis of the NMR spectra shows the anticipated 2-fold symmetry of the BODIPY. Single signals for the 2,6-hydrogens, the 1,7- and 3,5-dimethyl groups for 2,4-dimethyl pyrrole derived BODIPYs (**4.46**-**4.53**) and 2,6-diethyl, the 1,7- and 3,5-dimethyl groups for 3-ethyl-2,4-dimethyl pyrrole derived BODIPY (**4.54**-**4.60**) were observed in the ^{1}H-NMR spectra and ^{13}C signals for only half of the BODIPY core carbons in ^{13}C-NMR specifying a plane of symmetry extending through the boron and C-8. *meso*-Aryl substituted groups show characteristic ^{1}H proton resonances and carbon signals corresponding to aryl group carbons. Again, NMR resonances shifts for the BODIPY core were relatively same for different *meso*-aryl functionalization with water-soluble functionalization on the N-heteroatom of the *meso*-N-heterocycle for groups such as methyl (**4.46a**, **4.54a**, **4.48a** and **4.56a**), carboxylate (**4.46b**, **4.54b**, **4.48b** and **4.56b**) **and etherate (4.46c** and **4.54c**) or for boron-ethynyl-substituted BODIPY derivatives (**4.46d** and **4.50a**). The observed up-field shift in ^{1}H NMR for iodinated derivatives (**4.46e, 4.49a, 4.51a and 4.53a**) of the methyl groups in positions 1 and 7 (at approximately 1.6 ppm) compared with the 3,5-dimethyls (at approximately 2.5 ppm) is likely caused by shielding incurred by the *meso*-aryl groups. The lack of signal of the 2-hydrogen (at ~ 6.0 ppm) in the ^{1}H-NMR spectra indicated mono-iodination. Similar resonance shifts are observed TMS functionalized derivatives **4.46f** and **4.51b** and TMS-deprotected derivative **4.46g.**

4.5.2.   X-ray Crystal determination

4.5.2.1.   Crystallographic structural elucidation of BODIPY dyes

Crystal growth is a crucial step in characterizing a new molecular compound - a good quality crystal allows the determination of the structural details of the desired compound through X-ray diffraction.[46] A crystalline form of a drug affects properties such as its bioavailability, stability, solubility, dissolution rate, and bioavailability, and the crystalline state of a drug is crucial to understanding the pharmacology and is a critical step in commercialization through patent application.[47] The crystal engineering of organic molecules is an emerging field focused mainly on the identification and control of intermolecular and supramolecular features to yield a designed solid-state conformation or packing.

Our research group has been using BODIPY and related compounds for applications ranging from photo up-conversion to photosynthesis, incorporated into hydrogels and scaffolds.[48,49] Detailed X-ray studies on the structures of a range of BODIPY compounds has given insight into their photophysical properties; It has been shown that the conformation of the BODIPY has an effect on the measured photophysical properties of the molecule.[50]

1618 BODIPYs have been described and characterized in the crystallographic solid state and lodged with the Cambridge Crystallographic Data Centre (CCDC), a repository which catalogues this information. Among the most popular sub-classes of studied materials are the variously substituted *meso*-phenyl (1031 examples) 1,3,5,7-tetramethyl (776 examples) and aza-BODIPYs (i.e. 4,4-difluoro-3a,4a,8-triaza-4-bora-*s*-indacene, 80 examples. Examples of crystal structures of (*meso*-Ar) BODIPY compounds with Ar being an *N*-heterocycle include Ar = pyridine, quinoline, pyrimidine, phenanthroline among many others.[51,52] No obvious structural differences in the BODIPY core are apparent from the inclusion of different aryl or aromatic units. Inclusion of quaternary *N*-containing heterocycles in this position is rare, with only a few examples reported, and significant differences from the photophysical properties of the parent, neutral compounds owing to differences in the extent of the aromatic unit. These heterocycles can provide one half of a 'push-pull' architecture.[53] The structural characteristics of BODIPY compounds have been previously described by a combination of bond distances, plane-to-plane angles, as well as displacements from

mean planes. Compounds' photophysical attributes are similarly responsive to atom substitutions and ionic charges, aromaticity, and functional group, as well as induced intermolecular interactions and solvatochromic effects. While the structural minutiae may be observed in the solid-state, this observation is generally only of one conformational energetic minima of the electronic ground state; intuition is required to extrapolate from an individual snapshot.

X-ray crystallography of representative compounds allows for insight into the internal bonding, conformational shape, and molecular packing of compounds. Generally, crystals of these compounds were grown by slow evaporation of methanol or dichloromethane solution as described in the experimental section. The structure solution in each case corresponded to the indicated compound, in agreement with spectroscopic results.

Each of the molecules discussed here features the 1,3,5,7-tetramethyl substitution pattern on the BODIPY core; this should negatively influence the ability of the compound to approach coplanarity with the aryl ring or to delocalize the aryl charge to the BODIPY component. Thus, we expected the influence on the BODIPY core of different nitrogen-containing heterocycles, and therefore photophysical changes within this subset, to be minimal. Nonetheless, the influence of charge will dramatically influence solubility and likely solvatochromic effects.

4.5.2.2. *meso*-Aryl BODIPY derivatives

The single crystal X-ray crystallographic studies of compounds were kindly performed by Dr. Christopher J. Kingsbury. Compounds reported herein are shown in Figures 4.7-4.9 and Table 8, with selected structural data listed in Table 4.4. The N-heterocyclic group at the *meso*-position in each example is one of 4-pyridyl, 2-quinolinyl, 4-quinolinyl, 1-methyl-2-imidazolyl, 2-thiazolyl, 5-pyrimidinyl or 9-acridinyl, and the BODIPY substitution pattern is 1,3,5,7-tetramethyl (denoted Me_4) (**4.47**, **4.49**, **4.50** and **4.52**) , 2,6-diethyl-1,3,5,7-tetramethyl (Et_2Me_4) (**4.55**, **4.56**, **4.57**, **4.59** and **4.60**) or 2-Iodo-1,3,5,7-tetramethyl (Me_4I) (**4.49a**). In each case, the crystal structure acts as verification of the structural assignment, in agreement with NMR. Beyond using these structural determinations for the assignment of structure, we can investigate the conformational nature of the individual BODIPY components using symmetry coordinates. This methodology is intended to provide a single, simple value for

distortion, replacing intricate internal coordinate tables (*e.g.* for 8-(2-thienyl)BODIPY.[57]

Table 4.4. Compound formulae for the crystal structure determinations of neutral *N*-heterocyclic BODIPYs presented in this section.

BODIPY Derivative	*meso*-position	BODIPY sub.	Aryl rotation (°)
BODIPY 4.47	5-pyrimidine	Me_4	75.231(11)
BODIPY 4.49	2-quinoline	Me_4	73.84(5)
BODIPY 4.50	9-acridine	Me_4	77.41(3) 77.85(3)
BODIPY 4.52	2-methylimidazole	Me_4	83.34(6)
BODIPY 4.55	5-pyrimidine	Et_2Me_4	72.85(6)
BODIPY 4.56	4-quinoline	Et_2Me_4	79.102(19)
BODIPY 4.57	2-quinoline	Et_2Me_4	76.17(9)
BODIPY 4.59	2-thiazole	Et_2Me_4	82.38(7)
BODIPY 4.60	2-methylimidazole	Et_2Me_4	88.846 (16)
BODIPY 4.49a	2-quinoline	Me_4I	85.99(9)
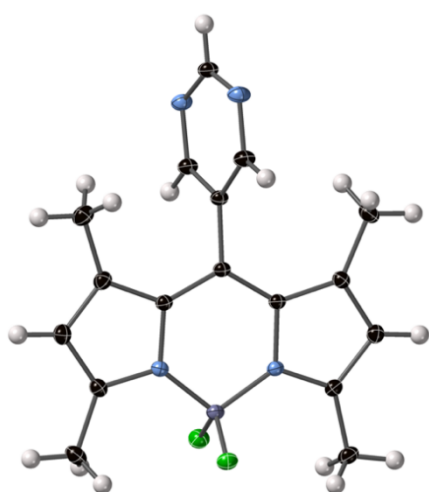
BODIPY **4.47**
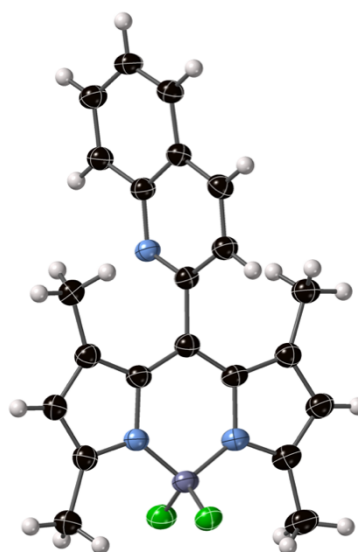
BODIPY **4.49**
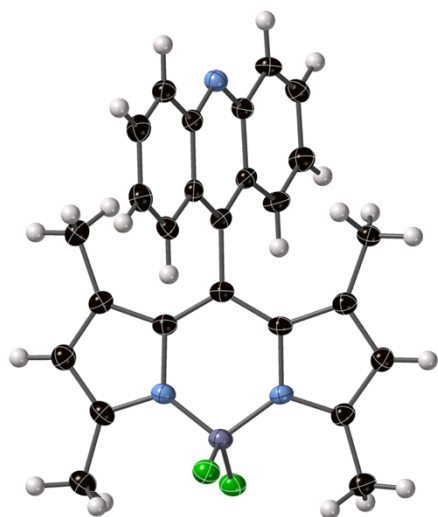
BODIPY **4.50**
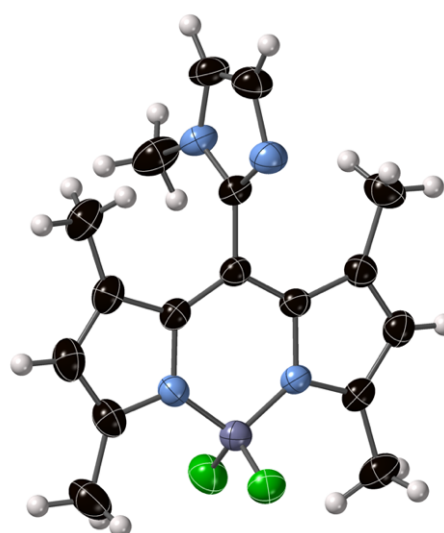
BODIPY **4.52**

Figure 4.7. View of the molecular structures of the BODIPYs **4.47**, **4.49**, **4.50** and **4.52** in the crystals. Thermal ellipsoids are plotted at 50%, H-atoms are represented as spheres of fixed radius.

BODIPY **4.55**

BODIPY **4.56**

BODIPY **4.57**
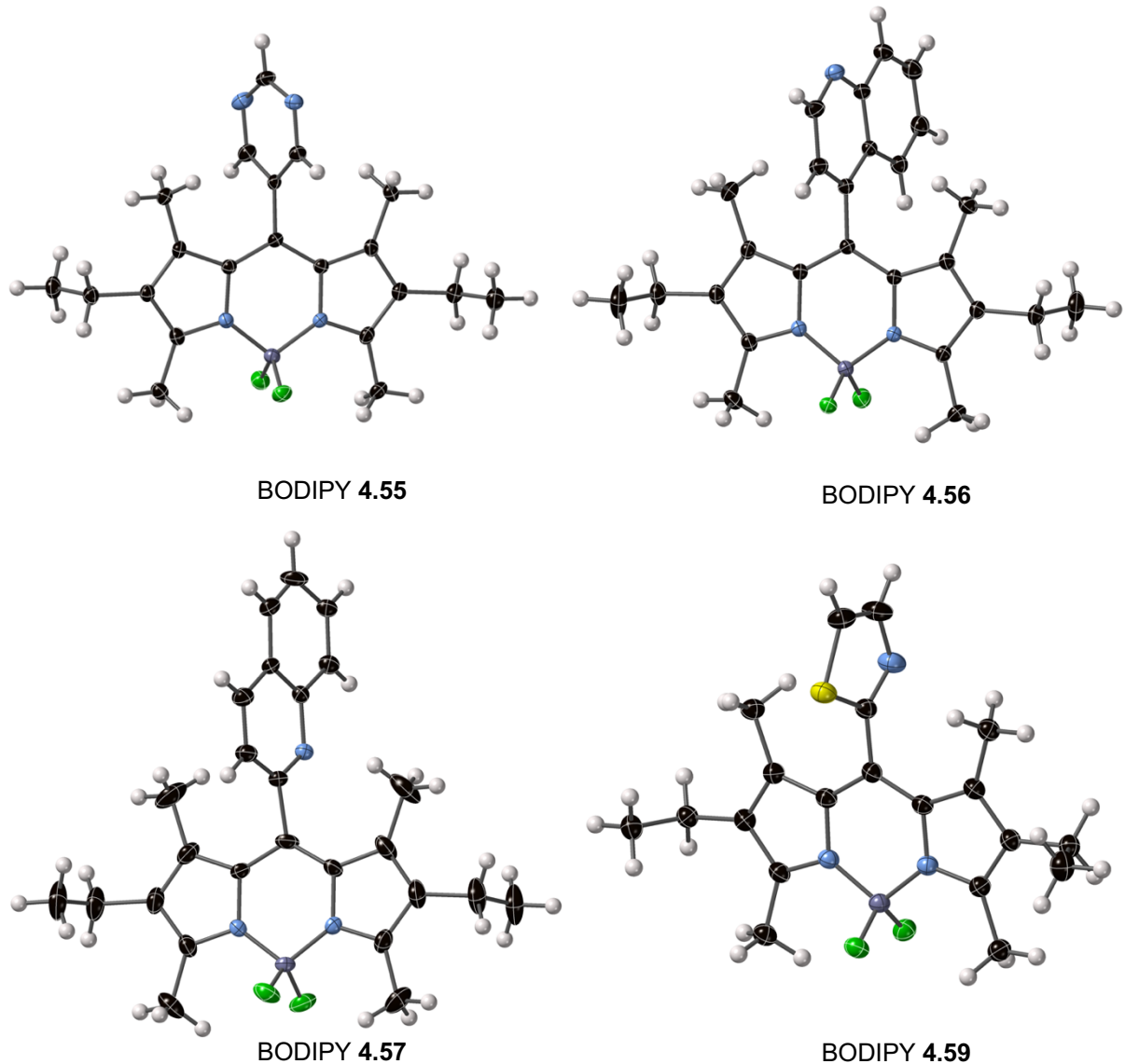
BODIPY **4.59**

Figure 4.8. View of the molecular structures of the BODIPY.**4.55**, **4.56**, **4.57** and **4.59** in the crystals. Thermal ellipsoids are plotted at 50%, H-atoms are represented as spheres of fixed radius.

BODIPY **4.60**   BODIPY **4.49a**
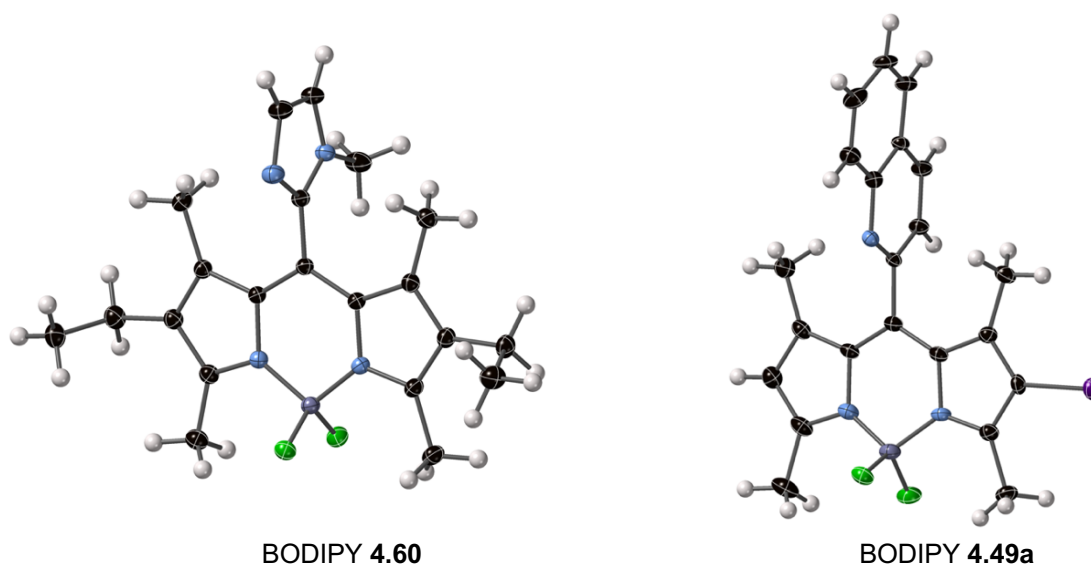
Figure 4.9. View of the molecular structures of the BODIPYs **4.60** and **4.49a** in the crystals. Thermal ellipsoids are plotted at 50%, H-atoms are represented as spheres of fixed radius.

Structural characterization of these derivatives generally shows that the influence of the 8-position group (i.e., phenyl-for-*N*-heterocycle substitution) is generally negligible when comparing external coordinate magnitudes, and therefore individual molecular structures, but has a significant structural effect on the formation of intermolecular accretion patterns. The clearest example is the crystal structures of the 5-pyrimidinyl-BODIPYs (**4.47** and **4.55**), which offer fascinating intermolecular interactions shown in Figure 31. Owing to the presence of activated C-H···X donors and N-acceptors on the pyrimidinyl ring, BODIPY **4.47** shows a one-dimensional pseudohexagonal lattice, shown in Figure 4.10(a). BODIPY **4.55**, with additional ethyl groups demonstrates a related zig-zag arrangement, shown in Figure 4.10(b).

(a)

BODIPY **4.47**

(b)

BODIPY **4.55**
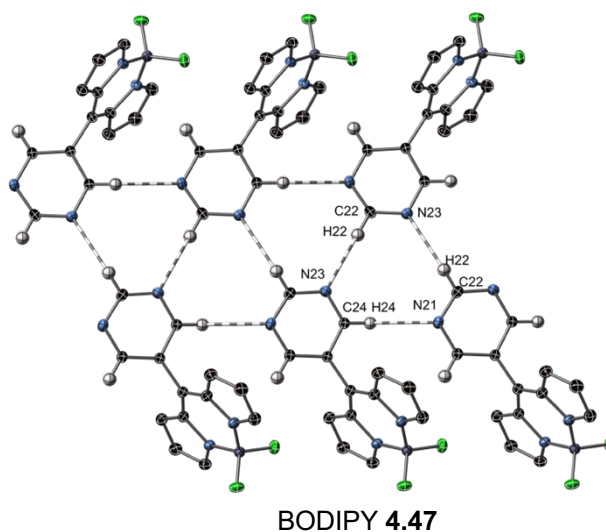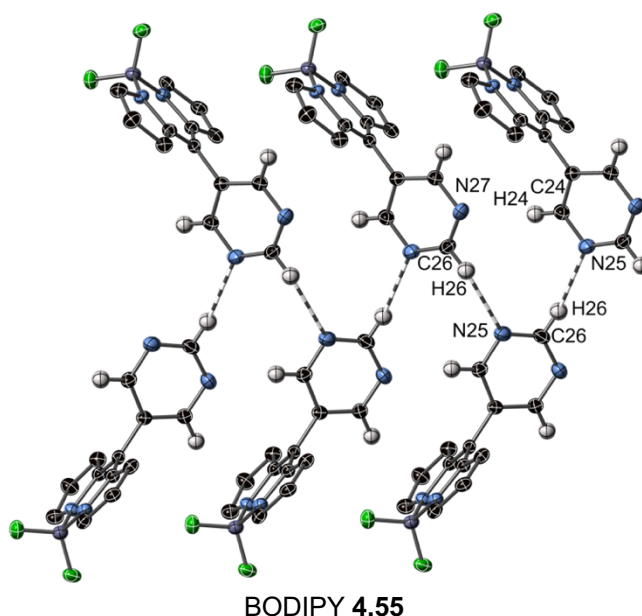
Figure 4.10. Intermolecular C-H⋯N interactions engaged by BODIPYs **4.47**(a) (C24⋯N21 3.42 Å, C22⋯N23 3.46 Å) and **4.55**(b) (C26⋯N25 3.43 Å). Methyl and ethyl groups on the BODIPY core are omitted.

Generally, the introduction of the N-heterocycle H or X- bond acceptor motif (formally a nitrogen with lone pair, *e.g.,* pyridine, 2- and 4-quinoline, acridine, pyrimidine) in these compounds demonstrates at least one non-negligible intermolecular interaction (e.g., C-H⋯N) around the van der Waals limit, similar to many aromatics.[58] This, however, is usually confounded with the C-H⋯F interactions in which these molecules are engaged. An example of these interactions is shown in Figure 4.11, for BODIPY **4.50**.
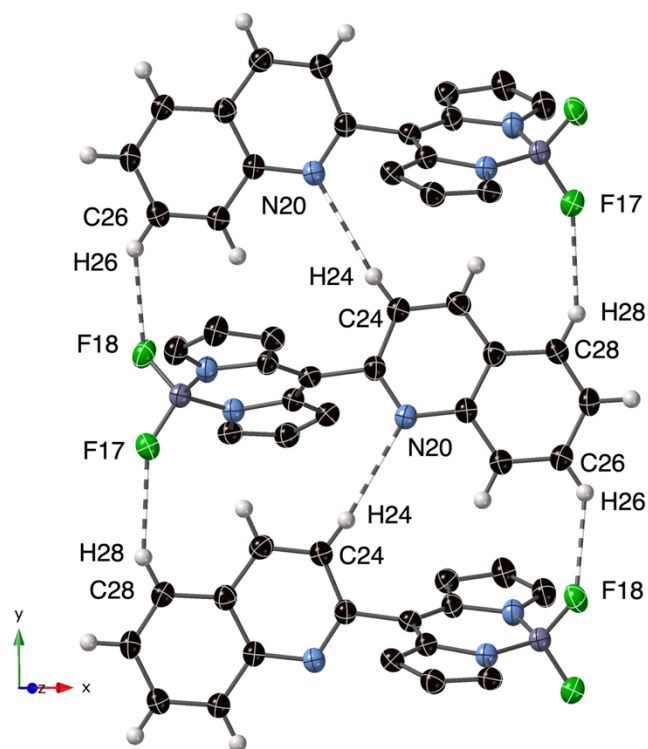
Figure 4.11. C-H···N and C-H···F "weak" interactions engaged by BODIPY **4.50**, C28···F17 3.347 Å; C26···F18 3.267 Å; N20···C24 3.621 Å.

The aggregation of individual molecules in the solid state (i.e., thermodynamic equilibrium) can often give an idea as to the dominant preferred interactions of these molecules in solution state or on surfaces. The molecules depicted above do not form strong dimeric arrangements in the solid state, and therefore would be unlikely to do so in a good solvent.

4.5.2.3. Water-soluble compounds

The quaternarization of the dorsal *N*-heterocycle on the BODIPY was our means to provide a charged group for heightened antimicrobial response. The introduction of charge has additional effects in the structural chemistry of these compounds, providing a charge separation, with additional anions to consider alongside the bond-order effects of pyridinium-based compounds.[59]

The structures of five compounds, each with a quaternary N-heterocycle on the 8-position of a BODIPY, are presented in Figures 4.12-4.14. Two of the substitution approaches used were able to be characterized as crystalline products; those employing

a simple uncharged methyl (**4.48a**) or 4-phenoxybutyl group (**4.54c**) with an appropriate counter-ion, and those introducing a zwitterionic motif (4-carboxybenzyl) (**4.48b**, **4.54b** and **4.56b**) as the acid halide. The two dominant BODIPY motifs described in this manuscript (1,3,5,7-tetramethyl- and 2,6-diethyl-1,3,5,7-tetramethyl) are both represented.

BODIPY **4.48a**   BODIPY **4.54c**
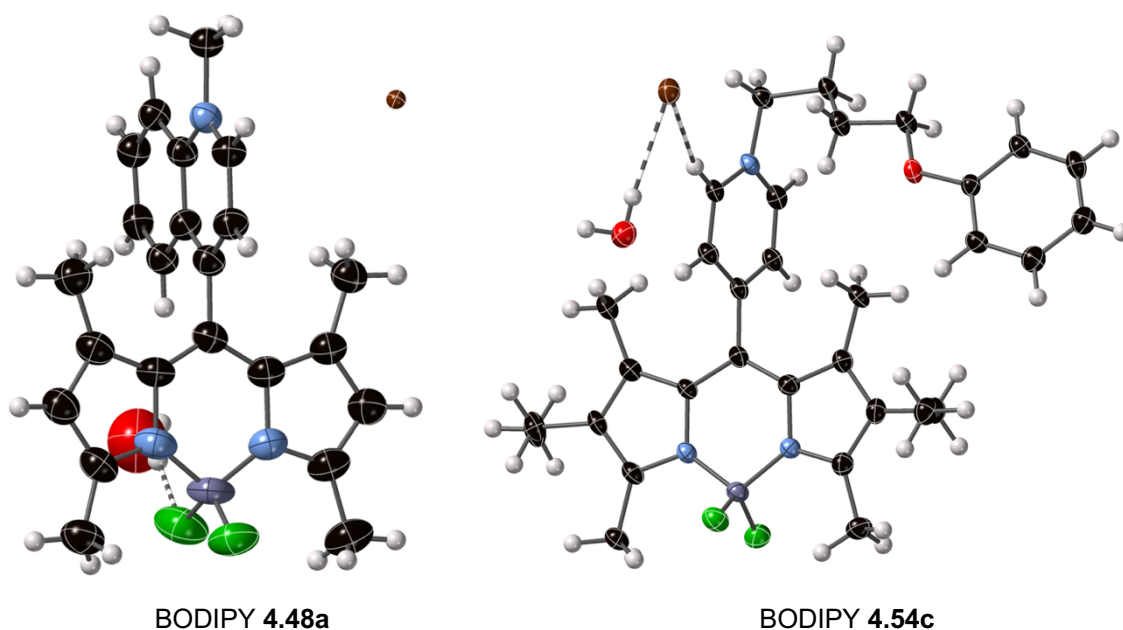
Figure 4.12. View of the molecular structures of the BODIPYs **4.48a** and **4.54c** in the crystals. Thermal ellipsoids are plotted at 50%, H-atoms are represented as spheres of fixed radius.

BODIPY **4.54b**   BODIPY **4.56b**
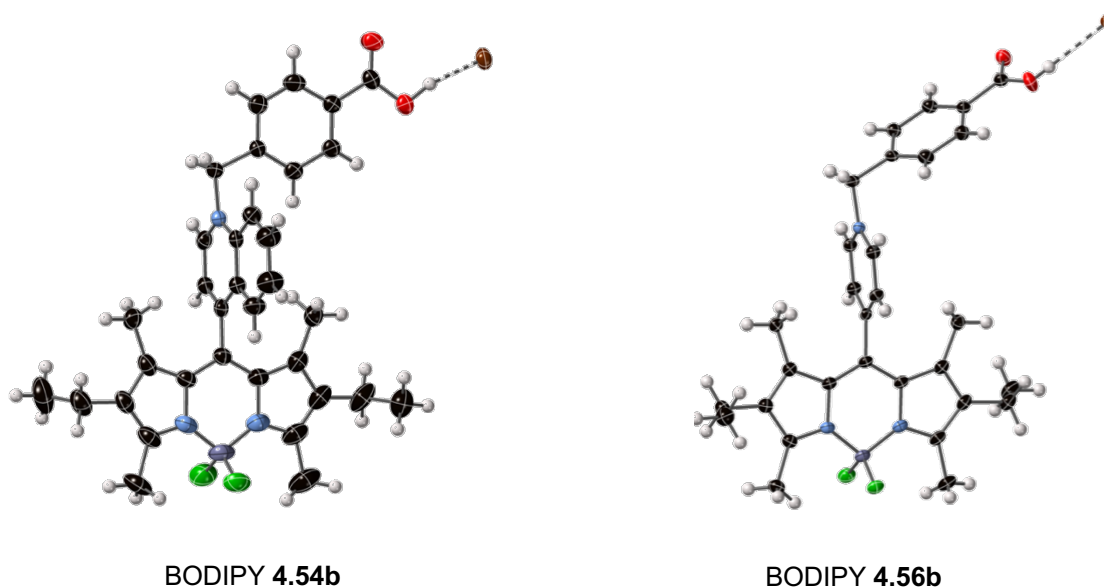
Figure 4.13. View of the molecular structures of the BODIPYs **4.54b** and **4.56b**. Thermal ellipsoids are plotted at 50%, H-atoms are represented as spheres of fixed radius.
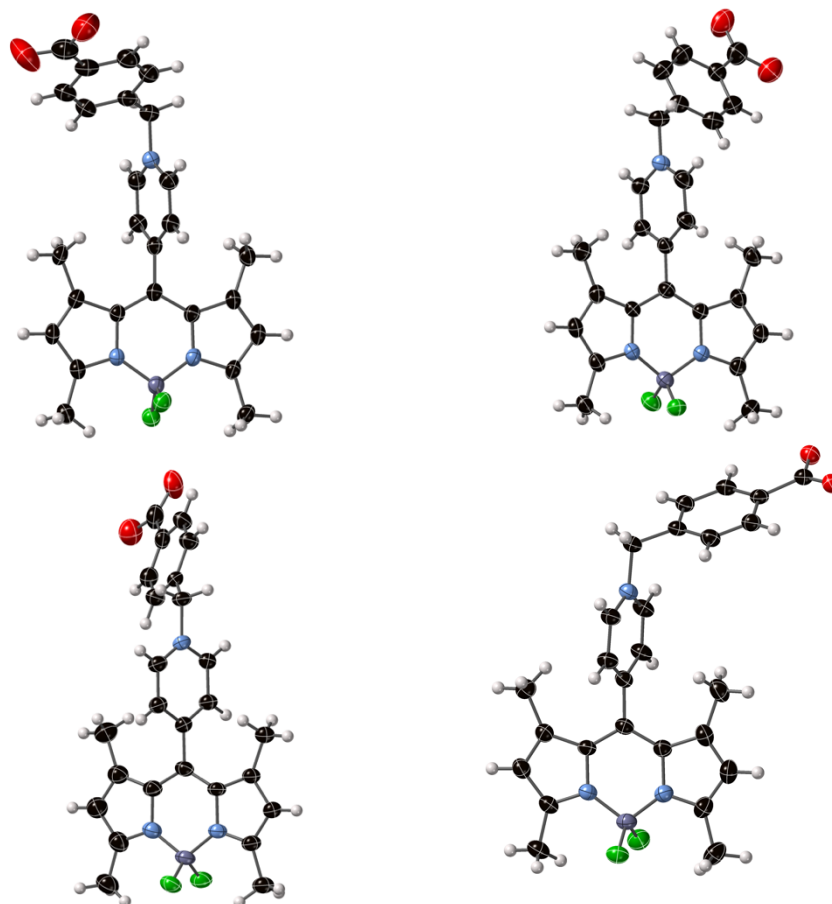
Figure 4.14. The four inequivalent molecules in the structure of BODIPY **4.48b** due to disorder present in solution

The five compounds reported here each exhibit the expected BODIPY structure, with pyridyl and quinolinyl rings with similar plane-to-plane angles with the BODIPY system as in their neutral counterparts, as seen in Table 4.5. if the compound had any double-bond character, we would have seen shortening of the C-C distance and a movement towards coplanarity as compared to a neutral molecule; the slight lengthening of this bond and variable angle are indications that this behavior is not occurring.

Table 4.5. Plane-to-plane angles of the *meso*-substituent and BODIPY system and C-C bridgehead distances* in each of the cationic BODIPY compounds and their neutral counterparts.

BODIPY	Plane-Plane angle (°)	P/P for neutral comparison compound (°)	C-C bridge head (Å)	C-C in neutral (Å)	B-F (Å)
BODIPY 4.48a	84.96(9)	79.102(19)	1.496(10)	1.4899(15)	1.370(11) 1.410(11)
BODIPY 4.54c	79.51(13)	81.328	1.499(7)	1.483(5) (10.1039/C4CP03343D)	1.381(7) 1.395(8)
BODIPY 4.54b	85.656 (44)	79.102(19)	1.494(3)	1.4899(15)	1.395(3) 1.395(2)
BODIPY 4.56b	87.946(81)	81.328	1.496(6)	1.483(5) (10.1039/C4CP03343D)	1.386(8) 1.397(7)
BODIPY 4.48b (C1)	73.14(7)	81.328	1.482(4)	1.483(5)	1.380(4) 1.411(4)
BODIPY 4.48b (C35)	79.99(6)		1.483(3)		1.395(3) 1.398(3)
BODIPY 4.48b (C69)	75.71(5)		1.483(4)		1.390(3) 1.405(4)
BODIPY 4.48b (C103)	75.91(5)		1.490(4)		1.391(3) 1.402(3)

* The bond involves two inverted carbon atoms, whose hybrids point away from each other.

The B-F distances, with a mean value of 1.393 Å, are additionally affected by the environment of the fluorine atoms; there is a clear indicator that the values for these cationic compounds are statistically longer when compared to the distribution for all BODIPY compounds in the literature (1.387(17) Å) with $p = 0.03$ for a one-tailed t-test. Each of these molecules engages in significant 'weak' interactions, a catch-all term for hydrogen bonding, π-stacking and other associative interactions generally weaker than a coordinate bond. Interactions with solvate (e.g. 2.720(9) Å O⋯F and 161(18) ° O-H⋯F H-bond from water in compound 11) are comparatively strong; charge-assisted interactions between pyridinium C-H and Br⁻ counter-anion (e.g. C⋯Br, Figure 4.11 (**4.48a**)), and between protonated carboxylate and counter-anion (e.g., Figure 4.12 (**4.54b** and **4.56b**)) are observed.

4.5.2.4.   BODIPYs with extended π-conjugated systems

The single crystal X-ray crystallographic studies of the compounds in this section were kindly performed by Dr. Brenden Twamley. As described in the synthesis section, the formation of compounds with two BODIPY units introduces extended conjugation and hence the optical window of such compounds. The three compounds herein are intermediates in the synthesis of an exemplar dyad – with ethynyl units and with the butadiyne-bridged dimer structure. Molecular units of the two precursor BODIPYs **4.46f** and **4.46g** are shown in Figure 4.15; in each case, no additional solvent was included within the unit cell.

BODIPY **4.46f**   BODIPY **4.46g**
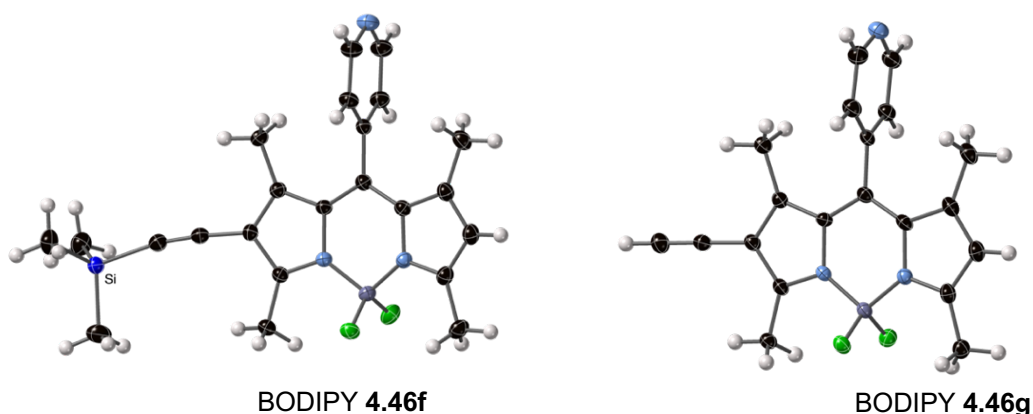
Figure 4.15. View of the molecular structures of the BODIPYs **46f** and **4.46g**. Thermal ellipsoids are plotted at 50%, H-atoms are represented as spheres of fixed radius.

For BODIPY **4.66**, as shown in Figure 4.16(a), the bridged structure contains the two BODIPY unit centroids separated by 13.33 Å; these units are bridged by a series of alternating longer and shorter bonded carbon atoms, at 1.411, 1.206, 1.369, 1.206 and 1.417 Å. The molecular structure has near-C_{2h} symmetry, with BODIPY units rotated at 179.18° to one another, plane to plane. Previous calculations of porphyrin unit rotation about a butadiyne linker indicate that a minimal (approx. 5.5 kJ/mol) rotational barrier is to be expected due to similar distances in the bridge.[61]

A selection of the intermolecular interactions engaged by this compound are demonstrated in Figure 4.16(a); each 4-pyridyl unit acts as both donor and acceptor to C-H···N interactions (3.33 Å (C15···N42) and 3.45 Å (C44···N17)). These interactions

form a three-dimensional hydrogen-mediated network; the three independent interpenetrating networks are indicated in Figure 4.16(b) in red, green, and blue.

(a)
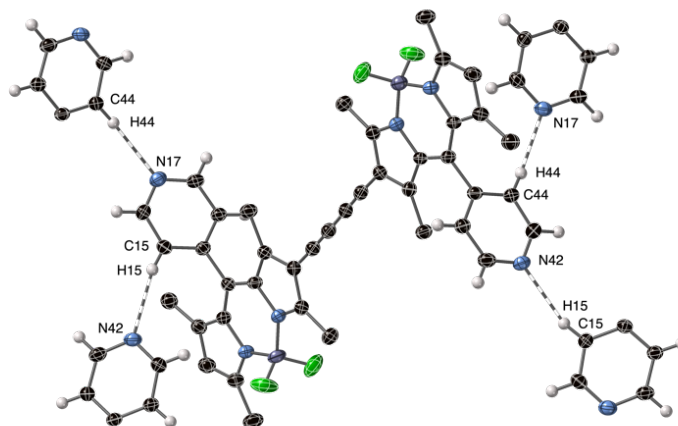
(b)
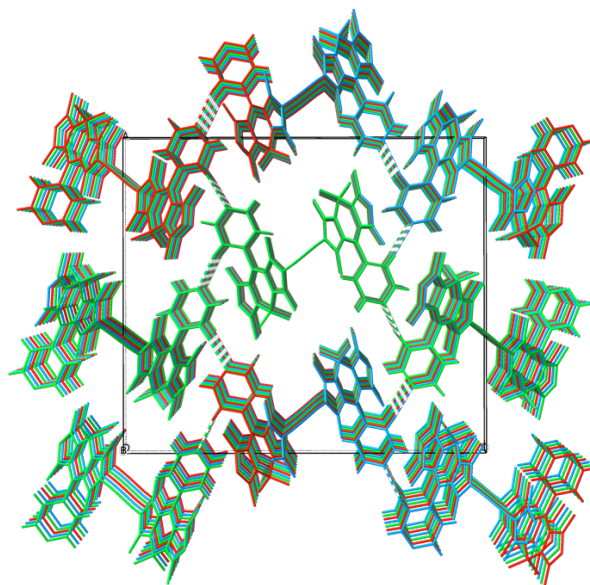
Figure 4.16. a) C-H⋯N interactions within the crystal structure of BODIPY **4.66**; b) these interactions form three, three-dimensional hydrogen-mediated networks in red, green, and blue.

4.5.2.5.   Non-BODIPY Structures

The single crystal X-ray crystallographic studies of compounds were kindly performed by Dr. Christopher J. Kingsbury. Two crystal structures were collected during this study which did not include the BODIPY motif and are described here. The formation of the 1,2,5,7-tetramethyl-2,6-diethyl-8-(2-thiazolyl)-4-bora-3a,4a-diaza-*s*-indacene (**4.52a**) resulted in a side-product which was visibly iridescent and crystalline upon evaporation

of the column fragment. The structure shows a tripyrrin-like arrangement of N-atoms and heterocycles – but with C-for-S replacement on the periphery. The structure of this compound is shown in Figure 4.17. This crystal consists entirely of the Z-Z-*cis-cis*-isomer, implying that the formation of the internal three-center H-bonding arrangement is a favorable conformational driver for this species. Investigating the potential N-to-S switchable metal coordination of this proligand is an interesting avenue for future research, potentially acting as a C-bridged-mimic of the activity of bis(2-thiazolylimino)isoindoline investigated as a potential ligand for catalysis.[62,63]
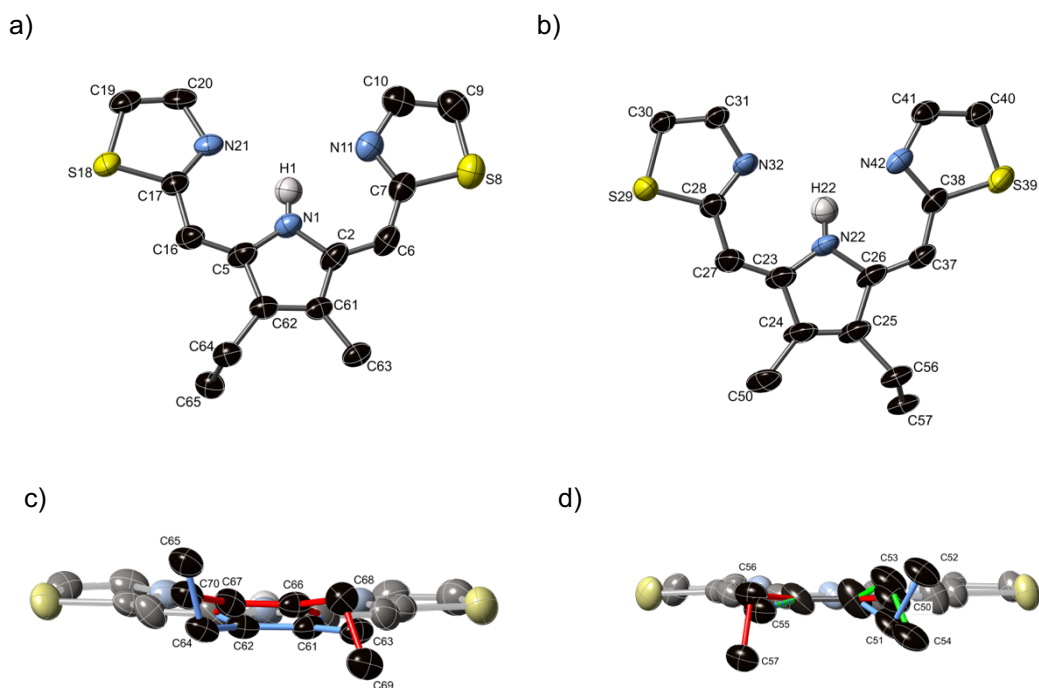
Figure 4.17. (a,b); Molecular structures of the dominant components of **4.52a**; (c,d) a side-on view of the molecules in **4.52a** (a and b) showing disorder of the methyl and ethyl groups on the pyrrole backbone in this crystal structure. H atoms are omitted, with non-H atom ellipsoids at 50%.

4.5.3.　　Spectroscopic investigations

The UV-vis spectroscopic properties of BODIPY dyes were investigated in dichloromethane and methanol (water-soluble BODIPY derivatives). The results are summarized in Table 4.6. There was little to no solvent effect observed in the absorption maxima wavelengths. The newly synthesized 2,4-dimethyl pyrrole derived *meso*-aryl BODIPYs (**4.46-4.53**) display absorptions between 508 nm and 520 nm and in between

533 nm and 547 nm for 3-ethyl 2,4-dimethyl derived *meso*-aryl BODIPYs (**4.54-4.60**) (Table 4.6). The main point of differentiation of the BODIPY dyes is with different substitution patterns on the pyrrole units. The 1,3,5,7-tetramethyl substituted BODIPY and 2,6-diethyl-1,3,5,7-tetramethyl substituted BODIPY derivative are differentiated by a red shift of 20-25 nm on introduction of the ethyl groups. For comparison, 5-pyrimidylBODIPY derivatives (**4.47**) (1,3,5,7-tetramethyl) and (**4.55**) (2,6-diethyl-1,3,5,7-tetramethyl-) substitutions as shown in Figure 4.18, with a λ_{max} shift of 24 nm for the later. The UV-vis absorption spectra for water-soluble derivatives does not show any significant change of absorption maxima from the parent *meso*-aryl-BODIPYs, implying that the core of BODIPY is unaffected by this process.

Table 4.6. Absorption spectral properties of *meso*-aryl BODIPYs **4.47-4.52** and **4.55-4.60** in DCM at room temperature.

BODIPY (2,4-dimethylpyrrole derivatives)	Absorption maxima (nm)	Extinction coefficient (ε) [x10^3 M^{-1} cm^{-1}]	BODIPY (3-ethyl-2,4-dimethylpyrrole derivatives)	Absorption maxima (nm)	Extinction coefficient (ε) [x10^3 M^{-1} cm^{-1}]
4.47	512	105.42	**4.55**	536	76.05
4.48	508	87.61	**4.56**	534	92.52
4.49	508	86.52	**4.57**	533	84.3
4.50	511	98.28	**4.58**	537	108.96
4.51	520	59.73	**4.59**	547	54.73
4.52	519	46.15	**4.60**	545	46.7
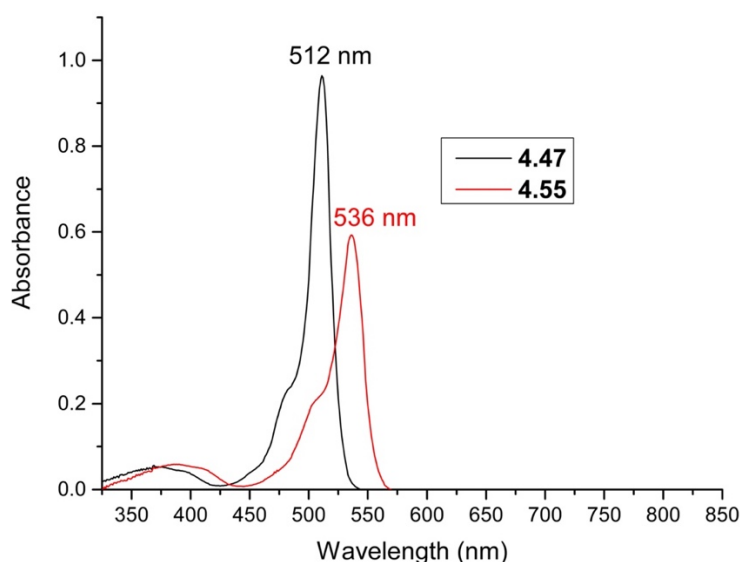
Figure 4.18. UV-vis absorption (nm) for BODIPY derivative **4.47** (1,3,5,7-tetramethyl derivative) and **4.55** (2,6-diethyl-1,3,5,7-tetramethyl derivative) in DCM.

The position of the absorption maximum was sensitive to the substituents in the 2-position as illustrated in Table 4.7.

Table 4.7. Absorption spectral properties of 2-position (iodine (**4.49a** and **4.51a**), TMS (**4.46f**), TMS deprotected (**4.46g**) and π-conjugated (**4.66**)) substituted derivatives in DCM at room temperature.

BODIPY	Absorption maxima (nm)	Extinction coefficient (ε) [x10^3 M^{-1} cm^{-1}]
4.49a	523	79.5
4.51a	551	37.56
4.46f	535	73.01
4.46g	526	16.76
4.66	559	82.05

The attachment of a bromo or iodo substituent is known to induce a significant red shift of absorption maxima of between 25 and 30 nm, respectively, due to electrostatic (withdrawing) contribution to the π-system of the BODIPY core (Table 4.7).[40] Similar functionalization of 2-position of BODIPYs **4.49a** and **4.51a**, caused a bathochromic shift in absorption as expected, into the orange/red spectral region as compared to their parent BODIPY (**4.49** and **4.51**) An example of this change is illustrated in Figure 4.19 where the UV-absorption maximum for derivative **4.51a** is red-shifted by 31 nm as

compared to the parent BODIPY **4.51**. The 2-position TMS-functionalized and TMS-deprotected derivatives also show a similar shift as the iodinated parent BODIPY in absorption spectra due to ligand-based π−π* transitions.[40] The UV-vis evaluation of TMS deprotected derivative **4.46g** when compared with coupled derivative **4.66** shows a shift in absorption maxima of 33 nm (Table 4.7), as expected for the increased conjugation across the butadiyne bridge as shown in Figure 4.20. This wavelength shift increases the therapeutic window of such derivative to be utilized in aPDT, should the solubility issues be able to be overcome.
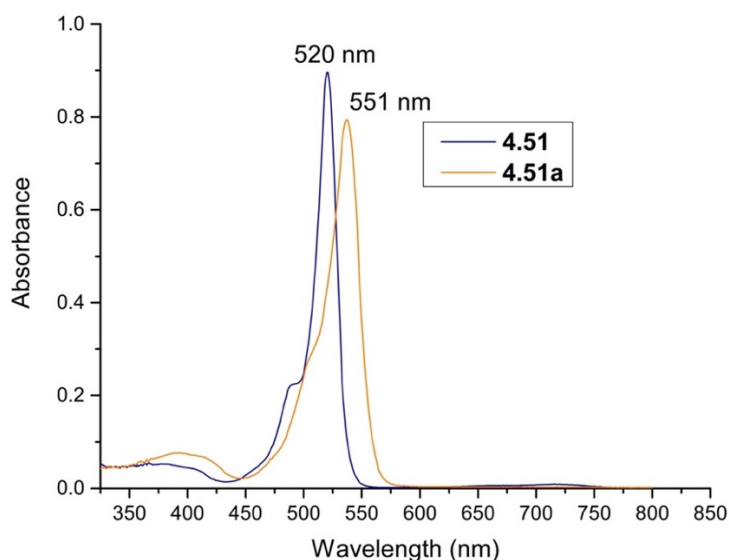
Figure 4.19. UV-vis absorption (nm) for BODIPY derivative **4.51** (Parent BODIPY) and **4.51a** (Iodinated derivative) in DCM.
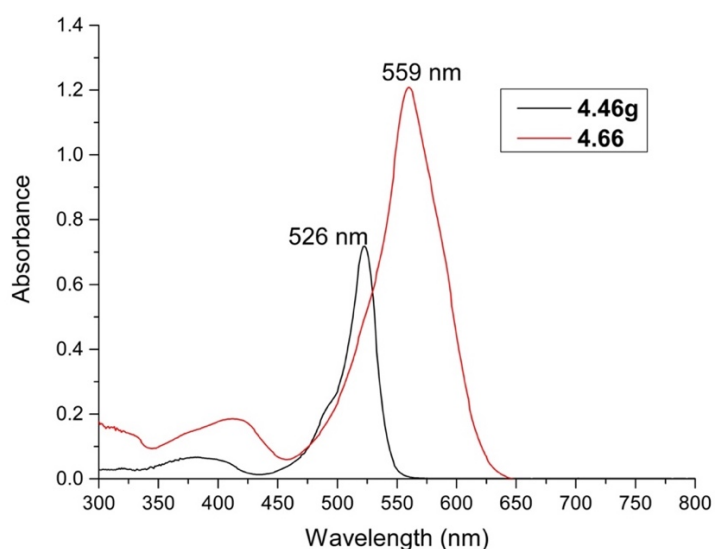
Figure 4.20. UV-vis absorption (nm) for BODIPY derivative **4.46g** (Parent BODIPY) and **4.66** (conjugated derivative) in DCM.

4.5.4. Singlet Oxygen Generation Studies

In chapter 3 we explained how important it is to evaluate the singlet oxygen production of our PSs to get an insight to the activity of these molecules for real world aPDT. Synthesized and post-functionalized BODIPYs were tested for production of singlet oxygen species using standard DPBF assay, like that used in Chapter 3. Each photosensitizer was referenced to an equivalent concentration of Rose Bengal (RB) (Φ_Δ = 0.76) (UV absorbance, RB (0.15 mM) in DCM).[64] (Figure 4.21).
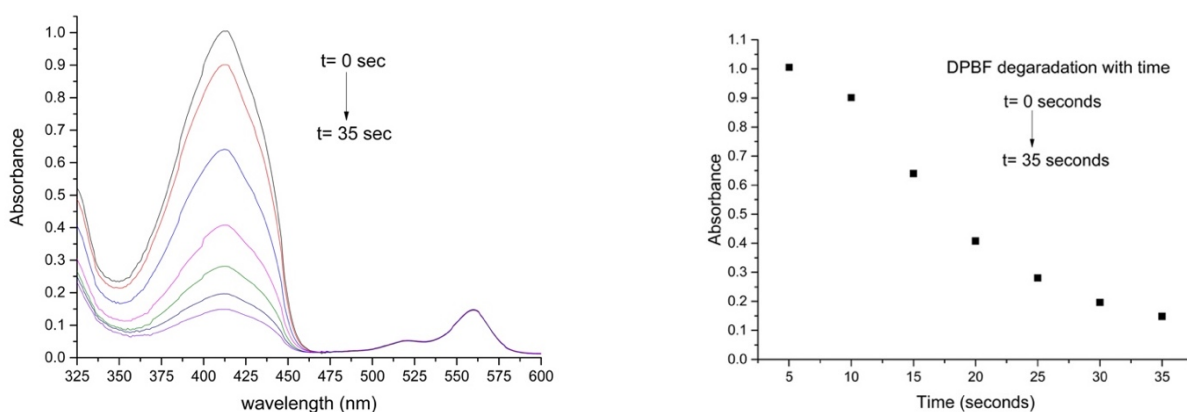
Figure 4.21. a) UV-Vis spectra of DPBF degradation of Rose Bengal (RB) (reference) and (b) DPBF consumption via RB measured at 415 nm in DCM/MeOH.

Table 4.8. Relative singlet oxygen production of for *meso*-N-heterocycle substituted BODIPYs **4.46-4.53** (1,3,5,7-tetramethyl substituted) and **4.54-4.60** (2,6-diethyl 1,3,5,7-tetramethyl substituted) in DCM/MeOH (1:1) using RB, Φ_Δ =0.76 as a reference.

BODIPYs	Singlet oxygen quantum yield (Φ_Δ)	BODIPYs	Singlet oxygen quantum yield (Φ_Δ)
BODIPY 4.46	0.01	**BODIPY 4.54**	0.01
BODIPY 4.47	0.01	**BODIPY 4.55**	0.49
BODIPY 4.48	0.01	**BODIPY 4.56**	0.01
BODIPY 4.49	0.01	**BODIPY 4.57**	0.08
BODIPY 4.50	0.09	**BODIPY 4.58**	0.50
BODIPY 4.51	0.01	**BODIPY 4.59**	0.02
BODIPY 4.52	0.32	**BODIPY 4.60**	0.49

The UV-absorbance degradation graphs of *meso*-aryl derivatives of BODIPYs are illustrated in Figure 4.22 and 4.23 and Table 4.8.
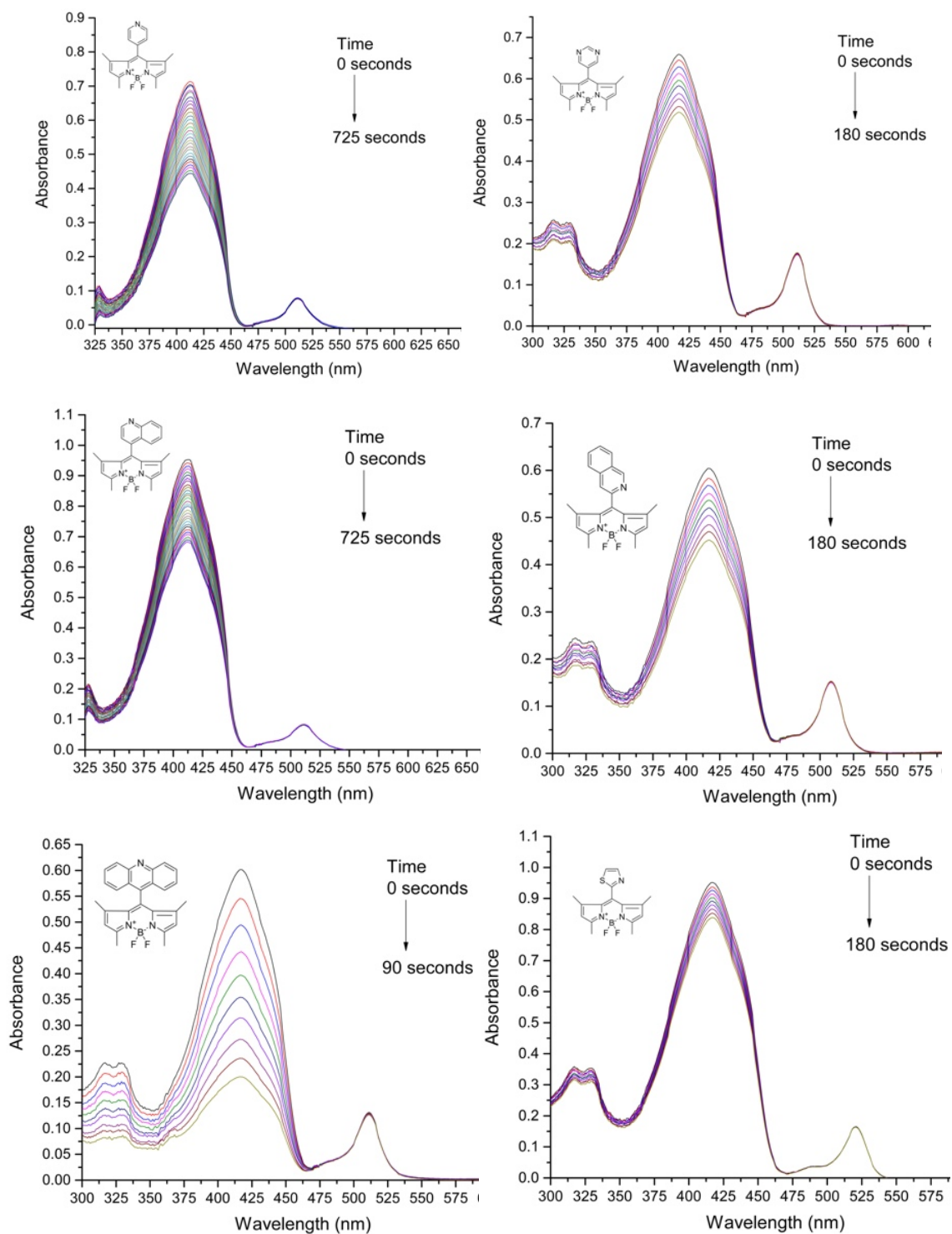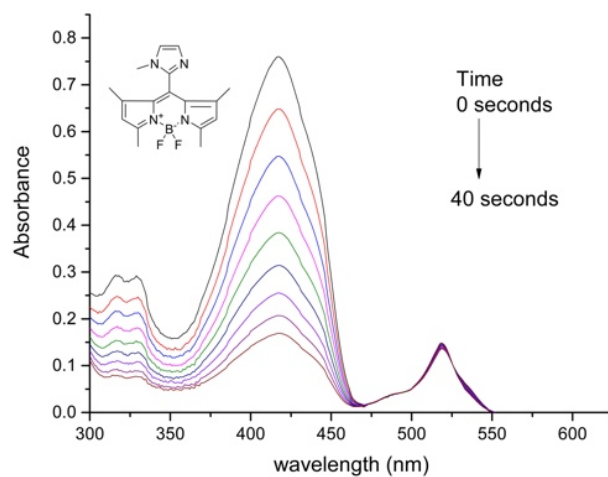
Figure 4.22. UV-vis DPBF consumption measured at 415 nm over time for *meso*-N-heterocycle substituted BODIPYs **4.46**-**4.53** (1,3,5,7-tetramethyl substituted) in DCM/MeOH.
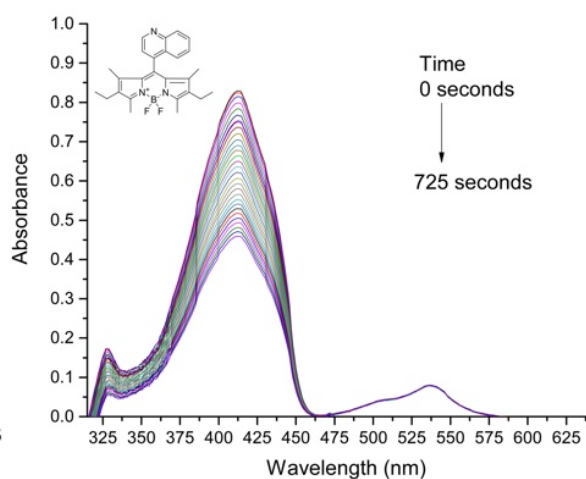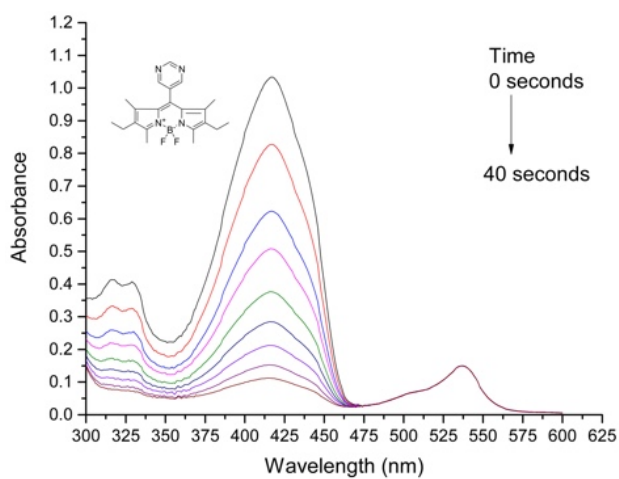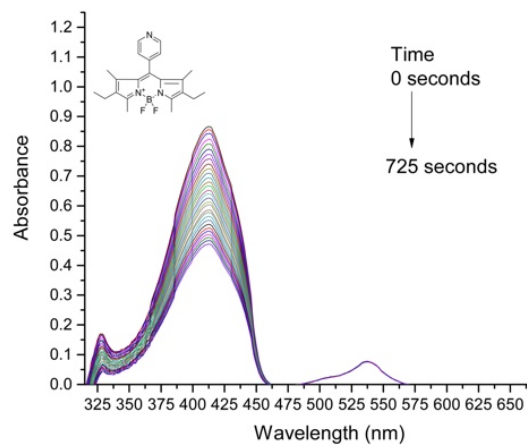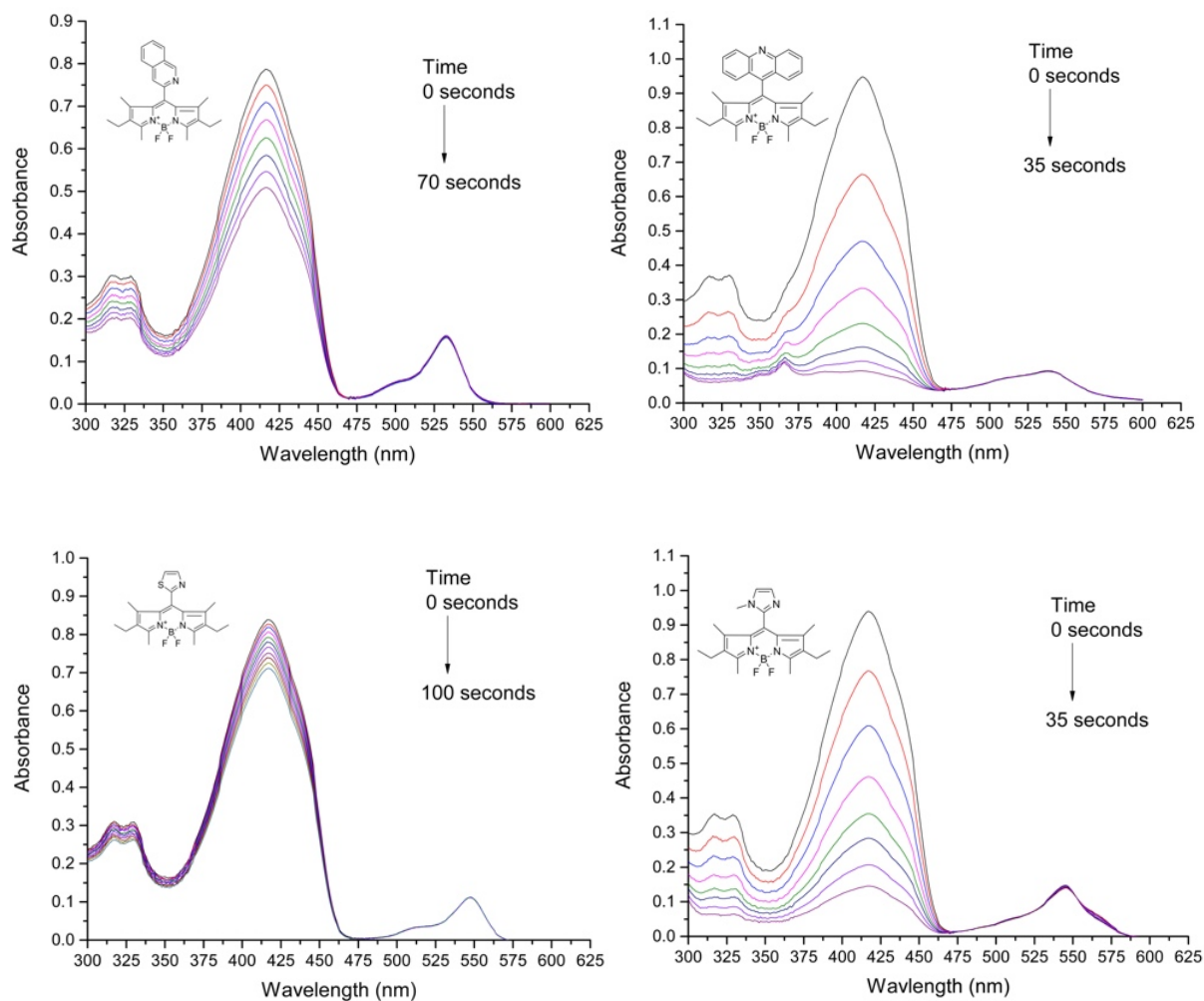
Figure 4.23. UV-vis DPBF consumption measured at 415 nm over time for *meso*-N-heterocycle substituted BODIPYs **4.54**-**4.60** (2,6-diethyl -1,3,5,7-tetramethyl substituted) in DCM/MeOH.

The compounds **4.52**, **4.55**, **4.58** and **4.60** are the most effective for $^1O_2$ generation with Φ_Δ= 0.32, 0.49, 0.50 and 0.49 respectively.
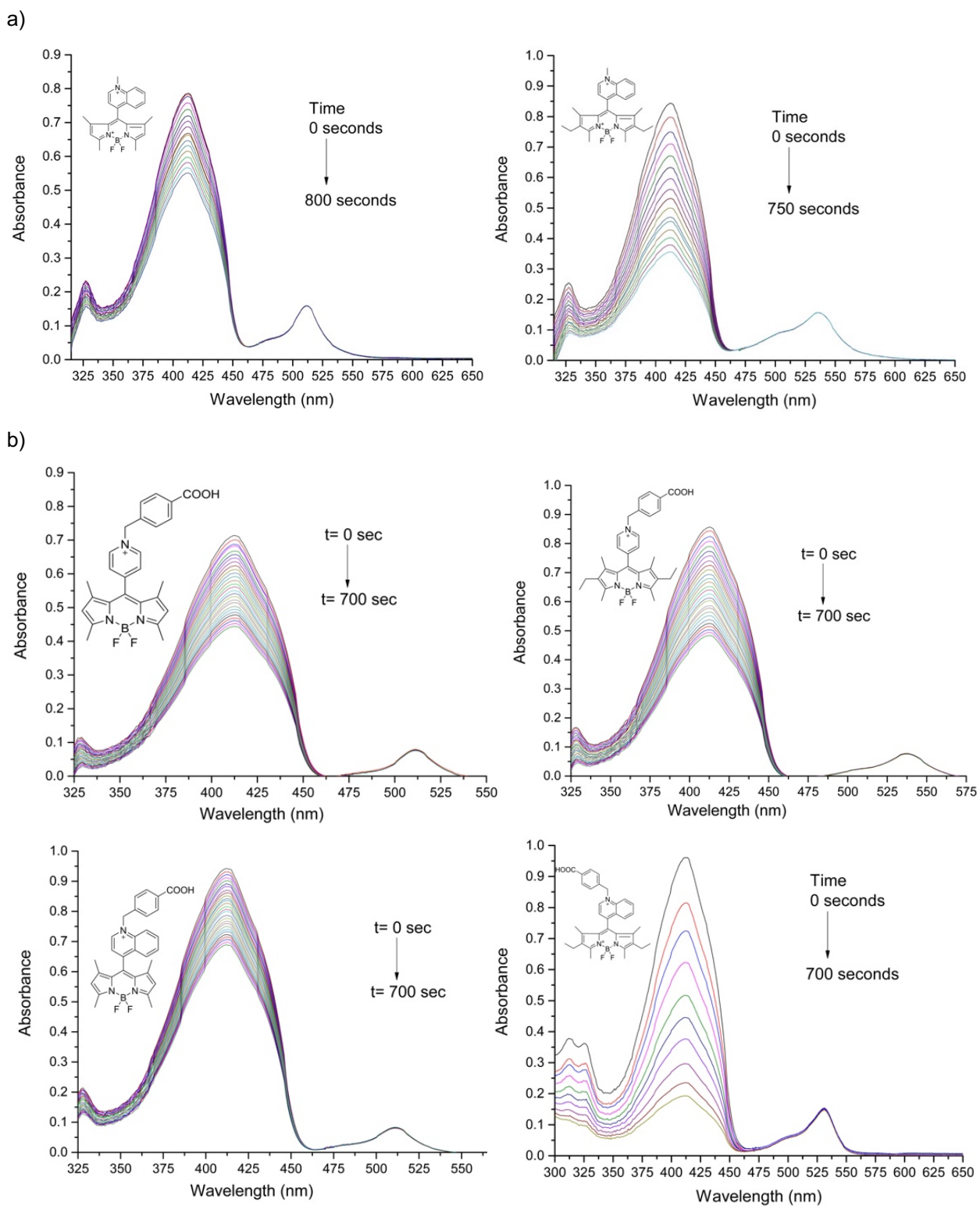
Figure 4.24. UV-vis DPBF consumption measured at 415 nm over time for charged water-soluble (a) methylated (**4.48a** and **4.56a**) (b) carboxylate derivatives (**4.46b**, **4.54b**, **4.48b** and **4.56b**) in DCM/MeOH.

Similar evaluations for a few charged water-soluble derivatives (methylates (Figure 4.24a) (**4.48a** and **4.56a**), carboxylates (Figure 4.24b) (**4.46b**, **4.54b**, **4.48b** and **4.56b**)

and etherates (**4.46c** and **4.54c**) (Figure 4.25)), boron-ethynyl functionalized precursor scaffolds (Figure 4.26) (**4.46d** and **4.50a**) and 2-position functionalized (iodine (**4.46e**, **4.49a**, **4.51a)** and TMS (**4.46f,4.51b**) derivatives (Figure 4.27) were performed and the results are illustrated in Table 4.9.
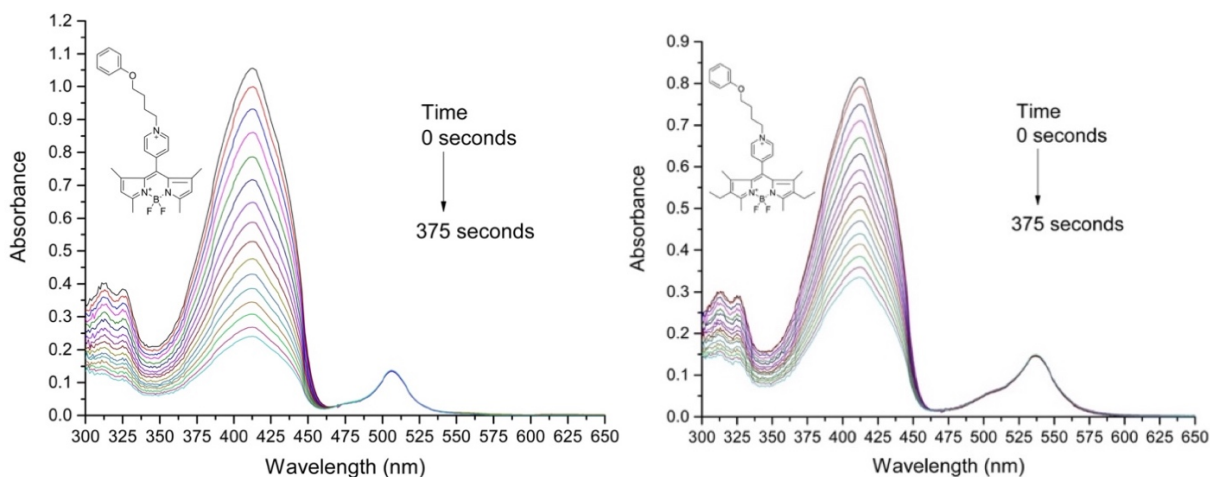
Figure 4.25. UV-vis DPBF consumption measured at 415 nm over time for charged water-soluble etherate derivatives (**4.46c** and **4.54c**) in DCM/MeOH.
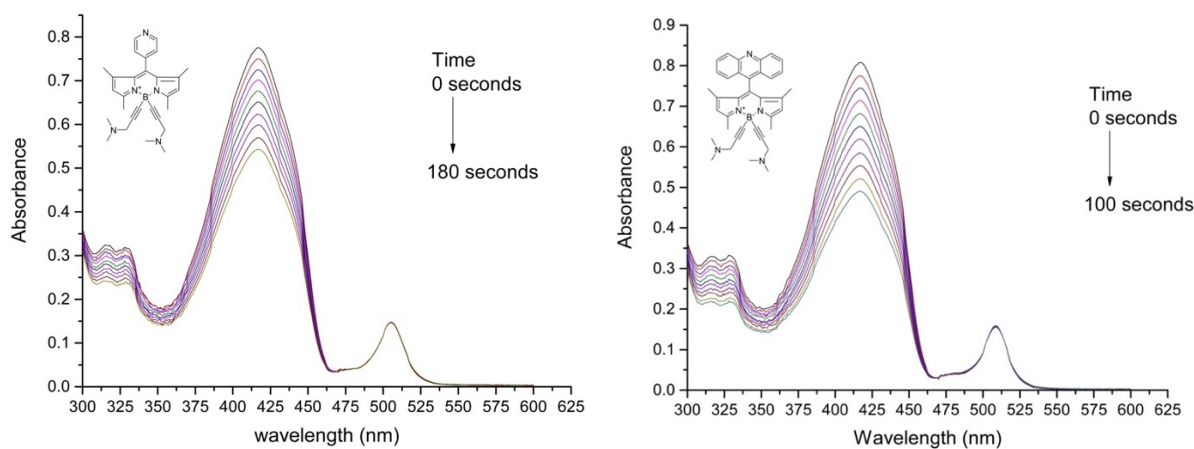
Figure 4.26. UV-vis DPBF consumption measured at 415 nm over time boron-ethynyl functionalized precursor scaffolds (**4.46d** and **4.50a**) in DCM/MeOH.

a)
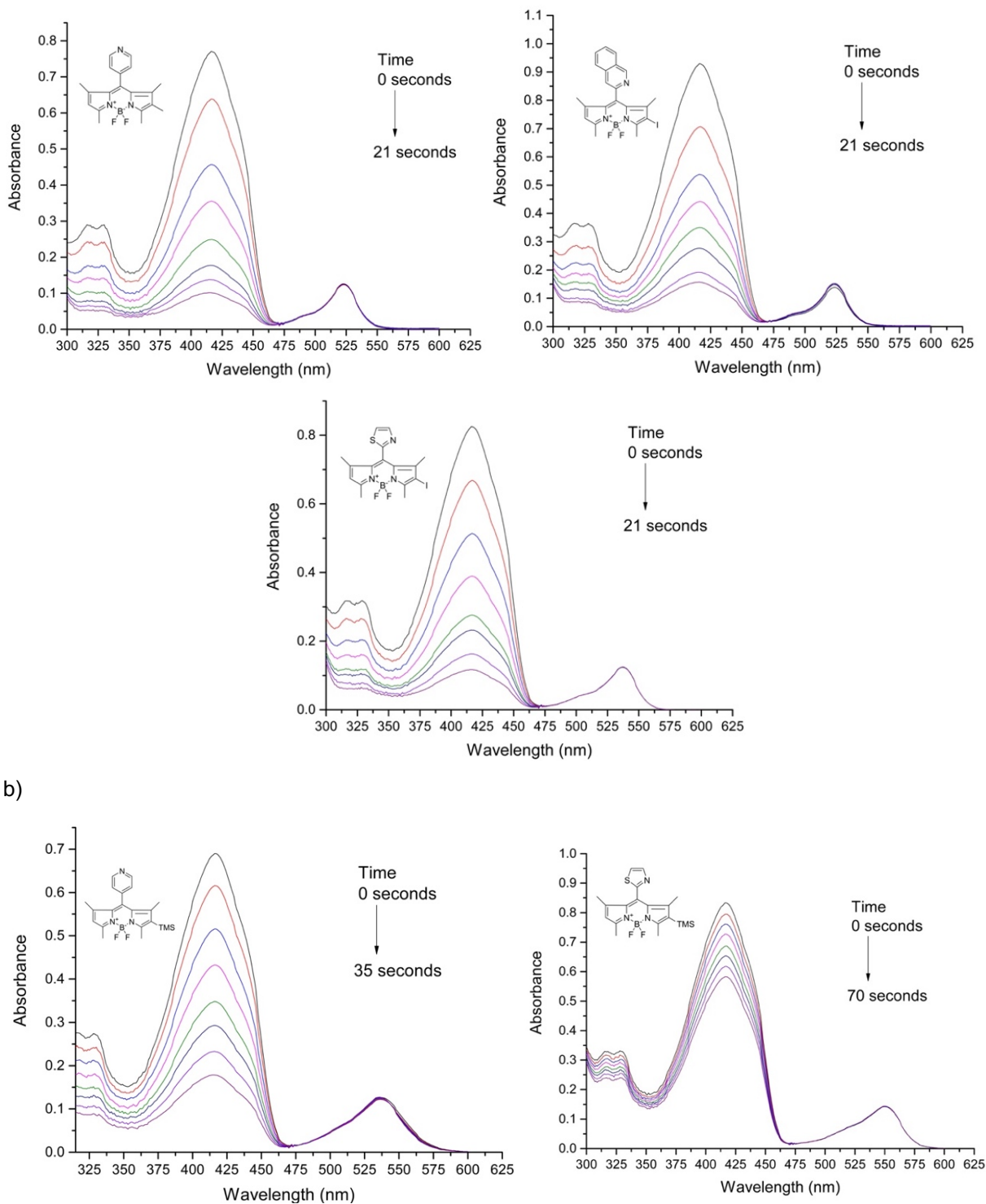
Figure 4.27. UV-vis DPBF consumption measured at 415 nm over time for (a) 2-position functionalized (iodine (**4.46e**, **4.49a**, **4.51a)** and (b) TMS (**4.46f,4.51b**) derivatives in DCM/MeOH.

Table 4.9. Relative singlet oxygen production of for water-soluble derivatives (methylates (**4.48a** and **4.56a**), carboxylates (**4.46b**, **4.54b**, **4.48b** and **4.56b**) and etherates (**4.46c** and **4.54c**)), boron-ethynyl functionalized (**4.46d** and **4.50a**) and 2-position functionalized (iodine (**4.46e**, **4.49a**, **4.51a**) and TMS (**4.46f,4.51b**) derivatives DCM/MeOH (1:1) using RB, Φ_Δ = 0.76 as a reference.

BODIPYs	Singlet oxygen quantum yield (Φ_Δ)	BODIPYs	Singlet oxygen quantum yield (Φ_Δ)
BODIPY 4.48a	0.01	BODIPY 4.46d	0.10
BODIPY 4.56a	0.01	BODIPY 4.50a	0.26
BODIPY 4.46b	0.01	BODIPY 4.46e	0.70
BODIPY 4.54b	0.01	BODIPY 4.49a	0.77
BODIPY 4.48b	0.01	BODIPY 4.51a	0.73
BODIPY 4.56b	0.01	BODIPY 4.46f	0.32
BODIPY 4.46c	0.05	BODIPY 4.51b	0.07
BODIPY 4.54c	0.03		

Singlet oxygen quantum yields ranged from 0.007 to 0.77 (shown in Table 4.8 and 4.9). *meso*-Aryl BODIPYs **4.52**, **4.55**, **4.58** and **4.60** have been identified to be moderate singlet oxygen generators (Φ_Δ = 0.5-0.3). Along with their key subcellular localization, such generation leads them to possess highly effective photosensitizer qualities.[65] Iodinated derivatives (**4.46e**, **4.49a** and **4.51a**) show high singlet oxygen quantum yields ($\sim\Phi_\Delta$ = 0.7) which is subsequently correlated to their inhibition efficiency as reported in next section.

4.5.5. *In-vitro* studies

4.5.5.1. Inhibition assays (MIC/MBC)

The inhibition assays of the compounds were performed with help of Ms. Charlotte Vernisse. Photo-induced antibacterial activity of synthesized BODIPY dyes were tested against two model organisms, the Gram-negative *P. aeruginosa* and the Gram-positive *S. aureus*, the minimal inhibitory concentration (MIC) and the minimal bactericidal concentration (PD-MBC) under light irradiation (25 J/cm²). The results (Tables 4.10 and 4.11) clearly indicate that different *meso* substituents of BODIPY dyes and difference in 2-6-subtitution impact the efficiency for aPDT. BODIPYs **4.47**, **4.53** and **4.55** display an efficiency at <50 µM (MIC/MBC) for inhibition of *S. aureus*. Iodinated derivatives (**4.46e**, **4.49a** and **4.53a**) as also display efficient inhibition at <100µM (MIC/MBC) of *S. aureus*. Derivative **4.53a** also inhibited the growth of *P. aeruginosa* at <100µM (MIC/MBC). These results could be explained with earlier arguments of induced heavy-atom effect of such derivatives which forms a long-lived, high-yield triplet excited state for an efficient singlet oxygen production, thus leading to an enhanced aPDT action of the dye. Water-soluble derivatives **4.48a** and **4.54c** displayed an exceptional inhibition *S. aureus* at <30µM (MIC/MBC), this could be due to charge aided interaction with the bacteria and enhancement in solubility across the bio-membranes of such PSs. Surprisingly derivatives **4.48a**, **4.56a** and **4.53a** also display dark toxicity assay which can be attributed to aggregation of these derivatives under the reaction conditions, hence these attributes need to be resolved to put in maximum output of such PSs against the microbes.

Table 4.10. Minimum inhibitory concentration (MIC) of BODIPYs tested against *S.aureus*

BODIPY derivatives	BODIPY	Minimum Inhibitory Concentration (µM)	
		S. aureus (Gram-positive)	
		Light conditions	Dark conditions
	BODIPY 4.46	41.7µM	>100µM
	BODIPY 4.47	16.7µM	>100µM
	BODIPY 4.48	16.7µM	>100µM
	BODIPY 4.49	>100µM	>100µM
	BODIPY 4.50	>100µM	>100µM
meso-Aryl BODIPYs	BODIPY 4.51	8.3µM	>100µM
	BODIPY 4.52	>100µM	>100µM
	BODIPY 4.53	3.1µM	>100µM
	BODIPY 4.54	25µM	>100µM
	BODIPY 4.55	8.3µM	>100µM
	BODIPY 4.56	>100µM	>100µM
	BODIPY 4.57	>100µM	>100µM
	BODIPY 4.58	>100µM	>100µM
	BODIPY 4.59	>100µM	>100µM
	BODIPY 4.60	>100µM	>100µM
	BODIPY 4.46a	>100µM	>100µM
	BODIPY 4.54a	83.3µM	>100µM
	BODIPY 4.48a	>100µM	>100µM
	BODIPY 4.56a	41.67µM	25µM
	BODIPY 4.46b	>100µM	>100µM
Water-soluble derivatives	BODIPY 4.54b	>100µM	>100µM
	BODIPY 4.48b	>100µM	>100µM
	BODIPY 4.56b	>100µM	>100µM
	BODIPY 4.46c	>100µM	>100µM
	BODIPY 4.54c	8.33µM	25µM
	BODIPY 4.46d	83.3µM	>100µM
	BODIPY 4.50a	100µM	>100µM
	BODIPY 4.46e	25µM	>100µM
Iodinated BODIPYs	BODIPY 4.49a	83.3µM	>100µM
	BODIPY 4.53a	1.5µM	>100µM
Pyridine dimer BODIPY	BODIPY 4.66	>100µM	>100µM

Table 4.11. Minimum inhibitory concentration (MIC) of BODIPYs tested against *P. aeruginosa*

BODIPY derivatives	BODIPY	Minimum Inhibitory Concentration (µM)	
		P. aeruginosa (Gram-negative)	
		Light	Dark
	BODIPY 4.48a	16.67µM	>100µM
	BODIPY 4.56a	6.67µM	>100µM
	BODIPY 4.46b	>100µM	>100µM
	BODIPY 4.54b	>100µM	>100µM
Water-soluble derivatives	BODIPY 4.48b	>100µM	>100µM
	BODIPY 4.56b	>100µM	>100µM
	BODIPY 4.46c	>100µM	>100µM
	BODIPY 4.54c	41.67µM	>100µM
	BODIPY 4.46d	>100µM	>100µM
	BODIPY 4.50a	>100µM	>100µM
Iodinated BODIPYs	BODIPY 4.49a	>100µM	>100µM
	BODIPY 4.53a	66.7µM	>100µM

4.5.5.2. Biofilm inhibition and eradication

Inhibition of the biofilm for BODIPYs **4.56b** and **4.54c** was tested against *S. aureus* and both the BODIPYs showed a decrease of biofilm growth under light illumination as shown in Figure 4.28 and 4.29, respectively.
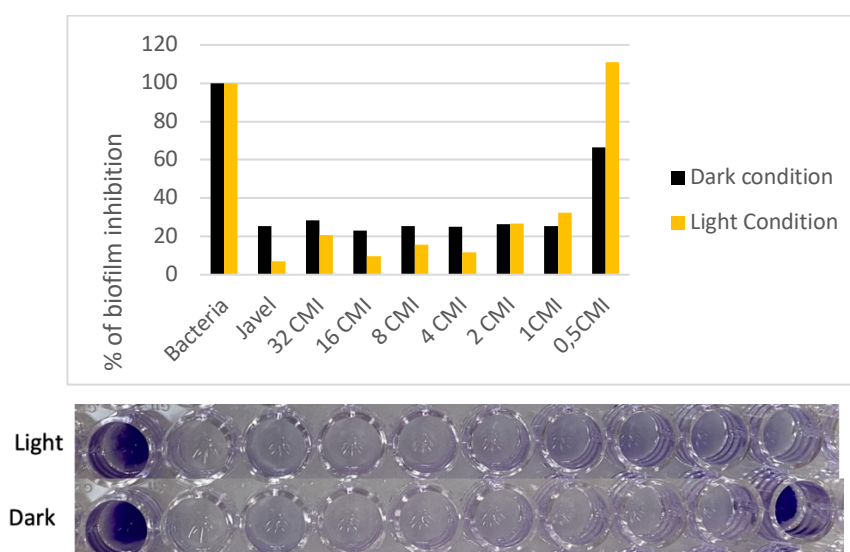
Figure 4.28. Percentage inhibition of the biofilm growth by BODIPY **4.56b** under dark and light conditions
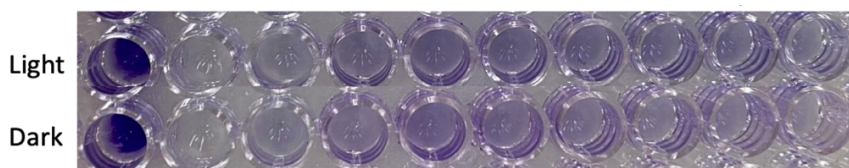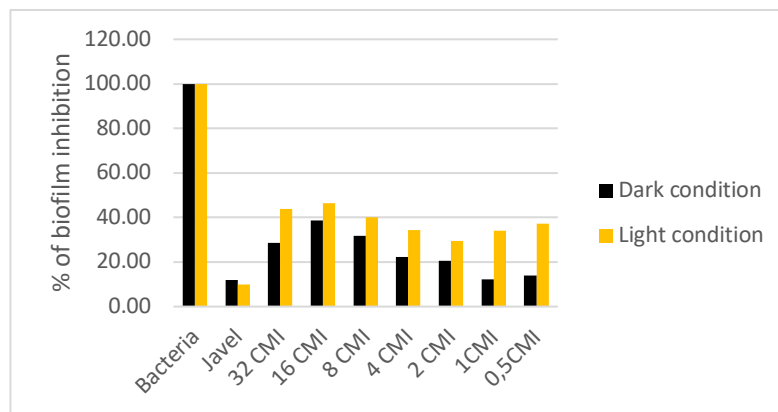
Figure 4.29. Percentage inhibition of the biofilm growth by BODIPY **4.54c** under dark and light conditions

The MIC was determined to be 41.72µM for BODIPY **4.56b** and 25µM for BODIPY **4.54c**. There was no eradication of the biofilms observed for derivatives **4.56b** and **4.54c**.

4.6. Conclusion and future perspectives

A very few examples of such a dynamic moiety, BODIPY dye has been reported in literature for their application in aPDT. With possibility of functionalizing the BODIPY on its core with different and specialized functional groups opens a window of utilization of these molecules against the microbes. To achieve this goal a series of photo-stable *meso*-aryl-BODIPYs and their derivatives bearing charged water-solubilizing groups, iodinated derivatives and conjugated dyes were synthesized in this chapter. These derivatives were synthesized with an aim to enhance the antimicrobial therapeutic window of BODIPY scaffold. Use of different synthetic and post-functionalization strategies gave a library of 31 novel BODIPYs. NMR characterizations and UV spectrometry of the synthesized BODIPY revealed the difference in resonance of corresponding protons and the shifts in absorption maxima corresponding to post-functionalization of the parent BODIPY core. With introduction of heavy atoms in the BODIPY core itself, the UV absorption maxima shifts to about 25-30 nm which is in agreement with literature reported derivatives and thus with this the optical window of these compounds expands against a wider strata of microbes and for treatment of deep tissue infections.[40] Similarly for the extended π-conjugated systems the shifts for absorption maxima correlates to literature reported compounds which on increase in conjugation undergo bathochromic shifts making their utilization for treatment of deep-seated infections more effective.[40] Different functionalization strategies and substitutions of BODIPY scaffolds affected the singlet oxygen production as measured via the DPBF degradation assays and the inhibition assays tested against the Gram-bacteria. Production of singlet oxygen species (Φ_Δ) with DPBF degradation assay showed good results for the BODIPY derivatives specially for 2-position nucleophilic iodide ion substitution which can be correlated with the enhanced ISC, a phenomenon correlating with introduction of the heavy atom in PSs.[40] Antimicrobial and biofilm inhibition assays of Gram-strains of bacteria revealed more details of efficacy of the scaffolds and these evaluations revealed that some of these post-functionalized and substituted scaffolds exhibit enhanced activities. These results can also be correlated to literature reported scaffolds where the post-functionalization strategies as described above with water-soluble groups and heavy atom introduction increases the efficacy of molecules against the microbes making these PSs an ideal candidate for aPDT.[40]

Thus, we can conclude from this chapter that with the versatility of the BODIPY molecule, these molecules could be utilized to their utmost potential following different synthetic and post-functionalization routes. Hence, this opens a window of exploration into future of aPDT with easy to make and chemically modifiable BODIPY and related dyes.

For future work related to this manuscript, these BODIPY dyes can possibly be formulated with a drug delivery platform as described in the previous chapter 1 and 2 via ionic interaction or covalent linkages and could be evaluated for their aPDT potential as a PS-biopolymer formulation with improved solubility, biocompatibility and enhanced interaction with the bacterial populations which could possibly enhance the aPDT potential as compared to their parent BODIPY molecules.

We have been preparing cellulose nanocrystals (CNCs), biopolymeric drug carriers to form a drug carrier platform for conjugated BODIPYs. For this CNCs have been oxidized under reaction with sodium hypochlorite, sodium bromide and TEMPO at pH=10 to obtain carboxylate functionalized CNCs as illustrated below in Figure 4.30.[67]
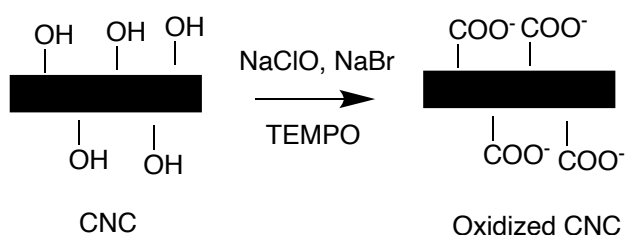
Figure 4.30. Schematic illustration to synthesize oxidized CNCs

In next step PEI (polyethylene amine) is grafted covalently via amide linkage with the carboxylate functionality of oxidized CNCs. And final step would be to graft BODIPY covalently or ionically onto these platforms to make PS delivery platforms for such BODIPYs.

4.7. References

1. Treibs A and Kreuzer F -H. *Justus Liebigs Ann. Chem.* 1968; **718**: 208-223.

2. Bañuelos J. *Chem. Rec.* 2016; **16**: 335-348.

3. Cetindere S. *Am. J. Biomed. Sci. Res.* 2020; **7**: 93-95.

4. Bassan E, Gualandi A, Cozzi PG and Ceroni P. *Chem. Sci.* 2021; **12**: 6607-6628.

5. Frein S, Camerel F, Ziessel R, Barbera J and Deschenaux R. *Chem. Mater.* 2009; **21**: 3950-3959.

6. Mhlongo NZ, Ebenhan T, Driver CHS, Maguire GEM, Kruger HG, Govender T and Naicker T. *Org. Biomol. Chem.* 2020; **18**: 7876-7883.

7. Lin G, Hu M, Zhang R, Zhu Y, Gu K, Bai J, Li J, Dong X and Zhao W. *J. Med. Chem.* 2021; **64**: 18143-18157.

8. Nascimento BFO, Lopes SMM, Pineiro M and Pinho e Melo TMVD. *Molecules* 2019; **24**: 4348-4375.

9. Ulrich G, Ziessel R and Haefele A. *J. Org. Chem.* 2012; **77**: 4298-4311.

10. Jameson LP and Dzyuba S V. *Beilstein J. Org. Chem.* 2013; **9**: 786-790.

11. Bacsa I, Konc C, Orosz AB, Kecskeméti G, Rigó R, zvegy-Laczka C and Mernyák E. *Molecules* 2018; **23**: 1-13.

12. Li L, Nguyen B and Burgess K. *Bioorg. Med. Chem. Lett.* 2008; **18**: 3112-3116.

13. Yogo T, Urano Y, Ishitsuka Y, Maniwa F and Nagano T. *J. Am. Chem. Soc.* 2005; **127**: 12162-12163.

14. Loudet A and Burgess K. *Chem. Rev.* 2007; **107**: 4891-4932.

15. Ulrich G, Goze C, Guardigli M, Roda A and Ziessel R. *Angew. Chem. Int. Ed.* 2005; **44**: 3694-3698.

16. Bartelmess J and Weare WW. *Dye. Pigm.* 2013; **97**: 1-8.

17. Rohand T, Baruah M, Qin W, Boens N and Dehaen W. *Chem. Commun.* 2006: 266-268.

18. Móczár I, Huszthy P, Maidics Z, Kádár M and Klára Tóth. *Tetrahedron* 2009; **65**: 8250-8258.

19. Niu SL, Massif C, Ulrich G, Ziessel R, Renard PY and Romieu A. *Org. Biomol. Chem.* 2011; **9**: 66-69.

20. Raymer B, Kavana M, Price A, Wang B, Corcoran L, Kulathila R, Groarke J and Mann T. *Bioorg. Med. Chem. Lett.* 2009; **19**: 2804-2807.

21. Mcdonnell SO and Shea DFO. *Synthesis* 2006: 2004-2007.

22. Donyagina VF, Shimizu S, Kobayashi N and Lukyanets EA. *Tetrahedron Lett.* 2008; **49**: 6152-6154.

23. Ulrich G, Goeb S, De Nicola A, Retailleau P and Ziessel R. *J. Org. Chem.* 2011; **76**: 4489-4505.

24. Shen Z, Röhr H, Rurack K, Uno H, Spieles M, Schulz B, Reck G and Ono N. *Chem. Eur. J.* 2004; **10**: 4853-4871.

25. Bonardi L, Ulrich G and Ziessel R. *Org. Lett.* 2008; **10**: 2183-2186.

26. Rohand T, Qin W, Boens N and Dehaen W. *Eur. J. Org. Chem.* 2006: 4658-4663.

27. Coskun A and Akkaya EU. *Tetrahedron Lett.* 2004; **45**: 4947-4949.

28. Coskun A and Akkaya EU. *J. Am. Chem. Soc.* 2005; **127**: 10464-10465.

29. Dost Z, Atilgan S and Akkaya EU. *Tetrahedron* 2006; **62**: 8484-8488.

30. Uriel C, Gómez AM, Garciá Martínez De La Hidalga E, Bañuelos J, Garcia-Moreno I and López JC. *Org. Lett.* 2021; **23**: 6801-6806.

31. Niu SL, Massif C, Ulrich G, Renard PY, Romieu A and Ziessel R. *Chem. Eur. J.* 2012; **18**: 7229-7242.

32. Youf R, Müller M, Balasini A, Thétiot F, Müller M, Hascoët A, Jonas U, Schönherr H, Lemercier G, Montier T and Le Gall T. *Pharmaceutics* 2021; **13**: 1995-2051.

33. Vinodh M, Alipour FH, Mohamod AA and Al-Azemi TF. *Molecules* 2012; **17**: 11763-11799.

34. Park W, Cho S, Han J, Shin H, Na K, Lee B and Kim DH. *Biomater. Sci.* 2018; **6**: 79-90.

35. Mai DK, Kang B, Vales TP, Badon IW, Cho S, Lee J, Kim E and Kim HJ. *Molecules* 2020; **25**: 3340-3358.

36. Bessette A and Hanan GS. *Chem. Soc. Rev.* 2014; **43**: 3342-3405.

37. Zhang XF. *J. Photochem. Photobiol. A Chem.* 2018; **355**: 431-443.

38. Niu SL, Ulrich G, Ziessel R, Kiss A, Renard PY and Romieu A. *Org. Lett.* 2009; **11**: 2049-2052.

39. Agazzi ML, Ballatore MB, Reynoso E, Quiroga ED and Durantini EN. *Eur. J. Med. Chem.* 2017; **126**: 110-121.

40. Caruso E, Banfi S, Barbieri P, Leva B and Orlandi VT. *J. Photochem. Photobiol. B Biol.* 2012; **114**: 44-51.

41. Agazzi ML, Ballatore MB, Durantini AM, Durantini EN and Tomé AC. *J. Photochem. Photobiol. C Photochem. Rev.* 2019; **40**: 21-48.

42. Lincoln R, Durantini AM, Greene LE, Martínez SR, Knox R, Becerra MC and Cosa G. *Photochem. Photobiol. Sci.* 2017; **16**: 178-184.

43. Kubheka G, Uddin I, Amuhaya E, Mack J and Nyokong T. *J. Porphyrins Phthalocyanines* 2016; **20**: 1016-1024.

44. Hohlfeld BF, Gitter B, Flanagan KJ, Kingsbury CJ, Kulak N, Senge MO and Wiehe A. *Org. Biomol. Chem.* 2020; **18**: 2416-2431.

45. Callaghan S, Vindstad BE, Flanagan KJ, Melø TB, Lindgren M, Grenstad K, Gederaas OA and Senge MO. *ChemPhotoChem* 2021; **5**: 131-141.

46. Taylor LS, Braun DE and Steed JW. *Cryst. Growth Des.* 2021; **21**: 1375-1377.

47. Mukesh S, Joshi P, Bansal AK, Kashyap MC, Mandal SK, Sathe V and Sangamwar AT. *Mol. Pharm.* 2021; **18**: 2334-2348.

48. Callaghan S, Vindstad BE, Flanagan KJ, Melø TB, Lindgren M, Grenstad K, Gederaas OA and Senge MO. *ChemPhotoChem* 2021; **5**: 131-141.

49. Belali S, Emandi G, Cafolla AA, O'Connell B, Haffner B, Möbius ME, Karimi A and Senge MO. *Photochem. Photobiol. Sci.* 2017; **16**: 1700-1708.

50. Duan C, Zhou Y, Shan GG, Chen Y, Zhao W, Yuan D, Zeng L, Huang X and Niu G. *J. Mater. Chem. C* 2019; **7**: 3471-3478.

51. Kukoyi A, He H and Wheeler K. *J. Photochem. Photobiol. A Chem.* 2022; **425**: 113686-113695.

52. Kukoyi A, Micheli EA, Liu B, He H and Stanley May P. *Dalton Trans.* 2019; **48**: 13880-13887.

53. Abualnaja KM, Abu-Saied MA, Ghareeb RY, Ibrahim AA and Abdelsalam NR. *J. Mater. Res. Technol.* 2021; **14**: 452-463.

54. Barut B, Baş H and Biyiklioğlu Z. *Turkish J. Chem.* 2021; **45**: 1567-1575.

55. Li L, Han J, Nguyen B and Burgess K. *J. Org. Chem.* 2008; **73**: 1963-1970.

56. Wang M, Vicente MGH, Mason D and Bobadova-Parvanova P. *ACS Omega* 2018; **3**: 5502-5510.

57. Choi SH, Kim K, Lee J, Do Y and Churchill DG. *J. Chem. Crystallogr.* 2007; **37**: 315-331.

58. Piacenza M and Grimme S. *J. Am. Chem. Soc.* 2005; **127**: 14841-14848.

59. Porter WW and Vaid TP. *J. Org. Chem.* 2005; **20**: 5028-5035.

60. Avellanal-Zaballa E, Prieto-Castañeda A, Díaz-Norambuena C, Bañuelos J, Agarrabeitia AR, García-Moreno I, De La Moya S and Ortiz MJ. *Phys. Chem. Chem. Phys.* 2021; **23**: 11191-11195.

61. Peeks MD, Neuhaus P and Anderson HL. *Phys. Chem. Chem. Phys.* 2016; **18**: 5264-5274.

62. Martić G, Engle JT and Ziegler CJ. *Inorg. Chem. Commun.* 2011; **14**: 1749-1752.

63. Bröring M and Kleeberg C. *Inorg. Chim. Acta* 2009; **362**: 1065-1070.

64. Gandra N, Frank AT, Le Gendre O, Sawwan N, Aebisher D, Liebman JF, Houk KN, Greer A and Gao R. *Tetrahedron* 2006; **62**: 10771-10776.

65. George M V. and Bhat V. *Chem. Rev.* 1979; **79**: 447-478.

66. Justino GJ, Shimizu K, Eduardo C, Bernardes S and Silva L. *Molecules* 2020; **25**: 2374-2388.

67. Zhao F, Repo E, Song Y, Yin D, Hammouda S Ben, Chen L, Kalliola S, Tang J, Tam KC and Sillanpää M. *Green Chem.* 2017; **19**: 4816-4828.

Chapter 5.

Experimentation

5. Experimental section

5.1. Synthesis of PSs and formulations

General chemicals

General chemicals were purchased from industrial suppliers and were used without further purification including polyethyleneimine (PEI) (600 Da), 4-acetamidobenzaldehyde, 4-pyridyl carboxaldehyde, pyrrole, propionic acid, trifluoroacetic acid (TFA), 1-ethyl-3-(3-dimethylaminopropyl)carbodiimide (EDC•HCl), N-hydroxysulfosuccinimide sodium salt (sulfo-NHS), iodomethane, 2,4-dimethylpyrrole, 3-ethyl-2,4-dimethylpyrrole, 4-pyridine carboxaldehyde, 5-pyrimidine carboxaldehyde, 4-quinoline carboxaldehyde, benzaldehyde, 2-quinoline carboxaldehyde, 9-acridine carboxaldehyde, 2-thiazole carboxaldehyde, 1-methyl-2-imidazol carboxaldehyde, 4-(bromomethyl)benzoic acid, 4-bromobutyl phenyl ether, trifluoracetic acid (TFA), N-iodosuccinimide, copper iodide (CuI), bis(triphenylphosphine)palladium(II) Pd(PPh$_3$)Cl$_2$, trimethylsilyl acetylene (TMSA), 3-dimethylamino-1-propyne, butyl lithium (n-BuLi), 3-dichloro-5,6-dicyano-1,4-benzoquinone (DDQ), triethylamine (TEA), boron trifluoride etherate (BF$_3$·OEt$_2$), tetra-n-butylammonium fluoride (TBAF), sodium bicarbonate (NaHCO$_3$), sodium sulphate (Na$_2$SO$_4$). All air and/or water sensitive materials were handled using standard high vacuum techniques. Anhydrous DCM was obtained via distillation over phosphorus pentoxide. Dry THF, toluene and acetonitrile were obtained by passing through alumina under N$_2$ in a solvent purification system and then further dried over activated molecular sieves. *Spirulina maxima* was obtained from l'Agriculture Biologique lot 190058. Analytical thin-layer chromatography was performed using silica gel 60 (fluorescence indicator F254, precoated sheets, 0.2 mm thick, 20 cm × 20 cm; Merck) plates and visualized by UV irradiation (λ = 254 nm). Column chromatography was carried out using Fluka Silica Gel 60 (230–400 mesh; Merck).

Spectroscopic evaluation

UV-vis absorption spectra were recorded using a Specord 210 (Analytic Jena) or Specord 250 from Analytic Jena (1 cm path length quartz cell) spectrophotometer with spectro-grade solvents. FTIR spectra were recorded on Perkins-Elmer 310 spectrum 1000 FTIR spectrophotometer. NMR spectra were recorded on a Bruker AV 600, Bruker Advance III 400 MH or a Bruker DPX400 400 MHz or an Agilent 400 spectrometer.

Accurate mass measurements (HRMS) were carried out using a Bruker microTOF-Q™ ESI-TOF mass spectrometer. Mass spectrometry was performed with a Q-Tof Premier Waters MALDI quadrupole time-of-flight (Q-TOF) mass spectrometer equipped with Z-spray electrospray ionization (ESI) and matrix assisted laser desorption ionization (MALDI) sources in positive mode with trans-2-[3-(4-tert-butylphenyl)-2-methyl-2-propenylidene] malononitrile as the matrix. Melting points were measured using an automated melting point machine, SMP50 (Stuart).

Material characterization

The freeze-dried conjugates were analyzed by scanning electron microscopy (SEM) using a Quanta FEG 450 ESEM with an accelerating voltage of 10-15 kV. Conjugates were fixed onto carbon-taped metal pins. Dynamic light scattering (DLS) was used for the measurement of average hydrodynamic diameters and polydispersity indexes (PDIs; Malvern Zetasizer Nano-ZS, Malvern Instruments, UK). Each sample was analyzed in triplicate at 20 °C at a scattering angle of 173°. Pure water was used as a reference dispersing medium. The ζ-potential data were collected through electrophoretic light scattering at 20 °C, 150 V, in triplicate for each sample (Malvern Zetasizer Nano-ZS, Malvern Instruments, UK). The instrument was calibrated with a Malvern -68 mV standard before each analysis cycle. Differential scanning calorimetry (DSC) analysis was carried out on a Model 910 Differential Scanning Calorimeter. Dynamic rheology properties were obtained using a rotational rheometer (Mars III, Thermo Scientific, RheoWin software), with a 35-mm plate-plate geometry configuration and a gap of 1.000 mm. The behavior of the different samples was determined by shear rate sweep tests at 25 °C. In addition, the rheological properties were measured in strain-controlled oscillatory tests. A strain amplitude of $\gamma_0 = 0.1$ [-] was selected to ensure a linear regime of oscillatory deformation. The conjugate was placed between the plates at 25 °C, and the measurements were carried out within the angular frequency range of 0.1−100 rad/s.

General Procedure A: PS-hyaluronate conjugate (2.25-2.26): Hyaluronic acid (100 mg) was dissolved in 20 mL of distilled water at a concentration of 5 mg. mL^{-1}. PS (30 mg) with 1 M ratios of HA repeating unit was added to the HA solution. After that, EDC•HCl (2 eq.) and sulfo-NHS (2 eq.) were added to activate the carboxyl groups of HA. The pH of the mixed solution was adjusted to pH 4.7 using 1 N NaOH and 1 N HCl.

After reaction overnight, the pH increased to the range of 6.8-7.2. Then, the resulting conjugate was dialyzed against deionized water for three days. The purified conjugate solution was lyophilized for two days.

General Procedure B: BODIPYs (4.46-4.53): 2,4-Dimethylpyrrole (2 eq.) and the appropriate benzaldehyde (1 eq.) were dissolved in anhydrous DCM (150 mL) under argon. Trifluoracetic acid (TFA) (0.2 mL) was added, and the reaction mixture was stirred at room temperature under constant stirring for 12 h. When the aldehyde was consumed (monitored by TLC), 3-dichloro-5,6-dicyano-1,4-benzoquinone (DDQ) (9 mmol) was added to the previous solution at room temperature. After stirring for 4 h at room temperature, triethylamine (TEA) (1 eq.) and boron trifluoride etherate ($BF_3 \cdot OEt_2$) (1 eq.) was added dropwise at 0 °C over a period of 10 min, and the mixture was stirred at room temperature for 3 h. The mixture was then filtered and washed with a solution of saturated $NaHCO_3$ followed by washing with deionized water. The resulting solution is dried over anhydrous $NaSO_4$ and evaporated in a rotavapor. The residue was purified by flash column chromatography eluting with DCM:Hexane solvent systems (varying for different derivatives) to yield the pure product as an orange crystalline solid.

General Procedure C: BODIPYs (4.54-4.60): 3-Ethyl-2,4-dimethylpyrrole (2 eq.) and the appropriate benzaldehyde (1 eq.) were dissolved in anhydrous DCM (150 mL) under argon. Trifluoracetic acid (TFA) (0.2 mL) was added, and the reaction mixture was stirred at room temperature under constant stirring for 12 h. When the aldehyde was consumed (monitored by TLC), DDQ (9 mmol) was added to the previous solution at room temperature. After stirring for 4 h at room temperature, TEA (1 eq.) and $BF_3 \cdot OEt_2$ (1 eq.) was added dropwise at 0 °C over a period of 10 min, and the mixture was stirred at room temperature for 3 h. The mixture was then filtered and washed with a solution of saturated $NaHCO_3$ followed by washing with deionized water. The resulting solution is dried over anhydrous sodium sulphate and evaporated in a rotavapor. The residue was purified by flash column chromatography eluting with DCM:Hexane solvent system (varying for different derivatives) to yield the pure product as a red crystalline solid.

General Procedure D: BODIPYs (4.46a, 4.54a, 4.48a and 4.56a): Previously synthesized BODIPY (1 eq.) were dissolved in 4mL anhydrous dry acetonitrile (4 mL), and methyl iodide (1 eq.) was added to the above mixture which was then refluxed for

about 1.5 h at 82 °C. The resulting solution was dried over anhydrous NaSO₄ and evaporated in a rotavapor. The residue was purified by washing the resulting solid with ethyl acetate to obtain the pure product as a red crystalline solid.

General Procedure E: BODIPYs (4.46b, 4.54b, 4.48b and 4.56b): Previously synthesized BODIPY (1 eq.) and 4-(bromomethyl)benzoic acid (8 eq.) were dissolved in anhydrous dry toluene (4 mL) and refluxed for about 18 h at 111 °C. The resulting solution is dried over anhydrous sodium sulphate and evaporated in a rotavapor. The residue was purified by washing the resulting solid with ethyl acetate to obtain the pure product as a red crystalline solid.

General Procedure F: BODIPYs (4.46b, 4.54b): Previously synthesized BODIPY (1 eq.) and 4-bromobutyl phenyl ether (8 eq.) were dissolved in anhydrous dry toluene (4mL) and refluxed for about 18 h at 111 °C. The resulting solution is dried over anhydrous sodium sulphate and evaporated in a rotavapor. The residue was purified by washing the resulting solid with ethyl acetate to obtain the pure product as a red crystalline solid.

General Procedure G: BODIPY (**4.46d** and **4.50a**): 3-Dimethylamino-1-propyne (4.5 eq.) was dissolved in dry THF (8 mL) at room temperature under argon. After 10 min *n*-BuLi in Hexane (4 eq.) was added dropwise and the reaction was stirred for 45 min under inert atmosphere of argon. BODIPY (1 eq.) was dissolved in dry THF and was then added to the above reaction dropwise and the reaction was refluxed for 2.5 hat 66 ºC. The reaction mixture was quenched with deionized water (20 mL) and was then filtered and washed with a solution of saturated NaHCO₃ (2 x 50 mL) followed by washing with deionized water (2 x 50 mL). The resulting solution is dried over anhydrous sodium sulphate and evaporated in a rotavapor. The residue was purified by flash column chromatography eluting with DCM:MeOH (2:1) to yield the pure product as an orange-green crystalline solid.

General Procedure H: BODIPYs (4.46e, 4.49a, 4.51a and 4.53a): Previously synthesized BODIPY (1 eq.) and *N*-iodosuccinimide (1 eq.) were dissolved in 10 mL of DCM at room temperature. The reaction mixture was stirred at room temperature for 30 min and *N*-iodosuccinimide (0.25 eq.) of was added twice at an interval of 40 min. The

mixture was then filtered and washed with a solution of saturated NaHCO$_3$ followed by washing with deionized water. The resulting solution is dried over anhydrous sodium sulphate and evaporated in a rotavapor. The residue was purified by flash column chromatography eluting with Hexane:DCM (1:2) to yield the pure product as a pinkish-red crystalline solid.

General Procedure I: BODIPYs (**4.46f and 4.51b**) Sonogashira cross-coupling: Previously synthesized BODIPY (1 eq.), CuI (0.1 eq.) and Pd(PPh$_3$)Cl$_2$ (0.05 eq.) were dissolved in 5 mL dry THF:TEA(4:1) at room temperature under inert atmosphere of argon. After stirring for 30 min trimethylsilyl acetylene (TMSA) (10 eq.) was added under argon. The reaction mixture was refluxed for 20 h. The mixture was then filtered and washed with a solution of saturated NaHCO$_3$ followed by washing with deionized water. The resulting solution is dried over anhydrous sodium sulphate and evaporated in a rotavapor. The residue was purified by flash column chromatography eluting with Hexane:Ethyl acetate (9:1) to yield the pure product as a pinkish-orange crystalline solid.

5.1.1. Ch 2: Formulating photosensitizer-conjugates and their antimicrobial evaluation

Purpurin-18 (2.17)
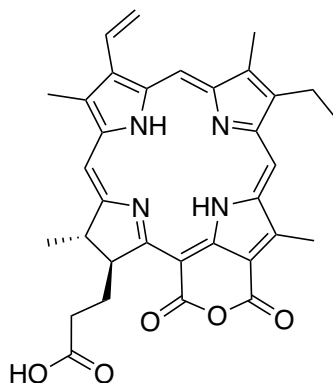
Purpurin-18 (**2.17**) was extracted and synthesized from *Spirulina maxima* powder (50 g) was used to extract pigments with acetone (1 L) followed by addition of 6 M NaOH (200 mL) and 100 mL concentrated HCl. Purification by column chromatography (silica gel; CHCl$_3$/EtOH, 8:2, v/v) and removal of solvents followed by recrystallization (CHCl$_3$/petroleum ether) to yield a purple solid. Analytical data is identical to the literature.[1,2] R$_f$ = 0.27 (CHCl$_3$/EtOH: 96/4); ^{1}H NMR (CDCl$_3$): δ (ppm) = 9.54, 9.33, 8.55 (s, 1H, 5-*H*, 10-*H*, 20-*H*); 7.86 (dd, *J* = 17.0, 11.4 Hz, 1H, 31-C*H*); 6.28 (dd, *J* = 17.0, 1.0 Hz, 1H, trans-32-C*H$_2$*); 6.19 (dd, *J* = 11.4, 1.0 Hz, 1H, cis- 32-C*H$_2$*); 5.15 (m, 1H, 17-*H*); 4.39 (q, *J* = 6.0 Hz, 1H, 18-*H*); 3.72 (s, 3H, 12-C*H$_3$*); 3.59 (q, *J* = 6.6 Hz, 2H, 81-C*H$_2$*); 3.32 and 3.15 (s, 3H, 2-C*H$_3$* and 7-C*H$_3$*); 2.70, 2.46, 2.35, 1.97 (m, 1H, 2 X 17^1-*H* and 2 X 17^2-*H*); 1.73 (d, *J* = 6.0 Hz, 3H, 18-C*H$_3$*); 1.65 (t, *J* = 6.8 Hz, 3H, 82-C*H$_3$*). UV-Vis (CHCl$_3$) λ$_{max}$ (ε [x10^3 M^{-1} cm^{-1}]) = 360 (22.9); 413 (44.6); 481 (1.9); 510 (3.9); 548 (10.9); 646 (4.7); 701 nm (23.2). HRMS (ESI+): m/z calcd for C$_{33}$H$_{32}$N$_4$O$_5$ [M]$^+$: 565.24455., found 565.24382.

Chlorin *p6*-PEI (2.18)
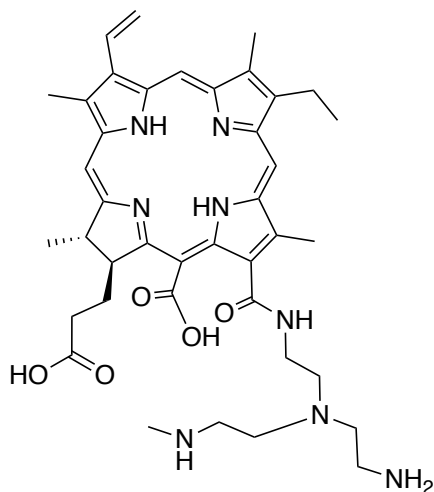
In accordance with previously used procedure by Sol lab to obtain chlorin *p6*-PEI (**2.18**) using purpurin-18 (**2.17**) (100mg, 1equiv.) PEI (polyethyleneimine) (600 Da) (98.1mg, 1equiv.) in 100 mL chloroform to yield a dark-green solid (98.1% yield). Analytical data is identical to the literature.[1] M.p. = >300°C; UV-Vis (CH$_2$Cl$_2$) λ$_{max}$ (ε [x10^3 M^{-1} cm^{-1}]) = 400 (52.4); 502 (6.0); 530 (2.8); 552 (1.9); 611 (2.4); 665 (14.1) nm.

5-(4-Acetamidophenyl)-10,15,20-tris(4-pyridyl)porphyrin (2.22)
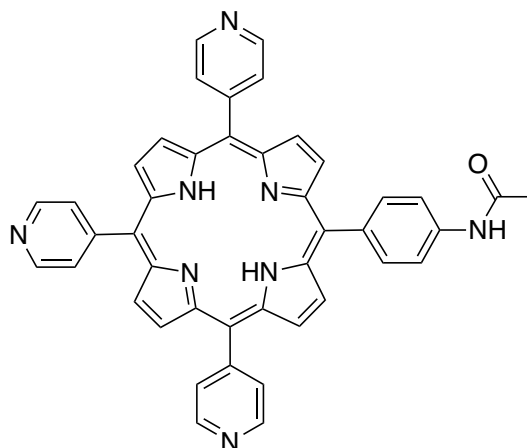
2.22

Porphyrin **2.22** was synthesized using a pyrrole (0.832 mL, 12.0 mmol), 4-pyridylcarboxaldehyde (0.847 mL, 9.0 mmol), 4-acetamidobenzaldehyde (489.3 mg, 3.0 mmol) and propionic acid (20 mL). Purification by column chromatography (silica gel; CHCl$_3$/EtOH, 1:0.1, v/v) and removal of solvents followed by recrystallization (CHCl$_3$/MeOH) gave the title compound as purple crystals (4% yield). Analytical data is identical to the literature.[3] M.p. = >300 °C; Rf = 0.54 (CHCl$_3$/EtOH: 90/10); UV-Vis (MeOH): λ$_{max}$ (ε [x10^3 M^{-1} cm^{-1}]) = 415 (5.33), 512 (3.95), 547 (3.52), 588 (3.44), 644 (3.13) nm. ^{1}H NMR (500 MHz, CDCl$_3$): δ (ppm) = 9.04 (m, 6H, *Ho*-py), 8.80 (m, 8H, *Hβ*-pyrrolic), 8.17 (d, *J* = 8.0 Hz, 2H, *Ho*-pheacetamido), 8.15 (m, 6H, *Hm*-py), 7.94 (d, *J* = 8.0 Hz, 2H, *Hm*-pheacetamido), 2.38 (s, 3H, -C*H$_3$*), -2.90 (s, 2H, N*H$_{int}$*).

5-(4-Aminophenyl)-10,15,20-tris(4-*N*-methylpyridinium)porphyrin triiodide (2.24)

2.24
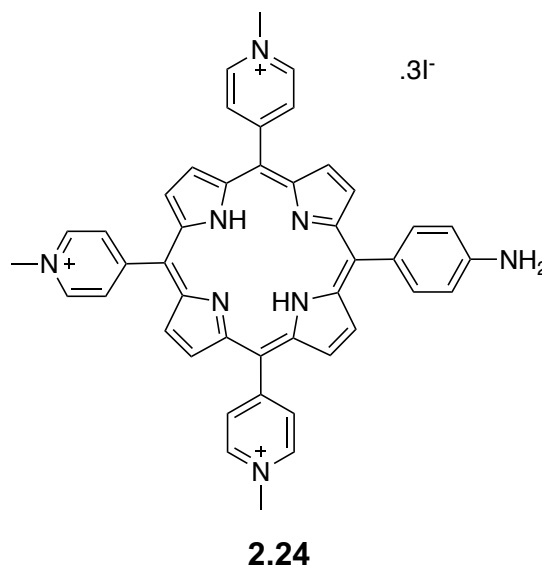
In accordance with general procedure porphyrin **2.24** was synthesized as described above using porphyrin **3** (50 mg, 0.30 mmol), iodomethane (0.24 mL, 3.96 mmol) and anhydrous DMF (10 mL) as starting material to yield a purple-brown powder (82% yield). Analytical data is identical to the literature.[3] M.p. = >300°C; UV-visible (MeOH), λ_{max} (ε [x10^3 M^{-1} cm^{-1}]): 428 (5.05), 521 (4.05), 564 (3.88), 593 (3.84), 656 nm (3.47). ^{1}H NMR (500 MHz, DMSO d6): δ (ppm) = 9.49 (d, *J* = 6.5 Hz, 6H, *Ho*-py), 9.11 – 8.80 (m, 8H, *H*pyrr), 9.00 (d, *J* = 6.5 Hz, 6H, *H*m-py), 7.94 (d, *J* = 8.5 Hz, 2H, *Ho*-phe), 7.15 (d, *J* = 8.5 Hz, 2H, *Hm*-phe), 4.73 (s, 9H, N+ -C*H₃*), -2.96 (s, 2H, N*H*$_{int}$). HRMS (ESI+): *m/z* calcd for C$_{44}$H$_{37}$I$_3$N$_8$ [M]$^{3+}$ 225.77, found 225.74.

Chlorin *p6*-PEI-HA conjugate (2.25)
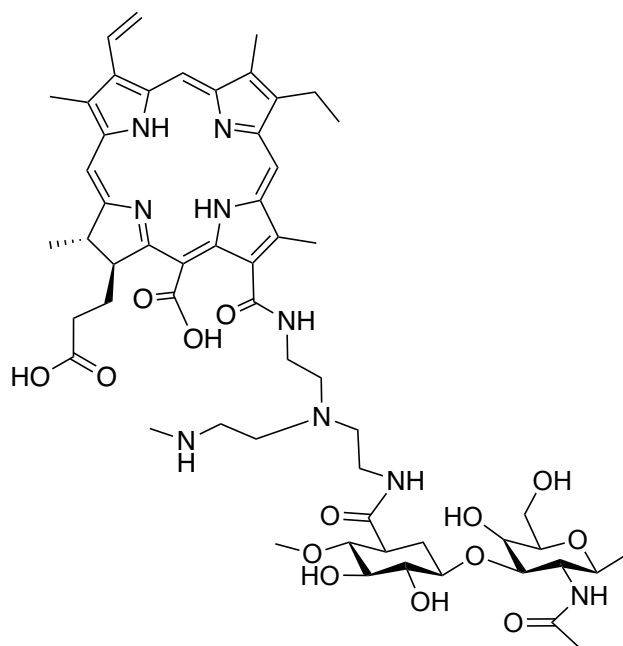
2.25

DSC analysis of conjugates: Thermogram shows a loss of water (endothermic) from around 80 °C, then an exotherm at about 240 °C for this hyaluronic acid conjugate.

SEM characterization: Representative SEM images (Figure S2) of the dried conjugate samples (with PSs) shows homogenous dispersion of the conjugate samples and cross-linking pattern with an average size of 105 ± 103 nm for **2.25**.

IR spectrum: 3360, 3325, 2930, 2947, 1642, 1574, 1596 and 1340 cm^{-1}.

DLS analyses and zeta potential analyses of conjugates: 2.25 has a diameter of 342 ± 52.8 nm and zeta potential of -34 mV.

UV-vis analysis: The relative molar percentage of photosensitizers in the conjugate structure was determined based on monomer concentration to be 3% for this conjugate.

CP-HA conjugate (2.26)
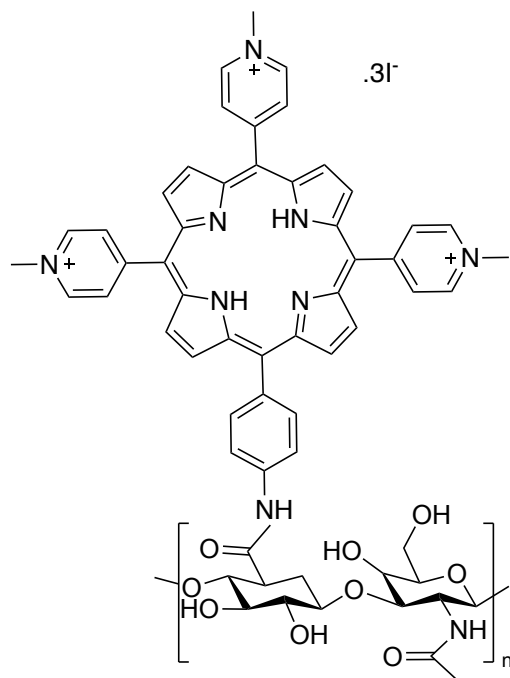
DSC analysis of conjugates: Thermogram shows a loss of water (endothermic) from around 80 °C, then an exotherm at about 240 °C for hyaluronic acid conjugate.

SEM characterization: Representative SEM images (Figure S2) of the dried conjugate samples (with PSs) shows homogenous dispersion of the conjugate samples and cross-linking pattern with an average size of 215 ± 105 nm for this conjugate.

IR spectra: 3360, 3325, 2930, 1642 and 1340 cm^{-1}.

DLS analyses and zeta potential analyses of conjugates: Hydrodynamic diameter of this conjugate is 435.1 ± 35.1 nm and zeta potential is -29.3.

UV-vis analysis: The relative molar percentage of photosensitizers in the conjugate structure was determined based on monomer concentration to be 18% for this conjugate.

5.1.2.   Ch 4: Synthesis of BODIPY derivatives for aPDT

1,3,5,7-Tetramethyl-8-(4-pyridyl)-4-bora-3a,4a-diaza-*s*-indacene (4.46)
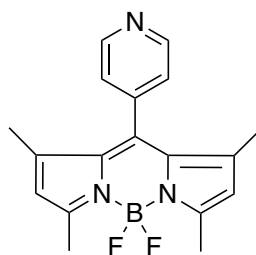
BODIPY **4.46**

In accordance with general procedure **B** as described above using 2,4-dimethylpyrrole (2.0 mL, 19.4 mmol) and 4-pyridine carboxaldehyde (0.84 mL, 9 mmol) and final product was obtained and purified by column chromatography (silica gel; DCM/Hex, 6:4, v/v) and removal of solvents followed by recrystallization (CHCl$_3$/Hex) to yield a green solid (16% yield). Analytical data is identical to the literature.[4] M.p. = 235 – 240 °C; R$_f$ = 0.52 (DCM/Hex: 90/10); ^{1}H NMR (400 MHz, CDCl$_3$): δ = 8.78 ppm (dd, *J* = 4.3, 1.6 Hz, 2H, Ar-*H*), 7.30 (dd, *J* = 4.3, 1.6 Hz, 2H, Ar-*H*), 6.00 (s, 2H, 2-*H*, 6-*H*), 2.55 (s, 6H, 3-C*H$_3$* and 5-C*H$_3$*), 1.40 (s, 6H, 1-C*H$_3$* and 7-C*H$_3$*). ^{19}F NMR (377 MHz, CDCl$_3$): δ = -145.90 – -146.39 ppm (m); ^{11}B NMR (128 MHz, CDCl$_3$): δ = 0.70 ppm (t, *J* = 32.5 Hz); IR (neat): *v* = 2963, 1536, 1436, 1360, 1138, 1049, 962 cm^{-1}. HRMS (ESI): *m/z* calcd for C$_{18}$H$_{18}$BF$_2$N$_3$ [M + H]$^+$: 326.163789, 326.163915 found.

1,3,5,7-Tetramethyl-8-(5-pyrimidinyl)-4-bora-3a,4a-diaza-*s*-indacene (4.47)

BODIPY **4.47**

In accordance with general procedure **B** as described above using 2,4-dimethylpyrrole (2.0 mL, 19.4 mmol) and 5-pyrimidine carboxaldehyde (0.97 g, 9 mmol) and final product was obtained and purified by column chromatography (silica gel; DCM/Hex, 8:2, v/v) and removal of solvents followed by recrystallization (DCM/Hex) to yield green solid (8%

yield). M.p. = 177 – 182 °C; R_f = 0.32 (DCM/Hex: 90/10); ^{1}H NMR (400 MHz, CDCl$_3$) δ 9.38 (s, 1H, Ar-*H*), 8.72 (s, 2H, Ar-*H*), 6.05 (s, 2H, 2-*H*, 6-*H*), 2.57 (s, 6H, 3-C*H$_3$*, 5-C*H$_3$*), 1.42 (s, 6H, 1-C*H$_3$*, 7-C*H$_3$*). ^{13}C NMR (101 MHz, CDCl$_3$) δ 159.06, 157.32, 155.92, 142.23, 133.03, 131.44, 129.80, 122.44, 15.59, 14.71. ^{19}F NMR (377 MHz, CDCl$_3$) δ -145.93 – -146.29 (m). ^{11}B NMR (128 MHz, CDCl$_3$) δ 0.69 (t, J = 32.3 Hz). IR (neat): 2956, 2922, 2853, 1731, 1546, 1410, 1306, 1183, 1076, 969 cm^{-1}. UV-Vis (CH$_2$Cl$_2$) λ$_{max}$ (ε [x10^3 M^{-1} cm^{-1}]) = 319 (5.54), 369 (6.18), 481 (24.92), 512 (105.42) nm. HRMS (APCI): m/z calcd for C$_{17}$H$_{17}$BF$_2$N$_4$ [M + H]$^+$: 327.159021, 327.158854 found.

1,3,5,7-Tetramethyl-8-(4-quinolinium-yl)-4-bora-3a,4a-diaza-*s*-indacene (4.48)

BODIPY **4.48**

In accordance with general procedure **B** as described above using 2,4-dimethylpyrrole (2.0 mL, 19.4 mmol) and 4-quinoline carboxaldehyde (1.41 g, 9 mmol) and final product was obtained and purified by column chromatography (silica gel; DCM/Hex, 7:3, v/v) and removal of solvents followed by recrystallization (DCM/Hex) to yield green solid (20% yield). M.p. = 252 – 257 °C ; Rf = 0.48 (DCM/Hex: 90/10); ^{1}H NMR (400 MHz, CDCl$_3$) δ 9.03 (d, J = 4.3 Hz, 1H, Ar-*H*), 8.19 (d, J = 8.5 Hz, 1H, Ar-*H*), 7.84 (d, J = 8.3 Hz, 1H, Ar-*H*), 7.78 (ddd, J = 8.3, 7.0, 1.2 Hz, 1H, Ar-*H*), 7.56 – 7.51 (m, 1H, Ar-*H*), 7.39 (d, J = 4.3 Hz, 1H, Ar-*H*), 5.97 (s, 2H, 2-*H*, 6-*H*), 2.59 (s, 6H, 3-C*H$_3$*, 5-C*H$_3$*), 1.09 (s, 6H, 1-C*H$_3$*, 7-C*H$_3$*). ^{13}C NMR (101 MHz, CDCl$_3$) δ 156.67, 150.42, 148.52, 142.80, 141.83, 136.43, 131.09, 130.58, 130.09, 128.18, 126.90, 124.98, 121.83, 120.99, 14.83, 14.19. ^{19}F NMR (377 MHz, CDCl$_3$) δ -145.98- -146.79. ^{11}B NMR (128 MHz, CDCl$_3$) δ 0.84 (t, J = 32.7 Hz). IR (neat): 3656, 2980, 1588, 1462, 1365, 1187, 969 cm^{-1}. UV-Vis (CH$_2$Cl$_2$) λ$_{max}$ (ε [x10^3 M^{-1} cm^{-1}]) = 321 (2.93), 348 (5.85), 477 (19.01), 508 (87.61) nm. HRMS (APCI): m/z calcd for C$_{22}$H$_{20}$BF$_2$N$_3$ [M + H]$^+$: 376.179507, 376.179858 found.

1,3,5,7-Tetramethyl-8-(2-quinolinium-yl)-4-bora-3a,4a-diaza-*s*-indacene (4.49)

BODIPY **4.49**

In accordance with general procedure **B** as described above using 2,4-dimethylpyrrole (2.0 mL, 19.4 mmol) and 2-quinoline carboxaldehyde (1.41 g, 9 mmol) and final product was obtained and purified by column chromatography (silica gel; DCM/Hex, 8:2, v/v) and removal of solvents followed by recrystallization (DCM/Hex) to yield green solid (14% yield). M.p. = >300 °C; Rf = 0.51 (DCM/Hex: 90/10); ^{1}H NMR (400 MHz, CDCl$_3$) δ 8.33 (d, *J* = 8.3 Hz, 1H, Ar-*H*), 8.17 (d, *J* = 8.4 Hz, 1H, Ar-*H*), 7.93 (d, *J* = 8.2 Hz, 1H, Ar-*H*), 7.81 (ddd, *J* = 8.4, 7.0, 1.4 Hz, 1H, Ar-*H*), 7.67 (ddd, *J* = 8.1, 7.0, 1.1 Hz, 1H, Ar-*H*), 7.53 (d, *J* = 8.4 Hz, 1H, Ar-*H*), 5.98 (s, 2H, 2-*H*, 6-*H*), 2.57 (s, 6H, 3-C*H$_3$*, 5-C*H$_3$*), 1.22 (s, 6H, 1-C*H$_3$*, 7-C*H$_3$*). ^{13}C NMR (101 MHz, CDCl$_3$) δ 156.63, 154.18, 148.20, 142.73, 138.92, 137.43, 131.49, 130.62, 129.84, 127.95, 127.80, 127.58, 121.82, 121.43, 14.83, 14.07. ^{19}F NMR (377 MHz, CDCl$_3$) δ -145.21- -147.31. ^{11}B NMR (128 MHz, CDCl$_3$) δ 0.81 (t, *J* = 32.8 Hz). IR (neat): 3401, 2971, 1596, 1507, 1339, 1185, 971 cm^{-1}. UV-Vis (CH$_2$Cl$_2$) λ$_{max}$ (ε [x10^3 M^{-1} cm^{-1}]) = 318 (12.4), 366 (7.59), 478 (21.22), 508 (86.52) nm. HRMS (ESI): m/z calcd for C$_{22}$H$_{20}$BF$_2$N$_3$ [M + H]$^+$: 376.179507, 376.180084 found.

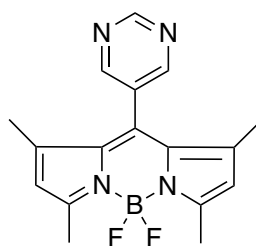## 1,3,5,7-Tetramethyl-8-(9-acridinyl)-4-bora-3a,4a-diaza-*s*-indacene (4.50)
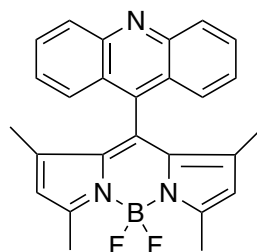
BODIPY **4.50**

In accordance with general procedure **B** as described above using 2,4-dimethylpyrrole (2.0 mL, 19.4 mmol) and 9-acridine carboxaldehyde (1.86 g, 9 mmol) and final product was obtained and purified by column chromatography (silica gel; DCM/Hex, 9:1, v/v) and removal of solvents followed by recrystallization (DCM/Hex) to yield green solid (14% yield). M.p. = 230 – 235 °C; Rf = 0.43 (DCM/Hex: 90/10); ^{1}H NMR (400 MHz, CDCl$_3$) δ 8.28 (d, J = 8.8 Hz, 2H, Ar-H), 7.96 (d, J = 8.7 Hz, 2H, Ar-H), 7.85 – 7.78 (m, 2H, Ar-H), 7.55 – 7.49 (m, 2H, Ar-H), 5.93 (s, 2H, 2-H, 6-H), 2.63 (s, 6H, 3-CH_3, 5-CH_3), 0.68 (s, 6H, 1-CH_3, 7-CH_3). ^{13}C NMR (101 MHz, CDCl$_3$) δ 156.82, 148.85, 142.87, 139.27, 135.32, 131.70, 130.88, 129.91, 127.46, 125.37, 124.86, 121.85, 14.89, 13.62. ^{19}F NMR (377 MHz, CDCl$_3$) δ -145.87- -146.13. ^{11}B NMR (128 MHz, CDCl$_3$) δ 0.98 (t, J = 32.7 Hz). IR (neat): 3659, 2981, 1965, 1538, 1406, 1299, 1150, 970 cm^{-1}. UV-Vis (CH$_2$Cl$_2$) λ$_{max}$ (ε [x10^3 M^{-1} cm^{-1}]) = 318 (5.20), 365 (17.94), 482 (22.77), 511 (98.28) nm. HRMS (APCI): m/z calcd for C$_{27}$H$_{23}$BF$_2$N$_3$ [M + H]$^+$: 426.195224, 426.195570 found.

1,3,5,7-Tetramethyl-8-(2-thiazolyl)-4-bora-3a,4a-diaza-*s*-indacene (4.51)
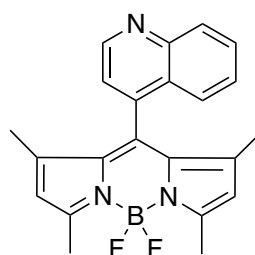

BODIPY **4.51**

In accordance with general procedure **B** as described above using 2,4-dimethylpyrrole (2.0 mL, 19.4 mmol) and 2-thiazole carboxaldehyde (1.02 g, 9 mmol) and final product was obtained and purified by column chromatography (silica gel; DCM/Hex, 8:2, v/v) and removal of solvents followed by recrystallization (DCM/Hex) to yield green solid (15% yield). M.p. = >300 °C; Rf = 0.37 (DCM/Hex: 90/10); ^{1}H NMR (400 MHz, CDCl$_3$) δ 8.00 (d, J = 3.2 Hz, 1H, Ar-H), 7.62 (d, J = 3.2 Hz, 1H, Ar-H), 6.02 (s, 2H, 2-H, 6-H), 2.56 (s, 6H, 3-CH_3, 5-CH_3), 1.46 (s, 6H, 1-CH_3, 7-CH_3). ^{13}C NMR (101 MHz, CDCl$_3$) δ 160.11, 157.43, 143.41, 143.00, 131.90, 122.25, 121.72, 121.70, 14.77, 13.24. ^{19}F NMR (377 MHz, CDCl$_3$) δ -145.22- -146.96. ^{11}B NMR (128 MHz, CDCl$_3$) δ 0.71 (t, J = 32.6 Hz). IR (neat): 3116, 2970, 2929, 1692, 1507, 1363, 1186, 966 cm^{-1}. UV-Vis (CH$_2$Cl$_2$) λ$_{max}$ (ε [x10^3 M^{-1} cm^{-1}]) = 322 (3.41), 384 (3.46), 488 (14.62), 520 (59.73) nm. HRMS (APCI): m/z calcd for C$_{16}$H$_{16}$BF$_2$N$_3$S [M + H]$^+$: 332.120180, 332.120779 found.

1,3,5,7-Tetramethyl-8-(1-methyl-1H-imidazol-2-yl)-4-bora-3a,4a-diaza-*s*-indacene (4.52)

BODIPY **4.52**
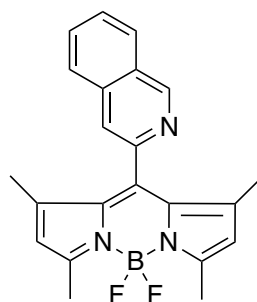
In accordance with general procedure **B** as described above using 2,4-dimethylpyrrole (2.0 mL, 19.4 mmol) and 1-methyl-2-imidazol carboxaldehyde (0.99 g, 9 mmol) and final product was obtained and purified by column chromatography (silica gel; DCM/Ethyl Acetate, 9:1, v/v) and removal of solvents followed by recrystallization (DCM/Hex) to yield green solid (8% yield). M.p. = 175 – 180 °C; Rf = 0.32 (DCM/Hex: 90/10); ^{1}H NMR (400 MHz, CDCl$_3$) δ 7.19 (s, 1H, Ar-*H*), 7.04 (s, 1H, Ar-*H*), 6.01 (s, 2H, 2-*H*, 6-*H*), 3.49 (s, 3H, Ar-N-C*H$_3$*), 2.54 (s, 6H, 3-C*H$_3$*, 5-C*H$_3$*), 1.41 (s, 6H, 1-C*H$_3$*, 7-C*H$_3$*). ^{13}C NMR (101 MHz, CDCl$_3$) δ 157.71, 142.96, 142.95, 140.14, 132.80, 129.58, 121.43, 121.25, 33.10, 14.90, 12.14. ^{19}F NMR (377 MHz, CDCl$_3$) δ -145.17- -146.93. ^{11}B NMR (128 MHz, CDCl$_3$) δ 0.73 (t, *J* = 32.7 Hz). IR (neat): 3151, 2980, 2919, 1690, 1547, 1406, 1151, 970 cm^{-1}. UV-Vis (CH$_2$Cl$_2$) λ$_{max}$ (ε [x10^3 M^{-1} cm^{-1}]) = 314 (3.14), 369 (4.36), 486 (12.00), 519 (46.15) nm. HRMS (APCI): m/z calcd for C$_{17}$H$_{19}$BF$_2$N$_4$ [M + H]$^+$: 329.174672, 329.174808 found.

1,3,5,7-Tetramethyl-8-phenyl-4-bora-3a,4a-diaza-*s*-indacene (4.53)
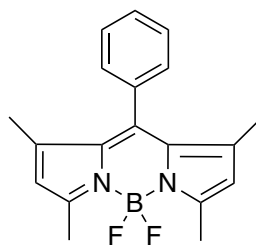
BODIPY **4.53**

In accordance with general procedure **B** as described above using 2,4-dimethylpyrrole (2.0 mL, 19.4 mmol) and the benzaldehyde (1.08 mL, 9 mmol) and final product was obtained and purified by column chromatography (silica gel; DCM/Hex, 1:1, v/v) and

removal of solvents followed by recrystallization (DCM/Hex) to yield green solid (21% yield). Analytical data is identical to the literature.[5] M.p. = 187 – 192 °C; Rf = 0.67 (DCM/Hex: 90/10); ^{1}H NMR (400 MHz, CDCl$_3$)) δ 7.56-7.43 (m, 3H, Ar-*H*), 7.28 (m, 2H, Ar-*H*), 5.98 (s, 2H, 2-*H*, 6-*H*), 2.53 (s, 6H, 3-C*H$_3$*, 5-C*H$_3$*), 1.35 (s, 6H, 1-C*H$_3$*, 7-C*H$_3$*). ^{19}F NMR (377 MHz, CDCl$_3$) δ -145.93 – -146.29 (m). ^{11}B NMR (128 MHz, CDCl$_3$) δ 0.69 (t, *J* = 32.3 Hz). IR (neat): 2956, 1598, 1408, 1325, 1164, 1040, 977 cm^{-1}. HRMS (ESI): m/z calcd for C$_{19}$H$_{19}$BF$_2$N$_2$ [M + H]$^+$: 325.168557, 325.169210 found.

2,6-Diethyl-1,3,5,7-tetramethyl-8-(4-pyridyl-4-bora-3a,4a-diaza-*s*-indacene (4.54)
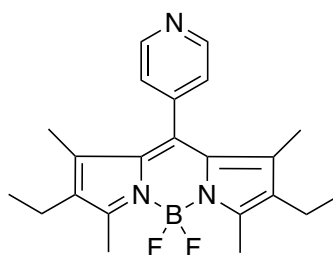
BODIPY **4.54**

In accordance with general procedure **C** as described above using 3-ethyl-2,4-dimethylpyrrole (2.2 mL, 17.9 mmol) and 4-pyridine carboxaldehyde (0.84 mL, 9 mmol) and final product was obtained and purified by column chromatography (silica gel; DCM/Hex, 6:4, v/v) and removal of solvents followed by recrystallization (DCM/Hex) to yield green-red solid (15% yield). Analytical data is identical to the literature.[6] M.p. = 165 – 170 °C; Rf = 0.52 (DCM/Hex: 90/10); ^{1}H NMR (400 MHz, CDCl$_3$) δ 8.77 (dd, *J* = 4.3, 1.6 Hz, 2H, Ar-*H*), 7.30 (dd, *J* = 4.3, 1.6 Hz, 2H, Ar-*H*), 2.53 (s, 6H, 3-C*H$_3$*, 5-C*H$_3$*), 2.30 (q, *J* = 7.6 Hz, 4H, 2-C*H$_2$*, 6-C*H$_2$*), 1.31 (s, 6H, 1-C*H$_3$*, 7-C*H$_3$*), 0.98 (t, *J* = 7.6 Hz, 6H, 2-C*H$_3$*, 6-C*H$_3$*). ^{19}F NMR (377 MHz, CDCl$_3$) δ -145.58 – -146.19 (m). ^{11}B NMR (128 MHz, CDCl$_3$) δ 0.73 (t, *J* = 33.2 Hz). IR (neat): 2956, 1598, 1408, 1325, 1164, 1040, 977 cm^{-1}. HRMS (ESI): m/z calcd for C$_{22}$H$_{26}$BF$_2$N$_3$ [M + H]$^+$: 382.226459, 382.226557 found.

2,6-Diethyl-1,3,5,7-tetramethyl-8-(5-pyrimidinyl)-4-bora-3a,4a-diaza-s-indacene (4.55)
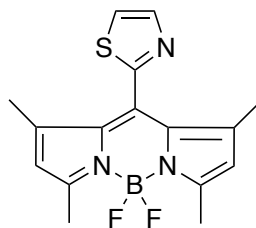

BODIPY **4.55**

In accordance with general procedure **C** as described above using 3-ethyl-2,4-dimethylpyrrole (2.2 mL, 17.9 mmol) and 5-pyrimidine carboxaldehyde (0.97 g, 9 mmol) and final product was obtained and purified by column chromatography (silica gel; DCM/Hex, 8:2, v/v) and removal of solvents followed by recrystallization (DCM/Hex) to yield green-red solid (10% yield). M.p. = 195 – 200 °C; Rf = 0.48 (DCM/Hex: 90/10); ^{1}H NMR (400 MHz, CDCl$_3$) δ 9.38 (s, 1H, Ar-*H*), 8.71 (s, 2H, Ar-*H*), 2.55 (s, 6H, 3-C*H$_3$*, 5-C*H$_3$*), 2.32 (q, *J* = 7.6 Hz, 4H, 2-C*H$_2$*, 6-C*H$_2$*), 1.32 (s, 6H, 1-C*H$_3$*, 7-C*H$_3$*), 0.99 (t, *J* = 7.6 Hz, 6H, 2-C*H$_3$*, 6-C*H$_3$*). ^{13}C NMR (101 MHz, CDCl$_3$) δ 158.94, 156.35, 155.73, 137.63, 134.05, 131.50, 130.94, 130.82, 17.22, 14.72, 13.04, 12.83. ^{19}F NMR (377 MHz, CDCl$_3$) δ -145.44 – -146.15 (m). ^{11}B NMR (128 MHz, CDCl$_3$) δ 0.73 (t, J = 32.9 Hz). IR (neat): 2962, 2929, 2872, 1723 IR (neat): 2956, 2922, 2853, 1723, 1580, 1543, 1401, 1281, 1183, 1041, 978 cm^{-1}. UV-Vis (CH$_2$Cl$_2$) λ$_{max}$ (ε [x10^3 M^{-1} cm^{-1}]) = 336 (2.01), 387 (7.47), 505 (26.28), 536 (76.05) nm. HRMS (APCI): m/z calcd for C$_{21}$H$_{25}$BF$_2$N$_3$ [M + H]$^+$: 383.221691, 383.221685 found.

2,6-Diethyl-1,3,5,7-tetramethyl-8-(4-quinolinium-yl)-4-bora-3a,4a-diaza-*s*-indacene (4.56)
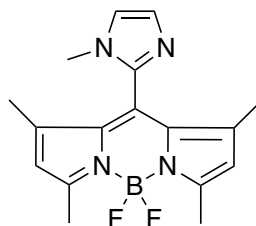

BODIPY **4.56**

In accordance with general procedure **C** as described above using 3-ethyl-2,4-dimethylpyrrole (2.2 mL, 17.9 mmol) and 4-quinoline carboxaldehyde (1.41 g, 9 mmol) and final product was obtained and purified by column chromatography (silica gel; DCM/Hex, 7:3, v/v) and removal of solvents followed by recrystallization (DCM/Hex) to yield green-red solid (14% yield). M.p. = 222 – 227 °C; Rf = 0.46 (DCM/Hex: 90/10); ^{1}H NMR (400 MHz, CDCl$_3$) δ 9.03 (d, *J* = 4.3 Hz, 1H, Ar-H), 8.19 (d, *J* = 8.5 Hz, 1H, Ar-*H*), 7.87 (d, *J* = 8.3 Hz, 1H, Ar-*H*), 7.78 (ddd, *J* = 8.3, 6.9, 1.3 Hz, 1H, Ar-*H*), 7.53 (ddd, *J* = 8.1, 7.0, 1.0 Hz, 1H, Ar-*H*), 7.40 (d, *J* = 4.3 Hz, 1H, Ar-*H*), 2.57 (s, 6H, 3-C*H$_3$*, 5-C*H$_3$*), 2.25 (q, *J* = 7.5 Hz, 4H, 2-C*H$_2$*, 6-C*H$_2$*), 0.99 (s, 6H, 1-C*H$_3$*, 7-C*H$_3$*), 0.94 (t, *J* = 7.6 Hz, 6H, 2-C*H$_3$*, 6-C*H$_3$*). ^{13}C NMR (101 MHz, CDCl$_3$) δ 162.24, 154.94, 150.44, 148.47, 142.75, 137.94, 134.84, 133.46, 130.48, 130.02, 128.05, 127.30, 125.29, 121.30, 17.18, 14.70, 12.79, 11.47. ^{19}F NMR (377 MHz, CDCl$_3$) δ -145.20- -146.08. ^{11}B NMR (128 MHz, CDCl$_3$) δ 0.87 (t, *J* = 33.2 Hz). IR (neat): 3658, 2980, 1587, 1471, 1362, 1180, 970 cm^{-1}. UV-Vis (CH$_2$Cl$_2$) λ$_{max}$ (ε [x10^3 M^{-1} cm^{-1}]) = 341 (5.21), 383 (10.77), 502 (33.18), 534 (92.52) nm. HRMS (APCI): m/z calcd for C$_{26}$H$_{28}$BF$_2$N$_3$ [M + H]$^+$: 432.242175, 432.242267 found.

2,6-Diethyl-1,3,5,7-tetramethyl-8-(2-quinolinium-yl)-4-bora-3a,4a-diaza-*s*-indacene (4.57)
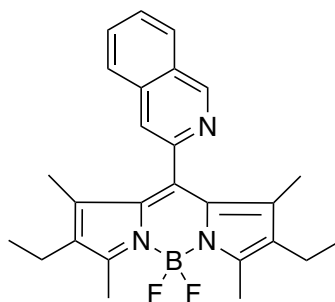
BODIPY **4.57**

In accordance with general procedure **C** as described above using 3-ethyl-2,4-dimethylpyrrole (2.2 mL, 17.9 mmol) and 2-quinoline carboxaldehyde (1.41 g, 9 mmol) and final product was obtained and purified by column chromatography (silica gel; DCM/Hex, 8:2, v/v) and removal of solvents followed by recrystallization (DCM/Hex) to yield green-red solid (13% yield). M.p. = 265 – 270 °C; Rf = 0.50 (DCM/Hex: 90/10); ^{1}H NMR (400 MHz, CDCl$_3$) δ 8.31 (d, *J* = 8.4 Hz, 1H, Ar-*H*), 8.17 (d, *J* = 8.4 Hz, 1H, Ar-*H*), 7.94 (d, *J* = 7.7 Hz, 1H, Ar-*H*), 7.81 (ddd, *J* = 8.4, 7.0, 1.4 Hz, 1H, Ar-*H*), 7.69 – 7.64 (m, 1H, Ar-*H*), 7.53 (d, *J* = 8.4 Hz, 1H, Ar-*H*), 2.54 (s, 6H, 3-C*H$_3$*, 5-C*H$_3$*), 2.28 (q, *J* = 7.6 Hz, 4H, 2-C*H$_2$*, 6-C*H$_2$*), 1.12 (s, 6H, 1-C*H$_3$*, 7-C*H$_3$*), 0.96 (t, *J* = 7.6 Hz, 6H, 2-C*H$_3$*, 6-C*H$_3$*). ^{13}C NMR (101 MHz, CDCl$_3$) δ 154.89, 154.72, 148.06, 137.73, 137.10, 132.94, 132.47, 130.65, 130.36, 129.74, 127.83, 127.48, 127.43, 122.08, 17.06, 14.61, 12.64, 11.27. ^{19}F NMR (377 MHz, CDCl$_3$) δ -144.86- -146.79. ^{11}B NMR (128 MHz, CDCl$_3$) δ 0.85 (t, *J* = 33.3 Hz). IR (neat): 3652, 2980, 1595, 1458, 1336, 1181, 971 cm^{-1}. UV-Vis (CH$_2$Cl$_2$) λ$_{max}$ (ε [x10^3 M^{-1} cm^{-1}]) = 321 (10.71), 376 (10.09), 506 (30.35), 533 (84.3) nm. HRMS (APCI): m/z calcd for C$_{26}$H$_{28}$BF$_2$N$_3$ [M + H]$^+$: 432.242175, 432.241948 found.

2,6-Diethyl-1,3,5,7-tetramethyl-8-(9-acridinyl)-4-bora-3a,4a-diaza-*s*-indacene (4.58)
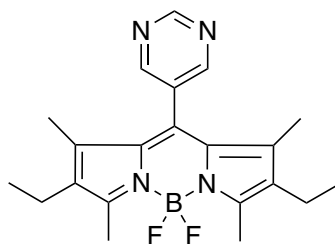

BODIPY **4.58**

In accordance with general procedure **C** as described above using 3-ethyl-2,4-dimethylpyrrole (2.2 mL, 17.9 mmol) and 9-acridine carboxaldehyde (1.86 g, 9 mmol) and final product was obtained and purified by column chromatography (silica gel; DCM/Hex, 9:1, v/v) and removal of solvents followed by recrystallization (DCM/Hex) to yield green-red solid (13% yield). M.p. = 255 – 260 °C; Rf = 0.43 (DCM/Hex: 90/10); ^{1}H NMR (400 MHz, CDCl$_3$) δ 8.28 (d, *J* = 8.8 Hz, 2H, Ar-*H*), 7.98 (d, *J* = 8.5 Hz, 2H, Ar-*H*), 7.84 – 7.79 (m, 2H, Ar-*H*), 7.51 (ddd, *J* = 8.5, 6.6, 1.0 Hz, 2H, Ar-*H*), 2.60 (s, 6H, 3-C*H$_3$*, 5-C*H$_3$*), 2.19 (q, *J* = 7.5 Hz, 4H, 2-C*H$_2$*, 6-C*H$_2$*), 0.90 (t, *J* = 7.6 Hz, 6H, 2-C*H$_3$*, 6-C*H$_3$*), 0.58 (s, 6H, 1-C*H$_3$*, 7-C*H$_3$*). ^{13}C NMR (101 MHz, CDCl$_3$) δ 155.02, 148.43, 137.84, 133.36, 130.95, 129.44, 127.24, 125.61, 125.05, 17.02, 14.55, 12.73, 10.74. ^{19}F NMR (377 MHz, CDCl$_3$) δ -145.40- -145.66. ^{11}B NMR (128 MHz, CDCl$_3$) δ 1.01 (t, J = 33.2 Hz). IR (neat): 3656, 2971, 1535, 1403, 1299, 1177, 971 cm^{-1}. UV-Vis (CH$_2$Cl$_2$) λ$_{max}$ (ε [x10^3 M^{-1} cm^{-1}]) = 346 (16.74), 364 (26.91), 503 (35.84), 537 (108.96) nm. HRMS (APCI): m/z calcd for C$_{30}$H$_{30}$BF$_2$N$_3$ [M + H]$^+$: 482.257890, 482.257869 found.

2,6-Diethyl-1,3,5,7-tetramethyl-8-(2-thiazolyl)-4-bora-3a,4a-diaza-*s*-indacene (4.59)
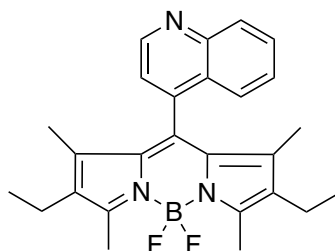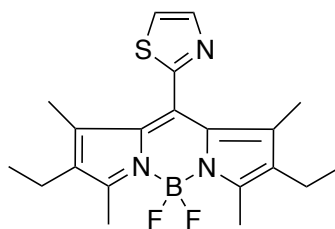

BODIPY **4.59**

In accordance with general procedure **C** as described above using 3-ethyl-2,4-dimethylpyrrole (2.2 mL, 17.9 mmol) and 2-thiazole carboxaldehyde (1.02 g, 9 mmol)

and final product was obtained and purified by column chromatography (silica gel; DCM/Ethyl acetate, 9.5:0.5, v/v) and removal of solvents followed by recrystallization (DCM/Hex) to yield green-red solid (13% yield). M.p. = >300 °C; Rf = 0.39 (DCM/Hex: 90/10); ^{1}H NMR (400 MHz, CDCl$_3$) δ 7.98 (d, *J* = 3.2 Hz, 1H, *Ar*-H), 7.61 (d, *J* = 3.2 Hz, 1H, *Ar*-H), 2.53 (s, 6H, 3-C*H$_3$*, 5-C*H$_3$*), 2.30 (q, *J* = 7.5 Hz, 4H, 2-C*H$_2$*, 6-C*H$_2$*), 1.34 (s, 6H, 1-C*H$_3$*, 7-C*H$_3$*), 0.98 (t, *J* = 7.6 Hz, 6H, 2-C*H$_3$*, 6-C*H$_3$*). ^{13}C NMR (101 MHz, CDCl$_3$) δ 154.63, 136.66, 132.42, 131.61, 118.59, 17.28, 14.59, 12.55, 9.37. ^{19}F NMR (377 MHz, CDCl$_3$) δ -144.88- -146.38. ^{11}B NMR (128 MHz, CDCl$_3$) δ 0.75 (t, *J* = 32.5 Hz). IR (neat): 3110, 2961, 2925, 1596, 1539, 1397, 1182, 969 cm^{-1}. UV-Vis (CH$_2$Cl$_2$) λ$_{max}$ (ε [x10^3 M^{-1} cm^{-1}]) = 337 (3.15), 394 (9.12), 513 (19.64), 547 (54.73) nm. HRMS (APCI): m/z calcd for C$_{20}$H$_{24}$BF$_2$N$_3$S [M + H]$^+$: 388.182851, 388.183008 found.

The formation of the BODIPY **4.59** resulted in a side-product (*Z,Z*)-2,5-bis(2-thiazolylmethanylidene)-3-ethyl-4-methylpyrrole (**4.59a**).
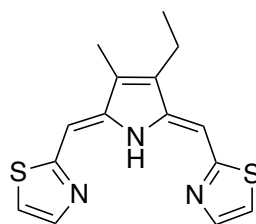
4.59a

M.p. = 200-205 °C; ^{1}H NMR (400 MHz, CDCl$_3$) δ 11.88 (s, 1H,), 7.92 (t, *J* = 5.5 Hz, 2H, Ar-H), 7.13 (d, *J* = 3.3 Hz, 2H), 5.97 (d, *J* = 9.3 Hz, 2H), 2.50 (q, *J* = 7.6 Hz, 2H, Ar-H), 2.06 (s, 3H, Ar-*H*), 1.19 (t, J = 7.6 Hz, 3H, Ar-*H*). ^{13}C NMR (101 MHz, CDCl$_3$) δ 166.21, 166.17, 146.96, 145.92, 143.68, 139.48, 132.73, 115.23, 90.80, 90.76, 17.50, 14.62, 9.14, 1.05. IR (neat): 2262, 1576, 1276, 811 cm^{-1}. HRMS (APCI): m/z calcd for C$_{15}$H$_{16}$N$_3$S$_2$ [M + H]$^+$: 302.078016, 302.078557 found.

**2,6-Diethyl-1,3,5,7-tetramethyl-8-(1-methyl-1H-imidazol-2-yl)-4-bora-3a,4a-diaza-s-indacene (4.60)**
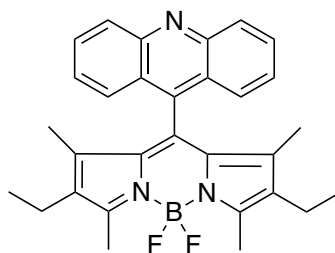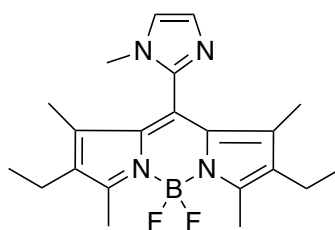

BODIPY **4.60**

In accordance with general procedure **C** as described above using 3-ethyl-2,4-dimethylpyrrole (2.2 mL, 17.9 mmol) and 1-methyl-2-imidazol carboxaldehyde (0.99 g, 9 mmol) and final product was obtained and purified by column chromatography (silica gel; DCM/Ethyl acetate, 9:1, v/v) and removal of solvents followed by recrystallization (DCM/Hex) to yield green-red solid (5% yield). M.p. = 205 – 210 °C; Rf = 0.35 (DCM/Hex: 90/10); ^{1}H NMR (400 MHz, CDCl$_3$) δ 7.20 (s, 1H, Ar-*H*), 7.04 (s, 1H, Ar-*H*), 3.48 (s, 3H, Ar-N-C*H$_3$*), 2.52 (s, 6H, 3-C*H$_3$*, 5-C*H$_3$*), 2.32 (q, *J* = 7.6 Hz, 4H, 2-C*H$_2$*, 6-C*H$_2$*), 1.30 (s, 6H, 1-C*H$_3$*, 7-C*H$_3$*), 1.00 (t, *J* = 7.6 Hz, 6H, 2-C*H$_3$*, 6-C*H$_3$*). ^{13}C NMR (101 MHz, CDCl$_3$) δ 155.84, 137.92, 133.20, 131.96, 129.37, 120.91, 46.91, 33.01, 29.71, 17.08, 14.55, 12.72, 9.36, 8.68. ^{19}F NMR (377 MHz, CDCl$_3$) δ -144.83- -146.61. ^{11}B NMR (128 MHz, CDCl$_3$) δ 0.75 (t, *J* = 33.1 Hz). IR (neat): 3093, 2961, 2926, 1708, 1551, 1411, 1162, 976 cm^{-1}. UV-Vis (CH$_2$Cl$_2$) λ$_{max}$ (ε [x10^3 M^{-1} cm^{-1}]) = 341 (3.56), 391 (6.93), 511 (17.70), 545 (46.7) nm. HRMS (APCI): m/z calcd for C$_{21}$H$_{27}$BF$_2$N$_4$ [M + H]$^+$: 385.237342, 385.237623 found.

1,3,5,7-Tetramethyl-8-(4-*N*-pyridinium)-4-bora-3a,4a-diaza-*s*-indacene (4.46a)
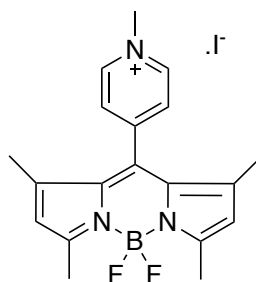
BODIPY **4.46a**

In accordance with general procedure **D** as described above using BODIPY **4.46** (0.1 g, 0.305 mmol) and methyl iodide (0.018 mL, 0.305 mmol) the product is obtained further recrystallized from DCM/MeOH gave red crystals (81% yield). Analytical data is identical to the literature.[7] M.p. = 250 – 255 °C; ^{1}H NMR (CDCl$_3$, 600 MHz): δ (ppm): δ 8.6 (d, *J*=5.8 Hz, 2H, Ar-*H*), 7.35 (d, *J*=5.8 Hz, 2H, Ar-*H*), 6.01 (s, 2H, 2-*H*, 6-*H*), 4.83 (s,3H, Ar-N$^+$-C*H$_3$*), 2.56 (s, 6H, 3-C*H$_3$*, 5-C*H$_3$*),1.41 (s, 6H, 1-C*H$_3$*, 7-C*H$_3$*). ^{19}F NMR (377 MHz, CDCl$_3$) δ -144.83- -146.61. ^{11}B NMR (128 MHz, CDCl$_3$) δ 0.75 (t, *J* = 33.1 Hz). IR (neat): 2950, 1550, 1418, 1290, 1140, 1051, 958 cm^{-1}. HRMS(APCI): m/z calcd for C$_{19}$H$_{21}$BF$_2$N$_3$ [M + H]$^+$: 326.163789, 326.164710 found.

2,6-Diethyl-1,3,5,7-tetramethyl-8-(4-*N*-methylpyridinium)-4-bora-3a,4a-diaza-*s*-indacene (4.54a)
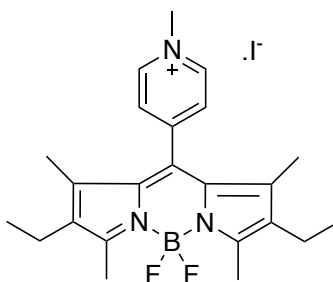
BODIPY **4.54a**

In accordance with general procedure **D** as described above using BODIPY **4.54** (0.1 g, 0.260 mmol) and methyl iodide (0.016 mL, 0.260 mmol) the product is obtained further recrystallized from DCM/MeOH and gave red crystals (73% yield). Analytical data is identical to the literature.[8] M.p. = 223 – 228 °C; ^{1}H NMR (CDCl$_3$, 600 MHz): δ (ppm): δ 8.6 (d, *J*=5.8 Hz, 2H, Ar-*H*), 7.35 (d, *J*=5.8 Hz, 2H, Ar-*H*), 4.79 (s,3H, Ar-N$^+$-C*H$_3$*), 2.51 (s, 6H, 3-C*H$_3$*, 5-C*H$_3$*), 2.32 (q, *J* = 7.6 Hz, 4H, 2-C*H$_2$*, 6-C*H$_2$*), 1.32 (s, 6H, 1-C*H$_3$*, 7-

C*H₃*), 1.0 (t, *J* = 7.6 Hz, 6H, 2-C*H₃*, 6-C*H₃*). ^{19}F NMR (377 MHz, CDCl₃) δ -144.78- -146.51 ^{11}B NMR (128 MHz, CDCl₃) δ 0.74 (t, *J* = 32.1 Hz). IR (neat): 2963, 1536, 1436, 1360, 1138, 1049, 962 cm^{-1}. HRMS(APCI): m/z calcd for $C_{23}H_{29}BF_2N_3$ [M + H]$^+$: 396.242126, 396.241808 found.

1,3,5,7-Tetramethyl-8-(4-*N*-methylquinolinium)-4-bora-3a,4a-*s*-indacene (4.48a)
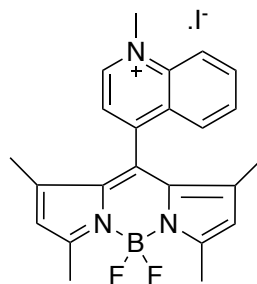
BODIPY **4.48a**

In accordance with general procedure **D** as described above using BODIPY **4.48** (0.1 g, 0.265 mmol) and methyl iodide (0.016 mL, 0.265 mmol) the product is obtained further recrystallized from DCM/MeOH and gave red crystals (85% yield). M.p. = 250 – 255 °C; ^{1}H NMR (CDCl₃, 500 MHz): δ (ppm): 10.61 (d, *J* = 5.2 Hz, 1H, Ar-*H*), 8.53 (d, *J* = 8.8 Hz, 1H, Ar-*H*), 8.31 – 8.26 (m, 1H, Ar-*H*), 8.24 (d, *J* = 8.0 Hz, 1H, Ar-*H*), 8.07 (d, *J* = 5.4 Hz, 1H, Ar-*H*), 7.95 (t, *J* = 7.4 Hz, 1H, Ar-*H*), 6.02 (s, 2H, 2-*H*, 6-*H*), 5.05 (s, 3H, Ar-N$^+$-C*H₃*), 2.60 (s, 6H, 3-C*H₃*, 5-C*H₃*), 1.18 (s, 6H, 1-C*H₃*, 7-C*H₃*). 13C NMR (101 MHz, CDCl3) δ 158.59, 153.04, 151.41, 142.21, 138.49, 136.80, 131.44, 131.12, 130.10, 128.91, 127.78, 123.04, 122.78, 119.25, 47.13, 15.14, 14.85. ^{19}F NMR (377 MHz, CDCl₃) δ -144.83 – -146.69 (m). ^{11}B NMR (128 MHz, CDCl₃) δ 0.71 (t, *J* = 31.7 Hz). IR (neat): 3640, 2976, 1590, 1399, 1365, 1185, 961 cm^{-1}. UV-Vis (CH₂Cl₂)) λ$_{max}$ (ε [x10^3 M^{-1} cm^{-1}]) = 322 (8.93), 388 (4.29), 481 (15.5), 512 (40.68) nm. HRMS(APCI): m/z calcd for $C_{23}H_{23}BF_2N_3$ [M + H]$^+$: 390.195174, 390.195769 found.

2,6-Diethyl-1,3,5,7-tetramethyl-8-(4-*N*-methylquinolinium)-4-bora-3a,4a-diaza-*s*-indacene (4.56a)
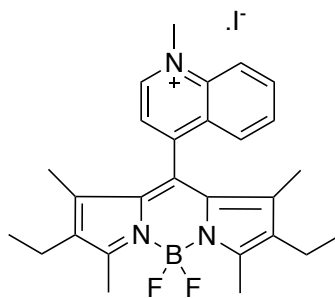
BODIPY **4.56a**

In accordance with general procedure **D** as described above using BODIPY **4.56** (0.1 g, 0.231 mmol) and methyl iodide (0.014 mL, 0.231 mmol) the product is obtained further recrystallized from DCM/MeOH to give red crystals (75% yield). M.p. = 184 – 189 °C; ^{1}H NMR (CDCl$_3$, 500 MHz): δ (ppm): 10.51 (d, *J* = 5.9 Hz, 1H, Ar-*H*), 8.53 (d, *J* = 8.8 Hz, 1H, Ar-*H*), 8.30 – 8.25 (m, 2H, Ar-*H*), 8.03 (d, *J* = 5.8 Hz, 1H, Ar-*H*), 7.94 (dd, *J* = 14.8, 6.9 Hz, 1H, Ar-*H*), 5.05 (d, *J* = 6.3 Hz, 3H, Ar-N$^+$-C*H$_3$*), 2.57 (s, 6H, 3-C*H$_3$*, 5-C*H$_3$*), 2.23 (q, 4H, 2-C*H$_2$*, 6-C*H$_2$*), 1.06 (s, 6H, 1-C*H$_3$*, 7-C*H$_3$*), 0.94 (t, J = 7.5 Hz, 6H, 2-C*H$_3$*, 6-C*H$_3$*). 13C NMR (101 MHz, CDCl3) δ 156.99, 154.31, 150.90, 138.43, 137.11, 136.81, 134.61, 131.46, 129.51, 129.48, 129.26, 128.12, 123.09, 119.09, 47.22, 17.05, 14.49, 12.85, 12.59. ^{19}F NMR (377 MHz, CDCl$_3$) δ -144.61 – -146.12 (m). ^{11}B NMR (128 MHz, CDCl$_3$) δ 0.73 (t, *J* = 32.4 Hz). IR (neat): 2980, 1708, 1544, 1306, 1155, 1081, 971 cm^{-1}. UV-Vis (CH$_2$Cl$_2$) λ$_{max}$ (ε [x10^3 M^{-1} cm^{-1}]) = 318 (9.3), 392 (7.53), 503 (20.10), 533 (35.63) nm. HRMS(APCI): m/z calcd for C$_{27}$H$_{31}$BF$_2$N$_3$[M + H]$^+$: 446.257842, 446.258194 found.

1,3,5,7-Tetramethyl-8-(4-pyridinium-yl-*N*-(benzyl-4-carboxylate))-4-bora-3a,4a-diaza-*s*-indacene (4.46b)

BODIPY **4.46b**

In accordance with general procedure **E** as described above using BODIPY **4.46** (0.1 g, 0.305 mmol) and 4-(bromomethyl)benzoic acid (0.524 g, 2.44 mmol) the product is obtained further recrystallized from DCM/MeOH and gave red crystals (82% yield). M.p. = 265 – 270 °C; ^{1}H NMR (400 MHz, MeOD) δ 9.33 (d, *J* = 6.7 Hz, 2H, Ar-*H*), 8.38 (d, *J* = 6.7 Hz, 2H, Ar-*H*), 8.14 (d, *J* = 8.3 Hz, 2H, Ar-*H*), 7.63 (d, *J* = 8.3 Hz, 2H Ar-*H*), 6.19 (s, 2H, Ar-N$^+$-C*H$_2$*), 6.10 (s, 2H, 2-*H*, 6-*H*), 2.52 (s, 6H, 3-C*H$_3$*, 5-C*H$_3$*), 1.47 (s, 6H, 1-C*H$_3$*, 7-C*H$_3$*). ^{13}C NMR (101 MHz, MeOD) δ 167.25, 157.92, 153.53, 146.23, 142.34, 137.91, 133.76, 132.22, 130.54, 129.39, 129.27, 128.51, 122.29, 64.05, 13.95, 13.28. ^{19}F NMR (377 MHz, MeOD) δ -146.89- -147.15. ^{11}B NMR (128 MHz, MeOD) δ 0.60 (t, *J* = 31.7 Hz). IR (neat): 3376, 2980, 1708, 1544, 1306, 1155, 1081, 971 cm^{-1}. UV-Vis (MeOH) λ$_{max}$ (ε [x10^3 M^{-1} cm^{-1}]) = 300 (5.54), 376 (4.83), 481 (12.75), 511 nm (44.18). HRMS (APCI): m/z calcd for C$_{26}$H$_{25}$BF$_2$N$_3$O$_2$$^+$ [M + H]$^+$: 460.200705, 460.199798 found.

2,6-Diethyl-1,3,5,7-tetramethyl-8-(4-pyridinium-yl-*N*-(benzyl-4-carboxylate))-4-bora-3a,4a-diaza-*s*-indacene (4.54b)


BODIPY **4.54b**

In accordance with general procedure **E** as described above using BODIPY **4.54** (0.1 g, 0.260 mmol) and 4-(bromomethyl)benzoic acid (0.447 g, 2.08 mmol) the product is obtained further recrystallized from DCM/MeOH and gave red crystals (75% yield). M.p. = 270 – 275 °C; ^{1}H NMR (400 MHz, MeOD) δ 9.33 (d, *J* = 6.6 Hz, 2H, Ar-*H*), 8.37 (d, *J* = 6.6 Hz, 2H, Ar-*H*), 8.15 (d, *J* = 8.3 Hz, 2H, Ar-*H*), 7.64 (d, *J* = 8.3 Hz, 2H, Ar-*H*), 6.12 (s, 2H, Ar-N$^+$-C*H$_2$*), 2.51 (s, 6H, 3-C*H$_3$*, 5-C*H$_3$*), 2.39 (q, *J* = 7.5 Hz, 4H, 2-C*H$_2$*, 6-C*H$_2$*), 1.39 (s, 6H, 1-C*H$_3$*, 7-C*H$_3$*), 1.01 (t, *J* = 7.6 Hz, 6H, 2-C*H$_3$*, 6-C*H$_3$*). ^{13}C NMR (101 MHz, MeOD) δ 168.83, 157.58, 155.81, 147.51, 147.00, 139.31, 138.58, 135.67, 133.78, 131.94, 130.99, 129.87, 65.42, 17.76, 14.87, 12.85, 12.79. ^{19}F NMR (377 MHz, MeOD) δ -146.59- -147.33. ^{11}B NMR (128 MHz, MeOD) δ 0.62 (t, *J* = 32.1 Hz). IR (neat): 3313, 2969, 2658, 1677, 1539, 1312, 1173, 1060, 969 cm^{-1}. UV-Vis (MeOH) λmax (ε [x10^3 M^{-1} cm^{-1}]) = 310 (3.24), 392 (5.40), 504 (12.49), 537 (33.02) nm. HRMS (APCI): m/z calcd for C$_{30}$H$_{33}$BF$_2$N$_3$O$_2$$^+$ [M + H]$^+$: 516.263372, 516.264548 found.

1,3,5,7-Tetramethyl -8-(4-quinolinium-yl-*N*-(benzyl-4-carboxylate))-4-bora-3a,4a-diaza-*s*-indacene (4.48b)


BODIPY **4.48b**

In accordance with general procedure **E** as described above using BODIPY **4.48** (0.1 g, 0.265 mmol) and 4-(bromomethyl)benzoic acid (0.455 g, 2.12 mmol) the product is obtained further recrystallized from DCM/MeOH and gave red crystals (63% yield). M.p. = 245 – 250 °C; ^{1}H NMR (400 MHz, MeOD) δ 9.81 (d, *J* = 6.0 Hz, 1H, Ar-*H*), 8.62 (d, *J* = 9.0 Hz, 1H, Ar-*H*), 8.46 (d, *J* = 6.0 Hz, 1H, Ar-*H*), 8.32 (s, 1H, Ar-*H*), 8.30 (d, *J* = 4.3 Hz, 1H, Ar-*H*), 8.08 (d, *J* = 8.4 Hz, 2H, Ar-*H*), 7.48 (d, *J* = 8.4 Hz, 2H, Ar-*H*), 6.59 (s, 2H, Ar-N$^+$-C*H$_2$*), 6.20 (s, 2H, 2-*H*, 6-*H*), 2.59 (s, 6H, 3-C*H$_3$*, 5-C*H$_3$*), 1.21 (s, 6H, 1-C*H$_3$*, 7-C*H$_3$*). ^{13}C NMR (101 MHz, MeOD) δ 168.78, 159.70, 155.16, 151.98, 143.67, 143.19, 139.69, 139.04, 138.47, 133.40, 131.85, 131.44, 130.98, 128.83, 128.30, 124.85, 123.73, 121.23, 62.32, 14.75, 14.59. ^{19}F NMR (377 MHz, MeOD) δ -146.76- -147.03. ^{11}B NMR (128 MHz, MeOD) δ 0.75 (t, *J* = 31.7 Hz). IR (neat): 2973, 2159, 1705, 1542, 1307, 1191, 1072, 973 cm^{-1}. UV-Vis (MeOH) λ_{max} (ε [x10^3 M^{-1} cm^{-1}]) = 322 (8.94), 394 (3.76), 481 (15.98), 510 (37.31) nm. HRMS (APCI): m/z calcd for C$_{30}$H$_{27}$BF$_2$N$_3$O$_2^+$ [M + H]$^+$: 510.216420, 510.214860 found.

2,6-Diethyl-1,3,5,7-tetramethyl-2,6-diethyl-8-(4-quinolinium-yl-*N*-(benzyl-4-carboxylate))-4-bora-3a,4a-diaza-*s*-indacene (4.56b)
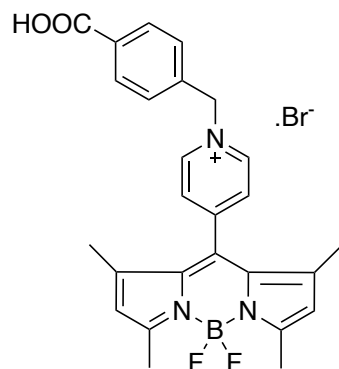

BODIPY **4.56b**

In accordance with general procedure **E** as described above using BODIPY **4.56** (0.1 g, 0.231 mmol) and 4-(bromomethyl)benzoic acid (0.395 g, 1.84 mmol) the product is obtained further recrystallized from DCM/MeOH and gave red crystals (68% yield). M.p. = 184 – 189 °C; ^{1}H NMR (400 MHz, MeOD) δ 9.80 (d, *J* = 6.0 Hz, 1H, Ar-*H*), 8.62 (d, *J* = 8.8 Hz, 1H, Ar-*H*), 8.43 (d, *J* = 5.8 Hz, 1H, Ar-*H*), 8.33 (d, *J* = 8.3 Hz, 1H, Ar-*H*), 8.30 (d, *J* = 8.9 Hz, 1H, Ar-*H*), 8.10 (d, *J* = 8.3 Hz, 2H, Ar-*H*), 8.05 (t, *J* = 7.7 Hz, 1H, Ar-*H*), 7.49 (d, *J* = 8.4 Hz, 2H, Ar-*H*), 6.60 (s, 2H, Ar-N$^+$-C*H$_2$*), 2.58 (s, 6H, 3-C*H$_3$*, 5-C*H$_3$*), 2.37 (q, *J* = 7.5 Hz, 4H, 2-C*H$_2$*, 6-C*H$_2$*), 1.13 (s, 6H, 1-C*H$_3$*, 7-C*H$_3$*), 0.99 (t, *J* = 7.5 Hz, 6H, 2-C*H$_3$*, 6-C*H$_3$*). ^{13}C NMR (101 MHz, MeOD) δ 159.70, 155.09, 151.85, 143.68, 139.72, 138.42, 133.37, 131.77, 131.72, 131.45, 130.97, 130.15, 128.80, 128.10, 124.81, 123.77, 121.26, 62.40, 47.95, 32.76, 23.74, 14.58, 14.43. ^{19}F NMR (377 MHz, MeOD) δ -146.21- -146.53. ^{11}B NMR (128 MHz, MeOD) δ 0.75 (t, *J* = 31.9 Hz). IR (neat): 3313, 2969, 1944, 1677, 1539, 1312, 1173, 1060, 969 cm^{-1}. UV-Vis (MeOH) λ$_{max}$ (ε [x10^3 M^{-1} cm^{-1}]) = 322 (9.66), 408 (5.73), 506 (18.55), 536 (30.80) nm. HRMS (APCI): m/z calcd for C$_{34}$H$_{35}$BF$_2$N$_3$O$_2^+$ [M + H]$^+$: 566.279085, 566.277708 found.

1,3,5,7-Tetramethyl-8-(*N*-(4-phenoxybutyl)pyridinium-4-yl)-4-bora-3a,4a-diaza-*s*-indacene (4.46c)
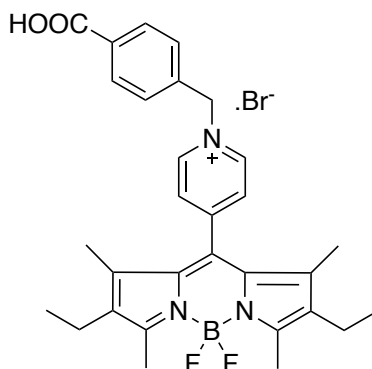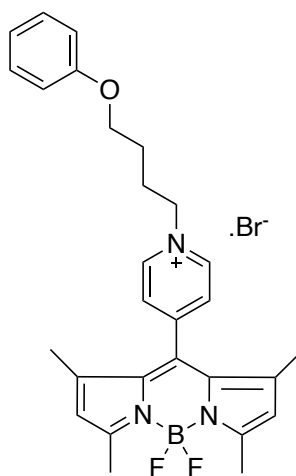

BODIPY **4.46c**

In accordance with general procedure **F** as described above using BODIPY **4.46** (0.1 g, 0.305mmol) and 4-bromobutyl phenyl ether (0.559 g, 2.44 mmol) the product is obtained further recrystallized from DCM/MeOH and gave red crystals (70% yield). M.p. = 240 – 245 °C; ^{1}H NMR (400 MHz, CDCl$_3$) δ 9.78 (d, *J* = 6.7 Hz, 2H, Ar-*H*), 8.00 (t, *J* = 9.7 Hz, 2H, Ar-*H*), 7.35 – 7.26 (m, 2H, Ar-*H*), 6.96 (t, *J* = 7.4 Hz, 1H, Ar-*H*), 6.87 (d, *J* = 7.8 Hz, 2H, Ar-N$^+$-C*H$_2$*), 6.06 (s, 2H, 2-*H*, 6-*H*), 5.34 (t, *J* = 7.5 Hz, 2H, Ar-*H*), 4.07 (t, J = 5.6 Hz, 2H, Ar-*H*), 2.57 (s, 6H, 3-C*H$_3$*, 5-C*H$_3$*), 2.37 (dd, *J* = 14.7, 7.5 Hz, 2H, Ar-*H*), 1.94 (dd, *J* = 13.7, 5.8 Hz, 2H, Ar-*H*), 1.41 (d, *J* = 4.5 Hz, 6H, 1-C*H$_3$*, 7-C*H$_3$*). ^{13}C NMR (101 MHz, CDCl$_3$) δ 158.77, 158.38, 146.03, 141.64, 132.24, 129.68, 129.27, 128.61, 123.31, 123.02, 121.23, 114.42, 66.85, 62.02, 29.61, 25.48, 15.51, 14.82. ^{19}F NMR (377 MHz, CDCl3) δ -145.80- -146.05. ^{11}B NMR (128 MHz, MeOD) δ 0.75 (t, *J* = 31.9 Hz). IR (neat): 2955, 1985, 1640, 1543, 1296, 1150, 1080, 970 cm^{-1}. UV-Vis (CH$_2$Cl$_2$) λ$_{max}$ (ε [x10^3 M^{-1} cm^{-1}]) = 307 (5.76), 367 (6.5), 476 (17.27), 506 (61.94) nm. HRMS (APCI): m/z calcd for C$_{28}$H$_{31}$BF$_2$N$_3$O$^+$ [M + H]$^+$: 474.252774, 474.251830 found.

2,6-Diethyl-1,3,5,7-tetramethyl-8-(*N*-(4-phenoxybutyl)pyridinium-4-yl)-4-bora-3a,4a-diaza-*s*-indacene (4.54c)
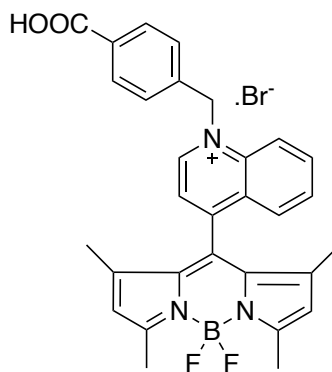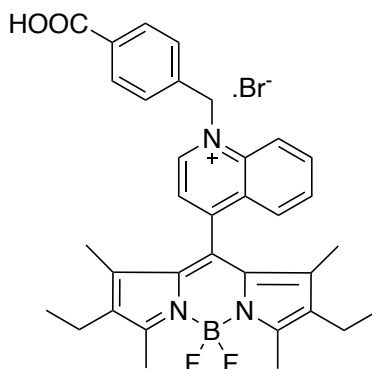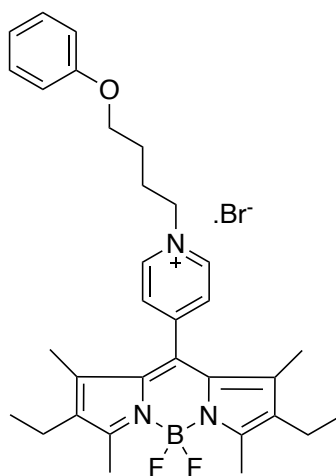

BODIPY **4.54c**

In accordance with general procedure **F** as described above using BODIPY **4.54** (0.1 g, 0.260 mmol) and 4-bromobutyl phenyl ether (0.476 g, 2.08 mmol) the product is obtained further recrystallized from DCM/MeOH (72% yield). M.p. = 210 – 215 °C; ^{1}H NMR (400 MHz, CDCl$_3$) δ 9.85 (d, *J* = 6.3 Hz, 2H, Ar-*H*), 8.00 (d, *J* = 6.4 Hz, 2H, Ar-*H*), 6.94 (t, *J* = 6.9 Hz, 1H, Ar-*H*), 6.87 (d, *J* = 7.8 Hz, 2H, Ar-N$^+$-C*H$_2$*), 5.38 (t, *J* = 7.3 Hz, 2H, Ar-*H*), 4.06 (t, *J* = 5.7 Hz, 2H, Ar-*H*), 2.54 (s, 6H, 3-C*H$_3$*, 5-C*H$_3$*), 2.37 (dd, *J* = 14.8, 7.3 Hz, 2H, Ar-*H*), 2.28 (q, *J* = 7.5 Hz, 4H, 2-C*H$_2$*, 6-C*H$_2$*), 1.92 (d, *J* = 12.1, 5.9 Hz, 2H, Ar-*H*), 1.67 (s, 2H, Ar-*H*), 1.30 (s, 6H, 1-C*H$_3$*, 7-C*H$_3$*), 0.97 (t, *J* = 7.5 Hz, 6H, 2-C*H$_3$*, 6-C*H$_3$*). ^{13}C NMR (101 MHz, CDCl$_3$) δ 158.54, 157.15, 154.68, 146.11, 146.05, 136.77, 134.90, 130.97, 129.77, 128.95, 121.28, 114.55, 66.97, 61.97, 29.75, 25.64, 17.19, 14.62, 13.05, 12.95. ^{19}F NMR (377 MHz, CDCl3) δ -145.42- -145.68. ^{11}B NMR (128 MHz, CDCl3) δ 0.59 (t, *J* = 32.4 Hz). IR (neat): 2964, 1976, 1635, 1540, 1312, 1157, 1075, 970 cm^{-1}. UV-Vis (CH$_2$Cl$_2$) λ$_{max}$ (ε [x10^3 M^{-1} cm^{-1}]) = 307 (5.76), 367 (6.5), 476 (17.27), 506 (61.94) nm. HRMS (APCI): m/z calcd for C$_{32}$H$_{39}$BF$_2$N$_3$O$^+$ [M + H]$^+$: 530.315440, 530.314255 found

1,3,5,7-tetramethyl-8-(4-pyridyl)-4,4-(3-(dimethylamino)prop-1-yn-1-yl)-4-bora-3a,4a-diaza-s-indacene (4.46d)
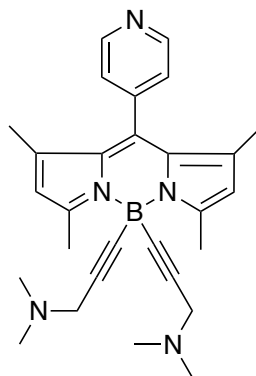
BODIPY **4.46d**

In accordance with general procedure, **G** as described above using BODIPY **4.46** (0.1 g, 0.307 mmol, 3-dimethylamino-1-propyne (0.147 mL, 1.38 mmol) and n-BuLi (1.15 mL, 1.228 mmol) and final product was obtained and purified by column chromatography (silica gel; DCM/MeOH, 9.9:0.1, v/v) and removal of solvents followed by recrystallization (DCM/Hex/MeOH) to yield pink solid (45% yield). M.p. = 155 – 160 °C; Rf = 0.35 (DCM/MeOH: 99/1); ^{1}H NMR (400 MHz, MeOD) δ 8.75 (dd, J = 4.5, 1.5 Hz, 2H, Ar-H), 7.51 (dd, J = 4.4, 1.6 Hz, 2H, Ar-H), 6.14 (s, 2H, 2-H, 6-H), 3.22 (s, 4H, CH_2), 2.77 (s, 6H, 3-CH_3, 5-CH$_3$), 2.30 (s, 12H, N-CH_3), 1.44 (s, 6H, 1-CH_3, 7-CH$_3$). ^{13}C NMR (101 MHz, MeOD) δ 156.31, 150.21, 145.24, 140.93, 138.24, 128.59, 124.66, 122.06, 43.21, 15.47, 13.92. ^{11}B NMR (128 MHz, MeOD) δ -13.34 (s). IR (neat): 2926, 2163, 1653, 1598, 1305, 1176, 1093, 978 cm^{-1}. UV-Vis (MeOH) λ$_{max}$ (ε [x10^3 M^{-1} cm^{-1}]) = 308 (6.69), 356 (5.22), 474 (13.41), 504 (57.21) nm. HRMS (APCI): m/z calcd for C$_{28}$H$_{34}$BN$_5$ [M + H]$^+$: 452.298501, 452.298621 found.

1,3,5,7-tetramethyl-8-(9-acridinyl)-4,4-(3-(dimethylamino)prop-1-yn-1-yl)-4-bora-3a,4a-diaza-s-indacene (4.50a)
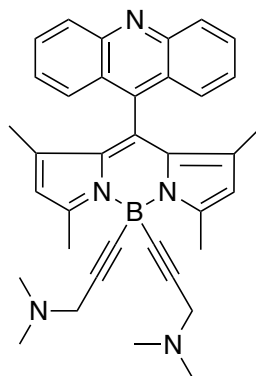
BODIPY **4.50**

In accordance with general procedure, **G** as described above using BODIPY **4.50** (0.1 g, 0.234 mmol, 3-dimethylamino-1-propyne (0.112 mL, 1.05 mmol) and n-BuLi (0.88 mL, 0.938 mmol) and final product was obtained and purified by column chromatography (silica gel; DCM/MeOH, 9.8:0.2, v/v) and removal of solvents followed by recrystallization (DCM/Hex/MeOH) to yield pink solid (30% yield). M.p. = 187 – 192 °C; Rf = 0.32 (DCM/MeOH: 99/1); ^{1}H NMR (400 MHz, CDCl$_3$) δ 8.28 (d, J = 8.8 Hz, 2H, Ar-H), 7.91 (d, J = 8.6 Hz, 2H, Ar-H), 7.84 – 7.80 (m, 2H, Ar-H), 7.54 – 7.49 (m, 2H, Ar-H), 5.99 (s, 2H, 2-H, 6-H), 3.59 (s, 4H, CH_2), 2.80 (s, 6H, 3-CH_3, 5-CH$_3$), 2.61 (s, 12H, N-CH_3), 0.67 (s, 6H, 1-CH_3, 7-CH$_3$). ^{13}C NMR (101 MHz, CDCl$_3$) δ 156.01, 148.74, 141.13, 139.31, 135.48, 130.73, 129.85, 129.63, 127.35, 125.17, 124.77, 122.26, 48.51, 43.09, 29.70, 16.33, 13.70. ^{11}B NMR (128 MHz, CDCl$_3$) δ -0.96 (s). IR (neat): 2923, 2163, 1653, 1548, 1361, 1176, 1094, 977 cm^{-1}. UV-Vis (CH$_2$Cl$_2$)) λ$_{max}$ (ε [x10^3 M^{-1} cm^{-1}]) = 310 (5.69), 362 (12.41), 477 (12.71), 507 (54.73) nm. HRMS (APCI): m/z calcd for C$_{36}$H$_{38}$BN$_5$ [M + H]$^+$: calcd. 552.329929, found 552.330228.

**2-Iodo-1,3,5,7-tetramethyl-8-(4-pyridyl)-4-bora-3a,4a-diaza-*s*-indacene (4.46e)**
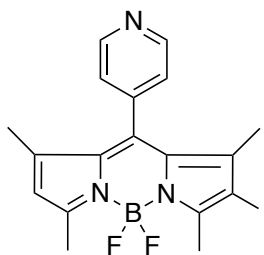
BODIPY **4.46e**

In accordance with general procedure **H** as described above using BODIPY **4.46** (0.1g, 0.305 mmol) and *N*-iodosuccinimide (0.085 g, 0.457 mmol) to yield a pinkish-red solid (81% yield). Analytical data is identical to the literature.[9] M.p. = 200 – 205 °C; Rf = 0.67 (DCM/Hex: 90/10); ^{1}H NMR (400 MHz, CDCl$_3$) δ 8.79 (s, 2H, Ar-*H*), 7.28 (d, *J* = 4.7 Hz, 2H, Ar-*H*), 6.05 (s, 1H, 6-*H*), 2.60 (d, *J* = 23.0 Hz, 6H, 3-C*H$_3$*, 5-C*H$_3$*), 1.44 (d, *J* = 19.3 Hz, 6H, 1-C*H$_3$*, 7-C*H$_3$*). ^{19}F NMR (377 MHz, CDCl$_3$) δ -146.17- -146.43. ^{11}B NMR (128 MHz, CDCl$_3$) δ 0.57 (t, *J* = 32.2 Hz). IR (neat): 2923, 2024, 1716, 1598, 1532, 1157, 977 cm^{-1}. HRMS (APCI): m/z calcd for C$_{18}$H$_{17}$BF$_2$IN$_3$ [M + H]$^+$: 452.060437, 452.060466 found.

2-Iodo-1,3,5,7-tetramethyl-8-(2-quinolinium-yl)-4-bora-3a,4a-diaza-*s*-indacene (4.49a)
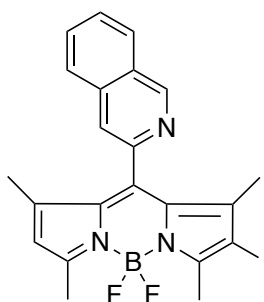
BODIPY **4.49a**

In accordance with general procedure **H** as described above using BODIPY **4.49** (0.1 g, 0.265 mmol) and *N*-iodosuccinimide (74.5 g, 0.397 mmol) and final product was obtained and purified by column chromatography (silica gel; DCM/Hex, 1:1, v/v) and removal of solvents followed by recrystallization (DCM/Hex) to yield pink solid (42% yield). M.p. = 220 – 225 °C; Rf = 0.47 (DCM/Hex: 90/10); ^{1}H NMR (400 MHz, CDCl$_3$) δ 8.35 (d, *J* = 8.3 Hz, 1H, Ar-*H*), 8.16 (d, *J* = 8.6 Hz, 1H, Ar-*H*), 7.94 (d, *J* = 7.8 Hz, 1H,

Ar-*H*), 7.83 (t, *J* = 7.8 Hz, 1H, Ar-*H*), 7.68 (t, *J* = 7.4 Hz, 1H, Ar-*H*), 7.52 (d, *J* = 8.4 Hz, 1H, Ar-*H*), 6.04 (s, 1H, 6-*H*), 2.61 (d, *J* = 25.8 Hz, 6H, 3-C*H₃*, 5-C*H₃*), 1.22 (s, 6H, 1-C*H₃*, 7-C*H₃*). ^{13}C NMR (101 MHz, CDCl₃) δ 158.86, 155.49, 153.76, 148.09, 144.61, 142.80, 138.54, 137.48, 130.67, 129.72, 127.86, 127.50, 122.41, 121.53, 84.15, 16.22, 14.16. ^{19}F NMR (377 MHz, CDCl₃) δ -145.03- -146.90. ^{11}B NMR (128 MHz, CDCl₃) δ 0.71 (t, *J* = 32.4 Hz). IR (neat): 2921, 1970, 1735, 1618, 1552, 1185, 970 cm^{-1}. UV-Vis (CH₂Cl₂) λ$_{max}$ (ε [x10^3 M^{-1} cm^{-1}]) = 319 (9.18), 383 (7.22), 490 (22.53), 523 (79.5) nm. HRMS (APCI): m/z calcd for C₂₂H₁₉BF₂IN₃ [M + H]$^+$: 502.076155, 502.076748 found.

2-Iodo-1,3,5,7-tetramethyl-8-(2-thiazolyl)-4-bora-3a,4a-diaza-*s*-indacene (4.51a)
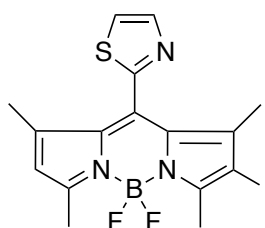
BODIPY **4.51a**

In accordance with general procedure **H** as described above using BODIPY **4.51** (0.1 g, 0.301 mmol) and *N*-iodosuccinimide (0.084, 0.451 mmol) t and final product was obtained and purified by column chromatography (silica gel DCM/Hex, 1:1, v/v) and removal of solvents followed by recrystallization (DCM/Hex) to yield pink solid (78% yield). M.p. = 184 – 189 °C; Rf = 0.65 (DCM/Hex: 90/10); ^{1}H NMR (400 MHz, CDCl₃) δ 8.02 (d, *J* = 3.3 Hz, 1H, Ar-*H*), 7.65 (d, *J* = 3.3 Hz, 1H, Ar-*H*), 6.08 (s, 1H, 6-*H*), 2.60 (d, *J* = 26.3 Hz, 6H, 3-C*H₃*, 5-C*H₃*), 1.45 (d, *J* = 7.9 Hz, 6H, 1-C*H₃*, 7-C*H₃*). ^{13}C NMR (101 MHz, CDCl₃) δ 158.86, 155.49, 153.76, 148.09, 144.61, 142.80, 138.54, 137.48, 131.89, 130.67, 129.72, 127.86, 127.50, 122.38, 121.53, 84.27, 16.22, 14.91. ^{19}F NMR (377 MHz, CDCl₃) δ -144.99- -146.50. ^{11}B NMR (128 MHz, CDCl₃) δ 0.60 (t, *J* = 31.9 Hz). IR (neat): 2961, 2161, 1709, 1612, 1454, 1054, 871 cm^{-1}. λ$_{max}$ (ε [x10^3 M^{-1} cm^{-1}]) = 309 (2.55), 406 (5.34), 520 (19.36), 551 (37.56) nm. HRMS (APCI): m/z calcd for C₁₆H₁₅BF₂IN₃S [M + H]$^+$: 458.016828, 458.016296 found.

2-Iodo-1,3,5,7-tetramethyl-8-phenyl-4-bora-3a,4a-diaza-s-indacene (4.53a)
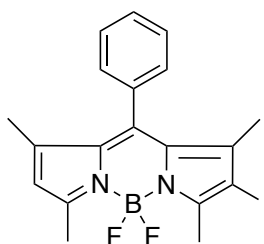
BODIPY **4.53a**

In accordance with general procedure **H** as described above using BODIPY **4.53** (0.1 g, 0.308 mmol) and *N*-iodosuccinimide (0.086 g, 0.462 mmol) and final product was obtained and purified by column chromatography (silica gel; DCM/Hex, 1:1, v/v) and removal of solvents followed by recrystallization (DCM/Hex) to yield pink solid (83% yield). Analytical data is identical to the literature.[10] M.p. = 146 – 151 °C; Rf = 0.65 (DCM/Hex: 90/10); ^{1}H NMR (400 MHz, CDCl$_3$) δ 7.51 – 7.47 (m, 3H, Ar-*H*), 7.27 – 7.24 (m, 2H, Ar-*H*), 6.04 (s, 1H, 6-*H*), 2.63 (d, *J* = 23.0 Hz, 6H, 3-C*H$_3$*, 5-CH$_3$), 1.37 (s, 6H, 1-C*H$_3$*, 7-CH$_3$). ^{19}F NMR (377 MHz, CDCl$_3$). ^{11}B NMR (128 MHz, CDCl$_3$) δ 0.71 (t, *J* = 32.4 Hz). IR (neat): 2921, 1970, 1735, 1618, 1552, 1185, 970 cm^{-1}. HRMS (APCI): m/z calcd for C$_{19}$H$_{18}$BF$_2$IN$_2$ [M + H]$^+$: 449.050651, 449.050778found.

1,3,5,7-tetramethyl-8-(4-pyridyl)-2-trimethylsilyl-4-bora-3a,4a-diaza-s-indacene (4.46f)
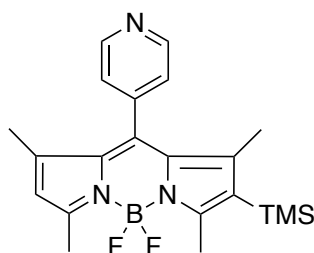
BODIPY **4.46f**

In accordance with general procedure **I** as described above using BODIPY **4.46e** (25 mg, 0.055 mmol), CuI (0.001 g, 0.005 mmol), Pd(PPh$_3$)Cl$_2$ (0.0014 g, 0.002 mmol) and TMSA (530 μl, 0.54mmol) and final product was obtained and purified by column chromatography (silica gel; DCM/Hex, 3:7, v/v) and removal of solvents followed by recrystallization (DCM/Hex) to yield pink solid (78% yield). M.p. = 175 – 180 °C; Rf = 0.63 (DCM/Hex: 90/10); ^{1}H NMR (400 MHz, CDCl$_3$) δ 8.79 (d, *J* = 2.5 Hz, 2H, Ar-*H*),

7.28 (d, J = 4.7 Hz, 2H, Ar-H), 6.05 (s, 1H, 6-H), 2.60 (d, J = 23.0 Hz, 6H, 3-CH_3, 5-CH$_3$), 1.44 (d, J = 19.3 Hz, 6H, 1-CH_3, 7-CH$_3$), 0.20 (s, 9H, 2-TMS). ^{13}C NMR (101 MHz, CDCl$_3$) δ 158.63, 157.83, 150.75, 144.08, 143.24, 142.88, 138.03, 131.41, 128.94, 123.18, 122.65, 116.00, 101.61, 97.04, 14.77, 13.52, 1.03. ^{19}F NMR (377 MHz, CDCl$_3$) δ -146.43- -146.17. ^{11}B NMR (128 MHz, CDCl$_3$) δ 0.57 (t, J = 32.2 Hz). IR (neat): 3044, 2959, 2147, 1733, 1599, 1537, 1309, 1059, 982 cm^{-1}. UV-Vis (CH$_2$Cl$_2$) λ$_{max}$ (ε [x10^3 M^{-1} cm^{-1}]) = 313 (4.00), 394 (9.06), 505(34.45), 535 (73.01) nm. HRMS (APCI): m/z calcd for C$_{21}$H$_{26}$BF$_2$N$_3$Si [M + H]$^+$: 422.203434, 422.203236 found.

1,3,5,7-tetramethyl-8-(2-thiazolyl)-2-trimethylsilyl-4-bora-3a,4a-diaza-s-indacene (4.51b)
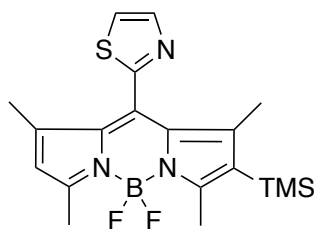
BODIPY **4.51b**

In accordance with general procedure **I** as described above using BODIPY **4.51a** (25 mg, 0.055 mmol), CuI (0.001 g, 0.005 mmol), Pd(PPh$_3$)Cl$_2$ (0.0014 g, 0.002 mmol) and TMSA (530 μl, 0.54mmol) and final product was obtained and purified by column chromatography (silica gel; DCM/Hex, 2:3, v/v) and removal of solvents followed by recrystallization (DCM/Hex) to yield pink solid (65% yield). M.p. = 155 – 160 °C; Rf = 0.65 (DCM/Hex: 90/10); ^{1}H NMR (400 MHz, CDCl$_3$) δ 8.02 (d, J = 3.3 Hz, 1H, Ar-H), 7.64 (d, J = 3.3 Hz, 1H, Ar-H), 6.06 (s, 1H, 6-H), 2.60 (d, J = 21.6 Hz, 6H, 3-CH_3, 5-CH_3), 1.49 (d, J = 14.2 Hz, 6H, 1-CH_3, 7-CH$_3$), 0.21 (s, 9H, 2-TMS). ^{13}C NMR (101 MHz, CDCl$_3$) δ 158.41, 155.31, 153.71, 148.23, 144.72, 143.1, 138.54, 137.38, 132.01, 130.51, 129.51, 128.10, 127.48, 122.37, 121.48, 84.27, 16.22, 14.6,1.02. ^{19}F NMR (377 MHz, CDCl$_3$) δ -144.99- -146.50. ^{11}B NMR (128 MHz, CDCl$_3$) δ 0.60 (t, J = 31.9 Hz). IR (neat): 2924, 2147, 15421, 1537, 1309, 1061, 980 cm^{-1}. UV/Vis (CDCl$_3$ λ$_{max}$ (ε [x10^3 M^{-1} cm^{-1}]) = 309 (2.55), 406 (5.34), 520 (19.36), 551 (37.56) nm. HRMS (APCI): m/z calcd for C$_{19}$H$_{24}$BF$_2$N$_3$SSi [M + H]$^+$: 428.159827, 428.159687 found.

1,3,5,7-tetramethyl-2-methyl-8-(4-pyridyl)-4-bora-3a,4a-diaza-s-indacene (4.46g)
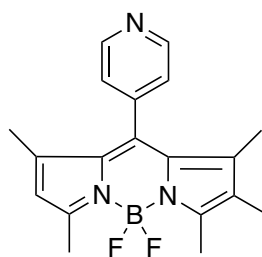
BODIPY **4.46g**

Previously synthesized BODIPY (**4.46f**) (1 eq.), CuI (0.1 eq.) and Pd(PPh$_3$)Cl$_2$ (0.05 eq.) were dissolved in dry THF:TEA(4:1) (5ml) at room temperature under inert atmosphere of argon. After stirring for 30 min trimethylsilyl acetylene (TMSA) (10 eq.) was added under argon. The reaction mixture was refluxed for 20 h. The mixture was then filtered and washed with a solution of saturated NaHCO$_3$ (2 x 50 ml) followed by washing with deionized water (2 x 50 ml). The resulting solution is dried over anhydrous sodium sulphate and evaporated in a rotavapor. The residue was purified by flash column chromatography eluting with Hexane:Ethyl acetate (9:1) to yield the pure product as a pinkish-orange crystalline solid (85% yield). M.p. = >300 °C; Rf = 0.69 (DCM/Hex: 90/10); ^{1}H NMR (400 MHz, CDCl$_3$) δ 8.81 (d, J = 0.6 Hz, 2H, Ar-H), 7.30 (d, J = 4.7 Hz, 2H, Ar-H), 6.06 (s, 1H, 6-H), 3.30 (s, 3H, 2-CH_3), 2.61 (d, J = 23.3 Hz, 6H, 3-CH_3, 5-CH$_3$), 1.45 (d, J = 21.2 Hz, 6H, 1-CH_3, 7-CH$_3$). ^{13}C NMR (101 MHz, CDCl$_3$) δ 158.86, 155.49, 153.76, 148.09, 144.61, 142.80, 138.54, 137.48, 131.89, 130.67, 129.72, 127.86, 127.50, 122.38, 121.53, 35.21, 16.22, 14.6. ^{19}F NMR (377 MHz, CDCl$_3$) δ -146.29- -146.03. ^{11}B NMR (128 MHz, CDCl$_3$) δ 0.56 (t, J = 32.2 Hz). IR (neat): 3044, 2959, 2147, 1733, 1599, 1537, 1309, 1059, 982 cm^{-1}. UV-Vis (CH$_2$Cl$_2$) λ$_{max}$ (ε [x10^3 M^{-1} cm^{-1}]) = 311 (0.94), 383 (1.79), 494 (5.81), 526 (16.76) nm. HRMS (APCI): m/z calcd for C$_{19}$H$_{20}$BF$_2$N$_3$ [M + H]$^+$: 350.163823, 350.163410 found.

2-((1,3,5,7-tetramethyl-8-(4-pyridyl)-4-bora-3a,4a-diaza-*s*-indacene)buta-1,3-diyn-1-yl)- 1,3,5,7-tetramethyl-8-(4-pyridyl)-4-bora-3a,4a-diaza-*s*-indacene (4.66)
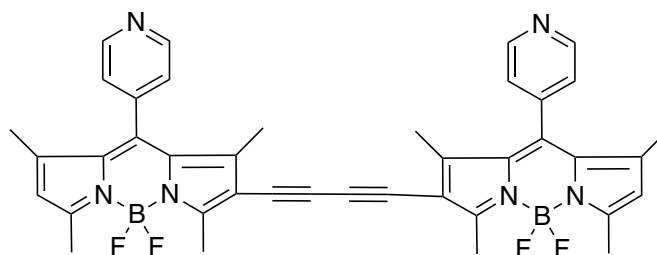
BODIPY **4.66**

BODIPY derivative **4.46g** (1 eq.), CuI (0.15 eq.) and Pd(PPh$_3$)Cl$_2$ (0.2 eq.) was dried under vacuum for about 4-5 hours and then were dissolved in dry THF:TEA(2:1) under inert Ar atmosphere. After 30 min BODIPY **4.46e** (1.5 eq.) was dissolved in 1 ml dry THF and was added to the previous mixture and the mixture was refluxed for 20 h at 66 ºC. The mixture was then filtered and washed with a solution of saturated NaHCO$_3$ (2 x 50 ml) followed by washing with deionized water (2 x 50 ml). The resulting solution is dried over anhydrous sodium sulphate and evaporated in a rotavapor. The residue was purified by flash column chromatography eluting with DCM:ethyl acetate (9:1) to yield the pure product as a purple crystalline solid (42% yield). M.p. = >300 °C; Rf = 0.21 (DCM/Ethyl acetate: 90/10); ^{1}H NMR (400 MHz, CDCl$_3$) δ 8.85 (s, 4H, Ar-*H*), 7.42 (s, 4H, Ar-*H*), 6.09 (s, 2H, 2-*H*, 6'-*H*), 2.65 (s, 6H, 3-C*H$_3$*, 5-CH$_3$), 2.59 (s, 6H, 1-C*H$_3$*, 7-CH$_3$), 1.47 (s, 6H, 3'-C*H$_3$*, 5'-CH$_3$), 1.42 (s, 6H, 1'-C*H$_3$*, 7'-CH$_3$). ^{13}C NMR (101 MHz, CDCl$_3$) δ 159.00, 159.00, 157.25, 157.25, 156.01, 156.01, 142.39, 133.01, 131.46, 131.44, 129.91, 129.91, 122.28, 122.28, 15.60, 14.71. ^{19}F NMR (377 MHz, CDCl$_3$) δ -145.97- -146.22. ^{11}B NMR (128 MHz, CDCl$_3$) δ 0.52 (t, *J* = 31.9 Hz). IR (neat): 2961, 1591, 1410, 1321, 1159, 1031, 980 cm^{-1}. UV-Vis (CH$_2$Cl$_2$) λ$_{max}$ (ε [x10^3 M^{-1} cm^{-1}]) = 328 (9.27), 412 (12.59), 520 (31.47), 559 (82.05) nm. HRMS (APCI): m/z calcd for C$_{40}$H$_{34}$B$_2$F$_4$N$_6$ [M + H]$^+$: 677.299074, 677.298843 found.

5.2. Singlet oxygen measurements

The photo-irradiation of the samples were performed in quartz cuvettes (2×1×1 cm) under an irradiation via a polychromatic light source (Philips, 15V-150W lamp), equipped with a 532 nm diode pumped solid state green laser system (CW532-04, average intensity of 10 mW·cm^{-2}). The temperature of the sample was maintained at 18 °C using a Peltier element (Cary Peltier 1×1 Cell Holder). Relative singlet oxygen ($^1O_2$) yields (Φ) were calculated from the degradation slopes of the 1,3-diphenylisobenzofuran (DPBF) conversion in the presence of different photosensitizers.

The slope of the curves of absorbance maxima of DPBF at 415 nm vs. irradiation time for each photosensitizer were calculated. Concentration of DPBF was adjusted such that UV-Vis absorbance of approximately in the air-saturated solvent system of DCM or MeOH before the photosensitizers were added to the cuvette. Relative singlet oxygen quantum yield ($\Phi_{\Delta PS}$) for each of these photosensitizers (PS) with 5,10,15,20-tetraphenylporphyrin (H$_2$TPP), Rose Bengal (RB) or methylene blue (MB) as a reference was calculated using the following equation.

$$\text{Equation 1; } \Phi_{\Delta PS} = \Phi_{\Delta ref} \times S_{PS}/S_{Ref}$$

where Φ represents quantum yield, S represents the slope, and PS and ref represent photosensitizer and reference molecule (H$_2$TPP, RB or MB), respectively.

5.3. Antimicrobial evaluation

General procedure for diffusion test for bacterial strains: Diffusion tests were performed through agar-tryptic soy (TSA) on Gram-positive *S. aureus* and Gram-negative *E. coli*. For PSs alone the concentration was set at 100µg/mL in TS broth, and for HA conjugates formulations with PSs the concentration was set to 350µg/ml. The stock solution (50 µL) was deposited onto each ring for each formulation and PSs. The Petri dishes were dried for 15 minutes and 2 of each inoculated Petri were kept under white LED light (total fluence: 25 J/cm²) and 2 of them were in dark condition at 37 °C. After irradiation, the Petri dishes were incubated at 37 °C in the dark.

General procedure for MIC/MBC evaluation: Two different plates for each strain were prepared: one plate for the dark condition and a second plate for light irradiation. Two controls were included: a bacterial growth control with no molecule added and negative control with PBS without bacterial inoculum and no molecule. The microplate was incubated at 37 °C for 1h in dark conditions. After that, bacteria were irradiated with white LED light (total fluence: 25 J/cm²). During the time of irradiation, the second plate was maintained in the dark. Then, 100 µL of 2-fold concentrated TS broth were added to each well and the microplate was incubated at 37 °C for 24 h. The Minimal Inhibition Concentration (MIC) is defined as the concentration of compound in µM, where a bacterial growth was observed. Three independent experiments were performed with each strain with CP-HA and the corresponding porphyrin.

General procedure for evaluation of inhibition of biofilm growth: The inhibition of biofilm formation was determined on bacterial cultures (*Staphylococcus aureus* CIP 76.25) by micro method in 96-well plates. Briefly, bacterial cultures in log-phase were diluted in TS broth and glucose (25mM) at a concentration equivalent to 4x10^6 CFU/mL. Serial dilutions of BODIPYs were performed in TS broth and glucose (25mM) to a final concentration from MIC 35µM to MIC 0.5µM and 100 µL of each dilution were added in the microplate wells. Then, 100 µl of diluted bacterial culture were added in each well. Two different plates were prepared: one plate for the dark condition and a second plate for light irradiation. Three controls were included; a bacterial growth control with no molecule added, a negative control with TS broth and glucose without bacterial inoculum and no molecule and a positive control with javel 3% added to the bacterial

inoculum. The microplate was incubated at 37°C for 5h with white light (total fluence: 25J/cm^2) or in the dark. After the microplate was left at 37°C for 24h.

The inhibition of biofilm formation was determined by Crystal violet Assay (biofilm reduction compared to the untreated control). The microplate was washed with distilled water. Then 125µL of 0.1% crystal violet was added in the microplate well for 15 min at RT. After incubation, the microplate was washed with distilled water and dried for 2 h. Then, 150µL of 33% acetic acid were added for 20 min at RT in the microplate wells to solubilize the biofilm. The optical density will be read at 595nm. Three independent experiments were performed.

General procedure for evaluation of biofilm eradication: Biofilm eradication was evaluated on bacterial cultures in 24-well plates. Briefly, bacterial cultures in log-phase were diluted in TS broth including glucose (25mM) for obtaining a concentration equivalent to 2x10^6 CFU/mL. 1mL of this diluted bacterial culture was added in each well. The microplate was incubated at 37°C, 100rpm for 24h in dark condition and in aerobic conditions. After this time, culture broth was removed. In parallel, serial dilutions of different molecules were performed in PBS to a final concentration from 32MIC to 1MIC and 500µL of each dilution was added in the microplate wells. Two different plates were prepared: one plate for the dark condition and a second plate for light irradiation. Three controls were included: a bacterial growth control with no molecule added, a negative control with culture broth without bacterial inoculum and no molecule and a positive control with bleach 3% added to the bacterial inoculum. The microplate was incubated at 37°C for 5h with white LED light (total fluence: 25J/cm²) or in the dark. Then, 500 µL of 2-fold concentrated TS broth and glucose (25mM) were added in each well and the microplate was incubated at 37°C for 24h.

Biofilm eradication was determined by Crystal violet Assay (biofilm reduction compared to the untreated control). The microplate was washed with distilled water. Then, 125µL of 0.1% crystal violet were added in the microplate well for 15 min at RT. After incubation, the microplate was washed with distilled water and dried for 2 h. Then, 150µL of 33% acetic acid were added for 20 min at RT in the microplate wells to solubilize the crystal violet. The optical density will be read at 595 nm. Obtained optical density (OD) for untreated control corresponded to 100% of biofilm. Obtained OD in other conditions (32MIC to 1MIC) were compared to untreated control to show the concentration of

compounds necessary to eradicate the biofilm. The results are the average of three independent experiments performed with *Staphylococcus aureus* CIP 76.25.

5.4. Experimental for X-ray crystallographic structure elucidations

Compounds were crystallized from slow evaporation of methanol (5) or dichloromethane (14). Individual single crystals were mounted on a nylon loop using crystallographic oil, and placed in a stream of N_2 at the temperature indicated in table 7, on a Bruker APEX-II Duo (030, 033, 036, 037, 039, 040, 043, 045, 058, 061, 062, 064, 067) or Bruker D8 ADVANCE ECO area detector (027, 032, 048, 050) diffractometer device, and reflections collected with $Cu_{K\alpha}$ or $Mo_{K\alpha}$ radiation as indicated in Table 8.[11,12]

Reflections were integrated and multi-scan absorption corrections performed using Bruker APEX3 software suite, and equivalent reflections merged with XPREP. Structure solution was performed with SHELXT (2018/2) and refinement performed with SHELXL (2018/3) in the Shelxle GUI.

All non-H atoms were refined anisotropically, with C-bound H- atoms constrained to idealized positions, and N- and O- bound H-atoms to geometric constraints, where appropriate. H atoms were refined with riding isotropic thermal parameters. In each case, aryl rotation was determined with MPLA instructions in ShelXL to obtain precise error margins.

Images were prepared using CrystalMaker software (CrystalMaker Ltd.).

5.4.1. Additional refinement details for each compound

BODIPY **4.47**: No special refinement necessary.

BODIPY **4.49**: No special refinement necessary.

BODIPY **4.50**: No special refinement necessary.

BODIPY **4.52**: No special refinement necessary. This compound exhibited a crystallographic void which was slightly smaller than a methanol molecule; Squeeze indicated that there was 1 electron in this void, indicating that there's not an additional missed solvent.

BODIPY **4.55**: Omitted 0 0 2, 1 0 1, -1 0 1, 1 0 0 due to presumed interference with the beamstop.

BODIPY **4.56**: No special refinement necessary.

BODIPY **4.57**: Disorder of the quinolinyl fragment was the correct model – an equivalent solution in Cc was unstable and gave 50:50 orientation of the two fragments at any rate. A loose ISOR restraint was used to constrain prolate behavior in C9, the terminal C1-bound methyl group.

BODIPY **4.59**: No special refinement necessary.

BODIPY **4.60**: Omitted ref. 0 1 5 and 6 1 6 due to stark disagreement with the model.

BODIPY **4.48a**: No special refinement necessary.

BODIPY **4.46b**: A squeeze model was chosen - the refinement was highly unstable when concerned with splitting individual solvent molecules, however the main fragment was well-ordered. Intermolecular hydrogen bonding which sits between O67 and its centrosymmetry partner indicate that this compound is at least $1/8^{th}$ protonated and that a disorder model is appropriate, given the inability to appropriately model counter-anions. As such, the exact protonation state of this compound is unknown.

BODIPY **4.48b**: No special refinement necessary.

BODIPY **4.56b**: Squeeze was used to account for disordered solvent (See: Spek, A. L., ActaCryst.(2015). C71, 9–18 doi:10.1107/S2053229614024929). The four-equivalent solvent-containing cavities sum to 17% of the total volume of the crystal (625 Å^3), slightly smaller than that expected for four ethyl acetate molecules at room temp. (650 Å^3).

BODIPY **4.54c**: generally poor diffraction at high angles, and unresolved dual pseudomerohedral twinning issues. Large Fourier ripples from Br.

BODIPY **4.49a**: Solution has residual Q-peaks from Fourier ripples from the I atom (B-alert, explicable). No special refinement.

BODIPY **4.46f**: No special refinement necessary.

BODIPY **4.46g**: No special refinement necessary.

BODIPY **4.66**: No special refinement necessary.

BODIPY **4.52a**: Disorder of the methyl and ethyl groups was fixed with PARTs 1,2,3 and SUMP for C50-57. SIMU was used to fix thermal parameters in the disordered fragments, and SADI was used to fix equivalent bonds between disordered atoms.

Table 5.1. Details of crystal structure determinations.

BODIPY	4.52	4.60	4.59	4.49	4.49a
Chemical Name	1,3,5,7-Tetramethyl-8-(1-methyl-1H-imidazol-2-yl)-4-bora-3a,4a-diaza-*s*-indacene	1,3,5,7-Tetramethyl-2,6-dimethyl-8-(1-methyl-2-imidazolyl)-4,4-difluoro-4-bora-3a,4a-diaza-s-indacene	1,3,5,7-Tetramethyl-2,6-diethyl-8-(2-thiazolyl)-4,4-difluoro-4-bora-3a,4a-diaza-s-indacene	8-(2-quinolinyl)-1,3,5,7-Tetramethyl-4,4-difluoro-4-bora-3a,4a-diaza-s-indacene	8-(2-quinolinyl)-2-iodo-1,3,5,7-Tetramethyl-4,4-difluoro-4-bora-3a,4a-diaza-*s*-indacene
Chemical Formula	$C_{18}H_{23}BF_2N_4$, CH_4O	$C_{21}H_{27}BF_2N_4$	$C_{20}H_{24}BF_2N_3$	$C_{22}H_{20}BF_2N_3$	$C_{22}H_{19}BF_2IN_3$
Crystal System	monoclinic	monoclinic	triclinic	monoclinic	monoclinic
Space Group	$P\,2_1/n$	$P\,2_1/c$	P -1	$P\,2_1/c$	$P\,2_1/n$
Crystal Description	plate	block	block	needle	block
Crystal Color	orange	dark red	red	green	red
a (Å)	7.0441(10)	11.1848(4)	9.9623(4)	11.4748(7)	11.3945(4)
b (Å)	13.9883(18)	9.8749(3)	10.7085(5)	10.9468(6)	12.3258(5)
c (Å)	19.426(3)	18.1421(6)	11.6635(5)	14.7520(9)	15.2655(6)
α (°)	90	90	63.911(2)	90	90
β (°)	90.823(4)	98.902(2)	89.778(3)	95.638(4)	109.5630(10)
γ (°)	90	90	63.148(2)	90	90
Volume (Å^3)	1913.9(4)	1979.64(11)	967.11(8)	1844.07(19)	2020.22(13)
Crystal Size (mm^3)	0.476 × 0.334 × 0.136	0.499 × 0.305 × 0.180	0.148 × 0.126 × 0.073	0.230 × 0.117 × 0.016	0.082 × 0.049 × 0.020
Density (a.u.)	1.250	1.289	1.330	1.352	1.648
μ (mm^{-1})	0.092	0.090	1.725	0.769	12.721
Absorption Correction	multi-scan	multi-scan	multi-scan	multi-scan	multi-scan
Tmin, Tmax	0.6977, 0.7454	0.6870, 0.7489	0.6718, 0.7531	0.5951, 0.7531	0.4196, 0.7531
Temp (K)	250(2)	100(2)	100(2)	100(2)	100(2)
λ (Å)	0.71073	0.71073	1.54178	1.54178	1.54178
Radiation type	Mo$_{K\alpha}$	Mo$_{K\alpha}$	Cu$_{K\alpha}$	Cu$_{K\alpha}$	Cu$_{K\alpha}$
Measured Reflections	25780	172163	12447	13292	19854
θ$_{max}$	26.893	45.507	68.737	68.432	68.373
Scan Mode	ω & φ	ω & φ	ω & φ	ω & φ	ω & φ
R$_1$ (all)	0.0761	0.0754	0.0608	0.0794	0.0491
R$_1$ (I > 2σ)	0.0533	0.0546	0.0537	0.0541	0.0489
wR$_2$ (all)	0.1508	0.1714	0.1763	0.1522	0.1220
wR$_2$ (I > 2σ)	0.1335	0.1503	0.1654	0.1358	0.1219
Goodness of Fit	1.056	1.060	1.098	1.061	1.051
H- atoms ref.	mixed	constr	constr	constr	constr
Independent Reflections	4106	16721	3513	3356	3714
Independent Reflections (I > 2σ)	3044	12210	3018	2403	3664
Max and Min residual	0.266, -0.242	0.801, -0.335	0.500, -0.336	0.244, -0.248	3.167, -1.347
Data / Parameters / Restraints	4106 / 243 / 1	16721 / 260 / 0	3513 / 250 / 0	3356 / 257 / 0	3714 / 266 / 0

BODIPY	4.57	4.56	4.47	4.55	4.50
Chemical Name	1,3,5,7-Tetramethyl-2,6-diethyl-8-(2-quinolinyl)-4,4-difluoro-4-bora-3a,4a-diaza-s-indacene	2,6-Diethyl-1,3,5,7-tetramethyl-8-(4-quinolyl)-4-bora-3a,4a-diaza-s-indacene	1,3,5,7-Tetramethyl-8-(5-pyrimidinyl)-4-bora-3a,4a-diaza-s-indacene	2,6-Diethyl-1,3,5,7-tetramethyl-8-(5-pyrimidinyl)-4-bora-3a,4a-diaza-s-indacene	1,3,5,7-Tetramethyl-8-(9-acridinyl)-4-bora-3a,4a-diaza-s-indacene
Chemical Formula	$C_{26}H_{28}BF_2N_3$	$C_{26}H_{28}BF_2N_3$	$C_{17}H_{17}BF_2N_4$	$C_{21}H_{25}BF_2N_4$	$C_{26}H_{22}BF_2N_3$
Crystal System	monoclinic	monoclinic	monoclinic	monoclinic	monoclinic
Space Group	$C\,2/c$	$P\,2_1$	$P\,2_1/c$	$P\,2_1$	$P\,2_1/n$
Crystal Description	needle	block	block	block	plate
Crystal Color	red	red	yellow	red	orange
a (Å)	18.4461(17)	7.6285(2)	18.4992(5)	10.1246(5)	7.2118(4)
b (Å)	13.3097(12)	18.9562(5)	6.1188(2)	5.5218(3)	19.5719(11)
c (Å)	11.1497(10)	7.8224(2)	15.1533(4)	17.7577(9)	29.2646(15)
α (°)	90	90	90	90	90
β (°)	124.286(2)	94.240(2)	113.7470(10)	104.2133(15)	94.0493(18)
γ (°)	90	90	90	90	90
Volume (Å³)	2261.7(4)	1128.08(5)	1570.02(8)	962.37(9)	4120.3(4)
Crystal Size (mm³)	0.620 × 0.395 × 0.103	0.343 × 0.242 × 0.178	0.476 × 0.324 × 0.160	0.448 × 0.114 × 0.067	0.425 × 0.184 × 0.054
Density (a.u.)	1.267	1.270	1.380	1.319	1.371
μ (mm⁻¹)	0.086	0.086	0.100	0.093	0.093
Absorption Correction	multi-scan	multi-scan	multi-scan	multi-scan	multi-scan
Tmin, Tmax	0.6872, 0.7461	0.6612, 0.7489	0.6986, 0.7489	0.7079, 0.7456	0.6404, 0.7452
Temp (K)	100(2)	100(2)	100(2)	100(2)	100(2)
λ (Å)	0.71073	0.71073	0.71073	0.71073	0.71073
Radiation type	MoK\a	MoK\a	MoK\a	MoK\a	MoK\a
Measured Reflections	30664	83770	103750	21525	39878
θ_{max}	30.523	45.276	45.361	27.587	25.482
Scan Mode	ω & φ	ω & φ	ω & φ	ω & φ	ω & φ
R_1 (all)	0.0739	0.0824	0.0529	0.0551	0.1204
R_1 (I > 2σ)	0.0557	0.0525	0.0406	0.0418	0.0563
wR_2 (all)	0.1542	0.1486	0.1239	0.1015	0.1546
wR_2 (I > 2σ)	0.1412	0.1302	0.1146	0.0939	0.1238
Goodness of Fit	0.863	0.989	1.052	1.057	1.031
H- atoms ref.	constr	constr	constr	constr	constr
Independent Reflections	3450	18857	13053	4431	7648
Independent Reflections (I > 2σ)	2631	13462	10338	3794	4409
Max and Min residual	0.536, -0.342	0.534, -0.284	0.727, -0.254	0.379, -0.267	0.254, -0.297
Data / Parameters / Restraints	3450 / 194 / 6	18857 / 295 / 1	13053 / 221 / 1	4431 / 259 / 1	7648 / 585 / 0

BODIPY	4.46f	4.46g	4.66	4.48a	4.54c
Chemical Name	1,3,5,7-Tetramethyl-8-(4-pyridyl)-2-trimethylsilyl-4-bora-3a,4a-diaza-*s*-indacene	1,3,5,7-Tetramethyl-2-methyl-8-(4-pyridyl)-4-bora-3a,4a-diaza-*s*-indacene	2-((1,3,5,7-Tetramethyl-8-(4-pyridyl)-4-bora-3a,4a-diaza-*s*-indacene)buta-1,3-diyn-1-yl)- 1,3,5,7-tetramethyl-8-(4-pyridyl)-4-bora-3a,4a-diaza-*s*-indacene	1,3,5,7-Tetramethyl-8-(4-*N*-methylquinolinium)-4,4-difluoro-4-bora-3a,4a-diaza-*s*-indacene	2,6-Diethyl-1,3,5,7-tetramethyl-8-(*N*-(4-phenoxybutyl)pyridinium-4-yl)-4-bora-3a,4a-diaza-*s*-indacene
Chemical Formula	$C_{23}H_{26}BF_2N_3Si$	$C_{20}H_{18}BF_2N_3$	$C_{40}H_{34}B_2F_4N_6$	$C_{23}H_{24}BBrF_2N_3O_{0.50}$	$C_{32}H_{41}BBrF_2N_3O_2$
Crystal System	triclinic	monoclinic	orthorhombic	monoclinic	monoclinic
Space Group	$P\bar{1}$	$P2_1/c$	$Pna2_1$	$C\,2/c$	$P\,2_1/c$
Crystal Description	needle	needle	oblong	oblong	oblong
Crystal color	red	red	Purple-violet	red	red
a (Å)	8.7870(3)	14.6509(18)	20.7649(5)	23.4395(8)	19.4295(15)
b (Å)	10.9761(4)	11.5401(13)	7.0387(2)	7.3588(3)	18.5995(15)
c (Å)	11.6926(4)	10.4773(12)	23.8366(6)	24.9912(8)	8.4588(7)
α (°)	11	90	90	90	90
β (°)	10	105.490(3)	90	91.5314(17)	93.377(4)
γ (°)	11	90	90	90	90
Volume (Å³)	1118.21(7)	1707.1(3)	3483.91(16)	4309.1(3)	3051.5(4)
Crystal Size (mm³)	0.43 x 0.11 x 0.08 mm3	0.27 x 0.15 x 0.11	0.129 x 0.071 x 0.033	0.256 × 0.081 × 0.020	0.326 × 0.220 × 0.042
Density (a.u.)	1.251	1.359	1.328	1.477	1.368
μ (mm^{-1})	1.182	0.096	0.773	2.895	1.393
Absorption Correction	Semi-empirical from equivalents	Semi-empirical from equivalents	Semi-empirical from equivalents	multi-scan	multi-scan
Tmin, Tmax	0.5545, 0.7533	0.5917, 0.7533	0.6153, 0.7533	0.5064, 0.7531	0.5525, 0.7461
Temp (K)	100.01	100(2)	100(2)	100(2)	100(2)
λ (Å)	1.54178	0.71073	1.54178	1.54178	0.71073
Radiation type	CuK\a	MoK\a	CuK\a	CuK\a	MoK\a
Measured Reflections	18442	22677	53878	18075	75140
θ_{max}	69.923	26.191	69.981	68.399	30.499
Scan Mode	ω & φ	ω & φ	ω & φ	ω & φ	ω & φ
R_1 (all)	0.0465	0.0912	0.0423	0.0681	0.1222
R_1 (I > 2σ)	0.0457	0.0553	0.0359	0.0625	0.0875
wR_2 (all)	0.1299	0.1254	0.0935	0.1980	0.2990
wR_2 (I > 2σ)	0.1290	0.1095	0.0893	0.1926	0.2669
Goodness of Fit	1.035	1.069	1.025	1.042	1.192
H- atoms ref.	mixed	mixed	mixed	mixed	mixed
Independent Reflections	4177	3400	6502	3939	9270
Independent Reflections (I > 2σ)	4350	8730	6560	3467	6801
Max and Min residual	0.397 and -0.370	0.286 and -0.296	0.262 and -0.167	1.561, -0.832	2.946, -1.580
Data / Parameters / Restraints	4177 / 278/0	3400 /240/0	6502 /478/1	3939 / 285 / 3	9270 / 383 / 3

BODIPY	4.48b	4.54b	4.56b	4.52a
Chemical Name	1,3,5,7-Tetramethyl-2,6-diethyl-8-(4-pyridyl-2-(benzyl-4-carboxylic acid))-4,4-difluoro-4-bora-3a,4a-diaza-s-indacene	1,3,5,7-Tetramethyl-2,6-diethyl-8-(4-quinolinium)-yl-2-(benzyl-4-carboxylic acid))-4,4-difluoro-4-bora-3a,4a-diaza-s-indacene	1,3,5,7-Tetramethyl-8-(4-pyridyl-yl-2-(benzyl-4-carboxylate))-4,4-difluoro-4-bora-3a,4a-diaza-s-indacene	(Z,Z)-2,5-Bis(2-thiazolylmethanylidene)-3-ethyl-4-methylpyrrole
Chemical Formula	$C_{30}H_{33}BBrF_2N_3O_2$	$C_{38}H_{43}BBrF_2N_3O_4$	$C_{26}H_{32.12}BCl_{0.12}F_2N_3O_6$	$C_{15}H_{15}N_3S_2$
Crystal System	monoclinic	orthorhombic	triclinic	monoclinic
Space Group	$P\,2_1/c$	$P\,2_12_12_1$	$P\,{-1}$	$P\,2_1/c$
Crystal Description	needle	plate	needle	plate
Crystal color	red	orange	red	red
a (Å)	10.0239(3)	8.7972(3)	11.0357(5)	13.3172(11)
b (Å)	29.6079(9)	12.7756(4)	20.6326(9)	10.2096(8)
c (Å)	9.8588(3)	32.3590(11)	24.0869(10)	22.0316(17)
α (°)	90	90	104.197(2)	90
β (°)	104.3361(14)	90	91.229(2)	102.2850(18)
γ (°)	90	90	100.238(3)	90
Volume (Å³)	2834.85(15)	3636.8(2)	5220.1(4)	2926.9(4)
Crystal Size (mm³)	$0.430 \times 0.104 \times 0.065$	$0.388 \times 0.181 \times 0.010$	$0.420 \times 0.097 \times 0.034$	$0.640 \times 0.387 \times 0.156$
Density (a.u.)	1.397	1.341	1.364	1.368
μ (mm⁻¹)	2.354	1.982	0.999	0.357
Absorption Correction	multi-scan	multi-scan	multi-scan	multi-scan
Tmin, Tmax	0.5741, 0.7531	0.5723, 0.7531	0.5791, 0.7531	0.6788, 0.7454
Temp (K)	100(2)	100(2)	100(2)	100(2)
λ (Å)	1.54178	1.54178	1.54178	0.71073
Radiation type	CuK\a	CuK\a	CuK\a	MoK\a
Measured Reflections	53661	26430	86688	39541
θ_{max}	68.416	68.361	68.438	26.559
Scan Mode	ω & φ	ω & φ	ω & φ	ω & φ
R_1 (all)	0.0331	0.0518	0.0837	0.0919
R_1 (I > 2σ)	0.0318	0.0434	0.0622	0.0701
wR_2 (all)	0.0913	0.1115	0.1966	0.1699
wR_2 (I > 2σ)	0.0904	0.1064	0.1776	0.1559
Goodness of Fit	1.057	1.016	1.066	1.128
H- atoms ref.	mixed	mixed	constr	constr
Independent Reflections	5183	6585	19030	6082
Independent Reflections (I > 2σ)	4903	5739	13396	4733
Max and Min residual	0.417, -0.516	0.306, -0.275	1.196, -0.364	0.521, -0.696
Data / Parameters / Restraints	5183 / 376 / 0	6585 / 398 / 0	19030 / 1241 / 0	6082 53 / 154

5.5. References

1. Drogat N, Barrière M, Granet R, Sol V and Krausz P. *Dye. Pigm.* 2011; **88**: 125-127.

2. Drogat N, Granet R, Le Morvan C, Bégaud-Grimaud G, Krausz P and Sol V. *Bioorg. Med. Chem. Lett.* 2012; **22**: 3648-3652.

3. Le Guern F, Sol V, Ouk C, Arnoux P, Frochot C and Ouk TS. *Bioconjug. Chem.* 2017; **28**: 2493-2506.

4. Thai HBD, Yu JK, Park BS, Park YJ, Min SJ and Ahn DR. *Biosens. Bioelectron.* 2016; **77**: 1026-1031.

5. Ongun O, Taşcı E, Emrullahoğlu M, Akın Ü, Tuğluoğlu N and Eymur S. *J. Mater. Sci. Mater. Electron.* 2021: 15707-15717.

6. Alamiry MAH, Harriman A, Mallon LJ, Ulrich G and Ziessel R. *Eur. J. Org. Chem.* 2008: 2774-2782.

7. Lamaster DJ, Kaufman NEM, Bruner AS and Vicente MGH. *J. Phys. Chem. A* 2018; **122**: 6372-6380.

8. Gotor R, Ashokkumar P, Hecht M, Keil K and Rurack K. *Anal. Chem.* 2017; **89**: 8437-8444.

9. Raza MK, Gautam S, Howlader P, Bhattacharyya A, Kondaiah P and Chakravarty AR. *Inorg. Chem.* 2018; **57**: 14374-14385.

10. Dong Y, Sukhanov AA, Zhao J, Elmali A, Li X, Dick B, Karatay A and Voronkova VK. *J. Phys. Chem. C* 2019; **123**: 22793-22811.

11. Hohlfeld BF, Gitter B, Flanagan KJ, Kingsbury CJ, Kulak N, Senge MO and Wiehe A. *Org. Biomol. Chem.* 2020; **18**: 2416-2431.

12. Kingsbury CJ and Senge MO. *Coord. Chem. Rev.* 2021; **431**: 213760-.213783.

SUMMARY

Photodynamic therapy (PDT) has been used as a minimally invasive therapeutic tool in clinical settings against malignant cells and infected tissue. The cytotoxicity is induced by a light source potentially exerting a selective activity against the infections. This approach has found potential anti-microbial uses in recent times against all types of microorganisms, such as Gram-positive and Gram-negative bacteria, fungi, parasites and even viruses. Antimicrobial Photodynamic therapy (aPDT) provides a possible way to eliminate diseases causing microbes efficiently, cost-effectively, and more importantly, without the associated mechanism of resistance. This manuscript describes inclusive study into synthetic and post-synthetic advances made towards enhancing the efficiency of photosensitizers (PSs) for this therapy. More explicitly, it provides an insight to making a PS aPDT compatible by combining it with a drug delivery system or synthetically altering the molecular skeleton of the PS with functionalities which induces better potency towards the site of infection.

In chapter 1, we describe the advancements and challenges for efficient antimicrobial therapy. Even though aPDT is emerging as a potential tool against the worlds tormenting issue of increasing number of drug-resistant pathogens, most PSs used for conventional therapies lack selectivity, target specificity and can undergo self-quenching in biological media due to aggregation. Several strategies to enhance the activity of such PSs have been discussed above which allows for a better solubility and selectivity of the PSs towards the target microbe. This concludes to have a good drug delivery system or chemically altering the molecular skeleton of the PS itself to introduce functionalities to help with problem of quenching and aggregation in aqueous media also aiding a better target selectivity and interaction.

In chapter 2, we describe the conjugating formulation of PSs that have been known in literature for their aPDT potential with an aim to enhance the solubility index of these PSs along with an aim to have better selectivity against the microbes. Hemi-synthesis and synthesis of PSs as polyaminated chlorin-*p6* and 5-(4-aminophenyl)-10,15,20-tris(4-*N*-methylpyridinium)porphyrin triiodide is performed and then their water stable and soluble formulation with hyaluronic acid bio-polymer (PS-HA) is achieved. Structures of porphyrin-HA formulations were characterized by IR, DSC, DLS, zeta

potential, SEM imaging, UV-vis analysis and rheological evaluation confirming the covalent conjugation of PSs on conjugate platform (hyaluronic acid). These conjugate formulations were tested against the Gram-negative *Escherichia coli* and Gram-positive *Staphylococcus aureus* bacteria for their potency for aPDT. The PS-HA conjugates with photo-bactericidal studies showed a minimal antimicrobial action in the presence of light which could be due to strong negative charges of the carboxylic acid residues of hyaluronic acid which might lead to a lower interaction between the formulation and the bacterial walls. This however could be potentially resolved with either increasing the number of PSs to be conjugated or by employing cross-linkers to accommodate the PSs within the conjugate synthesized.

In chapter 3, relative singlet oxygen yields of porphyrin and BODIPY based PSs are evaluated using the standard diphenyl benzofuran (DPBF) singlet oxygen degradation assay. DPBF molecule degrades in presence of singlet oxygen produced by PSs and this assay also used in Chapter 4 gives an insight to the photobiological activity of such synthesized chromophores and establishes the grounds of their efficiency to be evaluated against the microbes. These studies give an insight of how different functionalization influence the photophysical/photochemical properties of PSs to be used in aPDT.

In chapter 4 with an aim to build up a library of fluorescent aPDT active PSs and addressing the innate solubility issues, low selectivity with the bacterial culture different functionalization of such PSs with different strategies is done. A library of borondipyrromethenes difluoroboradiazaindacene (BODIPY) dyes synthesized via *meso*-aryl groups and post functionalized with suitable synthetic strategies on the *meso*-N-functionalized ring via methylation, carboxylation and etherate group introduction or by modifying the core of the BODIPY skeleton with heavy atoms or introduction of expanded π-conjugations via Sonogoshira cross-coupling reactions and as a final example by replacements and substitutions via Grignard reaction on B-F bond of the molecule. Only a few examples of such BODIPY scaffolds exist in literature even though it offers amazing opportunities to be synthetically alter and introduce the aPDT active functionalities on the BODIPY core. The synthesized BODIPY molecules have been characterized by UV-vis, NMR, HRMS spectrometry, X-ray crystal structure evaluation and lastly to identify the best synthetic strategy efficient for production of singlet oxygen species as measured by DPBF degradation assays and microbial growth inhibition assays (MIC/MBC) and biofilm inhibition and eradication against the

Gram-positive *Staphylococcus aureus* bacteria and Gram-negative *Pseudomonas aeruginosa* bacteria. 31 Novel BODIPY scaffolds have been synthesized and it can be concluded that the water-soluble derivatives do show an acceptable range of inhibition activity with production of singlet oxygen and microbial inactivation. Iodide substitution on the BODIPY core shows an explicit result in both enhancement in production of singlet oxygen species as measure via DPBF assay and for the inhibition against the bacteria. These examples open a window of exploration of how different functionalization can affect the antimicrobial action of the BODIPY dyes and opens an opportunity to synthetically enhance the scaffolds for the set goal.

Penultimate chapter 5 includes synthetic methods and procedures to synthesize the aPDT active PSs and conjugates as described for chapter 2 and chapter 4. These strategies can be used to synthesize more examples with similar strategies but an improve activity for aPDT. This chapter also encompasses the procedures to perform and elucidate the crystal-structures of some new BODIPY dyes, the inhibition assays for growth of microbes (Gram-positive and Gram-negative bacteria) and their biofilms and the singlet oxygen measurement protocol used in chapter 3 and 4 as for new BODIPY dyes and some synthetically derived porphyrins, homoporphyrins and tetraphenylethylene (TPE)-BODIPY scaffolds for their efficiency in degradation of DPBF in presence of light.

Overall, this manuscript has provided novel strategies for derivatizing molecules as conjugates or post-synthetic derivatives which have characteristics for an ideal PS to be utilized in and exemplifying a new generation of PSs and conjugates for aPDT.

RESUMÉ

Formulation antimicrobienne et fonctionnalisation de photosensibilisateurs pour la thérapie photodynamique antimicrobienne (aPDT)

Depuis une vingtaine d'année, le développement de nouvelles bactéries multirésistantes aux antibiotiques est un problème de santé public mondiale. Les scientifiques sont à la recherche de nouvelles approches capable d'éliminer des microbes pathogènes sans entrainer de résistances. La thérapie photodynamique antimicrobienne (aPDT) est un moyen innovant et non invasif de détruire les bactéries via la formation d'espèces réactives de l'oxygène (ROS) après illumination avec une longueur d'onde appropriée d'une molécule : un photosensibilisateur (PS). Cette technique pourrait fournir une solution de traitement durable face à ces différentes infections bactériennes. En effet, les ROS produits favorise alors l'endommagement des parois bactériennes mais également des cibles microbiennes telles que les acides nucléiques (ADN ou ARN), les protéines, les lipides, les complexes protéiques, ou en entravant la matrice du biofilm. Ce travail de thèse présente une étude sur les stratégies de synthése visant à améliorer l'efficacité des PS pour cette thérapie. Ainsi au cours de ce travail, nous avons développé différentes voies permettant de rendre un PS efficace pour des applications en aPDT. Pour cela, nous nous sommes, tout d'abord, attachés à augmenter l'efficacité de ces PS en les combinant avec un système d'administration de médicaments tels que des polysaccharides ou en modifiant synthétiquement le squelette moléculaire du PS avec des fonctionnalités qui induit une meilleure interaction avec les microorganismes. Les stratégies synthétiques, les caractérisations spectroscopiques et la caractérisation photophysique, y compris la production d'espèces d'oxygène singulet via des tests de dégradation DPBF, sont discutées tout au long de ce manuscrit. Différentes stratégies afin d'obtenir un PS idéal pour une utilisation en aPDT ont été mises en œuvre, notamment la fabrication de conjugués d'acide hyaluronique (HA) biopolymère solubles dans l'eau avec des PS synthétisés à base de macrocycles issu de la chlorophylle et de porphyrine de synthèses. La synthèse de nouveaux BODIPY portant différents groupements en position *méso* ont été réalisés. Ils ont été caractérisés par RMN, spectrométrie de masse, UV-visible et cristallographie. Enfin, tous ces conjugués ainsi que des dérivés de BODIPY ont été testés contre des bactéries, mettant ainsi en évidence que certaines de ces molécules étaient capables d'inhiber la croissance des bactéries et de leurs biofilms sous irradiation lumineuse, démontrant l'efficacité de telles stratégies pour une éventuelle application en photothérapie antimicrobienne.

Mots-clés: Photosensibilisateurs, Thérapie photodynamique antimicrobienne (aPDT), Acide hyaluronique, BODIPY, Oxygène singulet, Diphénylbenzofurane (DPBF)

Antimicrobial formulation and functionalization of photosensitizers for antimicrobial photodynamic therapy (aPDT)

To provide a long-lasting solution to infections affecting the current world scenario, antimicrobial photodynamic therapy (aPDT) offers a non-invasive means to destroy pathogenic microbes via formation of reactive oxygen species (ROS) on irradiation with an appropriate wavelength of light of a photosensitizing molecule, photosensitizer (PS). This ROS species promotes the damage of microbial targets such as nucleic acids (DNA or RNA), proteins, lipids, protein complexes, or by impeding the biofilm matrix. This manuscript work presents an inclusive study into synthetic and post-synthetic strategies made towards enhancing the efficiency of PSs for this therapy. More explicitly, it provides an insight to making a PS aPDT compatible by combining it with a drug delivery system or synthetically altering the molecular skeleton of the PS with functionalities which induces better potency towards the site of infection. The synthetic strategies, spectroscopic characterizations and photophysical characterization including the production of singlet oxygen species via DPBF degradation assays are discussed along this manuscript. Different strategies for making the PS ideal for use in aPDT have been done which includes making water-soluble biopolymeric hyaluronic acid (HA) conjugates with synthesized PSs based on chlorin and porphyrin macrocycles or by synthesizing BODIPY scaffolds with different *meso*-aryl groups and post functionalizing these derivatives with different functionalities enhancing their spectrum towards inactivation of bacterial cultures. Finally, these conjugates as well as BODIPY derivatives have been tested against bacteria, finding that some of these molecules were able to inhibit the growth of bacteria and their biofilms under light irradiation, demonstrating the efficiency of such strategies for a potential aPDT.

Keywords: Photosensitizers, Antimicrobial photodynamic therapy (aPDT), Hyaluronic acid, BODIPY, Singlet Oxygen, Diphenylbenzofuran (DPBF)